Computational Design of 3D Printed Personalized Artificial Spinal Disc

DISS. ETH NO. 27911

Computational Design of 3D Printed Personalized Artificial Spinal Disc

A thesis submitted to attain the degree of

DOCTOR OF SCIENCES of ETH ZURICH

(Dr. sc. ETH Zurich)

Presented by

Zhiyang Yu

MSc ETH

born on 29.01.1992

Citizen of China

Accepted on the recommendation of

Prof. Dr. Kristina Shea

Prof. Dr. Stephen J. Ferguson

Dr. Tino Stanković

2021

Abstract

Low back pain, which is a worldwide health problem, is the leading cause of activity limitation and work absence throughout much of the world and causes an enormous economic burden on society [1][2]. Literature shows that 70–85% of all people will have back pain at some time in life [3]. Compared to spinal fusion, total disc replacement (TDR) that uses an artificial spinal disc (ASD) to replace the degenerated intervertebral disc (IVD) is a motion-preserving surgical technique to treat serious back pain. Although ASD design is shown to be critical to the clinical outcomes of TDR and many attempts have been made to improve ASD designs, very little success has been achieved. The development of a reliable ASD that is able to restore the natural mechanics of the implanted spinal segment remains to be a substantial challenge, which is mainly due to the complicated biomechanical environment faced by the IVD and the complex mechanics of an IVD that consists of nonlinear, viscoelastic, and anisotropic behavior [4].

Inspired by the potential of second-generation viscoelastic ASDs and the design freedom provided by multi-material additive manufacturing (AM), this thesis explores the feasibility of using an elastomeric, multi-material, patient-specific ASD fabricated with multi-material AM for achieving anatomical match and reproducing customized mechanics. Five conceptual designs for multi-material ASD that either employ biomimicry or structures inspired by mechanical metamaterials are proposed. This thesis also proposes a general computational design method for the optimization of patient-specific ASDs to reproduce customized mechanics. The performance of five proposed conceptual designs is investigated using in-vitro mechanical testing to determine the most favorable design concept according to defined design criteria. Given this design concept and the manufacturing constraints, the overall workflow for patient-specific ASD design is implemented to examine the ability of this design concept to reproduce patient-specific mechanics. To improve the efficiency of the computational design method, the feasibility of several strategies such as problem dimension reduction and a regression model is also explored in this work. In the end, general guidelines for the design of multi-material ASDs are proposed from the knowledge gained throughout this thesis.

This thesis shows that ASD design concepts mimicking the structure found in an IVD have great potential for restoring natural mechanics. In addition, ASD design concepts that employ structures inspired by mechanical metamaterials are able to exhibit nature-mimicking nonlinear behavior that are otherwise difficult to achieve with the given materials and 3D printing technique. Furthermore, this thesis verifies the general applicability of computational method for patient-specific ASD design and strategies such as machine learning for improving the efficiency of the design process. This thesis demonstrates the great potential of a patient-specific, multi-material ASD fabricated with multi-material AM, and serves as inspiration for the future development of multi-material ASDs.

Zusammenfassung

Kreuzschmerzen, ein weltweites Gesundheitsproblem, sind in weiten Teilen der Welt die Hauptursache für Aktivitätseinschränkungen und Arbeitsausfälle und verursachen eine enorme wirtschaftliche Belastung für die Gesellschaft. Die Literatur zeigt, dass 70–85 % aller Menschen irgendwann im Leben Rückenschmerzen haben. Im Vergleich zur Wirbelsäulenfusion ist der totale Bandscheibenersatz, der eine künstliche Bandscheibe (ASD) verwendet, um die degenerierte Bandscheibe zu ersetzen, eine bewegungserhaltende Operationstechnik zur Behandlung schwerer Rückenschmerzen. Obwohl sich das ASD-Designkonzept als kritisch für die klinischen Ergebnisse von dem totalen Bandscheibenersatz erwiesen hat und viele Versuche unternommen wurden, das ASD-Design zu verbessern, wurde nur sehr wenig Erfolg erzielt. Die Entwicklung einer zuverlässigen ASD, die in der Lage ist, die natürliche Mechanik des implantierten Wirbelsäulensegments wiederherzustellen, bleibt eine große Herausforderung wegen der komplizierten biomechanischen Umgebung und des nichtlinearen, viskoelastischen und anisotropen Verhaltens einer Bandscheibe.

Inspiriert vom Potenzial viskoelastischer ASDs und der Gestaltungsfreiheit, die durch die Multimaterial additive Fertigung (Multimaterial-AM) geboten wird, untersucht diese Dissertation die Machbarkeit der Verwendung einer elastomeren, patientenspezifischen, Multimaterial-ASD, welche mit Multimaterial-AM produziert wird, um eine anatomische Übereinstimmung und Reproduktion einer angepassten Mechanik zu erreichen. Fünf Multimaterial-ASD-Designkonzepte werden vorgeschlagen, die entweder Biomimikry oder von mechanischen Metamaterialien inspirierte Strukturen verwenden. Diese Arbeit schlägt auch eine allgemeine Methode für die Optimierung einer ASD vor, um eine patientenspezifische Mechanik zu reproduzieren. Die Leistungsfähigkeit von fünf vorgeschlagenen ASD-Designkonzepte wird durch in-vitro-mechanische Tests untersucht, um das beste Designkonzept nach definierten Designkriterien zu ermitteln. Angesichts dieses Designkonzepts und der Herstellungsbeschränkungen wird der Gesamtworkflow für die patientenspezifische ASD implementiert, um die Fähigkeit dieses Designkonzepts zu untersuchen, patientenspezifische Mechanik zu reproduzieren. Um die Effizienz der Methode zu verbessern, wird in dieser Dissertation auch die Machbarkeit mehrerer Strategien wie der Reduzierung der Problemdimension und eines Regressionsmodells untersucht. Am Ende werden allgemeine Richtlinien für das Design von Multimaterial-ASD vorgeschlagen.

Diese Dissertation zeigt, dass ASD-Designkonzepte, die die Struktur einer Bandscheibe nachahmen, großes Potenzial zur Wiederherstellung der natürlichen Mechanik haben. Darüber hinaus können ASD-Designkonzepte, die von mechanischen Metamaterialien inspirierte Strukturen verwenden, ein naturnahes nichtlineares Verhalten aufweisen, das ansonsten mit den gegebenen Materialien und der 3D-Drucktechnik schwer zu erreichen ist. Zusätzlich verifiziert diese Arbeit die allgemeine Anwendbarkeit der Methode für das patientenspezifische ASD-Design und Strategien wie künstliche Intelligenz zur Verbesserung der Effizienz des Designprozesses. Diese Arbeit zeigt das große Potenzial

einer patientenspezifischen Multimaterial-ASD, die mit Multimaterial AM hergestellt wird, und dient als Inspiration für die zukünftige Entwicklung von Multimaterial-ASDs.

Acknowledgments

It is not the strongest of the species that survives, nor the most intelligent that survives. It is the one that is the most adaptable to change (by Charles Darwin). Throughout my five-year PhD experience, I am always amazed by how nature creates organs in creatures with so complex structures out of the grasp of our understandings. Yet everything created by nature exists for a reason and everything makes sense and works together to form a precise and accurate system. The journey to create an artificial spinal disc is like a journey through a philosophical world, to see to which degree we humans can recreate of the nature with our intelligences.

First and foremost, I would like to thank Prof. Dr. Kristina Shea for giving me the opportunity to do my PhD at the Engineering Design and Computing Laboratory (EDAC) and for supporting my research in many ways. I am especially grateful for her guide in deciding my thesis direction and her efforts in correcting my manuscripts, which helps me to grow to be an independent researcher. I really appreciate it to have spent five years of life with Prof. Dr. Kristina Shea.

Secondly, I would like to thank Dr. Tino Stanković, who is not only my supervisor in academics, but also is like a father to me. I really admire his brilliant mind and his speed of thinking. I want to thank him greatly for our many heated discussions, for his efforts in guiding me throughout my whole PhD. He has witnessed mostly of my joyful and sad moments, I feel very grateful to have had Dr. Tino Stanković as my supervisor.

Third, I would like to thank Prof. Dr. Stephen J. Ferguson for the insightful meetings and acknowledgements of my research, which each time gives me more confidence in further continuing my research. Especially, I want to thank him greatly for his big help to introduce me to Prof. Dr. Philippe Zysset for conducting my spinal disc tests in Bern. Without him I would not be able to finish the thesis. I want to express my big thanks to Prof. Dr. Philippe Zysset and Benjamin Voumard for letting me use their lab facilities and helping me with my spinal disc tests.

Another special thanks must be extended to Jung-Chew Tse for printing all my spinal discs. I would like to specially thank Joel Chapuis for his help in my research. He is the dream work college one could wish for, who gives you lots of constructive suggestions and is always very helpful. I would also like to thank Andreas Walker for helping me go through my manuscript. I would also like to thank all of the current and former lab members, namely: Bettina Melberg, Thomas Lumpe, Cosima du Pasquier, Zhiyang Yu, George Birchenough, Dr. Tim Chen, Prof. Dr. Paul Egan, Dr. Jochen Müller, Merel van Diepen, and of course, my one and only office mate Luca Zimmermann. Lastly, I would like to thank my family who has supported me throughout my entire PhD journey. In particular I would like to thank: My boyfriend, Michel Breyer, who is likewise a PhD candidate and shares much of my PhD struggle; My grandmother, who raised me and taught me how to be a stronger person despite all the hardships. Thank you!

Table of Contents

Abstract 1

Zusammenfassung 2

Acknowledgments 4

List of Symbols 8

Chapter 1. Introduction 9

1.1 Problem Statement 9

1.2 Scope of the thesis 11

1.3 Approaches and expected contributions 12

1.4 Structure of the thesis 13

Chapter 2. Background 15

2.1 Intervertebral disc and total disc replacement 15

2.2 ASD design criteria 18

2.3 Multi-material AM and ASD design 22

2.4 Implications for ASD design 23

Chapter 3. Computational method for the design of a biomimetic, multi-material ASD 24

3.1 Summary 24

3.2 Background 24

3.3 Methods 25

3.4 Results 31

3.5 Discussion 35

3.6. Conclusion 39

Chapter 4. Clustering-based design variable linking for the efficient design of a multi-material ASD 40

4.1 Summary 40

4.2. Background 41

4.3 Methods 42

4.4 Results 45

4.5 Discussion 51

4.6 Conclusion 52

Chapter 5. Artificial neural networks (ANNs) supported design of a lattice-based ASD 53

5.1 Summary 53
5.2 Background 54
5.3 Methods 55
5.4 Results 61
5.5 Discussion 67
5.6 Conclusion 71
Chapter 6. Design of a chainmail-based, multi-material ASD 72
6.1 Summary 72
6.2 Background 72
6.3 Materials and methods 73
6.4 Results 81
6.5 Discussion 85
6.6 Conclusion 88
Chapter 7. Design comparison and testing of various ASD designs 89
7.1 Summary 89
7.2 Methods 90
7.3 Results 95
7.4 Discussion 101
7.5 Conclusion 104
Chapter 8. Design of a patient-specific, chainmail-based, multi-material ASD 106
8.1 Summary 106
8.2 Methods 106
8.3 Results 110
8.4 Discussion 117
8.5 Conclusion 124
Chapter 9. General design guidelines for multi-material ASD fabricated with multi-material AM 125
9.1 Summary 125
9.2 Guidelines for developing multi-material ASD design concepts 125
9.3 Guidelines for computational methods for patient-specific ASD design 128
9.4 General guidelines of ASD design 129

Chapter 10. Discussion and outlook 132
10.1 Principle findings and contributions 132
10.2 Limitations and future work 138
Chapter 11. Summary and conclusion 140
References 141

List of Symbols

ASD	Artificial Spinal Disc
FE	Finite Element
TDR	Total Disc Replacement
IVD	Intervertebral Disc
LB, LLB, RLB	Lateral Bending, Left Lateral Bending, Right Lateral Bending
AR, LAR, RAR	Axial Rotation, Left Axial Rotation, Right Axial Rotation
DDD	Degenerative Disc Disease
LBP	Low Back Pain
ROM	Range of Motion
ICOR	Instant Center of Rotation
DOF	Degree of Freedom
NZ	Neutral Zone
EZ	Elastic Zone
DOE	Design of Experiments
NP	Nucleus Pulposus
AF	Annulus Fibrosus
ML	Machine Learning
ANN	Artificial Neural Network
IHA	Instant Helical Axis
GPS	Generalized Pattern Search
VNS	Variable Neighborhood Search
CT	Computed Tomography
FSA	Finite Screw Axis
CAD	Computer-Aided Design
VW	VeroWhite

Chapter 1. Introduction

1.1 Problem Statement

Low back pain (LBP), which is a worldwide health problem and is the main cause of disability, affects people at all ages [1]. According to literature, 75-85% of the population will suffer from back pain sometime during their life [3]. The main cause of LBP is intervertebral disc (IVD) degeneration [5]. The IVD, which is a fibrocartilage tissue that lies in between two vertebral bodies, helps maintain a deformable, flexible space in between the rigid vertebral bodies while simultaneously working as a shock absorber for compressive loads [6]. Like most biological tissues, the mechanics of IVDs consists of viscoelastic, nonlinear, and anisotropic behavior. In addition, IVDs exhibit a dynamic load response to applied loads [7]. The behavior of IVDs are shown to have large variance depending on age and position in the spinal cord [8]. The unique behavior of IVDs is mainly due to their heterogeneous composition and highly organized fiber structure [7][9].

When an IVD is seriously degenerated, one surgical treatment method is to use an artificial spinal disc (ASD) to replace the original IVD, which is referred to as total disc replacement (TDR). Compared to spinal fusion that totally eliminates the motion in the degenerated spinal segment, TDR is a motion-preserving technique that is expected to overcome the limitations of spinal fusion to achieve more satisfactory clinical outcomes [10]. The major goal of ASD design is to reproduce the mechanics of a natural IVD for restoring the physiological motion of the implanted spinal segment. The state-of-the-art ASD designs can be divided into two categories as illustrated in Fig. 1.1: the articulating design that is referred to as first-generation ASD design, and the non-articulating design that is referred to as second-generation ASD design. The majority of the existing ASD designs belonging to the category of articulating designs employ a ball-in-socket or ball-in-trough design that is composed of two or three solid discrete components, such as CHARITÉ™ and Mobi-C™. The biggest disadvantage of such articulating designs is the lack of a compressive component for restoring the shock absorbing function of an IVD. The rigid nature of the articulating designs also leads to the lack of elastic motion that helps distribute loads naturally within the nearby spinal tissues as well as provide a restoring force to allow the deformed spinal segment to return to the neural position [11]. Besides, the oversimplification of the articulating design leads to an abnormal motion pattern and an unnatural range of motion (ROM) of the implanted spinal segment [12]. The lack of stability provided by the articulating design also leads to overloading of the posterior spinal element [13]. Such limitations can potentially cause complications such as facet degeneration and adjacent level degeneration [14]. In comparison, the non-articulating design is often featured by a soft, compressible core and a higher design complexity, such as M6-C™ and Freedom™. The outstanding performance of non-articulating designs has been proven clinically in terms of a higher degree of natural motion recovery and a higher patient satisfaction rate [15]. However, the state-of-the-art non-articulating designs still suffer from suboptimal performance in terms of natural motion restoration [16][17], such as a lower torsional stiffness compared to a natural IVD. Furthermore,

one of the biggest disadvantages of the state-of-the-art ASDs is the standard size that often leads to anatomical mismatch between the implant and the adjacent vertebrae, which can cause implant subsidence and biomechanical failure of the implants [13]. Although many attempts have been made in ASD design, very little success has been made. The development of a reliable ASD remains to be a substantial challenge due to the complicated biomechanical environment faced by the IVD as well as the elaborate structure and functions of an IVD that pose multiple and often conflicting objectives on ASD design [4].

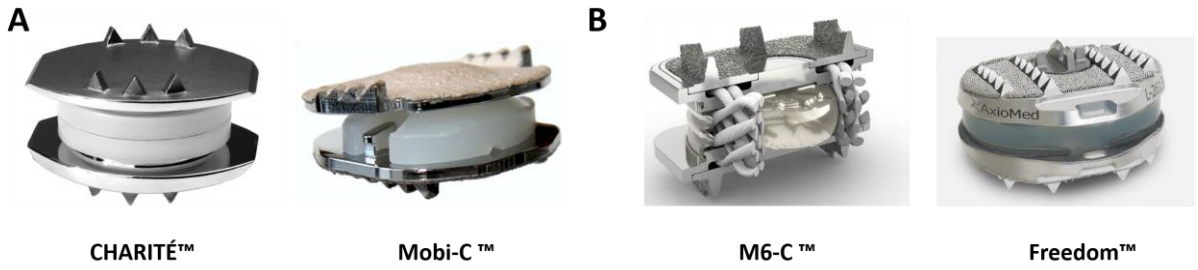

Fig. 1.1. The state-of-the-art ASD designs. (A) Articulating designs such as CHARITÉ™ [18] and Mobi-C™ [19]. (B) Non-articulating designs such as M6-C™ [19] and Freedom™ [16].

The recent development of additive manufacturing (AM) opens up new opportunities for ASD design. The ability of AM to efficiently produce freeform, customized parts facilitates the fabrication of patient-specific implants, which are clinically proven to improve surgical efficiency and clinical outcomes [20]. Especially, multi-material AM allows for the manufacturing of monolithic parts with pre-defined spatial distribution of materials controlled at the individual volumetric pixel level (voxels with a side length of 20-40 μm) [21]. Such multi-material AM techniques facilitate the fabrication of designs such as composites with functional gradients for higher stiffness and strength [21] and tunable, deployable structures with multi-stable states [22], which are otherwise difficult to realize with traditional manufacturing techniques. The application of multi-material AM to the design and fabrication of an ASD has the potential to overcome the common anatomical mismatch when using "off-the-shelf" implants by providing an implant with a customized shape for achieving anatomical fit [23]. In addition, the implementation of multi-material AM has the potential to tackle the challenge of ASD design by incorporating novel structures or composites into the ASD design to restore patient-specific, natural-mimicking mechanics.

Despite the new opportunities provided by multi-material AM, the design of a multi-material ASD fabricated using multi-material AM is still unexplored. Namely, it is still unclear in terms of what is the best ASD design given the opportunities and manufacturing constraints of a certain multi-material AM technique. Additionally, there lacks a method for designing such patient-specific, multi-material ASD efficiently and effectively within a clinically acceptable time frame [24]. Review of the literature shows that the state-of-the-art design of patient-specific implants often requires an iterative process between engineers and surgeons to ensure the safety and legal validity of patient-specific treatments [25][26]. This design process can be time-consuming and expensive, while the lack of access to in-house

engineers hinders the wide application of patient-specific implants [26]. Furthermore, the common trial-and-error strategy used for patient-specific implant design cannot ensure the optimal performance of the implant [27][28]. To realize efficiency, the design method is expected to produce a patient-specific ASD design within a clinically acceptable time frame and with reasonable amount of required resources [29]. Ideally, the design and manufacturing of patient-specific implants can be realized at the point of care [24]. Besides, to realize effectivity, the design method should provide a patient-specific ASD design that meets customized design criteria to achieve anatomical match and restore customized natural mechanics. An ideal workflow for patient-specific implant design is expected to be automated by incorporating design and manufacturing constraints beforehand to avoid the time-consuming iterative process between the surgeons and engineers, as well as involve an optimization step to improve the performance of implants. Computational design refers to a design process that involves computational methods to fulfill design requirements. Such design methods provide two major benefits: 1) computers can expand the range of solutions considered, and possibly improve novelty, and 2) computers can automate tasks while leaving more time for creative activities. Therefore, computational design is a promising methodology for realizing a workflow for patient-specific ASD design. In summary, the lack of a tuned ASD design that can be fabricated with multi-material AM and an effective, efficient design method hinder the development of multi-material, patient-specific ASDs fabricated using multi-material AM.

1.2 Scope of the thesis

The objective of this thesis is to develop a multi-material ASD design that can be fabricated with multi-material AM using an efficient and effective computational design process. Therefore, the main research questions (RQs) of this thesis are formulated as:

> **Main RQs:** Which multi-material ASD design concept has the potential to reproduce the patient-specific mechanics of an IVD while meeting the manufacturing constraints of a given multi-material AM technique? How can a design concept be automatically tuned to produce a patient-specific ASD that meets customized design requirements?

To address the main research questions, this work addresses the following additional RQs that explore potential ASD design concepts and complimentary computational design methods for realizing them.

RQ1: What are the design criteria for a patient-specific ASD that can be fabricated with multi-material AM?

RQ2: With the design criteria clarified in RQ1, what are the potential alternative design concepts?

RQ3: With the design criteria clarified in RQ1 and the ASD design concepts proposed in RQ2, how can a patient-specific ASD be automatically designed to restore customized mechanics?

RQ4: Given the ASD design concept proposed in RQ2 and the computational design method developed in RQ3, how can a patient-specific ASD be designed and fabricated given the manufacturing constraints of a multi-material AM technique?

1.3 Approaches and expected contributions

The approaches developed to answer the RQs and the expected contributions correspondent to the RQs are discussed in this section. The Stratasys Objet500 Connex3 inkjet-based, multi-material 3D printer (Stratasys Ltd., Eden Prairie, MN, USA) is used as a proof-of-concept technique for the ASD design and fabrication in this thesis thanks to its high printing resolution and printable materials with a big stiffness variance, while the biocompatibility of the materials is out of the scope of this thesis.

RQ1: The design criteria for ASD are clarified and categorized through literature review. In addition, the strengths and weaknesses of the state-of-the-art ASD designs are evaluated in terms of meeting the design criteria. Since the concept of a patient-specific ASD is relatively new, the clarification of the general design criteria helps guide the ASD design while discovering potential aspects for personalization. Additionally, review of the existing ASD designs provides insights into key aspects of ASD design and serves as inspiration for developing innovative ASD design concepts.

RQ2: Five ASD design concepts that either employ biomimicry and structures derived from mechanical metamaterials inspired by the manufacturing opportunities provided by multi-material AM are proposed. The biomechanical performances of different ASD design concepts in meeting the design criteria clarified in RQ1 are evaluated and compared. Several innovative conceptual designs of ASD are presented and the favorable ASD design concept for further development of a patient-specific ASD is determined.

RQ3: Given the design criteria in RQ1 and the ASD design concepts proposed in RQ2, the feasibility of using a computational design method for automatically generating a patient-specific ASD with a customized shape and customized mechanics is explored. Therefore, a general computational design workflow involving modeling and optimization for designing a patient-specific ASD is proposed. Finite element software ABAQUS and the numeric computing environment MATLAB are used for the computational design. Additionally, the feasibility of using methods and strategies such as model simplification, design variable dimension reduction, regression model build using artificial neural networks (ANNs) to improve the efficiency of the computational design method is explored.

RQ4: Given the manufacturing constrains, the computational design method developed in RQ3 is applied to develop patient-specific ASDs based on the favorable ASD design determined in RQ2. The results serve as a proof-of-concept to demonstrate the potential of multi-material AM for the design and fabrication of multi-material, patient-specific ASDs.

1.4 Structure of the thesis

The thesis structure is presented in Fig. 1.2. **Chapter 2** elaborates the background of the thesis, which includes the structure-function relationship in an IVD, the state-of-the-art ASD designs, the ASD design criteria, and the opportunities provided by multi-material AM technique for patient-specific ASD design. Chapter 2 clarifies the research gap and concludes with implications for this thesis, therefore answering RQ1. **Chapter 3** presents a biomimetic, fiber-reinforced composite ASD design concept together with a general computational design framework to allow such ASD design to restore patient-specific anisotropic behavior, which partially answers RQ2 and RQ3. To speed up the computational design process proposed in Chapter 3, **Chapter 4** and **Chapter 5** present two ways of incorporating ML techniques into the overall computational design workflow, which partially answers RQ3. Specifically, Chapter 4 introduces the strategy of using a clustering-based design variable linking method for reducing the problem dimension, while Chapter 5 presents a strategy of using ANNs to replace the time-consuming FE analysis. In addition, Chapter 4 and Chapter 5 propose three ASD design concepts and evaluate their performance in meeting the design criteria, which provide answers to RQ2. **Chapter 6** further proposes an ASD design concept involving an innovative chainmail-like structure aimed at reproducing the nonlinear, anisotropic rotational response of an IVD, therefore completing the answer to RQ2. In addition, Chapter 6 provides a strategy of using a simplified model to speed up the computational design process. Thus, a combination of Chapter 3-6 provide answers to RQ3. Given the ASD design concepts proposed in the previous chapters, **Chapter 7** fabricates and tests different ASD designs *in vitro*, and a conclusion is made on the favorable ASD design concept, i.e., the chainmail-based ASD, for developing patient-specific ASDs, which completes the answer to RQ2. **Chapter 8** then combines the knowledge obtained from the previous chapters by applying a computational design method to optimize a patient-specific ASD with the favorable chainmail-based ASD design concept concluded from Chapter 7 given the manufacturing constraints, which answers RQ4. **Chapter 9** summarizes the challenges in the design of a multi-material ASD fabricated with multi-material AM and presents general guidelines for the future development of multi-material ASD fabricated with multi-material AM. **Chapter 10** discusses the principle findings and contributions of this thesis regarding the RQs, and lists the limitations and possible future studies. Lastly, **Chapter 11** summarizes the thesis and concludes this work.

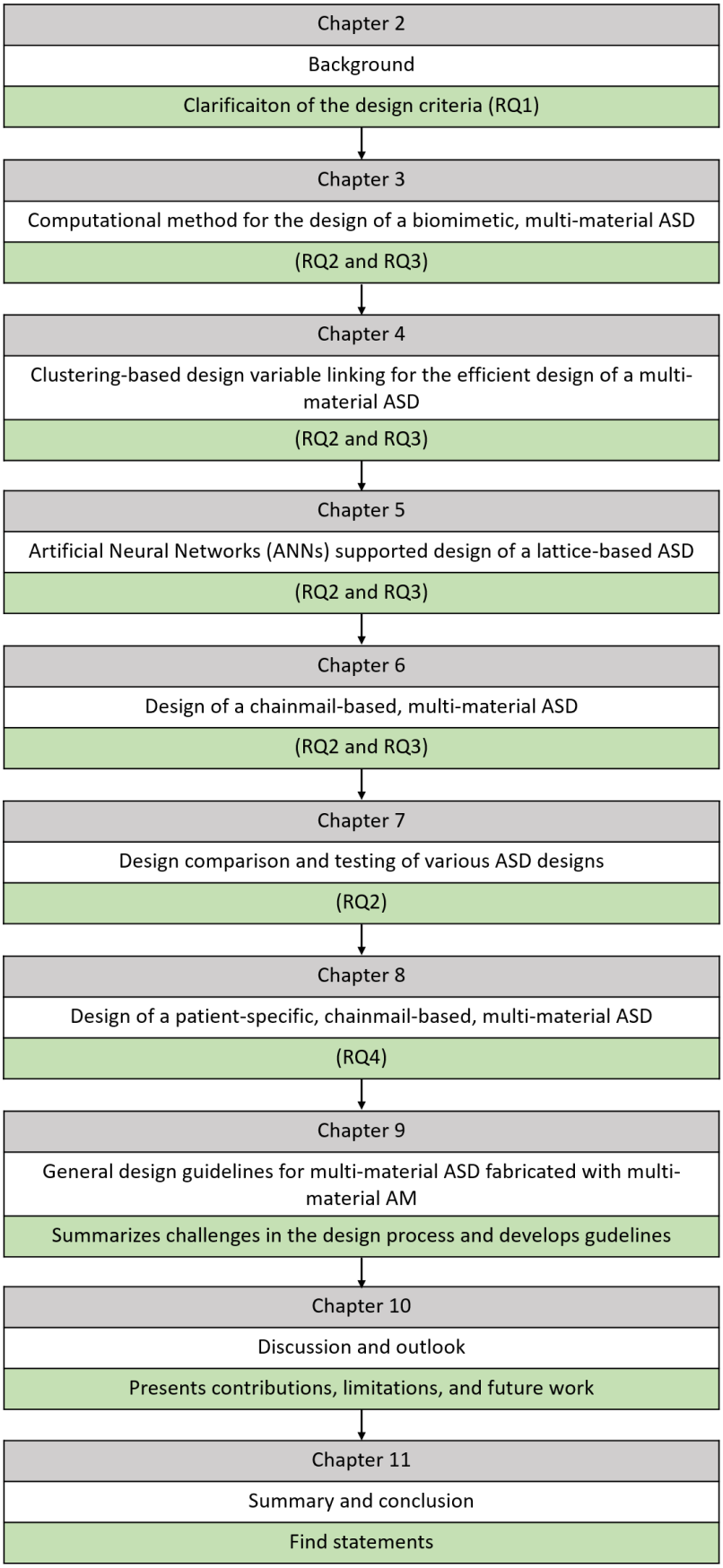

Fig. 1.2. Structure of the thesis.

Chapter 2. Background

This chapter first presents the composition and biomechanical functions of an IVD, as well as the state-of-the-art ASDs for TDR (Section 2.1). Next, Section 2.2 discusses the design criteria of an ASD with metrics to evaluate its performance. The principle of multi-material AM and the design opportunities for the ASD design are stated in Section 2.3. Lastly, Section 2.4 states the implications of literature review for ASD design.

2.1 Intervertebral disc and total disc replacement

IVD, which is a soft connecting tissue in the spinal segment, is composed of three functional components: the soft, highly hydrophilic substance nucleus pulposus (NP) in the center, the surrounding annulus fibrosus (AF), and the hyaline cartilage endplate. The NP and AF are sandwiched inferiorly and superiorly by the two cartilage endplates. NP is structurally and mechanically isotropic with a high water content, and is primarily made from a network of type collagen II interspersed with proteoglycans. AF is featured by a multi-lamellar composition with an organized fiber network, while the fibers in each lamella are initially in a crimped state before load bearing and oriented at alternating angles to the longitudinal axis with a crisscross pattern [30].

The major biomechanical functions of IVD are to provide flexibility for the spinal column by permitting motion, as well as transmitting and absorbing load through energy dissipation [31]. The movement of the spinal segment is both allowed and constrained by the IVD [4]. All the possible loading scenarios of a spinal segment that includes two vertebrae and the in-between IVD are illustrated in Fig. 2.1, among which the seven most frequent loading scenarios in everyday life considered in the scope of this thesis are illustrated in Fig. 2.2: compression, flexion/extension, left/right lateral bending (LB), and left/right axial rotation (AR) [32]. The IVD exhibits an anisotropic load response in various loading scenarios with a mobile center of rotation (COR) [4]. Besides, the IVD has a nonlinear and dynamic response to the applied load [7]. The resultant progressive resistance allows for a physiological laxity of the spine while maintaining its stability [19]. The unique mechanics of IVD are determined by its distinctive composition and the nonlinear interactions among its structural components [33]. For example, the structural and compositional spatial variation of AF are crucial for the anisotropic behavior of an IVD [34][35]. Besides, the gradual un-crimping of the fibers in the AF upon loading contributes to IVD's nonlinear load response [36][37]. Regarding the nonlinear interactions among an IVD's structural components, one typical example is the redistribution of the compressive pressure from the NP to the fibers in AF under compressive loads [12]. The close relationship between the structure and mechanics presented in an IVD, which is also referred to as the structure-function relationship, is a common feature of biological soft tissues [38].

Unfortunately, the IVD is susceptible to damage and degeneration, which leads to degenerative disc disease (DDD) that is shown clinically to be closely associated with LBP that is one of the major health

problems in Western countries [39][40]. The mechanism of how DDD leads to LBP is illustrated in Fig. 2.3, which shows that the soft, jelly-like NP from the herniated IVD is pushed all the way through the AF and causes compression on the nearby nerve roots. In addition to pain, IVD degeneration also results in an abnormal motion and instability of the spinal segment [40]. When the conservative method fails to relieve LBP's symptoms, surgical treatment is a commonly used method [41]. For a long period, spinal fusion based on bone grafts is considered to be the "gold standard" treatment for DDD. However, the long-term results of spinal fusion is suboptimal regarding pain relief and there is a high occurrence rate of related complications such as adjacent-level degeneration and pseudoarthrosis [42]. Compared to spinal fusion that totally eliminates the motion at the spinal segment, TDR that uses an ASD to replace the degenerated IVD is a motion-preserving technique. The goal of TDR is to allow for motion, thus avoiding complications resulting from the abnormal motion pattern after spinal fusion [43]. Clinical results show that compared to spinal fusion, TDR leads to a shorter hospitalization, a lower rate of reoperations, and a higher long-term patient satisfaction [44]. An ideal ASD is expected to fully reproduce the biomechanical functions of a healthy IVD while restoring the disc height as well as physiological spinal alignment [42].

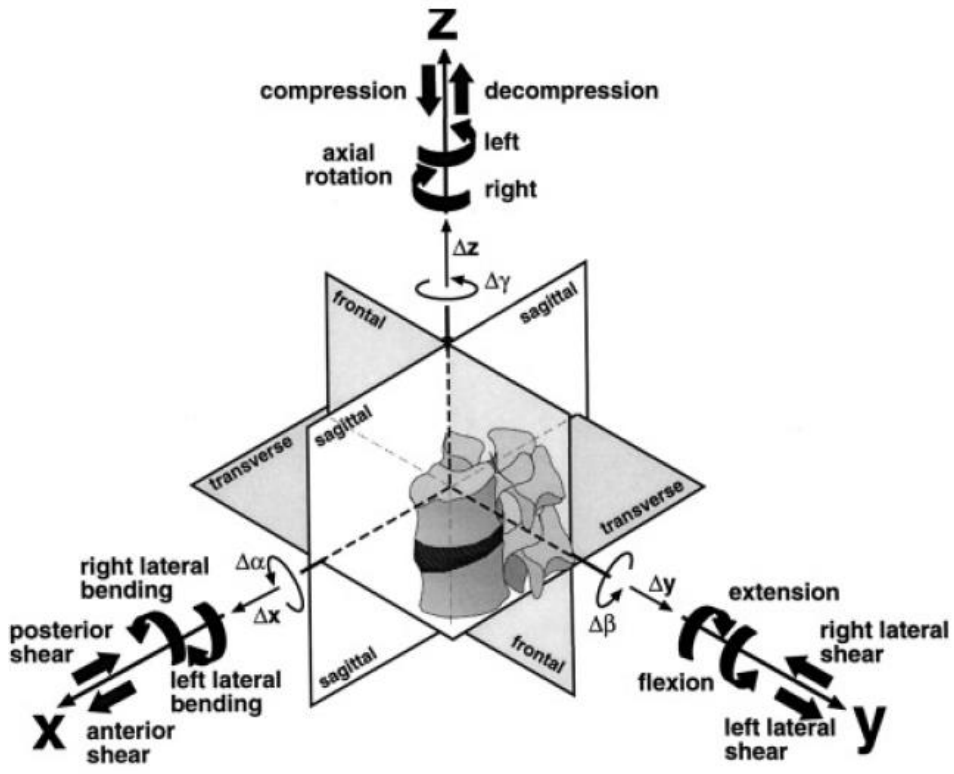

Fig. 2.1. Illustration of all the possible loading scenarios of a spinal segment [45]. The positive loading directions are illustrated with the motion components $\triangle\alpha$, $\triangle\beta$, $\triangle\gamma$, $\triangle x$, $\triangle y$, $\triangle z$.

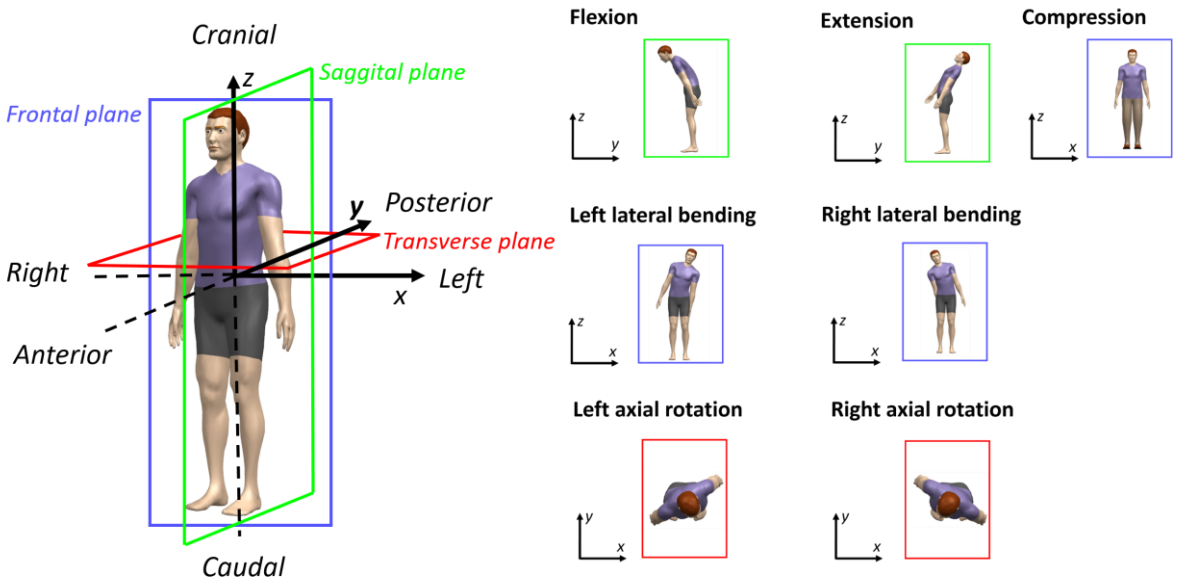

Fig. 2.2. The seven most frequent loading scenarios of an IVD considered in the scope of this thesis. The seven loading scenarios are flexion/extension, left/right lateral bending (LB), left/right axial rotation (AR), and compression.

Fig. 2.3. The mechanism of IVD degeneration and low back pain. The herniated IVD leads to the soft, jelly-like NP (shown in red) to be pushed all the way through the AF, which causes compression on the nearby nerve roots (shown in yellow) and leads to pain. ("© [Teeradej] / Adobe Stock")

The first ASD design in history is a single metallic ball and is first proposed in late 1950s [46], while the surface of the metallic ball can slide freely relative to the adjacent vertebrae after implantation. There are two major categories of state-of-the-art ASD designs: designs that focus on the reproduction of an IVD's mobility, and designs that focus on the reproduction of an IVD's viscoelasticity [4]. Different ASD designs impose different motion constraints that influence the implanted spinal segment's kinematics and load distribution [19][47]. The mobility-focused ASD design, which is often referred to as the first-generation ASD, often employs an articulating, ball-and-socket design initially derived from knee and hip implants with metal-on-metal or metal-on-polymer bearing surface [48]. Examples of first-generation ASDs are SB Charité™ ASD (DePuy Spine, Raynham, MA) and ProDisc®-L ASD (Synthes Spine, West Chester, PA). Although the first-generation ASD is proven clinically to contribute to a lower rate of long-term disability compared to spinal fusion [44], it is based on a sliding motion and thus fails to reproduce the damping and energy storage function of an IVD. Besides, its simplified design

is incapable of mimicking an IVD's complex anatomy or reproducing an IVD's motion pattern and kinematics. The accompanying abnormal motion can cause an unnatural load sharing among the same-level and adjacent-level spinal components, such as ligaments, muscles, and facet joints, which can lead to a subsequent degeneration of these spinal components [49][50]. In comparison, the viscoelasticity-focused ASD design, which is referred to as the second-generation ASD, is compressible and preserves the viscoelastic behavior of an IVD. With its deformation-dependent behavior, the second-generation ASD allows for motion in all six degrees of freedom (DOFs) together with coupled motions. Besides, the viscoelastic ASD has the potential to provide a nature-mimicking, mobile COR as well as a friction-free, wear-free movement to avoid wear debris related inflammation [51]. Examples of second-generation ASD designs are Rhine ASD (Rhine, K2m Inc., Leesburg, Virginia), LP-ESP® ASD, and M6 ASD (Spinal Kinetics, Inc., Sunnyvale, CA). The second-generation ASD designs can be further divided into without-endplate designs and endplate-sandwiched designs that further include a monolithic design where all the components are bonded together and a mobile bumper design where the components are not firmly bonded [48].

2.2 ASD design criteria

This section first gives an overview of the ASD design criteria and the state-of-the-art ASDs in meeting the design criteria in Section 2.2.1. Next, Section 2.2.2 introduces the constraint type imposed by an ASD. This section ends with a Section 2.2.3 that gives a detailed explanation of the terminologies and definitions of the metrics used for quantifying ASD's performance.

2.2.1 Overview

The major ASD design criteria summarized in Table 2.1 are divided into two categories: clinical and biomechanical design criteria [52]. Clinical design criteria focus on the clinical outcomes of TDR, whereas biomechanical design criteria focus on preserving and restoring the biomechanical functions of the implanted spinal segment. The biomechanical design criteria are closely related to the clinical design criteria. The biomechanical design criteria aim to relieve the abnormal stress or strain on the same-level and adjacent-level spinal components caused by IVD degeneration, as well as to avoid producing harmful biomechanical effects on the spinal components [52]. The criteria of natural motion restoration can be further categorized into restoring the *quantity* and *quality* of motion of the implanted spinal segment. In general, the *quantity* of motion only concerns the ASD's end motion (i.e. the total translation or total rotation achieved), while the *quality* of motion concerns ASD's response along the load path (i.e. how the motion occurs) [53][54][55]. The criterion of shock absorption requires that the ASD allows for a proper portion of load transmission and a certain degree of shock damping/attenuation to relieve abnormal stress or strain on the surrounding spinal components. Implantation stability is mainly focused on avoiding implant subsidence and migration by having a stable interface bonding between the implant and the vertebrae [56]. Restoration of the IVD height and sagittal alignment aims to preserve the sagittal balance to avoid complications such as adjacent segment degeneration, chronic LBP, and muscle fatigue

[57]. Table 2.2 gives an overview of the state-of-the-art ASDs in terms of their performance in meeting the biomechanical design criteria.

Table 2.1. Summary of the major ASD design criteria [52][58]**.**

Clinical design criteria	**Biomechanical design criteria**	
1. Successful pain relief and successfully functional recovery	Restoration of the natural motion	1. *Quantity* of motion: ROM
		2. *Quality* of motion: stiffness, motion pattern, COR
2. An acceptable level of morbidity, equal to or less than morbidities of spinal fusion	3. Shock absorption: load damping	
3. A shorter postoperative recuperation time	4. Implantation stability: stable implant-vertebrae interface bonding	
4. An ease of surgical implantation and revision	5. Restoration of natural IVD height and sagittal alignment	

Table 2.2. Evaluation of the state-of-the-art ASD designs regarding the biomechanical design criteria [59]**.**

Design criteria	First-generation ASD (Ball-and-socket ASD)	Second-generation ASD (Viscoelastic ASD)
1. *Quantity* of motion	-	-
2. *Quality* of motion	-	(-)
3. Shock absorption	-	+
4. Implantation stability	(+)	(+)
5. Restoration of IVD height and sagittal alignment	(+)	(+)

* - = Totally not matching, + = totally matching, (-) = partially not matching, (+) = partially matching

* 1. No state-of-the-art ASDs are able to totally restore the natural ROM in various loading scenarios, while the first-generation ASD is featured by hypermobility in most DOFs.

2. There is no available ASDs that are able to completely restore the *quality* of motion.

3. First-generation ASDs don't allow shock absorption due to their rigid nature, while viscoelastic ASDs are featured by their ability of load damping.

4. & 5. The implantation stability and restoration of IVD height and sagittal alignment are dependent on the available sizes and wedge angle (the angle formed in between the top and bottom surface) of the ASD.

2.2.2 ASD constraint degree and type

To restore the natural kinematics, an ASD is expected to impose nature-mimicking constraints in each DOF for the implanted spinal segment. According to [60], the constraint imposed by an ASD can be described by the degree of constraint (Fig. 2.4) and the type of constraint (Fig. 2.5). The degree of constraint is defined as the allowed motion range, while an ideal ASD is expected to allow the implanted spinal segment to reach a *critically constrained* state. In contrast, an *underconstrained* ASD and an *overconstrained* ASD fail to restore the natural motion range of the implanted spinal segment, as they either allow for motions out of the physiological motion range or hinder motions within the physiological motion range. The state-of-the-art ASD designs are unable to reach a critically constrained state in each DOF, which requires future design improvements [60]. Restoration of the natural degree of constraint of the intact spinal segment is further complicated by surgical procedures in TDR that often includes an resection of critical ligaments such as anterior longitudinal ligament for implant insertion, which ideally should be compensated when designing an ASD [12][61].

As illustrated in Fig. 2.5, the type of constraints refers to the motion pattern, i.e., the trend of the force-displacement curve. An ideal ASD is expected to exhibit a soft constraint similar as IVD's, whereas the response of the first-generation ASD is featured by a hard constraint [12]. This hard, non-

elastic constraint shows a small resistance at small rotational angles due to the sliding between its rigid components, followed by an abrupt resistance increase due to the entrapment and locking of the core between the endplates. Such unnaturally high laxity causes an abnormal load sharing within the same-level and adjacent-level spinal segments. This can possibly cause additional spinal musculature straining to compensate for the impaired spinal stability, which can cause pain due to the increased stress added on the spinal muscles [62]. The high laxity of the ball-and-socket design can also cause a shift of the lordosis angle (neutral position) of the implanted spinal segment [19]. In comparison, the M6 ASD (Spinal Kinetics, Sunnyvale, CA), which is a second-generation ASD, mimics IVD's structure and is able to exhibit an angular response with a nature-mimicking progressive resistance [19].

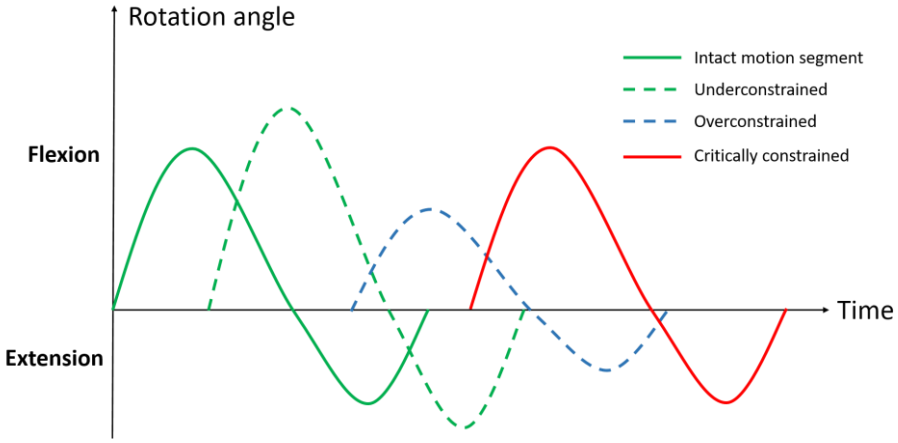

Fig. 2.4. Illustration of the degree of constraint. The figure is recreated from Fig. 4 of [60]. The degree of constraint is illustrated based on the rotation angle versus time graph of the flexion/extension movement of a spinal segment. The underconstrained and overconstrained response curves show an increased and reduced ROM, respectively, while the critically constrained curve reproduces the natural ROM of an intact motion segment.

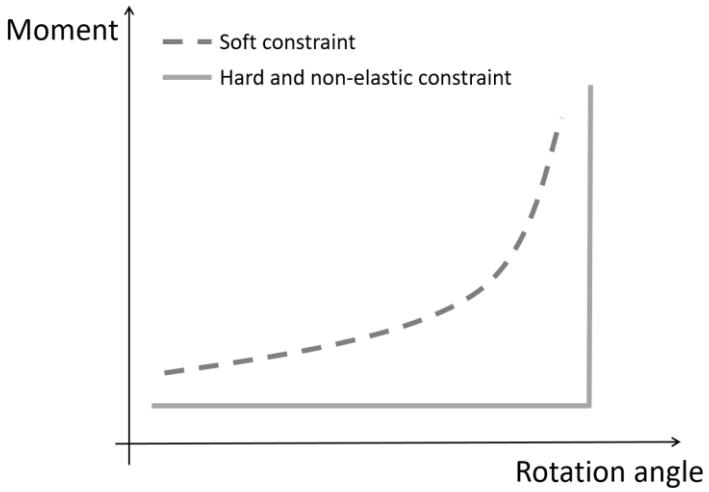

Fig. 2.5. Illustration of the types of constraint. The figure is recreated from Fig. 5 of [60]. The constraint type is illustrated using the hypothetical moment versus rotation angle curves. IVD is featured by a soft constraint without abrupt tuning point (black dashed line), while the first-generation ASD designs often show an abrupt and non-elastic constraint trend (black solid line).

2.2.3 Metrics for ASD behavior quantification

To facilitate the evaluation and comparison of ASD's performance, some metrics are recommended by [45] to quantify the behavior of an ASD. The terminologies and the definitions of the metrics are illustrated and listed in Fig. 2.6 and Table 2.3, respectively. Fig. 2.6 shows a typical nonlinear

load-displacement response of an IVD that is characterized by an initial neutral zone (NZ) over which the IVD moves with a high compliance, followed by an elastic zone (EZ) with a bigger stiffness. The slopes of the moment-angle load response in NZ and EZ are defined as NZ stiffness and EZ stiffness, respectively. Sigmoidity, which is defined as the ratio of the NZ stiffness to EZ stiffness, is used to measure the nonlinearity of the ASD's load response. ROM is defined as the maximum displacement from the initial neutral position to the maximally loaded position. The hysteresis area is defined as the area enclosed by the moment-angle response. The current ASD designs only focus on restoring the ROM [63][64][65][66], while an ideal ASD is expected to restore the physiological values of all the listed metrics. Some recent innovative ASD designs also target at restoring the *quality* of motion, such as the ASD design based on a Stewart-Gough system for achieving the nature-mimicking finite screw axis (FSA) [67] and the ASD design based on a cubic three-dimensional fabric to reproduce the nature-mimicking nonlinear load response [68].

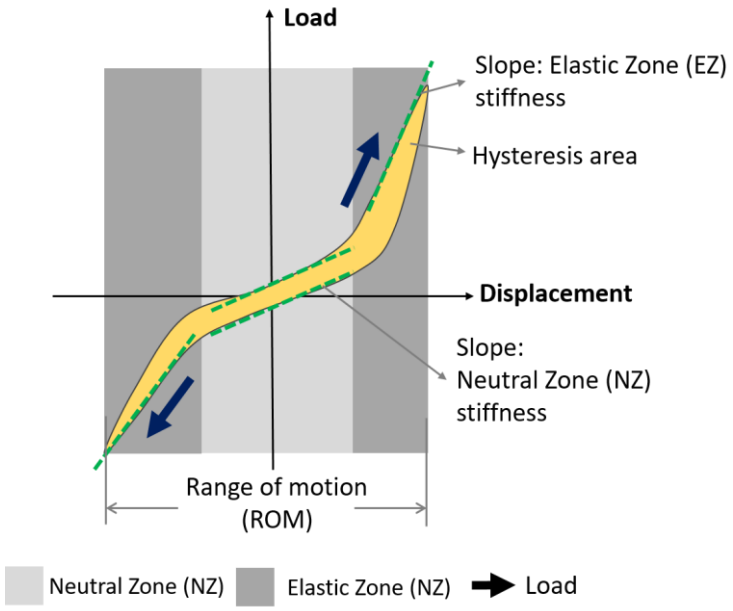

Fig. 2.6. A typical load-displacement curve of an IVD and the metrics used for behavior quantification. The IVD's nonlinear load response is characterized by an initial neutral zone (NZ) over which the IVD moves with a high compliance, and a subsequent elastic zone (EZ) with a bigger stiffness. The slopes of the moment-angle load response in NZ and EZ are defined as NZ stiffness and EZ stiffness, respectively. ROM is defined as the maximum displacement from the initial neutral position to the maximally loaded position. The hysteresis area is defined as the area enclosed by the moment-angle curve.

Table 2.3. The definitions of the metrics used for quantifying ASD's behavior.

Terminology	Definition
Neutral zone (NZ)	Measurement of the motion laxity. It is the range over which the ASD moves with a high compliance.
Elastic zone (EZ)	It is the range over which the ASD moves with a big stiffness.
Range of motion (ROM)	It is the maximum displacement or rotational angle from the initial position to the maximally loaded position.
Neutral zone stiffness (NZS)	The stiffness of the load-displacement curve when in NZ.
Elastic zone stiffness (EZS)	The stiffness of the load-displacement curve when in EZ.
Sigmoidity (NZS/EZS)	A measurement of the nonlinearity of the load response.
Hysteresis area	It is the area enclosed by the load-displacement curve and describes the viscoelastic behavior.

2.3 Multi-material AM and ASD design

AM or three-dimensional (3D) printing that is capable of fabricating parts with complex shapes and structures has been widely used in the medical field [69]. Its application involves fabrication of customized implants, surgical guides, and anatomical models [70]. Recently, patient-specific implant fabricated with AM has gained more and more attention as it helps shorten the surgical time, simplify the surgical procedure, and improve surgical outcomes. Customized implants are able to adapt to anatomical variance, which spares the time-consuming procedure of implanted site preparation and implant positioning. The anatomical match realized by the customized implants also contributes to an increased stability of the implantation, which helps achieve better long-term clinical outcomes [71]. In contrast, the "off the shelf" implants only have standard sizes available [72]. The general workflow for the design and fabrication of a patient-specific implant consists of three steps: patient-specific anatomical data acquisition through medical imaging, anatomical modeling using computer-aided design (CAD), and implant fabrication [28].

The two critical geometric factors of an ASD are footprint defined as the interfacing surface to adjacent vertebrae and wedge angle defined as the angle between the top and end surface of an ASD on the sagittal plane. A shape-matching footprint ensures an early-stage stability to prevent implant migration. Besides, the matching footprint also contributes to a homogeneous load distribution at the implant-vertebrae interface, which significantly reduces the risk of implant subsidence [73]. A physiological wedge angle helps maintain the physiological spinal curvature (lordosis), while the loss of the natural spinal lordosis is closely related to adjacent-level spinal degeneration due to abnormal stress distribution among the spinal components [74].

As one advanced AM technique, multi-material AM [75] facilitates the fabrication of monolithic parts with a heterogeneous material distribution, which provides great design opportunities for developing a monolithic, viscoelastic ASD. In addition to helping realize anatomical match, multi-material AM facilitates the fabrication of an multi-material ASD design that can potentially reproduce patient-specific mechanics through varying its material distribution [47][76]. Stratasys Objet500 Connex3 inkjet-based, multi-material 3D printer (Fig. 2.7. A) is a promising technique to fabricate such multi-material ASD design thanks to its high printing resolution and fourteen materials available that provide a wide range of stiffnesses. Fig. 2.7. B shows some monolithic cubes fabricated with the Connex3 inkjet-based, multi-material 3D printer, where cube has a color distribution pattern that indicates a heterogeneous material distribution.

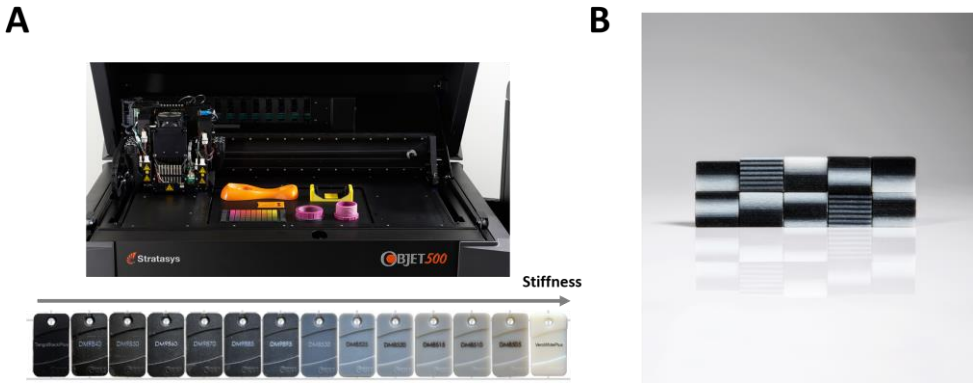

Fig. 2.7. Stratasys Objet500 Connex3 inkjet-based, multi-material 3D printer and example of objects fabricated with this printer. (A) Stratasys Objet500 Connex3 inkjet-based, multi-material 3D printer and its fourteen printable materials: the stiffness of the fourteen materials increases from the left to the right indicated by a gradual color change from black to white. (B) Example of fabricated objects with a heterogeneous material distribution.

Table 2.4. Fourteen materials and their Young's moduli provided by the given 3D printer [77]**.**

Material index	Material name	Young's modulus [MPa]	Material index	Material name	Young's modulus [MPa]
1	TangoBlackPlus/Agilus	0.486	8	RGD8530	2038
2	F9840	1.36	9	RGD8525	2242
3	F9850	2.65	10	RGD8520	2396
4	F9860	22.5	11	RGD8515	2455
5	F9870	52.5	12	RGD8510	2463
6	F9885	125	13	RGD8505	2465
7	F9895	375	14	VeroWhitePlus (VW)	2559

2.4 Implications for ASD design

The design of an ASD is crucial to achieve satisfactory clinical outcomes of TDR. The over-simplified design employed by the first-generation ASDs fails to reproduce an IVD's complex behavior while lacking shock absorbing behavior. Thanks to the soft constituent material, second-generation ASDs exhibit a nature-mimicking viscoelastic behavior. However, the performances of the current ASDs are still unsatisfactory and the majority of the ASD designs neglect restoring an IVD's *quality* of motion, although *quality* of motion is proven to be equally important as *quantity* of motion [78]. Multi-material AM offers new design opportunities for multi-material ASD design. First, multi-material AM facilitates the fabrication of parts with a complex structure, which helps mimic the structure-function relationship in an IVD. Second, multi-material AM facilitates the fabrication of monolithic parts with a controlled material distribution, which can potentially restore patient-specific mechanics and adapt to various surgical procedures. Such concept coincides with that of some studies that try to reproduce an IVD's natural mechanics through tuning the local fiber orientation and material distribution in an FE model [79][80][81]. Additionally, a method for the design of a multi-material ASD with reasonable development time and cost and potential for automation is required to speed up the traditional time-consuming iterative process between engineers and surgeons.

Chapter 3. Computational method for the design of a biomimetic, multi-material ASD

This chapter has been adapted from a manuscript published in *Journal of Mechanical Design* [82]:

Yu, Z., Shea, K., Stankovic, T., 2019. A Computational Method for the Design of an Additively Manufactured Personalized Artificial Spinal Disc With Physiological Stiffness Under Multiple Loading Conditions. J. Mech. Des. 141, 101406. https://doi.org/10.1115/1.4043931

3.1 Summary

This chapter proposes a general computational method for the design of a multi-material ASD with the given 3D printer. To validate the proposed method, a biomimetic ASD design concept based on a fiber-reinforced composite is proposed, inspired by the crisscross fiber network found in an IVD that is shown to be critical for the IVD's unique mechanics. The computational method is then applied to evaluate the performance of such ASD design concept in reproducing patient-specific mechanics. The computational method involves an initial patient-specific FE modeling, design variable determination, and material optimization. First, modified superquadratics are used for the geometric modeling of the freeform intervertebral space. Next, a bio-inspired design variable linking strategy is used for reducing the dimension of the design variables, followed by a design variable verification using random forest method that is a technique to identify the relative importance of each design variable. The goal of the material optimization is to allow the ASD to exhibit nature-mimicking anisotropic stiffnesses in five frequent loading scenarios of an IVD in everyday life. The stiffnesses of the optimized multi-material ASD match well with those of an IVD and the multi-material ASD outperforms the ball-and-socket ASD in terms of natural mechanics restoration. The potential of achieving an improved stiffness match with an IVD given a larger range of available 3D printable materials is demonstrated. Results shown in this chapter verifies the biomimetic ASD design concept in restoring patient-specific anisotropy, as well as the effectivity of the proposed computational method for multi-material ASD design.

3.2 Background

This section first introduces the principle of FE analysis in Section 3.2.1. Next, the concept of simulation-based optimization as well as the derivative-free Nelder-Mead method are introduced in Section 3.2.2.

3.2.1 FE analysis

The FE analysis constructs and tries to solve a system of equations $\mathbf{K}\,\mathbf{u} = \mathbf{f}$, where $\mathbf{K}$ represents the stiffness matrix of the system and $\mathbf{u}$ and $\mathbf{f}$ are the displacements and externally applied forces at the nodal points. The stiffness matrix $\mathbf{K}$ contains the geometric and material behavior information of the structural elements in the system and thus it determines the deformation behavior of the structural elements when subjected to load [83]. In this chapter, the stiffness matrix $\mathbf{K}$ formulated is nonlinear and calculated iteratively as a function of the displacement field $\mathbf{u}$ using ABAQUS. The lack of an analytical formulation to obtain $\mathbf{K}$ make it difficult to obtain the derivatives of $\mathbf{K}$ and the objective function, thus

hindering the implementation of an adjoint method that is suitable for an efficient sensitivity calculation given a large number of design variables [84].

3.2.1 Simulation-based optimization and Nelder-Mead method

Simulation-based design is defined as a process where design evaluation and verification is primarily based on simulation [85]. When combined with an appropriate validation process, the resulting simulation-based system is able to design superior products with less time and lower costs. Further, simulation-based optimization refers to optimization problems that optimize the results from computer simulations and therefore the various quantities needed by the optimization algorithm is obtained by repeatedly running a computer simulation [86]. Complex simulations such as nonlinear FE analysis where the simulation output is calculated through mesh generation, partial differential equation solving, and post-processing usually result in noisy output and non-smooth objective function [87]. Therefore, it is recognized in the simulation-based optimization community that the level of precision of the simulation output is inadequate to obtain the numeric derivatives accurately, which therefore makes gradient-based optimization infeasible [86][88] .

The simplex method that is first introduced in the work by Spendley et al. [89] is the most well-known direct search method that systematically reduces the region of interest in a n dimensional search space in order to find the optimum point [90]. The optimization process initiates with the objective function evaluated at $n+1$ equidistant points that form a regular simplex. Based on the evaluation the vertex with the largest value is reflected in the centroid of the other n vertices [90]. This constitutes a new regular simplex and reinitiates the evaluation procedure. The optimized point is produced after series of iterations involving expansion or contraction of the regular simplex to avoid unintended oscillations and improve the efficiency of the algorithm. Since the original method introduced by Spendley, many derivatives are reported including the Nelder-Mead method [91] that uses irregular simplexes to capitalize on the information based on the search space geometry and extending the method for constrained problems [92]. The simplex method performs worse in terms of efficiency and problem size scaling when compared to other gradient-based methods but is useful when applied to non-smooth objective functions or problems whose derivatives are unreliable or unavailable [90][93]. Due to the fact that the performance of simplex and other similar methods is hindered by the high dimensionality of the search space, as approximately n^3 objective function evaluations is required to produce the optimum point for a n-dimensional search space [90], data dimension reduction is required to improve the performance of the optimizer.

3.3 Methods

The section first presents the workflow for the design and fabrication of a patient-specific ASD and the proposed biomimetic, multi-material ASD design to validate the computational design method in Section 3.3.1. Next, the detailed process of geometric modeling of the patient-specific ASD is given in Section 3.3.2. The computational design method is presented in Section 3.3.3.

3.3.1 Design process overview and proposed ASD design

The workflow for the design and fabrication of a patient-specific, multi-material ASD includes three main steps, as shown in Fig. 3.1: patient-specific ASD geometric modeling from medical imaging data (Step A), computational design (Step B), and ASD fabrication followed by medical application (Step C). This chapter focuses on Step A and Step B: the geometric modeling and the computational design of an ASD. Step A aims to extract the freeform shape of the IVD from medical imaging to build a patient-specific ASD model using a superquadratic equation [94]. Next, the computational design process (Step B) starts with a dimensionality reduction and a sensitivity analysis to determine the design variable **x**. The optimization problem is formulated as to optimize the material distribution within the ASD to reproduce the IVD's stiffness in multiple loading scenarios. Lastly, the optimized design is expected to be 3D printed and implanted into patients (Step C). The ASD design (Fig. 3.2) that is composed of a matrix and a crisscross fiber network that is embedded in the matrix is used for verifying the proposed computational design method.

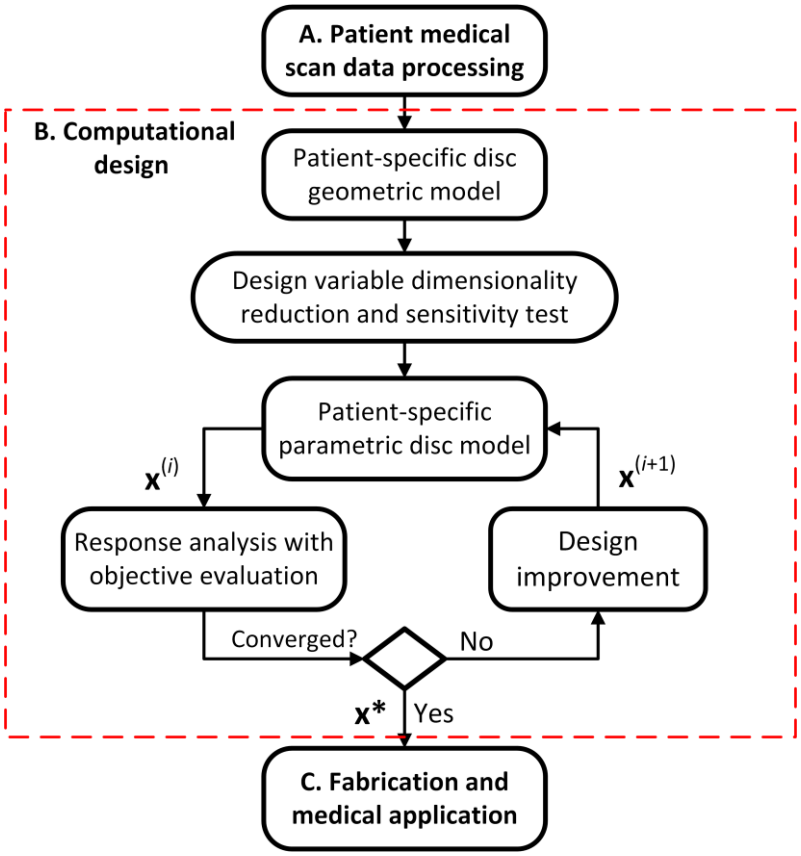

Fig. 3.1. Workflow for the design and fabrication of a patient-specific ASD. The workflow consists of three steps: patient-specific disc geometric modeling from medical imaging (Step A), computational design (Step B), and ASD fabrication followed by medical application (Step C). Design variable dimensionality reduction and sensitivity test help build a patient-specific parametric model through determining design variable $\boldsymbol{x}$. Through a certain optimization algorithm, design variable $\boldsymbol{x}$ will be updated in each optimization iteration to $\boldsymbol{x}^{(i+1)}$ after response analysis with objective evaluation to improve the current design. This update process is ended when the optimization process converges based on certain convergence criteria, whereas the optimized ASD is then fabricated for implantation.

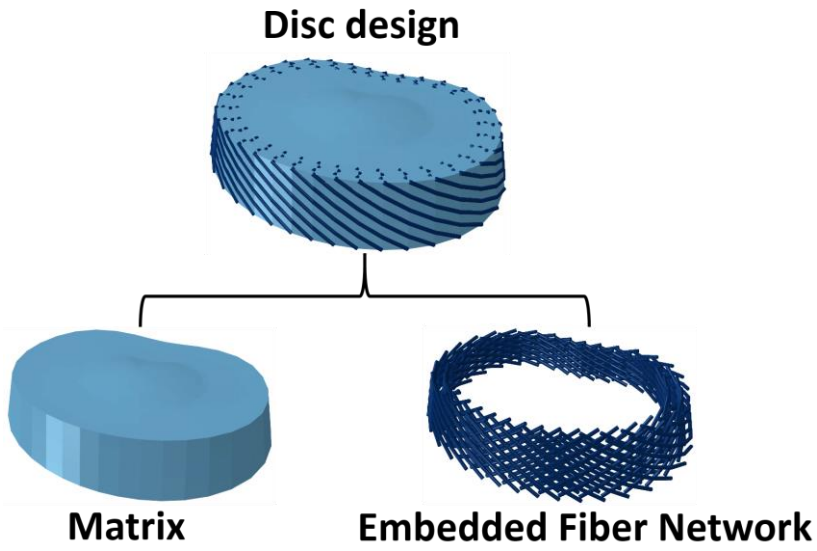

Fig. 3.2. The proposed biomimetic ASD design based on a fiber-reinforced composite. The ASD is composed of a matrix and a crisscross fiber network that is embedded in the matrix.

3.3.2 Geometric modeling

This section aims to use superquadratics for the parametric modeling of the freeform intervertebral space. The ASD is designed to have the same shape as the intervertebral space to achieve an anatomical match. The parameters in the parametric model, which are summarized in Table 3.1, can be adjusted to match individual anatomy extracted from medical imaging. According to [94], the modeling starts with an implicit form of the superquadratic equation to mimic the truncated elliptical conical morphology of an IVD:

$$F(x,y,z) = \left(\frac{x^2+y^2}{r(\theta)^2}\right)^{10} + \left(\frac{z}{h}\right)^{20} \tag{3.1}$$

where

$$r(z,\theta) = \frac{1}{2}\left(1+\frac{z}{h}\right)\frac{a_{\sup}b_{\sup}}{\sqrt{\left(a_{\sup}\sin\theta\right)^2+\left(b_{\sup}\cos\theta\right)^2}} + \frac{1}{2}\left(1-\frac{z}{h}\right)\frac{a_{\inf}b_{\inf}}{\sqrt{\left(a_{\inf}\sin\theta\right)^2+\left(b_{\inf}\cos\theta\right)^2}} \tag{3.2}$$

Subsequently, two local modifications are made to revise the superquadratic equation. The first local modification is to superimpose Gaussian functions on the contour curves of the transverse plane (x-y plane as shown in Fig. 3.3.A) with parameters that define the position, amplitude, and variance of the superimposed Gaussian curves. Thus, the radius of the directrix curve is modified by

$$r_{\mathrm{m}}(z,\theta) = r(z,\theta)\cdot\left(1+\sum_{i\in\{lp,rp,f,a\}} m_i e^{-(\theta-\varphi_i)^2/(2\sigma_i^2)}\right) \tag{3.3}$$

, where lp, rp, f, a represent the positions of left pedicle, right pedicle, vertebral foramen, and anterior disc, respectively (Fig. 3.3.A), and each combination of $\{\varphi, m, \sigma\}$ defines the angle position, amplitude,

and variance of the superimposed Gaussian curve at a certain position (lp, rp, f, a). Fig. 3.3.B illustrates $r(z,\theta)$ and $r_{\mathrm{m}}(z,\theta)$ in Eq. (3.3) that represent the original radius and the modified radius of the directrix curve, respectively. The second local modification is to introduce bumps to the superior and inferior surfaces. A bump with an amplitude of c at (x', y') is added to the surface by modifying the height using

$$h_{\mathrm{m}}(z,\theta) = h(z,\theta) \cdot \left(1 - c \cdot \cos\left(\frac{\pi\sqrt{(x-x')^2 + (y-y')^2}}{r_{\mathrm{m}}(z,\theta)}\right)\right) \tag{3.4}$$

, where $h(z,\theta)$ and $h_{\mathrm{m}}(z,\theta)$ represent the initial height and the modified height, respectively (Fig. 3.3.C), *x'* and *y'* represent the *x* and *y* coordinate of the added bump, c is the bump amplitude, $r_{\mathrm{m}}(z,\theta)$ is the modified directrix curve radius as in Eq. (3.3). Next, the sagittal inclination is generated by bending the superior and inferior surfaces with an amplitude of s and an angle of β using Eq. (3.5) and Eq. (3.6):

$$\begin{pmatrix} x \\ y \\ z \end{pmatrix} \rightarrow \begin{pmatrix} x + (b_{\mathrm{R}} - b_{\mathrm{r}}) \cdot \cos\beta \\ y + (b_{\mathrm{R}} - b_{\mathrm{r}}) \cdot \sin\beta \\ z + (s^{-1} - b_{\mathrm{r}}) \cdot \sin(z \cdot s^{-1}) \end{pmatrix} \tag{3.5}$$

where
$$b_{\mathrm{r}} = \cos(\beta - \theta) \cdot \sqrt{x^2 + y^2},\ b_{\mathrm{R}} = s^{-1} - (s^{-1} - b_{\mathrm{r}}) \cdot \cos(z \cdot s^{-1}). \tag{3.6}$$

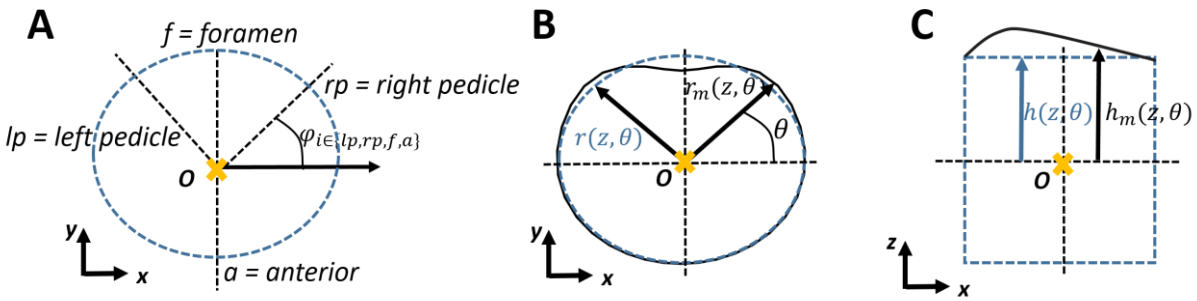

Fig. 3.3. Modification of the superquadratics for the geometric modeling of an ASD. (A) The four positions for Gaussian curve superimposition on the horizontal plane. (B) The horizontal contour before (dotted line) and after (solid line) local modification. (C) The height contour before (dotted line) and after (solid line) local modification.

Table 3.1. Parameters for the geometric modeling of a freeform patient-specific ASD.

Step No.	Goal	Control Parameters		
		Symbols	No. of Parameters	Level
1	Generate truncated elliptical cone.	$a_{\mathrm{sup}},\ b_{\mathrm{sup}}, a_{\mathrm{inf}}, b_{\mathrm{inf}},\ h_{sup}, h_{inf}$	6	Global
2	Superimpose Gaussian curves on the contour curves of the transverse plane.	$\{\varphi_i, m_i, \sigma_i\}$, $i \in \{lp, rp, f, a\}$	12	Local
3	Superimpose bumps to the superior and inferior surface.	$x'_{\mathrm{sup}}, y'_{\mathrm{sup}}, c_{\mathrm{sup}}$, $x'_{\mathrm{inf}}, y'_{\mathrm{inf}}, c_{\mathrm{inf}}$	6	Local
4	Add wedge angle/sagittal inclination.	$s_{\mathrm{sup}},\ \beta_{\mathrm{sup}}, s_{\mathrm{inf}},\ \beta_{\mathrm{inf}}$	4	Global

3.3.3 Computational design

FE modeling

This section builds a FE model of the ASD design after generating the ASD's geometric model in the previous step. Three additional parameters $r_{\mathrm{d}}, c_{\mathrm{d}}, h_{\mathrm{d}}$ are introduced to define the amount of mesh

divisions in the radial, circumferential, and height direction, respectively. The matrix is modelled using a 6-node wedge element (C3D6) and an 8-node hexahedron element with reduced integration (C3D8R), while the fiber is modeled with a one-dimensional truss element (T3D2) that only has tensile resistance to mimic the behavior of natural fibers. One fiber is modeled using five truss elements. The fibers and matrix share the same nodes to model a tight bonding between the fiber network and the matrix. The resultant FE model is illustrated in Fig. 3.4. Based on the coordinate system defined in Fig. 3.4.A, the boundary conditions are added to mimic the *in vitro* ASD mechanical test: all the nodes lying on the inferior/bottom surface (the surface parallel to the x-y plane on the caudal side of the ASD in Fig. 3.4.A) are fixed in all DOFs, while all the nodes on the superior/top surface (the surface parallel to the x-y plane on the cranial side of the disc in Fig. 3.4.A) are coupled to a reference point at all DOFs. The rotational angle and displacement are added to the reference point, where the corresponding reaction moment and reaction force are read out to calculate the ASD's stiffness. A nonlinear FE analysis is performed to calculate the ASD's response. The nonlinearity of the FE model stems from two sources: the material nonlinearity from the fibers with tensile resistance only, and the geometric nonlinearity from the large displacements of the ASD.

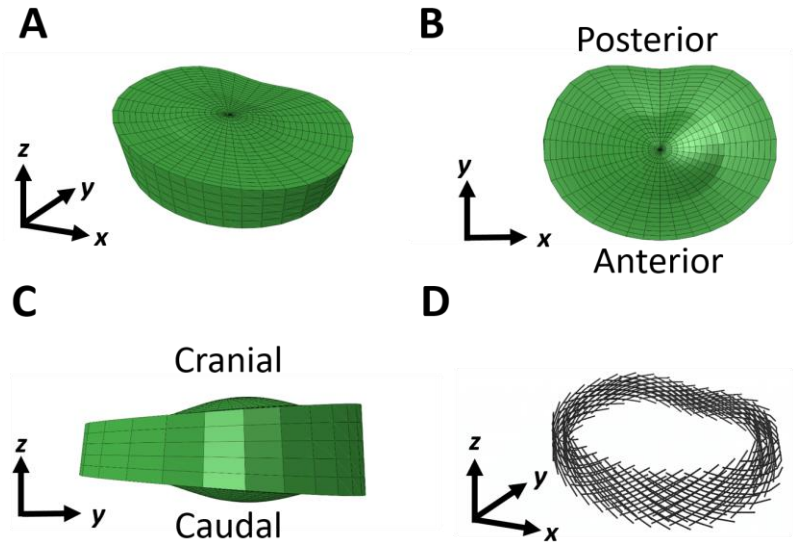

Fig. 3.4. FE model of the proposed ASD design. (A) Isometric view of the matrix mesh. (B) Top view of the matrix mesh. (C) Right-side view of the matrix mesh. (D) Isometric view of the mesh of the embedded fiber network that consists of four alternatively oriented crisscross fiber layers.

Design variable determination

This section determines design variable **x** for the subsequent material optimization. The matrix is divided into four sections, i.e. nucleus, anterior, lateral and posterior region (Fig. 3.5.A). This division yields four design variables $x_1, x_2, x_3,$ and x_4, which represent the Young' s modulus of the nucleus, anterior, lateral, and posterior matrix part, respectively. Inspired by the circumferential and radial material stiffness gradient in an IVD [95][32] and the importance of such gradient to an IVD's unique mechanics [96], a design variable linking strategy that assigns a certain stiffness to a fiber based on its circumferential and radial position is used. The Young's modulus of the material assigned to a certain

fiber is therefore determined based on Eq (3.7), which includes design variables $x_5, x_6,$ and x_7 that represent the fiber base Young's modulus, radial and circumferential gradient of fiber stiffness, respectively. The values of r, c in Eq (3.7), i.e. the radial and circumferential coordinates of a fiber, are calculated based on the bottom truss element's coordinates in the disc coordinate system as illustrated in Fig. 3.5.B. After using a Latin hypercube sampling method to obtain a training dataset, a random forest method is then implemented to verify the design variable selection by identifying their relative contribution to ASD's response in different load scenarios.

$$E\ (\mathbf{x}, r, c) = x_5 + x_6 * r + x_7 * c$$

where

E =Young's modulus of single fiber;
r = Fiber radial-direction coordinate;
c = Fiber circumferential-direction coordinate;
x_5 = Fiber base Young's modulus;
x_6 = Fiber Young's modulus gradient in radial direction;
x_7 = Fiber Young's modulus gradient in circumferential direction

(3.7)

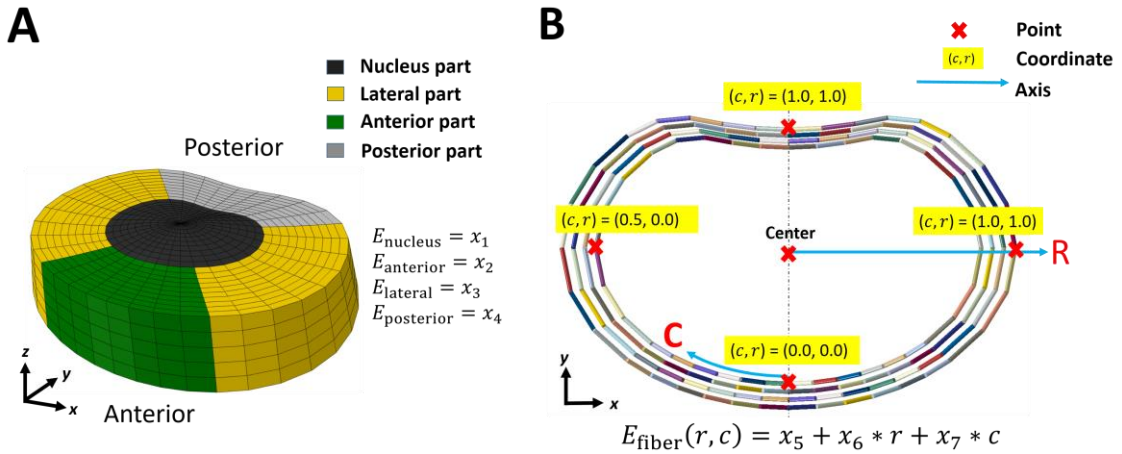

Fig. 3.5. Division of the ASD for design variables assignment. (A) Matrix division and the design variables x_1, x_2, x_3, x_4 that represent the Young's modulus of the nucleus, the anterior, lateral and posterior part of the matrix, respectively. (B) Fiber network division and the design variables x_5, x_6, x_7 that represent the fiber base Young's modulus, fiber radial Young's modulus gradient, and fiber circumferential Young's modulus gradient, respectively.

Optimization formulation

Given the fourteen base materials whose Young's moduli are given in Table 2.4, this section optimizes the material distribution in an ASD to allow it to exhibit nature-mimicking stiffnesses in five loading scenarios (Fig. 3.6): flexion, extension, left LB, left AR, and axial compression. The optimization problem is formulated as:

$$\min_{\mathbf{x}} f = \sum_{i=1}^{5} (\text{ASD Stiffness}(\mathbf{x}, E(\mathbf{x}, r, c)) - \text{IVD Stiffness})^2{}_i$$

where

i = flexion, extension, left LB, left AR, compression

Subject to:

$$\mathbf{x}_{\text{lb}} \leq \mathbf{x} \leq \mathbf{x}_{\text{ub}}$$

(3.8)

, where $\mathbf{x}$ represents the design variable with seven elements illustrated in Fig. 3.5: Young's modulus of the nucleus, the anterior, lateral, and posterior part of the matrix, the fiber base stiffness Young's modulus, fiber radial Young's modulus gradient, and the fiber circumferential Young's modulus

gradient. Based on the constraints of the formulated optimization problem as stated in Section 3.2, a derivative-free search algorithm Nelder–Mead method [97] is used for solving the optimization problem.

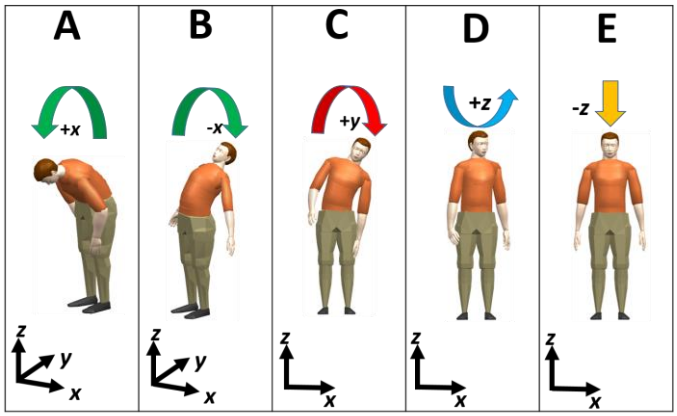

Fig. 3.6. Five loading scenarios of an IVD considered. The five loading scenarios are flexion (A), extension (B), left LB (C), left AR (D) and axial compression (E). The arrow in each figure shows the direction of the imposed force or moment, and the human manikin is created using Siemens NX 10.

3.4 Results

The optimized results of two representative ASDs are presented in this section: a lumbar and a cervical ASD. The following sections present the FE model of the ASD, the design variable verification results using a random forest method, and the optimized results sequentially.

3.4.1 Personalized FE model build

The representative geometric data shown in Table 3.2 from literature is used for describing the global morphology of the ASD [94,98–100]. Due to lack of data from literature, the local morphology parameters shown in

Table ***3.3*** for the ASD are determined to generate a nature-mimicking freeform IVD shape. In a real clinical situation, the values of all the global and local morphology parameters can be determined through an optimization process as suggested in [94]. The detailed views of the FE model of a lumbar ASD is shown in Fig. 3.7.

Table 3.2. Values of parameters for global morphology control

Disc type	Endplate geometry[mm]				Height/2 [mm]	Sagittal inclination	
Lumbar ASD	a_{sup}	b_{sup}	a_{inf}	b_{inf}	h	$s_{\mathrm{sup}}, s_{\mathrm{inf}}$	$\beta_{\mathrm{sup}}, \beta_{\mathrm{inf}}$
	20.75	16.20	22.35	16.70	4.60	-53.50	10°
Cervical ASD	a_{sup}	b_{sup}	a_{inf}	b_{inf}	h	$s_{\mathrm{sup}}, s_{\mathrm{inf}}$	$\beta_{\mathrm{sup}}, \beta_{\mathrm{inf}}$
	9.75	7.85	9.50	7.55	3.00	-47.50	8°

Table 3.3. Values of parameters for local morphology control

	Transverse plane curvature control				Bumped surface control			
		lp	rp	f	a		x'	y'	c'
Lumbar/cervical ASD	$\varphi*$	$3\pi/4$	$\pi/4$	$\pi/2$	$3\pi/2$	superior	1.0	1.0	-0.5
	m	0.1	0.1	-0.1	0.001	inferior	1.0	1.0	-0.5
	σ	$\pi/10$	$\pi/10$	$\pi/10$	$\pi/10$				

* The positive angle is the counter-clockwise angle as displayed in Fig. 3.3.

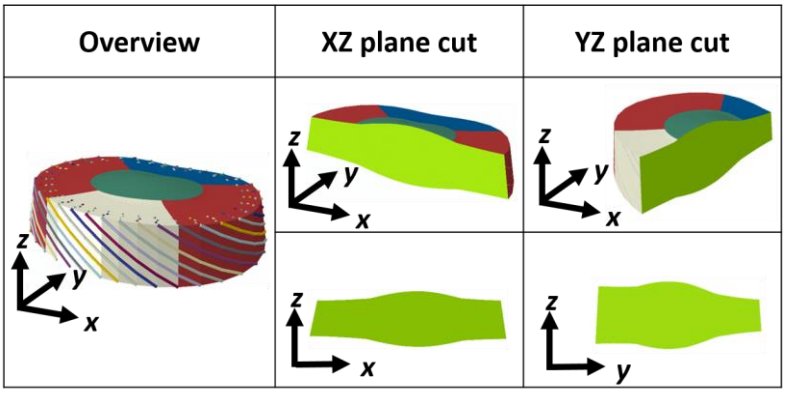

Fig. 3.7. FE model of the lumbar ASD with cut views alongside x-z and y-z plane.

3.4.2 Design variable verification

The selected design variables are verified by calculating their relative importance to the ASD's response in five loading scenarios using the random forest method, which is trained on a total of 100 data points. The results of the sensitivity analysis are shown in Fig. 3.8.

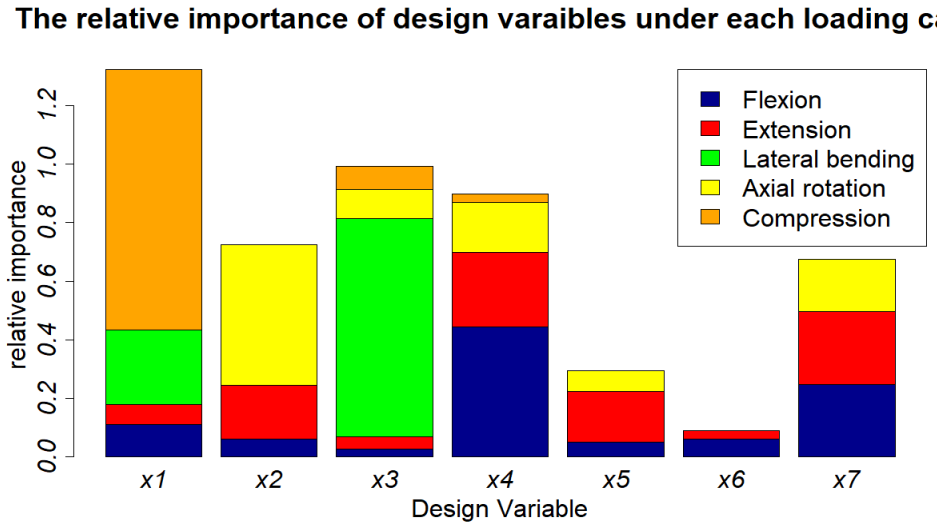

Fig. 3.8. Relative importance of each design variable on the ASD's response in five loading scenarios.

3.4.3 Optimization results of lumbar and cervical ASD

After pre-tests based on simulation to ensure that the target stiffness of an IVD lies in the range achievable by the ASD given the fourteen base materials, the fiber radius of the lumbar ASD is set to 0.25mm, while the fiber radius of the cervical ASD is set to 0.1mm. Table 3.4 shows the target stiffnesses in different loading scenarios for the ASD design [101][102]. Two different optimization bounds are used (Table 3.5): PolyJet material bounds (Material Range 1) and an extended set of material bounds (Material Range 2). The PolyJet material bounds are determined based on the stiffness range achievable with the given materials (Table 2.4), while the extended material bounds are used to examine the potential of further improvement of the ASD's performance without limitations from the given materials. The evaluation of each objective function value requires running five parallel jobs for the five loadings scenarios, followed by a deviation calculation of the ASD's stiffnesses from target values. A

modified Nelder-Mead algorithm with bounds [103] is used for the optimization. The material used to fabricate a certain part is then determined using a material mapping procedure: the optimized material for a certain part is mapped to the available material with the nearest stiffness among the fourteen materials that is at least as great as the optimized value, i.e. rounding up. For example, the optimized stiffness of the cervical posterior part of the matrix is 52.235 MPa, therefore the digital material F9870 with a Young's modulus of 52.5 MPa is used. The stiffness of the optimized multi-material ASD is then compared to that of an IVD and a ball-and-socket ASD. The optimization, which takes a total of 10 hours with 16 cores that are each assigned 4 GB memory, is performed on a high-performance computing cluster (the Euler cluster, ETH Zurich). The optimization process terminates at 855 objective function evaluations for the lumbar ASD and 719 evaluations for the cervical ASD. Fig. 3.9 and Fig. 3.10 show the optimized stiffnesses of the lumbar ASD and the cervical ASD, respectively. The mapped material distributions of the optimized lumbar and cervical ASD are shown in Fig. 3.11 and Fig. 3.12, respectively.

Table 3.4. Target stiffnesses for the lumbar and cervical ASD

	Rotational stiffness [Nm/deg]				**Compression stiffness [N/mm]**
	Flexion	**Extension**	**Left LB**	**Left AR**	**Compression**
Lumbar IVD	1.36	2.08	1.75	5.00	2000.00
Cervical IVD	0.43	0.73	0.68	1.16	1058.50

Table 3.5. Overview of the design variable bounds for the optimization.

Design variable	**PolyJet material bounds [MPa]**	**Extended material bounds [MPa]**	**Design variable**	**PolyJet material bounds [MPa]**	**Extended material bounds [MPa]**
x_1: E(nucleus)	[0.486, 100.0]	[0.1, 200.0]	x_5: coefficient in Eq.(3.7)	[500.5, 2000]	[500, 8000]
x_2: E(anterior matrix)	[0.486, 100.0]	[0.1, 200.0]	x_6: coefficient in Eq.(3.7)	[-250, 300]	[-500, 1000]
x_3: E(lateral matrix)	[0.486, 100.0]	[0.1, 200.0]	x_7: coefficient in Eq.(3.7)	[-250, 300]	[-500, 1000]
x_4: E(posterior matrix)	[0.486, 100.0]	[0.1, 200.0]			

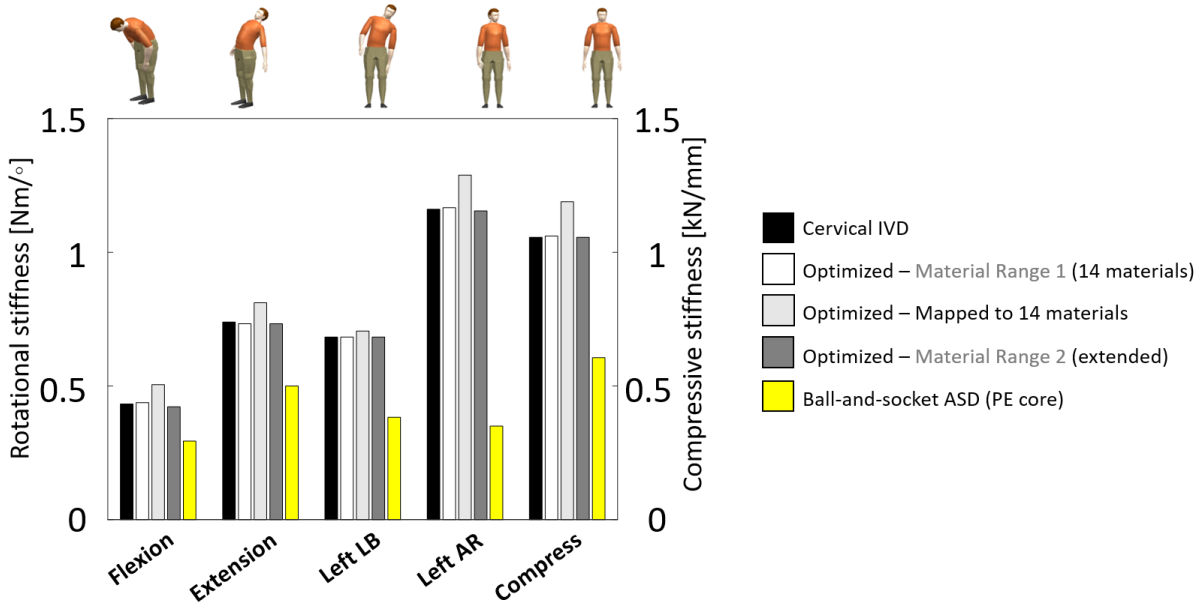

Fig. 3.9. Comparison of the optimized lumbar ASD's stiffnesses to an IVD's and a ball-and-socket ASD's with a polyethylene core.

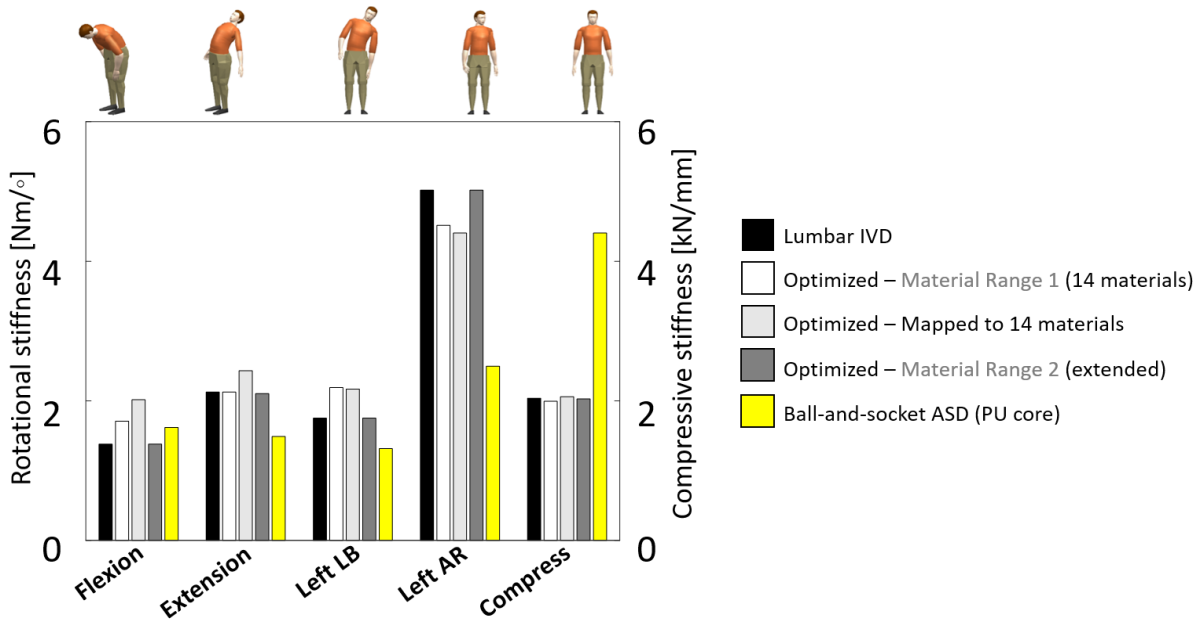

Fig. 3.10. Comparison of the optimized cervical ASD's stiffnesses to an IVD's and a ball-and-socket ASD's with a polyurethane (PU) core.

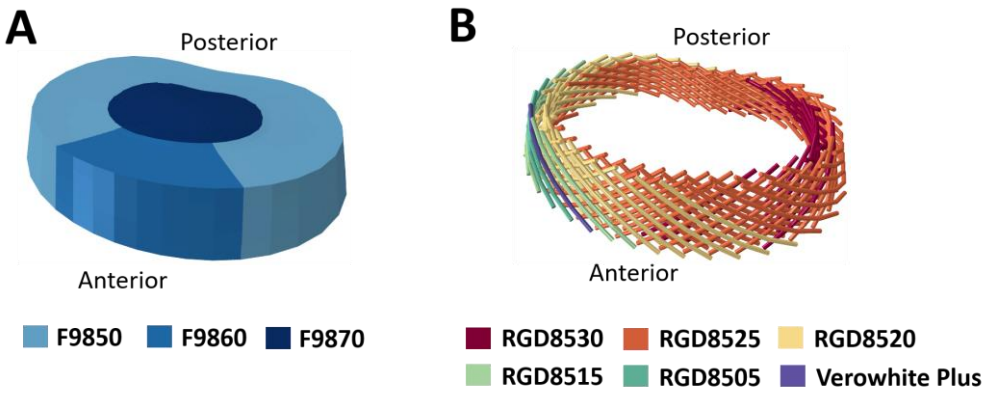

Fig. 3.11. Optimized material distribution in the lumbar ASD. (A) Material distribution in the matrix and (B) material distribution in the fiber network.

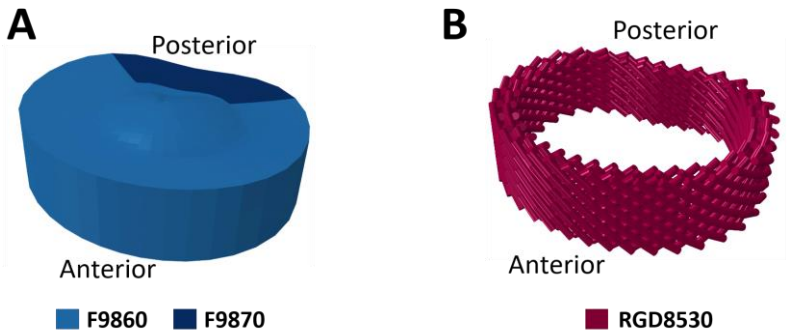

Fig. 3.12. Optimized material distribution in the cervical ASD. (A) Material distribution in the matrix and (B) material distribution in the fiber network.

3.5 Discussion

This section discusses the results, limitations of the modeling and optimization, the optimization algorithm performance, and implications for the thesis.

3.5.1 Results interpretation and assessment

The nature-mimicking shape of the ASD in Fig. 3.7 shows the feasibility of using a superquadratics-based method for the geometric modeling of the freeform IVD. The resultant ASD design helps achieve an anatomical match to homogenize the stress distribution at the implant-vertebrae interface. With a better control over the mesh quality, this parametric modeling method overcomes the limitation of geometric modeling based on 3D segmentation of medical imaging whose quality depends on segmentation threshold [104]. In addition, compared to the method that only uses 2D parameters, the parametric modeling method used improves the modeling precision by using 3D parameters.

The design variables are initially determined using a bio-inspired design variable linking strategy for reducing the design variable dimension. The result of the random forest method (Fig. 3.8) indicates that although all the design variables influence the ASD's load response in more than one loading scenario, the level of importance varies. For example, x_1, the stiffness of nucleus, has a dominant effect on the compression response, while the variables relating to the fiber stiffness, i.e.: x_5, x_6, x_7, have no effect on compression response; x_3, the stiffness of the lateral matrix section, has a

dominant effect on ASD's LB response. These conclusions comply with the assumption that the matrix contributes more to the compressive response compared to fibers and that the lateral matrix is the main load bearing component in LB.

In comparison to a ball-and-socket ASD (grey bars in Fig. 3.9 and Fig. 3.10) that exhibits almost equal stiffnesses in different rotational load scenarios, the stiffness of the optimized multi-material ASD using continuous design variables (red bars in Fig. 3.9 and Fig. 3.10) show a good match to an IVD's. After material mapping, a slightly larger stiffness deviation (orange bars in Fig. 3.9 and Fig. 3.10) is observed, which is due to the rounding up of the optimized material to the nearest material available. The optimized lumbar ASD given an extended material range (green bars in Fig. 3.9) show a better stiffness match to an IVD's compared to the optimized ASD with a limited PolyJet material range (red bars in Fig. 3.9), which demonstrates the potential of further improvement in stiffness match with an extended range of 3D printable materials.

This chapter does not consider structural design variables such as fiber radius and fiber orientation. The reason why fiber radius is not included in the optimization is due to the limited geometric design space and the minimum allowable feature size of the given 3D printing technique, both of which lead to a small search space for fiber radius. The reason why fiber angle is not included in the optimization is the concern of computational efficiency, as a re-meshing is otherwise needed for each fiber orientation change due to the mesh dependency between the matrix and the fibers, which leads to a significant increase in the computational time.

There are several challenges in this work. First is the selection of an appropriate modeling method that not only predicts ASD's response accurately, but also allows for material optimization to be conducted. After determining the modeling method, the second challenge is design variable determination and the implementation of effective heuristics to reduce the dimension of design variables. Different heuristics were experimented with, such as dividing fibers into several regions in the same way as the division of the matrix or using homogenous fiber material distribution. Another challenge is the convergence issue of the FE model during the optimization, which mainly results from local stress accumulation due to inappropriately selected material stiffness assigned to the fibers and the matrix.

3.5.2 Limitations

Several model simplifications are used to improve computational efficiency. First, the patient-specific FE model used in this chapter only includes the ASD, while other functional spinal unit components such as adjacent vertebrae and ligaments are not included. Second, a linear elastic material model is used, which neglects the nonlinearity of the material behaviors. Such simplifications are based on the concern that introducing contact and material nonlinearity will significantly increase the computational time for objective evaluation. Third, this chapter only considers five loading scenarios among all the possible scenarios. Nevertheless, the computational method is easily extendable to include more modeling details and loading scenarios.

3.5.3 Optimization algorithm performance

According to the results in Fig. 3.8, the two design variables that contribute the least to the ASD's load response are x_5 and x_6. Thus, the optimization process of the lumbar ASD with extended material bounds is repeated with six design variables by fixing the value of x_6 to the middle value of the extended material bounds. The results in Fig. 3.13.A show that the biggest deviation among all the loading scenarios is 2.6% in left LB. Additionally, the optimization of the lumbar ASD with five design variables by fixing x_5 and x_6 to the middle values of the extended material bounds is performed. The results in Fig. 3.13.B show that the biggest deviation among all the loading scenarios is 13.8% in left LB. It can be concluded that the stiffness match worsens with fewer variables due to a reduced search space. This again proves the importance of variables x_5, x_6, although their relative contributions are less significant.

Fig. 3.14 shows that fibers at certain locations are responsible for the ASD's response in several loading scenarios, which implies the coupling and dependency of multiple objectives. Thus, the design variables are not separable with regard to different loading scenarios, which complicates the solving of the multi-objective optimization problem due to conflicting objectives. Nevertheless, the fiber behavior with negligible compressive stiffness allows for a certain level of decoupling. For example, in flexion the posterior fibers are the major contributor to the ASD's load response, while in extension the anterior fibers are the major contributor.

Surrogate model based optimization is not used in this chapter for two reasons. First, the surrogate model is problem-specific and is dependent on a certain ASD geometry. That is to say, with a change in the ASD's geometry, new dataset based on design of experiment (DOE) needs to be generated. Therefore, the application of a surrogate model will harm the general applicability of the proposed computational method. Second, in particular cases with complex response surfaces the surrogate model can be misleading [105]. Thus to ensure the prediction accuracy of the surrogate model, a tuning of the surrogate model is required [105]. In summary, surrogate model based optimization is not always efficient and reliable in solving computationally expensive problems.

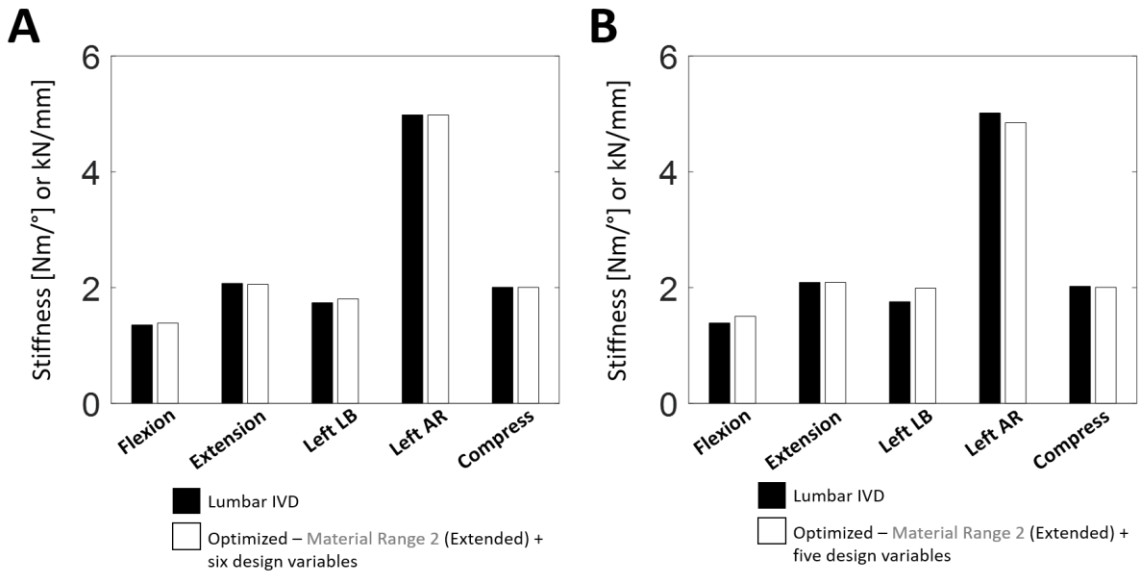

Fig. 3.13. Comparison of the optimized lumbar ASD's stiffnesses with an IVD's given six design variables (A) and five design variables (B).

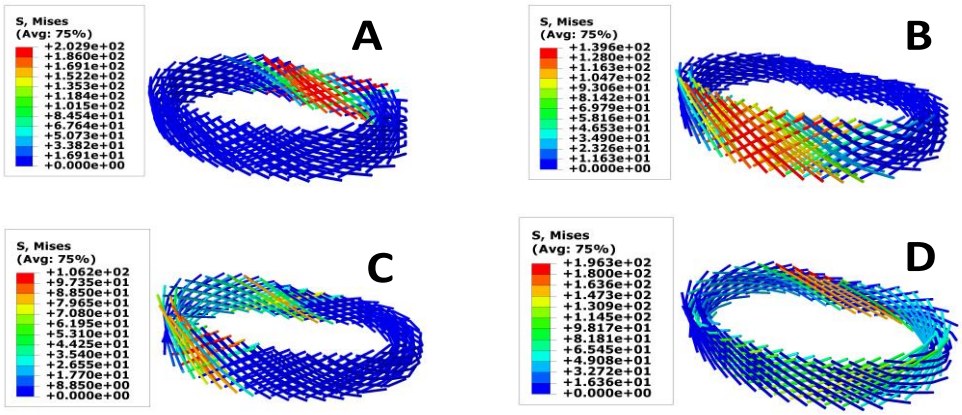

Fig. 3.14. The stress distribution in the fiber network of the lumbar ASD in different loading scenarios. The loadings scenarios are (A) flexion, (B) extension, (C) left LB, and (D) left AR.

3.5.4 Implications for the thesis

The overall computational design method is proven to be effective in realizing a patient-specific ASD design demonstrated by the good match of the optimized ASD's stiffnesses to an IVD's. However, there are some aspects to be improved in the future study. First, the most time-consuming step in the overall computational method is FE analysis. Therefore, to realize a computationally efficient design process, strategies to speed up the design process are required. Second, the bio-inspired design variable linking strategy used in this chapter is ASD design dependent and lacks general applicability. To achieve general applicability of the proposed computational design method, a design variable linking strategy independent of the ASD design is required. Third, the proposed ASD design exhibits a mostly linear load response. In an IVD, the fibers are initially in a crimped state and are able to un-crimp upon load, which contributes to its nonlinear load response. The strategy of incorporating nature-mimicking crimped fibers into the ASD design is however hindered by the micromillimeter-scale crimp amplitude

of the fibers in an IVD [106], which is far below the minimum feature size with the given 3D printer. Therefore, novel strategies or mechanisms to restore the IVD's nonlinear load response need to be developed. Lastly, the FE model of the ASD design ignores the bending stiffness of the 3D printed fibers, while in reality the filaments fabricated using the given 3D printer do not exhibit behaviors of traditional fibers. Considering the critical role of the fiber behavior in decoupling the multi-objective optimization problem, future study needs to explore other decoupling strategies with the given 3D printing technique.

3.6. Conclusion

This chapter presents a generally applicable computational method for the design of a multi-material ASD with patient-specific geometry and nature-mimicking stiffnesses in five critical loading scenarios. The effectivity of the computation method is verified by the good match of the optimized ASD's stiffnesses to an IVD's, which partially answers RQ3. Additionally, this chapter provides answer to RQ2 by proposing a biomimetic, fiber-reinforced composite ASD design and evaluating its performance in meeting the design criteria listed in RQ1. With a patient-specific geometry, the ASD is expected to achieve implantation stability and restore the IVD's height and sagittal alignment. In addition, this design is able to absorb shock when manufactured with viscoelastic elastomers. Furthermore, this design has the ability to restore natural ROM in different loading scenarios through varying its material distribution, although being limited in reproducing an IVD's nonlinear load response. The efficiency of the computational method needs further improvement, which is mainly due to the time-consuming FE analysis. Besides, the bio-inspired design variable linking strategy is design-specific and lacks general applicability, which requires the exploration of other strategies for design variable dimension reduction.

Chapter 4. Clustering-based design variable linking for the efficient design of a multi-material ASD

This chapter has been adapted from the manuscript published in International Design Engineering Technical Conferences and Computers and Information in Engineering Conference (American Society of Mechanical Engineers, 2019):

Yu, Z., Shea, K., Stanković, T., 2019b. Computational design of a personalized artificial spinal disc with a data-driven design varaible linking heuristic. Proc. ASME Des. Eng. Tech. Conf. 2A-2019. https://doi.org/10.1115/DETC2019-97777

4.1 Summary

In Chapter 3 a general computational method for the design of a patient-specific, multi-material ASD fabricated with multi-material AM is proposed. Due to the dependence of the objective function evaluation on FE analysis and the multiple objectives imposed on the ASD design for natural mechanics restoration, the formulated optimization problem has the following features:

1) Multi-objective optimization with conflicting objectives.
2) Costly and noisy function evaluations with implicit models due to the dependence on numerical simulations for objective evaluation [93][107].
3) Reliable derivatives are not directly available and difficult to obtain due to the high computational cost and noisy function evaluations [93].

This justifies the application of an initial step of design variable linking to reduce the problem dimension followed by a derivative-free optimization method [108]. The design variable linking used in Chapter 3 is based on a bio-inspired strategy where the stiffness of the fiber is linked to its circumferential and radial position in an ASD. Although such strategy is proven to be effective, its optimality is not yet justified and the method lacks general applicability, which requires an exploration of different strategies of design variable linking for multi-material ASD design.

ML, which is defined as a set of methodologies that are able to automatically or semi-automatically detect patterns in data [109], has been used in many studies to solve computationally expensive engineering problems. Typical applications of ML in engineering optimization are problem dimension reduction [110] and building surrogate model to replace the expensive objective function [93]. This chapter (Chapter 4) and the following chapter (Chapter 5) perform studies to evaluate the effectivity of using ML in helping achieve an efficient computational design of a multi-material ASD. Namely, this chapter focuses on using ML in design variable linking for problem dimension reduction, whereas Chapter 5 focuses on using ML in building surrogate model to replace the time-consuming FE analysis. Fig. 4.1 summaries the features of the formulated multi-material ASD design problem together

with two possible strategies to tackle the challenges through using ML for realizing an efficient computational design process.

This chapter first presents the overall workflow of the computational design process with a clustering-based design variable linking strategy for the design of a multi-material ASD. The rationale of clustering elements with similar mechanical responses together coincides with the structural adaption of biological tissues to external mechanical stimuli [111]. The workflow includes an initial patient-specific FE model build, clustering-based design variable linking, material optimization, followed by a fabrication through 3D printing and final medical application. Based on the proposed workflow, two multi-material ASD designs, i.e., a solid ASD design and a biomimetic ASD design, are used as case studies to verify the effectivity of the proposed methodology. Results show that the biomimetic ASD outperforms the solid ASD design in terms of reproducing IVD's anisotropic stiffness. In addition, the clustering-based design variable linking strategy is demonstrated to provide a good balance between objective matching and computational time.

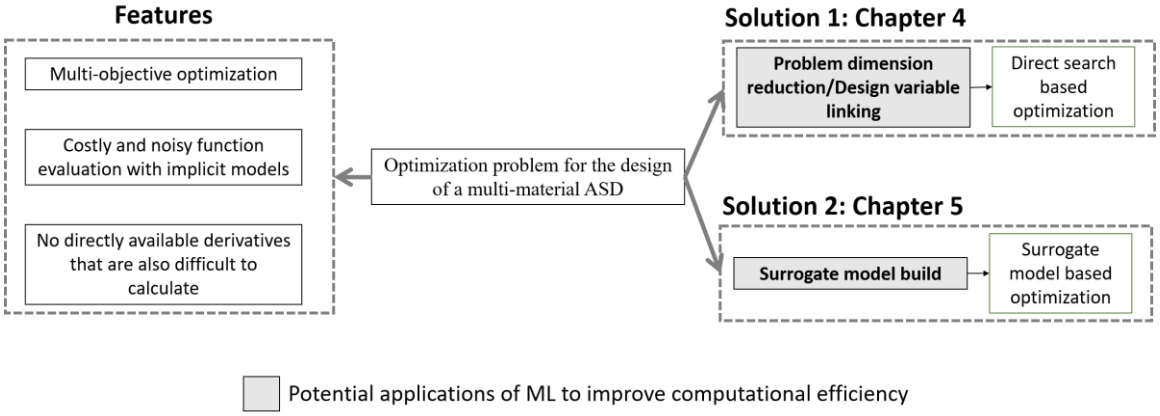

Fig. 4.1. Features of the formulated multi-material ASD design problem and two possible strategies to tackle the challenge through ML. The formulated multi-material ASD design problem is multi-objective. In addition, due to the dependence on ABAQUS for objective function evaluation, the formulated problem has implicit objective functions that are costly and noisy to evaluate, as well as not-directly-available and difficult-to-obtain derivatives. There are two possible strategies to tackle the challenge: problem dimension reduction followed by a direct search based optimization (Chapter 4), and surrogate model build followed by a surrogate model based optimization (Chapter 5). Potential applications of ML to improve computational design process are highlighted in light grey rectangular.

4.2. Background

This section introduces the applications of design variable linking and k-means clustering in structural optimization. The principle of design variable linking to achieve an efficient structural optimization is first introduced in 1973 by Schmit and Farshi [112]. It is considered as one global approximation technique and is targeted for problems with a large problem size either in terms of design variables dimension and/or local constraints whose explicit handling affects the efficiency of the optimization process [113]. Thus, symmetrical structural members are grouped together and their cross section sizes are regarded as one independent design variable [112]. Another study groups structural members based on similar cross section areas, and near optimal solutions are obtained from the reduced search space with much less computational time [114]. Different from the abovementioned strategies, Hajela and Sobieski [115] propose an adaptive design variable linking scheme that ranks all the design

variables according to their combined measure of effectiveness at each optimization iteration, while only the design variables with high effectiveness, i.e. big contribution to the system response, get updated. Instead of linking design variables based on their relative importances, an automatic variable linking method based on enforcing cardinality constraints in the genetic algorithm encoding is used to group similar trusses [116].

As an unsupervised learning method in ML, clustering groups similar data instances together while separating different data instances [117]. Clustering has been used in structural optimization to reduce the dimension of the design space in order to reduce the computational cost of the optimization process. This approach is approved effective for optimization problems with strong nonlinearities and implicit simulations that can result in multi-modal, noisy, discontinuous objective functions [118]. For example, one study [119] uses clustering to group finite elements with similar material properties together in the conceptual design generated after an initial material optimization based on a simplified FE model. A surrogate model is then built in the reduced design space for the subsequent optimization [119]. In another study, elements in a FE model are first clustered based on features such as energy or displacement, followed by a topology optimization in the reduced design space using evolutionary algorithms [118]. Clustering is also used to guide the search direction during optimization by dividing the search space into multiple subspaces [120] or to reduce the number of stress constraints [121]. As a widely used clustering algorithm in the scientific and industrial field, k-means partitions a set of *n* data points $\{\mathbf{y}_1, \mathbf{y}_2, \mathbf{y}_3, \dots, \mathbf{y}_n\}$ into *k* disjoint subsets $S = \{S_1, S_2, S_3, \dots, S_k\}$ by minimizing the sum-of-squares as presented in Eq. (4.1) where $\boldsymbol{\mu}_i$ is the geometric centroid of the data points in S_i. The optimization process then iteratively updates the centroids $\boldsymbol{\mu}_i$ and then assigns the data points to the new centroids until the assignment does not change any more [122].

$$\arg\min_{\mathbf{S}} \sum_{i=1}^{k} \sum_{n \in S_i} \left|\mathbf{y}_j - \boldsymbol{\mu}_i\right|^2 \text{, where } j \in [1, n] \tag{4.1}$$

4.3 Methods

This section first presents the overview of the clustering-based computational design. Next, the detailed procedure of FE model build, clustering-based design variable linking, and optimization problem formulation are presented sequentially.

4.3.1 Overview

As shown in Fig. 4.2, the overall workflow for the clustering-based computational design includes three steps: patient-specific FE model build and an initial FE run, clustering-based design variable linking, and a nonlinear optimization. The patient-specific FE model is supposed to have a personalized geometry, while an initial FE analysis is performed to obtain the mechanical responses of the mesh elements in the FE model. The mechanical responses are treated as features of the mesh elements and denoted as $\{\mathbf{y}_1, \mathbf{y}_2, \mathbf{y}_3, \dots, \mathbf{y}_n\}$ (Step one). Ideally each mesh element can be treated as one design variable for material optimization. However, this will produce a high-dimensional search space

that hinders the efficient solving of the formulated optimization problem. Therefore, a clustering-based design variable linking is performed to cluster mesh elements into subsets **S** to convert the initial high-dimensional design space to a design space with a reduced dimension (Step two). The final step (Step three) is a determination of the optimal material distribution in the ASD by solving a nonlinear optimization problem with discrete variables in the reduced design space.

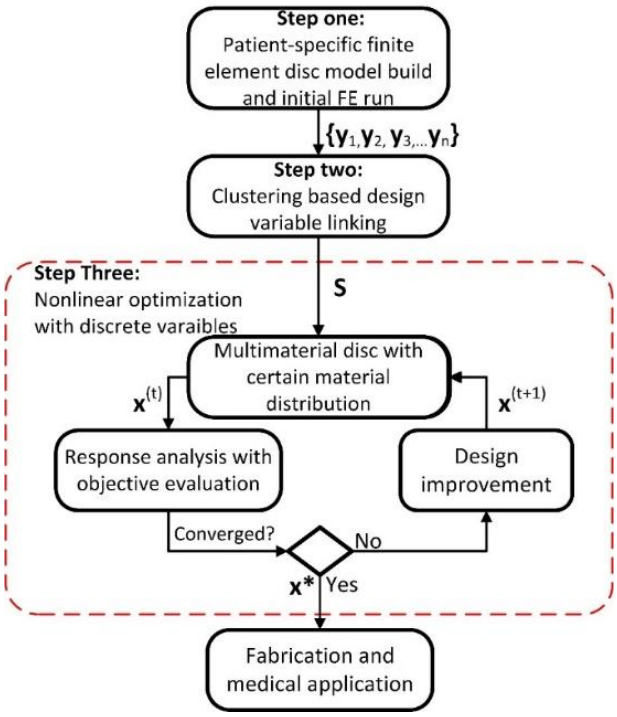

Fig. 4.2. Workflow for the computational design process using clustering-based design variable linking. The computational design process starts with building a patient-specific FE model with a personalized geometry and an initial set of design variables. Next, an initial FE run is performed to obtain the features of the design variables (Step 1), followed by a clustering-based design variable linking to cluster design variables into subsets **S** to form a reduced design space (Step 2). The final step (Step 3) determines the optimized material distribution in the ASD by solving a nonlinear optimization problem with discrete variables in the reduced search space.

4.3.2 FE model build and initial FE analysis

Correspondent to Step one in Fig. 4.2, this step builds a patient-specific FE model of a multi-material ASD. After mesh generation, boundary conditions are added to simulate the *in vitro* mechanical test of an ASD, which is the same as in Chapter 3 [45]. Displacement control mode is used in the FE analysis where a rotational angle of 2° in rotational loading scenarios and a displacement of 1.5 mm in the compressive loading scenario are added to the reference point. The corresponding reaction moments and reaction force of the ASD are then read out from the reference point. The rotational stiffness and compression stiffness of the ASD, which are denoted as SA, are calculated by dividing either the reaction moment by the rotational angle or the reaction force by the displacement. This is justified based on an almost linear response of the ASD with a relatively small deformation. After an initial FE analysis, the stresses in the mesh elements are read out and used as features for the subsequent design variable linking.

4.3.3 Clustering-based design variable linking

Correspondent to Step two in Fig. 4.2, this step groups mesh elements with similar stresses together to reduce the dimension of the design space. The process of extracting the features, i.e., element stresses, is illustrated in Fig. 4.3. Next, clustering is performed using an extension [92] of the original k-means implementation [123] with an integrated Elbow method [124] that determines the number of clusters k used to cluster n design variables ($k \leq n$). The elbow method determines the number of clusters by plotting the explained variation as a function of the number of clusters and uses the elbow of the curve (i.e. the turning point of the curve) as the optimal number of clusters. Mesh elements that belong to the same cluster are assigned the same material property, therefore significantly reducing the dimension of the design space.

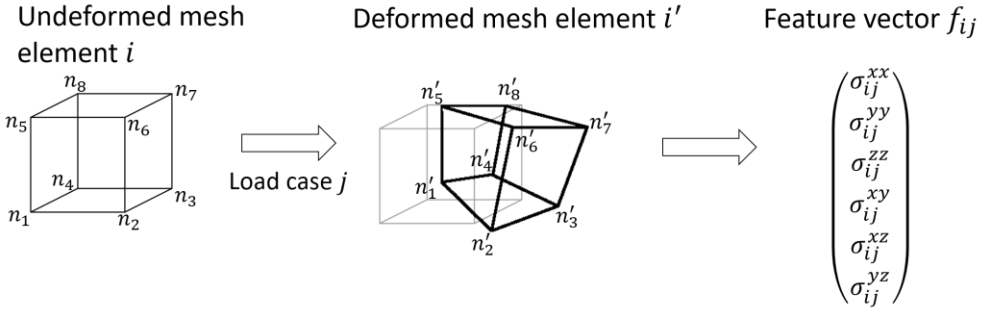

Fig. 4.3. Feature extraction based on the stress responses in mesh elements. Under loading case *j*, the eight-node solid element *i* is deformed. The feature vector f_{ij} with a dimension of 6×1 represents the resultant stress in the eight-node solid mesh element.

4.3.4 Optimization problem formulation

Correspondent to Step three in Fig. 4.2, material optimization is performed in the reduced design space. The optimization problem is formulated as solving a discrete problem to minimize the deviation of the ASD's stiffnesses from an IVD's in five loading scenarios (flexion, extension, right LB, left AR, and compression) [30, 31]:

$$\min_{\mathbf{x}} f = \sum_{c=1}^{5} (SA_c(E(\mathbf{x})) - SN_c)^2 \tag{4.2}$$

s.j.t:

$$\mathbf{K}\big(E(\mathbf{x})\big)\mathbf{u} = \mathbf{F} \tag{4.3}$$

$$\sum_{j=1}^{l_i} \sigma_j \leq l_i \sigma_y(x_i) \tag{4.4}$$

$$x_i \in \{1, 2, \dots, z\}, i = 1, 2, 3, \dots . k \tag{4.5}$$

The design variable **x** represents the material distribution in the ASD and each item in **x** denoted as x_i is an integer that lies in between 1 and *z* (number of base materials provided by the given 3D printer) to represent the material assigned to the mesh elements that belong to the same cluster. In Eq.(4.2), *SA* and *SN* refer to the stiffness of ASD and IVD, respectively, while *c* with a value in between 1 to 5 represents compression, flexion (F), extension (E), right LB, and left AR, respectively. E is the function that maps the design variable **x** to the material assignment of each mesh element that belongs to cluster *i*. In Eq.(4.3), **K**(*E*(**x**)) is the stiffness matrix of the FE model, **u** is the prescribed displacement vector that

serves as boundary conditions, and **F** is the force response of the FE model. In Eq.(4.4), l_i is the number of mesh elements in cluster i, σ_j is the von Mises stress of a certain mesh element j that belongs to cluster i, while $\sigma_y(x_i)$ is the yield stress of the material assigned to cluster i. In Eq. (4.5), k is the total number of clusters. The constraint in Eq. (4.3) is automatically satisfied by the FE analysis, while the stress constraint in Eq. (4.4) is added to avoid material failure. The clusters are not updated during the optimization as it has been shown that the convergence is more smooth without re-clustering [121].

4.4 Results

This section will show the optimization results of two multi-material ASD designs to verify the workflow proposed in Fig. 4.2: a solid ASD and a biomimetic ASD with a separate crisscross fiber-like structure. The dimensions of the two ASD designs are shown in Table 4.1 to mimic the dimensions of a human lumbar L4-L5 IVD. Table 4.2 lists the nine material candidates and their yield stresses to cover a wide range of stiffnesses, thus z is set as 9 in Eq. (4.5).

In the FE model the materials behaviors are modeled as being linear elastic, which is a reasonable assumption considering the relatively small deformation of the ASD. A maximum cluster number of 40 is used for the elbow method to define the number of clusters k. The optimization problem is solved using a Generalized Pattern Search (GPS) algorithm [35] within the NOMAD framework [36]. The optimization settings include a 0.15 probability of initiating Variable Neighborhood Search (VNS) [37] to avoid that the optimizer gets stuck in a local optimum, while the optimization constraints are treated using a progressive barrier method [38] in NOMAD.

Table 4.1. The dimensions of a human lumbar L4-L5 IVD.

Disc Type	Endplate geometry [mm]		Height [mm]	Wedge angle [°]
Human lumbar L4-L5 disc	Transverse diameter	43.2	10.0	10.0
	Anterior-posterior diameter	32.9		

Table 4.2. List of the nine material candidates and their yield stresses [77]**.**

Material code	Material name	Yield Stress [MPa]
1	TangoBlack Plus	0.85
2	F9840	1.5
3	F9850	2.65
4	F9860	0.45
5	F9870	1.00
6	F9885	2.50
7	F9895	7.50
8	RGD8530	49.0
9	VW	50.0

4.4.1 Case study one: Solid ASD

The solid ASD is a monolithic design whose FE model is illustrated in Fig. 4.4. The clustering is only performed on the eight-node mesh elements that comprise the majority of the mesh, while a constant material property is assigned to the six-node wedge elements. After the initial FE run, the stress responses of the mesh elements are read out and used as the elements' features. The feature of each mesh element has a dimension of 30×1 (six stress components × five loading scenarios). The clustering yields a total of 30 clusters with the elbow method, which results in a total of 30 design variables. Fig.

4.5 illustrates the initial high-dimensional design space before clustering and the reduced design space after clustering. A material optimization process is then performed in the reduced design space, the stiffness of the optimized ASD and the optimized material distribution in the solid ASD are shown in Fig. 4.6 and Fig. 4.7, respectively.

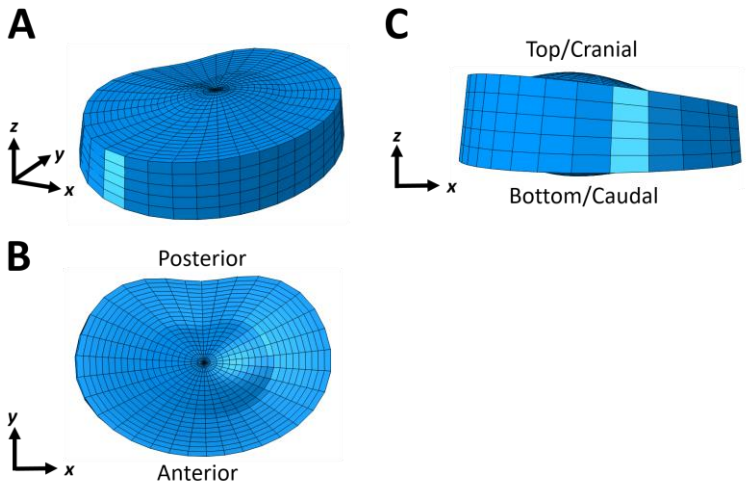

Fig. 4.4. FE model of the solid ASD: (A) isometric view, (B) right view, and (C) top view.

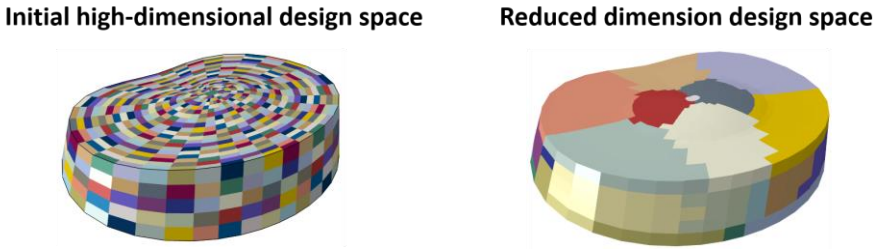

Fig. 4.5. The initial design space before clustering (left) and the reduced design space after clustering (right). Each mesh element is one design variable and plotted with one color in the initial high-dimensional design space (left), while the mesh elements that belong to the same cluster are plotted with the same color (right).

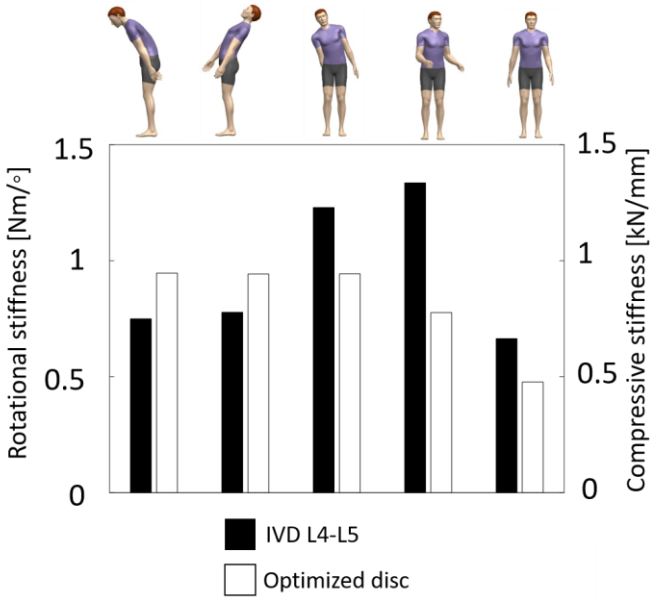

Fig. 4.6. Comparison of the optimized solid disc's stiffnesses to a lumbar L4-L5 IVD's in five loading scenarios.

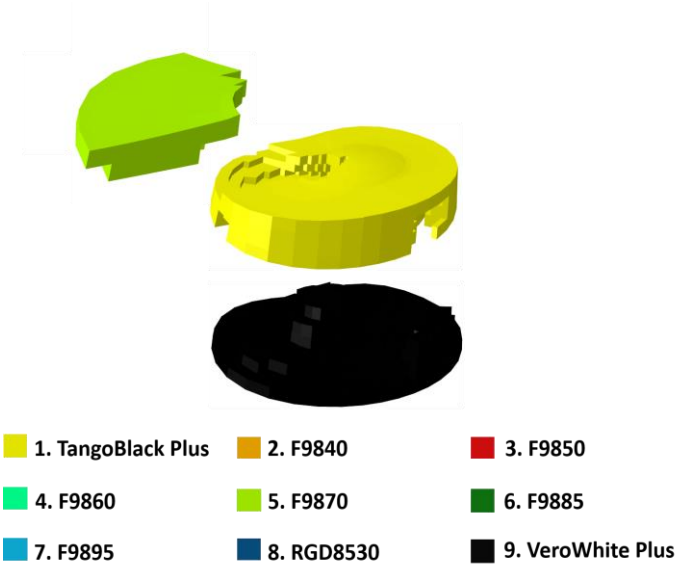

Fig. 4.7. The material distribution in the optimized solid ASD.

4.4.2 Case study two: Biomimetic ASD with a separate crisscross fiber-like structure

The design of the biomimetic ASD (Fig. 4.8) consists of two rigid endplates for interfacing with adjacent vertebrae, a central cylinder that works as an artificial NP surrounded by a layer of crisscross fiber-like structure that works as an artificial AF. The fiber-like structure that consists of several crisscross fiber layers is designed to lie on several circumferentially parallel cylindrical surfaces in the ASD. The 2D projected view of the fiber-like structure that includes four fiber layers is shown in Fig. 4.9 where the fiber-like structure is divided into four design regions: anterior, posterior, left, and right region. The procedure of generating individual fiber layers is illustrated in Fig. 4.10. First, the circumferential contour of the cylindrical surface is discretized using equally distanced N_{angular} discrete points that are denoted as green dots in Fig. 4.10.A. Similarly, the height contour is discretized using N_{vertical} equally distanced discrete points. The cylindrical surface is therefore discretized into a $N_{\text{angular}} \times N_{\text{vertical}}$ grid, where the fibers are then generated by connecting discrete dots in the grid as illustrated in Fig. 4.10.B to generate individual fiber layers. The adjacent fiber layers in the fiber-like structure are oriented alternatively relative to the longitudinal axis to form a biomimetic crisscross pattern. The artificial NP is designed for primarily supporting compressive loads, while the artificial AF is designed to primarily provide support in rotational loading scenarios. The material composition of the artificial NP is first optimized for compression. Next, the contribution of the artificial NP to ASD's rotational load responses is calculated and a subsequent material optimization of the artificial AF is performed.

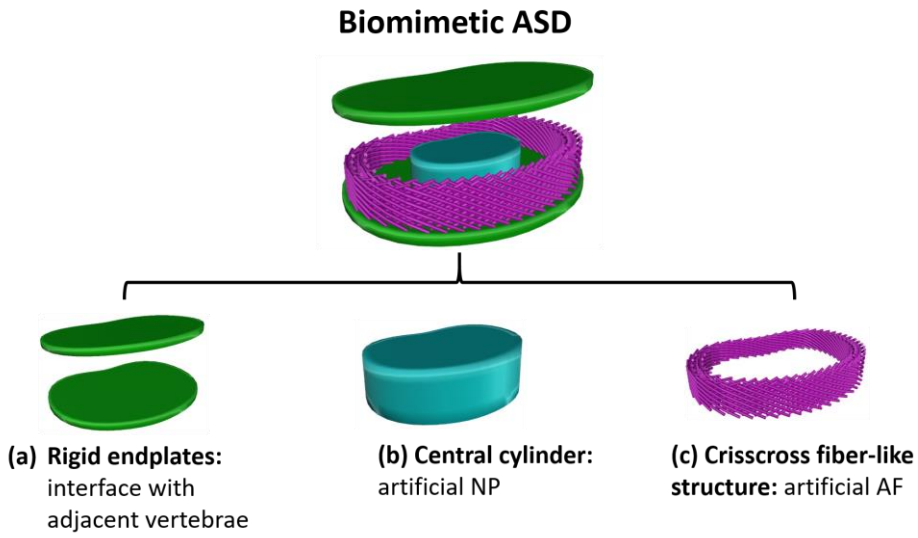

Fig. 4.8. The design of the biomimetic ASD. The biomimetic ASD consists of (a) two rigid endplates for interfacing with adjacent vertebrae, (b) a central cylinder that works as an artificial NP, and (c) a crisscross fiber-like structure that works as an artificial AF.

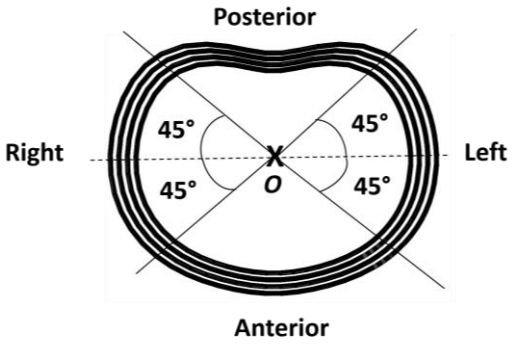

Fig. 4.9. Division of the disc design space into four design regions. The two lines that are perpendicular to each other divide the design domain into four design regions: anterior, posterior, left, and right region.

Optimization of the artificial NP for compression

The initial design space of the central cylinder, i.e., the artificial NP, is divided into nine concentric circles, and the material property of each concentric circle is defined as one design variable (Fig. 4.11.A). The FE model of the nucleus consists of six-node and eight-node solid mesh elements. The optimized material distribution is shown in Fig. 4.11.B. Next, the contribution of the artificial NP to the rotational stiffness of the ASD is calculated and shown in Table 4.3.

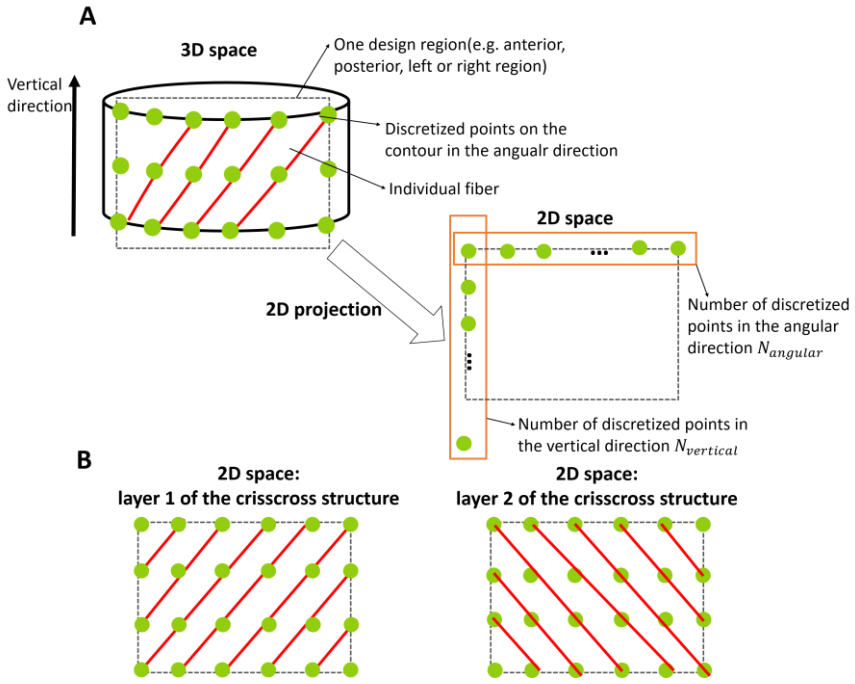

Fig. 4.10. Illustration of the generation of fiber layers in the fiber-like structure. (A) For generating one layer of the fiber-like structure, the circumferentially oriented cylindrical surface is discretized into a $N_{angular} \times N_{vertical}$ grid. (B) Illustration of fiber layer generation through connecting adjacent dots in the grid, which results in a crisscross structure.

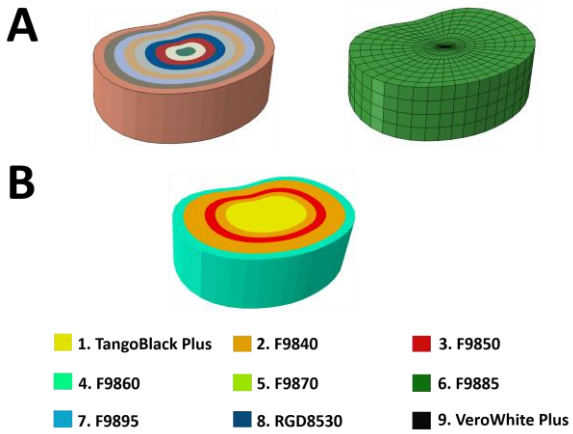

Fig. 4.11. Illustration of the design space and mesh of the artificial NP (A) and the optimized material distribution in the artificial NP (B). The design space of artificial NP is divided into nine concentric circles, and the material property of each concentric circle is defined as one design variable. The mesh is composed of six-node and eight-node mesh elements.

Table 4.3. The rotational stiffness of the optimized artificial NP: unit [Nm/°].

	F	E	Right LB	Left AR
Optimized artificial NP	0.0991	0.1006	0.1000	0.0900

Optimization of the crisscross fiber-like structure for rotation

This chapter uses a vertical division of 5 (N_{vertical} = 6) to avoid the overlap of fibers. Five two-node beam elements are used to model each fiber, while the fiber diameter is set to 0.6 mm that is the minimum allowable feature size of the given 3D printer for reliable mechanical properties. Results from pre-tests show that with a direct material optimization based on equal numbers of N_{angular} in the four design regions (the anterior, posterior, left, and

right regions), the biomimetic ASD performs poorly in matching the stiffness of an IVD. Therefore, an initial structure optimization is performed to search for the optimal angular division in each design region to ensure that the fiber-like structure exhibits natural relative amplitudes of stiffness: left AR > right LB > extension > flexion. The optimization leads to N_{angular} of 12, 8, 23, 8 in the anterior, posterior, left, and right design region, respectively. Next, an initial FE analysis is run and the stress responses of the beam elements are read out and used as features for clustering. The average stress value of the five beam elements that compose a single fiber is treated as the fiber's feature with a dimension of 5 ×1. A k-means clustering is then performed, which generates 21 clusters based on which the material optimization is performed. The stiffness of the optimized biomimetic ASD after material optimization is shown in Fig. 4.12, while the optimized material distribution in the ASD's fiber-like structure is shown in Fig. 4.13.

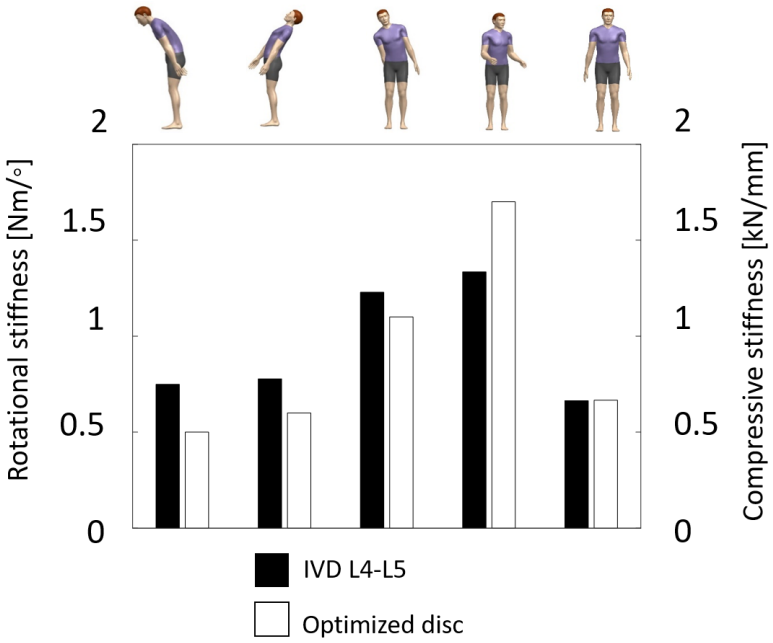

Fig. 4.12. Comparison of the optimized biomimetic disc's stiffnesses to a lumbar L4-L5 IVD's in five loading scenarios.

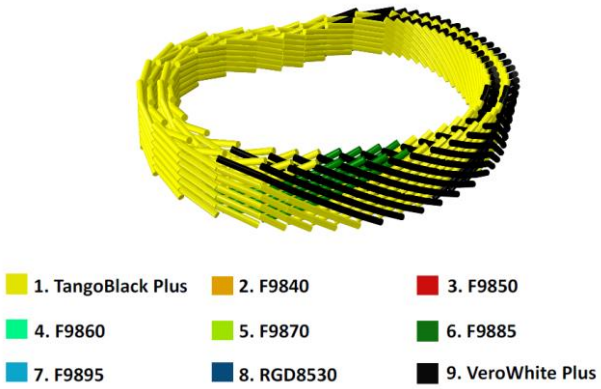

Fig. 4.13. The optimized material distribution in the fiber-like structure of the biomimetic ASD.

4.5 Discussion

This section first discusses the results in Section 4.5.1. Next, Section 4.5.2 presents the implications of the results obtained in this chapter for the thesis.

4.5.1 Results interpretation

This chapter uses a data-driven method to obtain the implicit form of the design variable linking matrix that relates the high dimensional search space to a lower dimensional search space. The motivation of using a k-means method is the high-dimensional features of the structural members. The principle of clustering is similar as a sensitivity test that examines the relative contributions of each structural member to the mechanical responses of the whole system, while structural members with similar levels of contributions are grouped together and one design variable is assigned. Compared to the bio-inspired design variable linking strategy used in Chapter 3, the clustering-based design variable linking strategy used has more general applications and is independent of a specific ASD design.

The proposed methodology is used for designing two ASDs for restoring the natural anisotropic stiffnesses in five loadings scenarios. Fig. 4.6 shows that the stiffnesses of the optimized solid ASD deviate from an IVD's by 36.0%, 36.0%, 40.6%, 54.9%, and 58.9% in flexion, extension, right LB, left AR, and compression, respectively. Moreover, the same relative amplitudes of stiffness are observed throughout the optimization process, i.e., extension > flexion > right LB > left AR. The stiffness mismatch and the unnatural relative amplitudes of stiffness imply that the solid ASD design is insufficient for reproducing IVD's anisotropy. In comparison, the biomimetic ASD shows a good stiffness match (Fig. 4.12), which is mainly due to the introduction of a crisscross fiber-like structure in the biomimetic ASD that exhibits a higher torsional stiffness than its compressive stiffness. With a crisscross fiber-like structure that is mainly responsible for the ASD's torsional resistance and the artificial NP that is mainly responsible for the ASD's compressive resistance, the biomimetic ASD partially decouples the multi-objective optimization problem.

4.5.2 Implications for the thesis

This chapter shows that a solid ASD design is insufficient for restoring IVD's anisotropic stiffness due to conflicting objectives imposed on the design, which implies the importance of incorporating a decoupling mechanism in ASD design to reproduce an IVD's anisotropic stiffness. Specifically, the ASD design needs to include components that contribute to ASD's responses in different loading scenarios at different degrees. For example, the fiber-like structure included in the biomimetic design exhibits a higher rotational stiffness than its compressive resistance, which allows the biomimetic design to more closely mimic an IVD's anisotropic stiffness.

Before the material optimization, an angle optimization of the fiber-like structure in the biomimetic design is performed to reproduce the relative amplitudes trend of an IVD's rotational stiffnesses. This demonstrates the importance of ASD design concepts on which the material

optimization is based for natural anisotropy restoration. Ideally the material and structural optimization should be performed simultaneously, which however will significantly increase the dimension of the search space and adds complexity to the efficient solving of the optimization problem. Therefore, a two-step optimization, i.e., an initial structural optimization and a subsequent material optimization, is used in this chapter for designing the biomimetic ASD.

The clustering method for design variable dimension reduction has general applicability thanks to its independency on a specific ASD design. Compared to the problem-specific, bio-inspired design variable linking strategy used in Chapter 3, the clustering-based design variable linking may suffer from suboptimal solutions. The clustering performed in this chapter is based on stress features derived from FE analysis in multiple loading cases, therefore the different loading cases are treated as equally important as they fairly contribute to the feature formulation. However, such design variable linking may not be the optimal strategy, as the relative importance of some particular loading scenarios is not reflected in the design variable linking. For studies that likewise use k-means for clustering similar design variables [119], only one load case is considered, therefore the relative importance of loading scenarios is not an issue. In conclusion, despite the general applicability of the clustering-based design variable linking method, its optimality requires further exploration.

4.6 Conclusion

This chapter explores the feasibility of using a clustering-based design variable linking strategy for reducing the dimension of the high-dimensional search space to realize an efficient ASD design process. The proposed methodology is verified through the design of two multi-material ASD designs: a solid ASD, and a biomimetic ASD with a separated crisscross fiber-like structure. Results show that the clustering-based design variable linking strategy provides a good trade-off between saving the computational time and meeting the design objectives. The results shown in this chapter partially answer RQ3 by providing a generally applicable strategy to help realize an efficient computational design. Besides, the exploration of the performance of two ASD designs partially answers RQ2. The solid ASD design is insufficient for reproducing IVD's natural anisotropy, while the biomimetic ASD design has the potential to restore the natural anisotropy given an initial angle optimization of the fiber-like structure. Both designs show a mostly linear load response, which requires further design improvement.

Chapter 5. Artificial neural networks (ANNs) supported design of a lattice-based ASD

This chapter has been adapted from the manuscript submitted to *Additive Manufacturing:*
Yu, Z., Shea, K., & Stanković, T. (2021). "Artificial neural networks supported design automation of a lattice-based artificial spinal disc for the restoration of patient-specific anisotropic mechanics."

5.1 Summary

Chapter 4 shows two possible applications of ML to help realize an efficient computational design process. Whereas Chapter 4 shows the application of ML for reducing the problem dimension, this chapter explores the feasibility of using ML technique as a surrogate model to replace the time-consuming FE analysis to speed up the ASD design process. Besides, this chapter proposes an innovative lattice-based ASD design for restoring patient-specific anisotropic mechanics. Lattice structure belongs to cellular structures that are widely adopted by nature in biological organisms such as bones and wood [127]. The main motivations of using lattice structures for ASD design are: 1) the ability of lattices to conform to a freeform 3D space [128] and 2) the ability of lattices to exhibit a controlled anisotropy through topology variation [129]. Additional motivation is the conclusion drawn in Chapter 4 that the structure of an ASD is crucial for natural anisotropy restoration. The design strategy of reproducing a specific anisotropic behavior through adapting a lattice's topology is comparable to the structure-function relationship in an IVD. Such design concept also coincides with the state-of-the-art concept of meta-biomaterials defined as materials with a rationally designed small-scale architecture to achieve an unusual combination of properties present in living tissues [130].

Therefore, the goal of this chapter is to explore the feasibility of a novel lattice-based ASD to reproduce the patient-specific anisotropic behavior, as well as to propose an ANN-supported, systematic methodology to design such lattice-based ASD. The overall workflow of the methodology starts with a discretization of the patient-specific disc space based on a certain cell size that determines the grid division and a unit-cell library to generate a lattice-based ASD. Next, a ML-supported topology optimization of ASD is performed based on an ANN regression model that captures the relationship between the lattice-based ASD's topology and its stiffness in six rotational loading scenarios. The goal of the topology optimization is to restore the relative amplitudes of the stiffness of the lattice-based ASD in six loading scenarios. After a fine-tuning of the material composition and member size in the lattice-based ASD to restore the absolute values of the stiffness, the optimized lattice-based ASD is to be fabricated using AM. A unit-cell based parameterization is used in this chapter mainly due to two reasons. First, a unit-cell based design guarantees the manufacturability of the lattice by including manufacturable cells for a specific 3D printing technique in the unit-cell library. This overcomes the limitation of a voxel-based parametrization that can possibly lead to small features whose sizes are below the printing limit [131]. Second, a unit-cell based parameterization reduces the problem dimension and allows for the potential incorporation of predefined heuristics in the unit-cell library selection to facilitate the problem solving [132].

The application of ML in the patient-specific ASD design can potentially speed up the design process while allowing clinicians to focus on applying their medical expertise on the ASD design by sparing them from the tedious engineering task [133]. This will not only benefit the patients by improving the clinical outcomes, but also help bring personalized implants closer to clinics. Additionally, ML has the potential to discover novel lattice topologies that do not exist in the nature for obtaining a controlled anisotropy. The contribution of this chapter is as follows:

- First, a novel lattice-based ASD design is proposed for matching patient-specific anatomy and reproducing patient-specific anisotropic stiffness in six rotational loading scenarios.
- Second, a conceptual ML-supported framework is proposed for the efficient design of such lattice-based ASD.
- Third, the effectivity of incorporating problem-specific heuristics into the ML-supported design framework to balance the computational cost and design freedom is proven.
- Lastly, the great potential of ML and mechanical metamaterials for patient-specific implant design is demonstrated.

5.2 Background

Despite the potential of lattice structures, there is no systematic and effective methodology for the design of such lattice structures to achieve a controlled anisotropy [129]. The conventional method is to select one or several unit-cells and make modifications on them, which is time-consuming as the whole process is based on trial-and-error while the existence of the desired anisotropy is not guaranteed [134]. The design of a lattice-based ASD for restoring the anisotropic behavior can be approached by stating and solving an inverse structure optimization problem. The efficient solving of such inverse design problem is challenging, which is predominantly due to the high computational cost of structure analysis and the requirement of tuning initial guesses and constraint formulation. The solving of such optimization problem is further challenged by the multimodal and nonconvex search space [135]. ML is a promising approach to mitigate this challenge through automating the time-consuming engineering tasks given a sufficient amount of existing data. As one ML technique, ANN has been used for classification [136] and real-time response prediction [137]. Specifically, ANN has been used to solve the inverse optimization problem for the design of metamaterials that usually have a large design space or a large response space to achieve certain mechanical functions [135][138]. There are two major applications of ML for solving the inverse design problem of metamaterials: as a surrogate model for response prediction, or as a generative model for automatic design generation.

Examples of ML models commonly used as a surrogate model are multi-layer perceptron (MLP) and convolutional neural network (CNN). For such application, the ML-based model is used to capture the nonlinear, complex relationship between the design space and the response space of metamaterials. Afterwards, the ML-based model is usually combined with an optimization algorithm for the structure optimization of metamaterials. For example, a combination of MLP and genetic algorithm (GA) is used to design modular metamaterials for producing tunable bandgaps [139]. MLP is also combined with a

self-learning algorithm for designing cross section size of a beam to realize high strength and stiffness [140] or for designing material distribution in a composite to realize high toughness and strength [141]. Examples of using CNN for the metamaterial design are a lattice-based actuator for obtaining a desired movement [142] and kirigami-based metamaterial for achieving high tensile yield strain [143].

One frequently used ML technique as a generative model is variational autoencoder (VAE), which is able to map the discrete, high-dimensional design space into a continuous, low-dimensional latent space. This latent space can either be directly used to map to the response space of metamaterials, or be used as low-dimensional features to extract similarities among different metamaterials [144]. Wang et al [144] shows that tuning of the mechanical properties of metamaterials can be accomplished through simple vector operations in the latent space generated by VAE. Similarly, new microstructure designs with extremal elastic material properties have been generated through clustering microstructures in the latent space [131]. The latent space can also be combined with a Bayesian optimization for metamaterial design [145]. VAE is used for designing metamaterials whose both design and response space are high-dimensional [146].

5.3 Methods

This section first introduces the general workflow for the lattice-based ASD design to restore patient-specific anisotropy in Section 5.3.1. Next, the detailed procedure for the discrete space discretization is stated in Section 5.3.2, followed by a Section 5.3.3 that elaborates the process of ANN-supported topology optimization.

5.3.1 Workflow overview

As illustrated in Fig. 5.1, the overall workflow starts with a discretization of the patient-specific disc space based on a certain cell size that determines the grid division and a unit-cell library to generate a lattice-based ASD (Step 1). Next, a ML-supported topology optimization is performed (Step 2) based on an ANN regression model that captures the relationship between the lattice-based ASD's topology and its stiffness in six rotational loading scenarios as illustrated in Fig. 5.2: flexion (F), extension (E), left LB/right LB(LLB/RLB), and left AR/right AR (LAR/RAR). The goal of Step 2 is to enable the lattice-based ASD to restore the normalized stiffness of an IVD in six loading scenarios, while the normalized stiffness is calculated by dividing the ASD's stiffness in each loadings scenario by its stiffness in flexion. This is targeted at reproducing natural relative amplitudes of stiffnesses in six rotational loading scenarios. For example, the stiffness in extension needs to be 30 percent higher than the stiffness in flexion. In Step 3, the material composition and size of the bars in the ASD are fine-tuned to restore the absolute values of the stiffnesses in six loading scenarios. Step 4 includes a fabrication of the optimized lattice-based ASD. It is to be noted that Step 3 and Step 4 are dependent on the given 3D printing technique together with its printable materials. The detailed processes of the design space discretization (Step 1) and ML-supported topology optimization (Step 2) are explained in the following subsections.

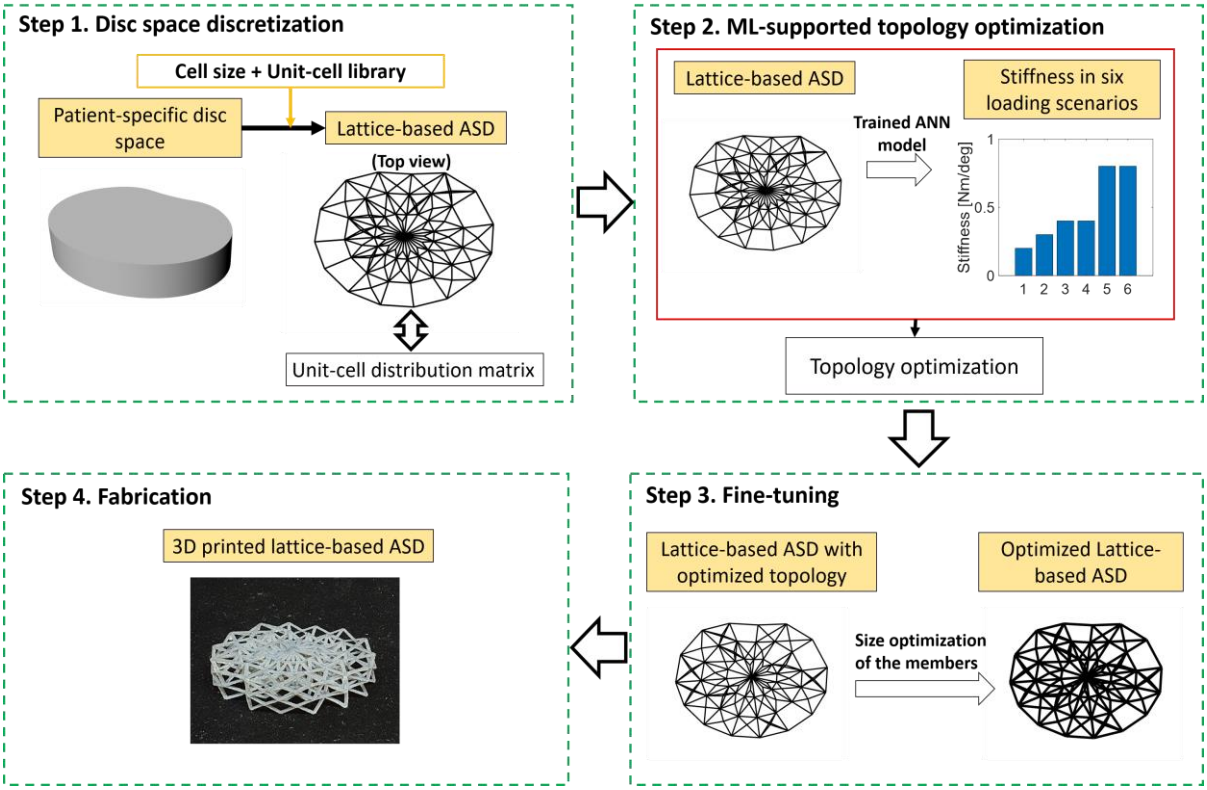

Fig. 5.1.The overall workflow for the design of a lattice-based patient-specific ASD. It is to be noted that Step 3 and Step 4 are dependent on the given 3D printing technique together with its printable materials.

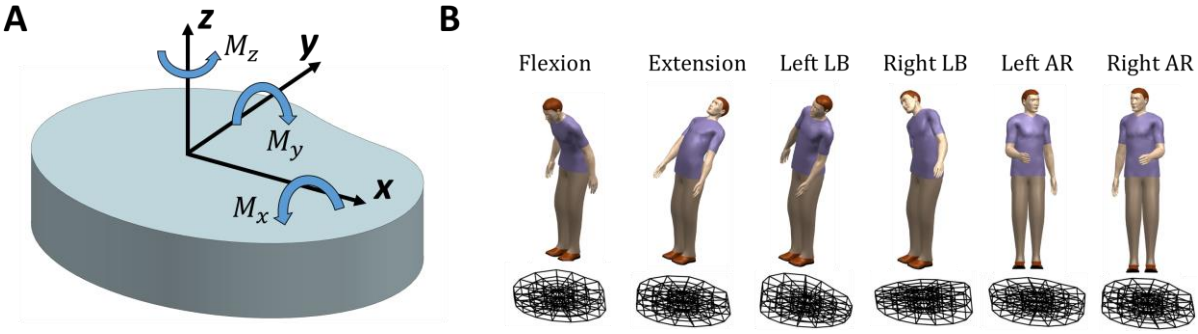

Fig. 5.2. Six rotational loading scenarios of an IVD. (A) Pure rotational moment added to the IVD: the arrow direction represents the positive moment ($M_{x^+}, M_{y^+}, M_{z^+}$), while the opposite direction of the arrow represents the negative moment ($M_{x^-}, M_{y^-}, M_{z^-}$). (B) Illustration of the six loading scenarios and the deformed ASDs. Flexion corresponds to the moment M_{x^+}, while extension corresponds to the moment M_{x^-} . Left LB corresponds to the moment M_{y^+}, while right LB corresponds to the moment M_{y^-}. Left AR corresponds to the moment M_{z^+}, while right AR corresponds to the moment M_{z^-}.

5.3.2 Disc space discretization

This section explains the detailed process for generating a lattice-based ASD from the patient-specific disc space through disc space discretization. The pseudo-code for the disc space discretization is shown in

Table ***5.1***. The patient-specific disc space is expected to be extracted from medical imaging to capture patient-specific geometric information. The cell size that determines the grid division in the circumferential (n_{angular}), radial (n_{radial}), and height (n_{height}) direction is determined to provide enough design freedom while avoiding the overlap of bars. Thus, the design space is discretized into a grid with a total of $n_{\text{angular}} \times n_{\text{radial}} \times n_{\text{height}}$ cells. The discretization is performed using the toolbox IntraLattice [147] that is a conformal lattice generator plugin in GRASSHOPPER (v1.0.0007 2021)

visual algorithm and modeling environment for RHINO 6 (Fig. 5.3.A), which results in six-node and eight-node cells (Fig. 5.3.B). The next step is to assign a certain unit-cell to each cell in the grid based on a unit-cell library that contains unit-cells with various topologies and diverse anisotropies. The size of the unit-cell library is determined to balance design freedom and the computational cost for generating training dataset in Step 2. This is due to the rationale that a larger neural network is required to learn a more complex relationship between the input and output, which in turn requires a larger training dataset. With limited capacity in the unit-cell library, we explored two strategies to determine the unit-cells included in the unit-cell library:

- Library A: A unit-cell library with randomly selected unit-cells,
- Library B: A unit-cell library with unit-cells determined based on heuristics.

The second strategy allows for the incorporation of problem-specific heuristics that favor unit-cells with certain anisotropies that are quantified using the following constitutive law:

$$\{\delta\} = [C]\{\varepsilon\} \tag{5.1}$$

where $\{\delta\}$ and $\{\varepsilon\}$ represent the stress and strain vectors of the unit-cell in the coordinate system defined in Fig. 5.3.B, $[C]$ is the elasticity tensor that relates the strain to the stress and is calculated by asymptotic homogenization (AH) method [148]. For comparability, the elastic tensors of different unit-cells are compared with the same relative density through varying the bar radius. The volume of the unit-cell is calculated by summing up the volumes of all bars, while the volumes of the bars lying on the edge or on the faces of the cell are scaled by a factor of ¼ and ½, respectively. The compliance matrix is then obtained based on $[S] = [C]^{-1}$. The engineering constants, i.e., the effective Young's modulus and shear modulus, are calculated based on $[S]$ following

$$E_x = \frac{1}{S_{11}}, E_y = \frac{1}{S_{22}}, E_z = \frac{1}{S_{33}}, G_{yz} = \frac{1}{S_{44}}, G_{xz} = \frac{1}{S_{55}}, G_{xy} = \frac{1}{S_{66}} \tag{5.2}$$

After determining the unit-cell library with a size of *N*, each cell in the grid is assigned a certain unit-cell, where different assignment combinations lead to varying topologies and anisotropies of the lattice-based ASD. To facilitate the quantification of the resultant topology of the lattice-based ASD determined by a specific unit-cell distribution, the concept of unit-cell distribution matrix is introduced. As shown in Fig. 5.4, each element in the cell distribution matrix corresponds to one cell in the grid, where the spatial information is partially reserved in the matrix, such as the adjacent cells in the radial direction of the grid are represented as adjacent elements in the unit-cell distribution matrix. With *N* unit-cells, each element in the unit-cell distribution matrix is assigned an integer that lies in between 1 and *N* to represent the unit-cell assigned. This results in a total of $(n_{\text{angular}} \times n_{\text{radial}} \times n_{\text{height}})^N$ possibilities of lattice topology, while the amount increases exponentially with the increase of unit-cell library size.

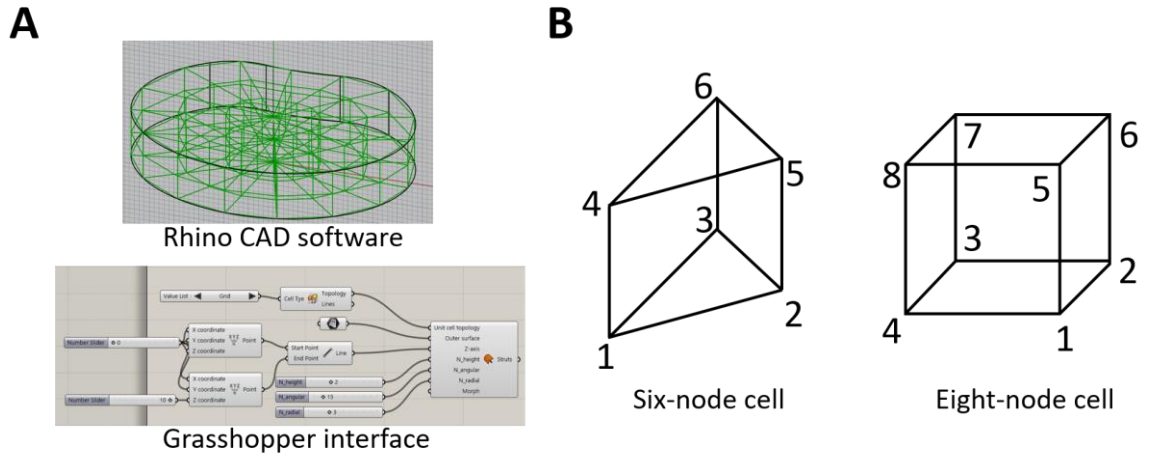

Fig. 5.3. Design space discretization. (A) Illustration of the grasshopper/Rhino interface for grid generation. (B) Example of six-node and eight-node cells of the grid together with the local coordinate system. The nodes are indexed in a counter-clockwise manner.

Table 5.1. The pseudo-code for disc space discretization.

Input: the grid division $[n_{\text{angular}}, n_{\text{radial}}, n_{height}]$, the unit-cell distribution matrix **D**, the unit-cell library L that contains N unit-cells, initial node set **p** of the grid, initial connection $\mathbf{b} = []$
Output: the node set $\mathbf{p}'$ and connection $\mathbf{b}'$ of the lattice-based ASD

Initialization and set $\mathbf{p}' = \mathbf{p}$, $\mathbf{b}' = \mathbf{b}$
For $i = 1: n_{angular}$
  For $j = 1: n_{radial}$
    For $k = 1: n_{height}$
      Find the nodes of the cell (six-node or eight-node) in the initial node set **p**
      Check the cell's corresponding element in the unit-cell distribution matrix $\mathbf{D}(i, j, k)$
      Find the assigned unit-cell in the unit-cell library $L(\mathbf{D}(i, j, k))$
      Get the unit-cell connections $\mathbf{b}_{cell}$ and new node $\mathbf{p}_{cell}$ based on $L(\mathbf{D}(i, j, k))$
      Append the new connections and nodes by $\mathbf{b}' = [\mathbf{b}' \ \mathbf{b}_{cell}]$ and $\mathbf{p}' = [\mathbf{p}' \ \mathbf{p}_{cell}]$
    End
  End
End

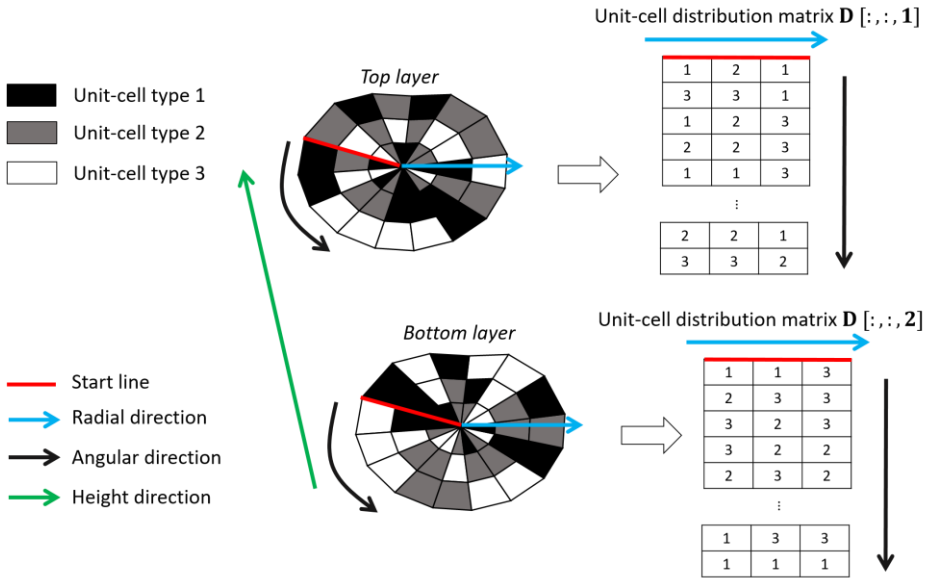

Fig. 5.4. Formulation of the unit-cell distribution matrix that represents the topology of the lattice-based ASD. The arrow direction represents the positive direction. A unit-cell library with three unit-cells that are represented as different colours is used as an example for illustration. The unit-cell distribution in the lattice, i.e., the topology of the lattice, is then represented using a unit-cell distribution matrix where each element corresponds to one cell in the grid. Each element in the unit-cell distribution matrix is assigned an integer that lies in between one and three. The spatial information of the unit-cell distribution is partially reserved, such as the adjacent cells in the radial direction of the grid are represented as adjacent elements in the unit-cell distribution matrix.

5.3.3 ML-supported topology optimization

As illustrated in Fig. 5.5, this section first builds an ANN regression model and then performs a topology optimization of the lattice-based ASD whose topology is represented as a unit-cell distribution matrix using the ANN model to efficiently calculate the lattice's response. In ML step 1, the training data is generated based on FE analysis. The input of the training data is the lattice-based ASD's unit-cell distribution matrix and the output is the ASD's stiffness in six loading scenarios. In the FE model, the boundary conditions are the same as stated in Chapter 3, and the ASD's top surface is rotated for 5º in each loading scenario. The stiffnesses in six loading scenarios denoted as $S_{\mathrm{F}}, S_{\mathrm{E}}, S_{\mathrm{LLB}}, S_{\mathrm{RLB}}, S_{\mathrm{LAR}}, S_{\mathrm{RAR}}$ are calculated by dividing the reaction moment in each loading scenario by the rotation angle, i.e., 5º.

In ML step 2, two ANN models typical for the inverse design of metamaterials are built: a MLP [139] and a CNN [141]. The building and training of the two ANN models are implemented in PyTorch. Fig. 5.6 shows the detailed architectures of the two ANN models. The unit-cell distribution matrix is flattened into a one-dimensional array for the input of MLP and is transformed to a list of 2D matrices for the input of CNN. The number of 2D matrices for the input of CNN equals to the grid division in the height direction n_{height}, while each matrix has a dimension of $n_{\mathrm{radial}} \times n_{\mathrm{angular}}$. The output of both ANN models is set as six neurons that represent the ASD's stiffness in six loading scenarios. The MLP only has one hidden layer of size 512. In comparison, the CNN has two convolutional layers, where the first layer computes 32 features using a 3 by 3 patch and the second layer computes 64 features using a 3 by 3 patch. A stride of one with one padding is used when generating the features for the convolutional layers. The second convolutional layer is then connected to a pooling layer with a kernel size of 2 by 2. The output is then flattened to feed into a fully connected layer with 256 neurons. The training loss is set as L1 loss that calculates the deviation of the six stiffnesses predicted by the ANN model and the FE analysis. The training process updates the model's parameters using Adam that is a stochastic optimization algorithm implemented in PyTorch. The prediction accuracy of the two ANN models is verified in ML step 3 by comparing the stiffness predicted by the ANN model with that calculated by FE analysis, and the model with a higher prediction accuracy is used as a regression model for structural analysis. ML step 4 then performs a topology optimization whose goal is to search for the optimal unit-cell distribution that allows the lattice-based ASD to restore the relative amplitudes of IVD's stiffness in six loading scenarios. Thus, the objective function for the topology optimization is formulated as:

$$\min f(\mathbf{x}) = \sum_{i=1}^{6} \left({S_i(\mathbf{x})}/{S_{\mathrm{F}}(\mathbf{x})} - {S_i'}/{S_{\mathrm{F}}'} \right)^2 \qquad (5.3)$$

$$i = \text{loading case } \{1, \ldots, 6\} \text{ denoting flexion, extension, left/right LB, and left/right AR, respectively,}$$

where $\mathbf{x}$ is the unit-cell distribution matrix, S_{F}' and S_{F} represent the flexion stiffness of an IVD and a lattice-based ASD, respectively, S_i' and S_i represent the stiffness of an IVD and a lattice-based ASD in

six loading scenarios. S_i/S_F and S_i'/S_F' are referred to as the normalized stiffness of the lattice-based ASD and the IVD, respectively. The optimization is performed using an open-source python-implemented GA algorithm (PyGAD) with default settings, while each solution with $n_{\text{angular}} \times n_{\text{radial}} \times n_{\text{height}}$ genes correspond to one unit-cell distribution matrix. The optimization is terminated after 500 iterations and the optimized lattice-based ASD is validated through FE analysis.

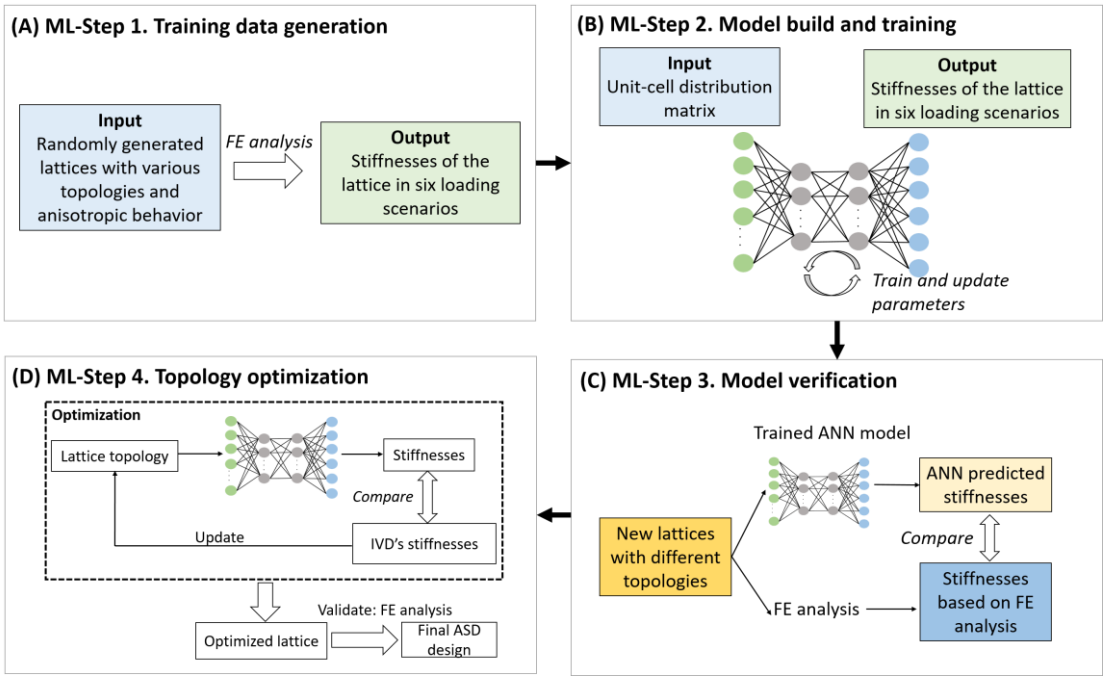

Fig. 5.5. The workflow for the ML-supported topology optimization. (A) ML Step 1: training dataset generation. (B) ML Step 2: ML model training. (C) ML Step 3: ML model verification. (D) ML Step 4: topology optimization and result validation.

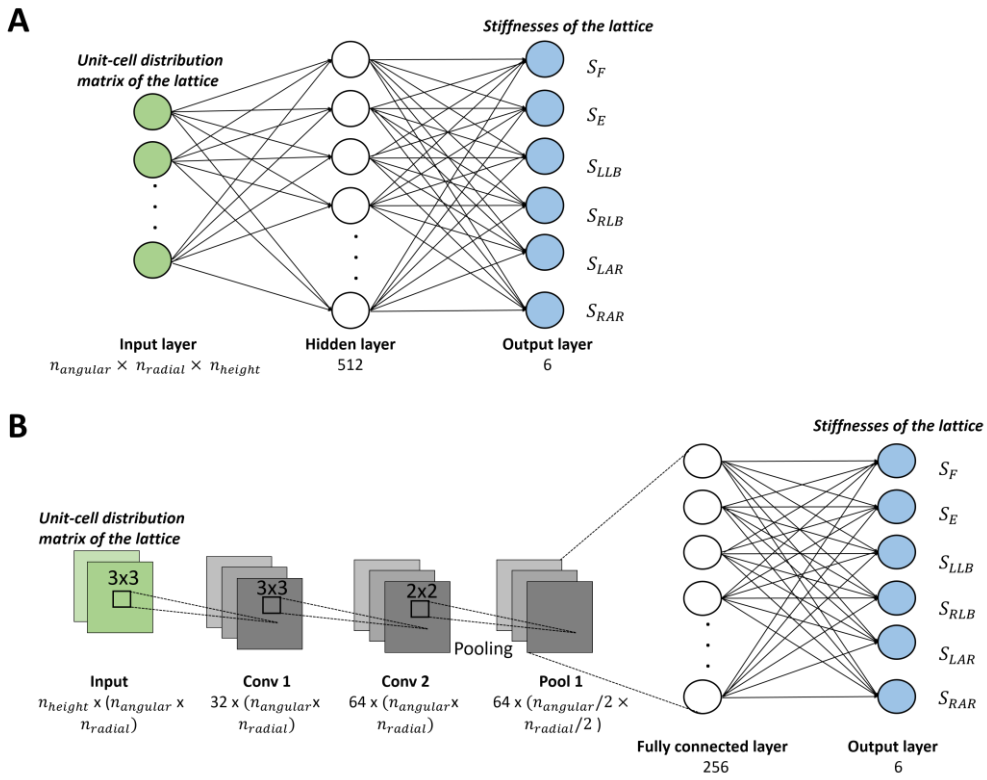

Fig. 5.6. The architectures of (A) MLP and (B) CNN.

5.4 Results

In this section, the digital material FLX9895 (Young's modulus ~= 5.36 MPa) is used as a proof-of-concept base material for the ASD design and fabrication. Given a design space that equals to the average size of a human lumbar IVD shown in Fig. 5.7, two patient-specific ASDs with various stiffness requirements are designed: a L2-L3 lumbar disc and a L4-L5 lumbar disc [126]. A lattice with a grid division of 15×3×2 ($n_{\text{angular}} \times n_{\text{radial}} \times n_{\text{height}}$) is used for the ASD design. The size of the unit-cell library is set as three to balance the computational cost and design freedom. The bar diameter of the lattice is set to 0.5 mm, which is within the allowable feature size of the given 3D printer for reliable mechanical properties [82]. In the following subsections, Section 3.1 presents the mechanical properties of thirteen unit-cells as potential candidates to be included in the unit-cell library. Next, Section 3.2 shows the ANN model prediction accuracy, the topology optimization process, and the optimized topologies of two lattice-based ASDs based on a unit-cell library with randomly selected unit-cells (Library A). Section 3.3 repeats the whole process in Section 3.2 based on a unit-cell library with unit-cells selected according to predefined heuristics (Library B).

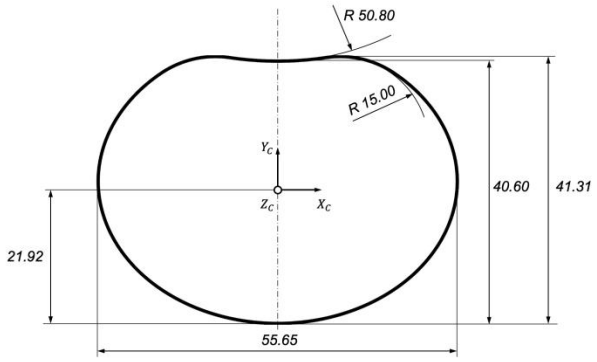

Fig. 5.7. Dimensions of the disc design space that equals to the size of an average human lumbar IVD (unit: mm). The height is 10 mm measured in the z-direction.

5.4.1 Mechanical properties of unit-cell candidates

Thirteen unit-cells (Fig. 5.8) with a cubic shape to guarantee the connectivity between the adjacent cells are considered as candidates for the unit-cell library. Based on the coordinate system defined in Fig. 5.8, the nomenclature of the unit-cells are determined based on [149]. A primitive cube consists of 12 bars lying on the edges, BCC is a body-centered cube, while BCCz is BCC with reinforcement bars in the "z" direction. FCC is a face-centered cube, while FCC_cube is the combination of FCC with a primitive cube, FBCC is a combination of FCC and BCC. The suffixes -n-1, -n-2, and -n-3 represent no reinforcements members that lay parallel to the y-z plane, x-z plane, and x-y plane, respectively. To facilitate the engineering constants comparison, all the unit-cells are set to have an edge length of 1 mm and a relative density of 0.01. The summary of the engineering constants of the thirteen unit-cells are listed in Table 5.2.

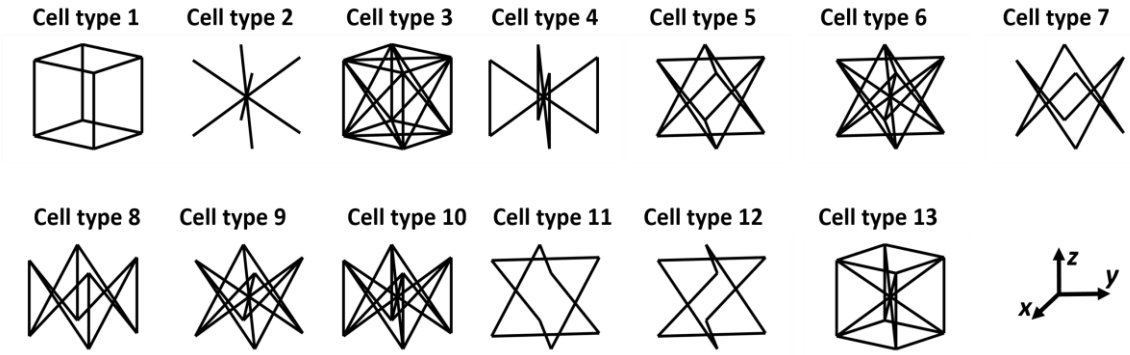

Fig. 5.8. Thirteen unit-cells as potential candidates for the unit-cell library and the defined coordinate system. (1) Primitive cube, (2) BCC, (3) FCC_cube, (4) BCCz, (5) FCC, (6) FBCC, (7) S-FCC-n-3, (8) FCCz-n-3, (9) FBCC-n-3, (10) FBCCz-n-3, (11) FCC-n-1, (12) FCC-n-2, (13) BCC_cube.

Table 5.2. The engineering constants of the thirteen unit-cells with a relative density of 0.01: [MPa]

Cell index	E_x	E_y	E_z	G_{yz}	G_{xz}	G_{xy}
1	178.19	178.19	178.19	0.14	0.14	0.14
2	0.49	0.49	0.49	29.73	29.73	29.73
3	97.49	97.49	97.49	16.47	16.47	16.47
4	0.50	0.50	67.80	25.98	25.98	25.97
5	59.48	59.48	59.48	22.29	22.29	22.29
6	34.53	34.53	34.53	25.62	25.62	25.62
7	0.45	0.45	0.45	33.42	33.42	0.03
8	18.01	18.01	43.51	15.35	15.35	0.01
9	15.94	15.94	10.54	31.38	31.38	16.36
10	30.92	30.92	49.09	29.07	29.07	15.16
11	0.45	0.45	0.45	33.42	0.03	33.42
12	0.45	0.45	0.45	0.03	33.42	33.42
13	148	148	148	43.60	43.60	43.60

*all the values are scaled up by 1e4 and rounded up to two decimal places

5.4.2 Designs based on a unit-cell library determined without heuristics

This section shows the optimization process and the optimized results of two lattice-based ASDs using a unit-cell library that contains three randomly selected unit-cells (Library A), as shown in Fig. 5.9.A: unit-cell 1 (primitive cube), 3 (FCC_cube), and 13 (BCC_cube). The assignment of a certain unit-cell to a six-node cell is performed based on the same reinforcement concept as an eight-node cell. For example, a six-node cell with unit-cell 1 (primitive cube) means that the cell is purely composed of edge members. A dataset with 600,000 randomly generated samples is used for the ANN model training with a learning rate of 1e-4 and a batch size of 128. The dataset is split into 80 percent training data and 20 percent verification data. The training data is further split into 90 percent training data and 10 percent validation data for each epoch during the training process. The training process is terminated after 500 epochs. The training hyper-parameters, such as the number of epochs, learning rate, and batch size, are determined through pre-tests to maximize the prediction accuracy of the ANN model. The convergence plot and the prediction accuracy of the MLP and CNN are shown in Fig. 5.9.B and Fig. 5.9.C, respectively. Both ANN models show an excellent prediction accuracy (>0.99) and thus qualify as candidates for a regression model for the subsequent topology optimization. Based on the MLP model, the convergence plot of the topology optimization and the optimized topologies of two lattice-based ASDs are shown in Fig. 5.10 and Fig. 5.11, respectively.

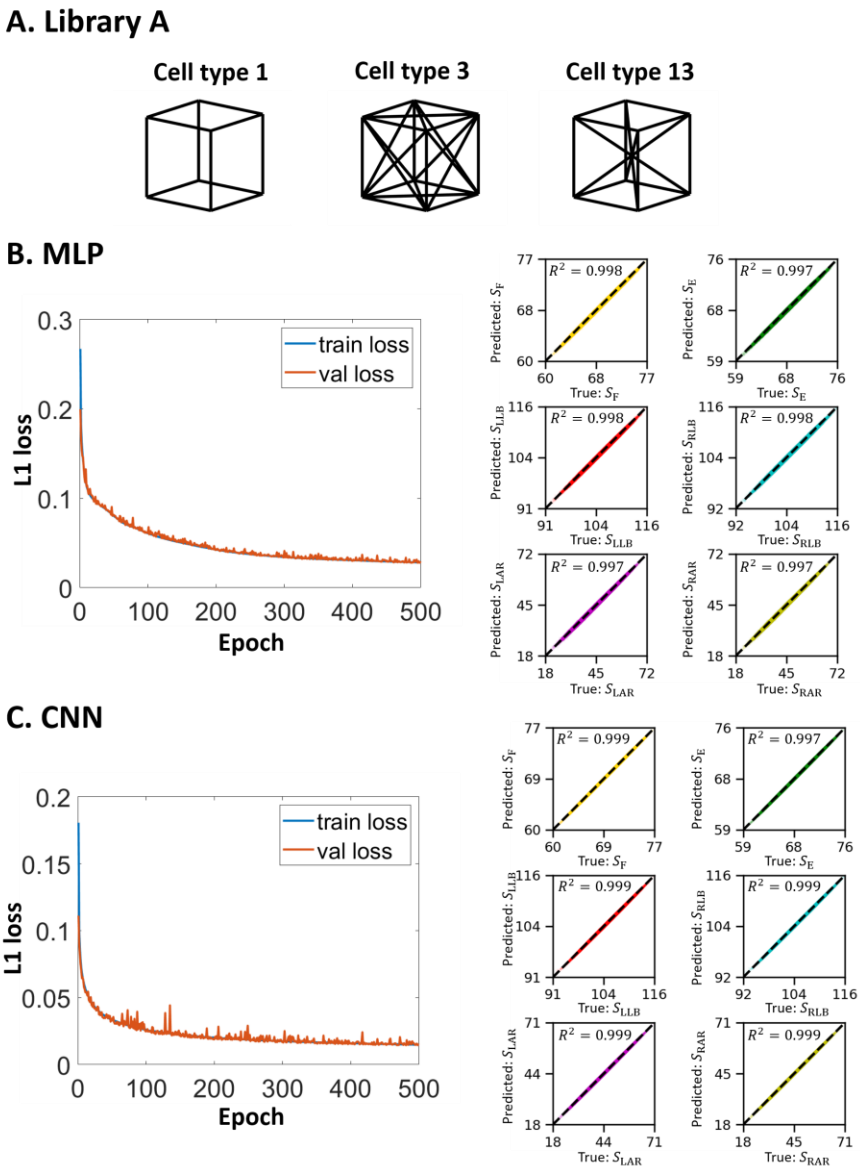

Fig. 5.9. The unit-cell library with randomly selected unit-cells (Library A) and the ANN model training process together with the model prediction accuracy. (A) Randomly selected unit-cell library (Library A) that contains unit-cell 1, 3, and 13. (B) The training process and the prediction accuracy of MLP model (unit: Nmm/deg). (C) The training process and the prediction accuracy of the CNN model (unit: Nmm/deg). In (B) and (C), The stiffness calculated through FE analysis is plotted on the *x*-axis and labelled as "True", while the stiffness predicted by the ANN models are plotted on the y-axis and labelled as "Predicted".

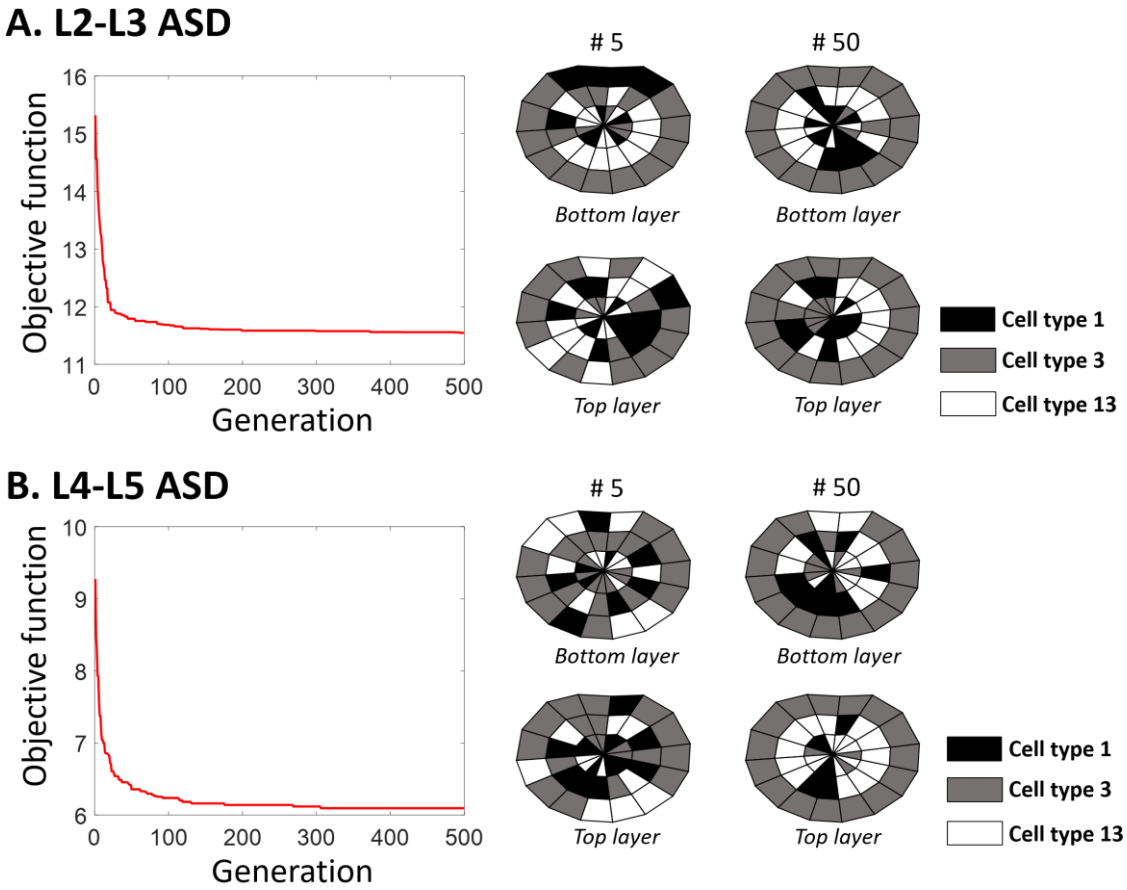

Fig. 5.10. The optimization process given Library A for a (A) lumbar L2-L3 ASD and a (B) lumbar L4-L5 ASD. (left) The objective function values versus generation in the GA optimization process. (right) Unit-cell distribution of the best solution in generation 5 and 50 during the optimization process.

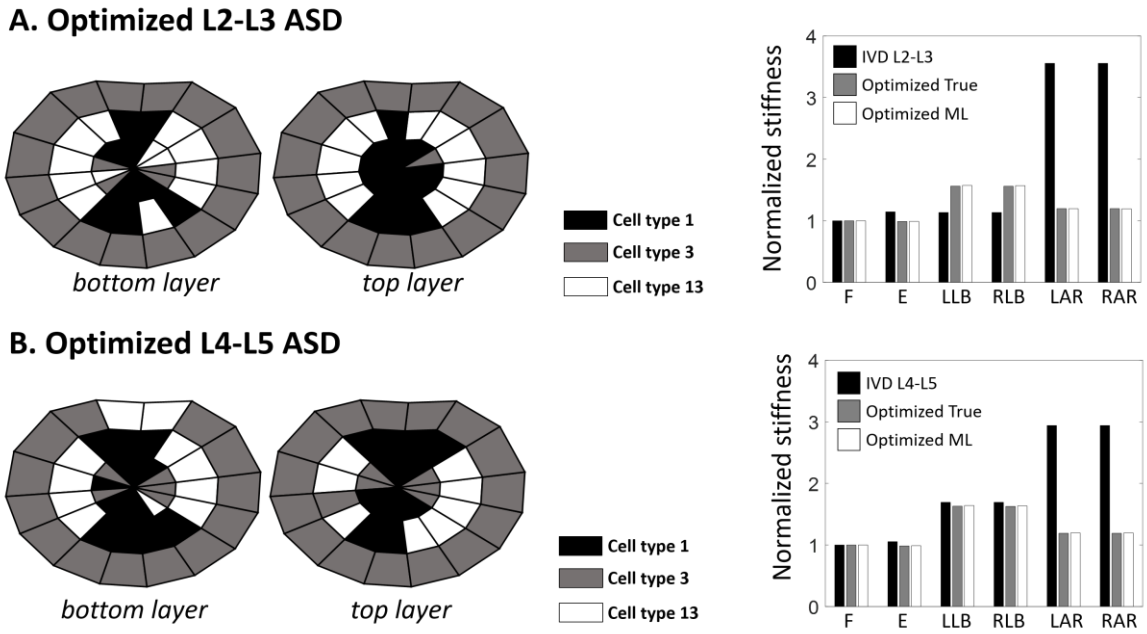

Fig. 5.11. The unit-cell distribution of the optimized ASD and its corresponding normalized stiffness given Library A for a (A) lumbar L2-L3 ASD and a (B) lumbar L4-L5 ASD. (left) The optimized unit-cell distribution. (right) The normalized stiffness of the optimized ASD in six loading scenarios: "optimized true" and "optimized ML" are the stiffness calculated using FE analysis and the trained ML model, respectively, while "IVD L2-L3" and "IVD L4-L5" are the stiffness of an IVD.

5.4.3 Designs based on a unit-cell library determined with heuristics

Similar as the previous section, this section shows the optimization process and the optimized results of two lattice-based ASDs based on a unit-cell library that contains three unit-cells selected based on a predefined heuristic that prefers unit-cells with a relatively high shear/compressive stiffness ratio (Library B), as shown in Fig. 5.12.A. The three unit-cells are: unit-cell 2 (BCC), 7 (FCC-n-3), and 12 (FCC-n-2). The convergence plot and the prediction accuracy of the MLP and CNN are shown in Fig. 5.12.B and Fig. 5.12.C, respectively. The optimization process and the optimized results are presented in Fig. 5.13 and Fig. 5.14, respectively. To illustrate the optimized topologies of the two lattice-based ASDs, Fig. 5.15 shows two 3D printed proof-of-concept prototypes.

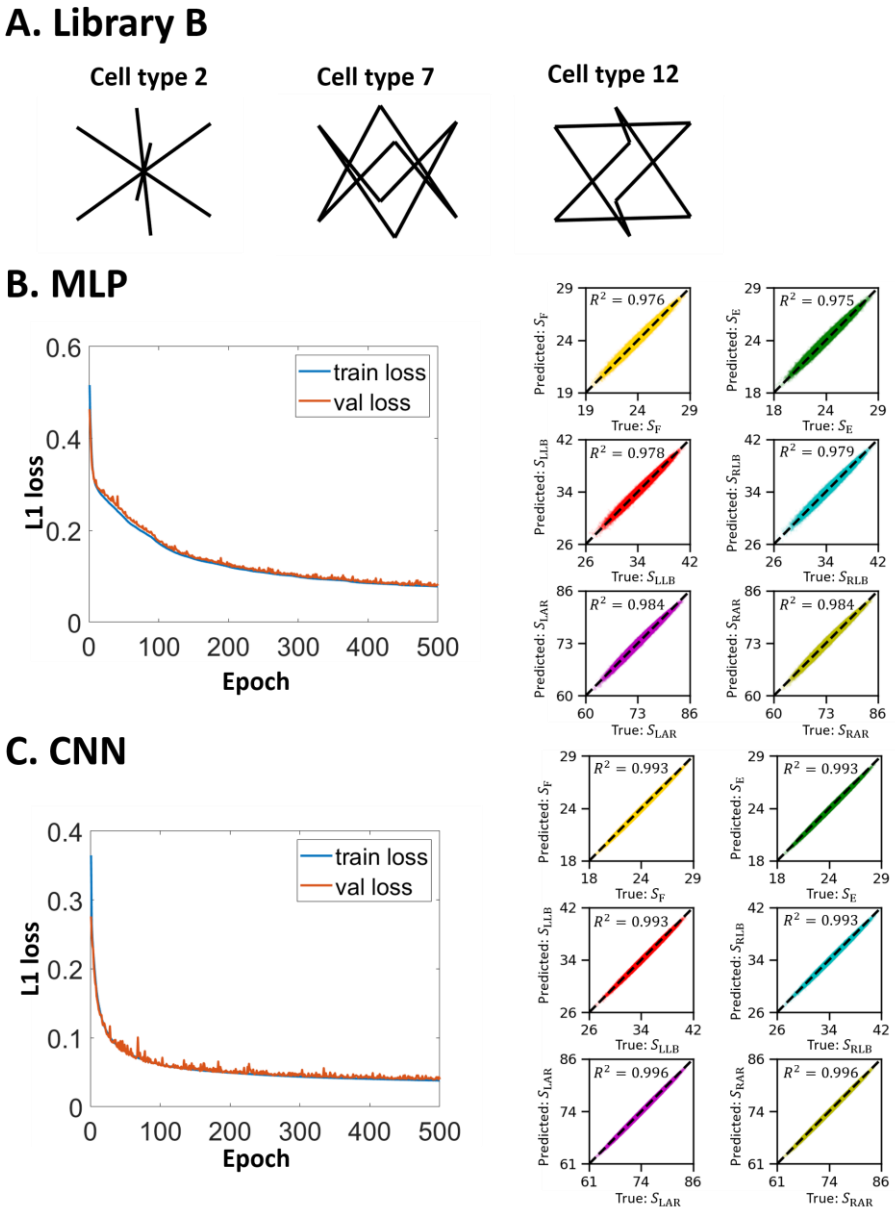

Fig. 5.12. The unit-cell library selected based on a predefined heuristic that prefers unit-cells with a higher shear/compressive stiffness ratio (Library B) and the ANN model training process together with the model prediction accuracy. (A) Unit-cell library (Library B) that contains unit-cell 2, 7, and 12. (B) The training process and the prediction accuracy of MLP model (unit: Nmm/deg). (C) The training process and the prediction accuracy of the CNN model (unit: Nmm/deg). In (B) and (C), The stiffness calculated through FE analysis is plotted on the *x*-axis and labelled as "True", while the stiffness predicted by the ANN models are plotted on the y-axis and labelled as "Predicted".

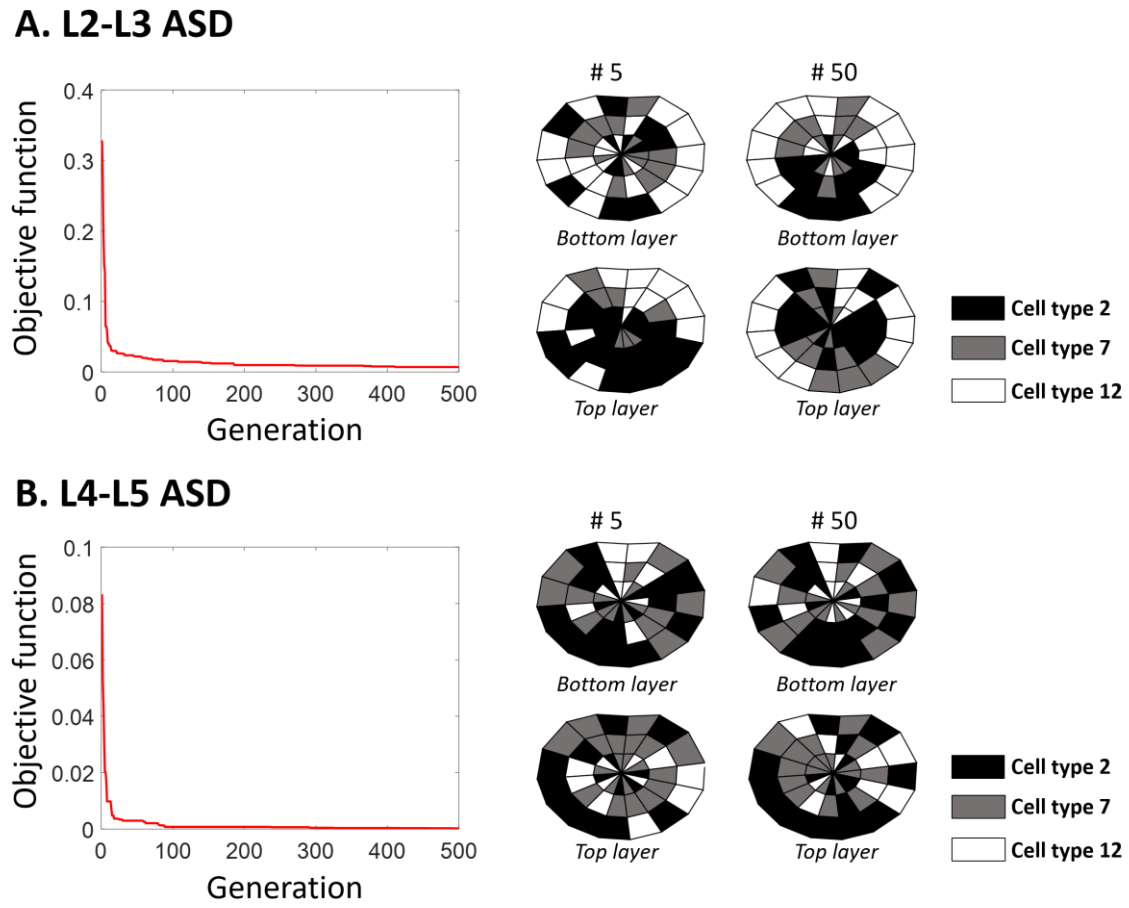

Fig. 5.13. The optimization process given Library B for (A) lumbar L2-L3 ASD and (B) lumbar L4-L4 ASD. (left) The objective function values versus generation in the GA optimization process. (right) Unit-cell distribution of the best solution in generation 5 and 50 during the optimization process.

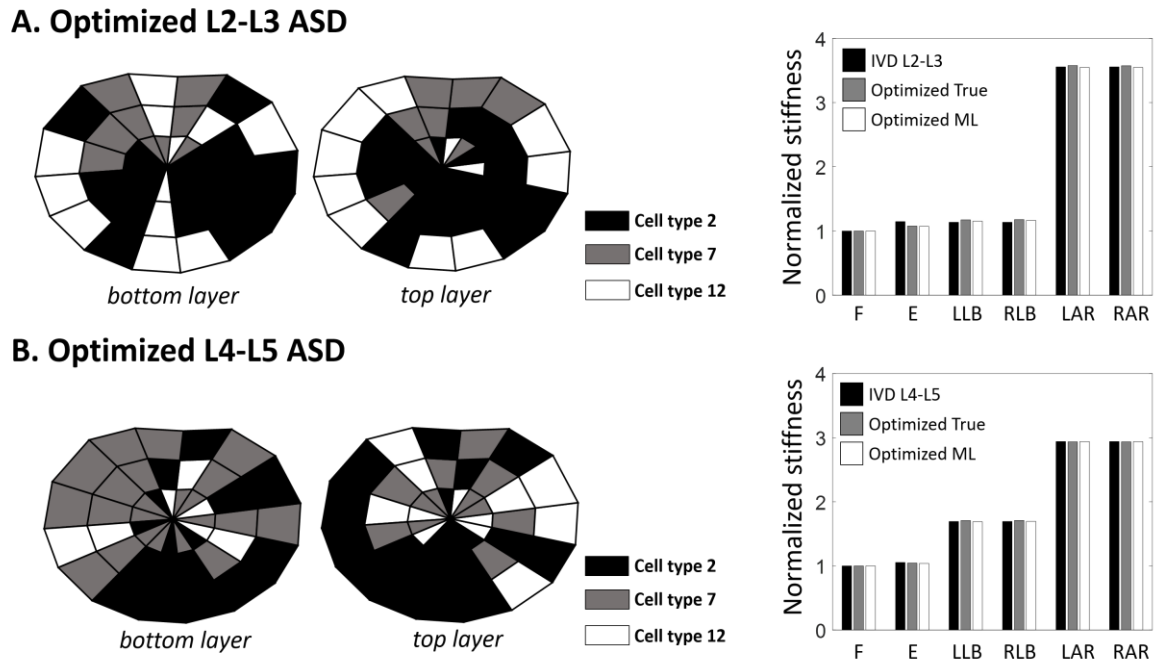

Fig. 5.14. The unit cell distribution of the optimized ASD and its corresponding normalized stiffness given Library B for a (A) lumbar L2-L3 ASD and a (B) lumbar L4-L5 ASD. (left) The optimized unit-cell distribution. (right) The normalized stiffness of the optimized ASD in six loading scenarios: "optimized true" and "optimized ML" are the stiffness calculated using FE analysis and the trained ML model, respectively, while "IVD L2-L3" and "IVD L4-L5" are the stiffness of an IVD.

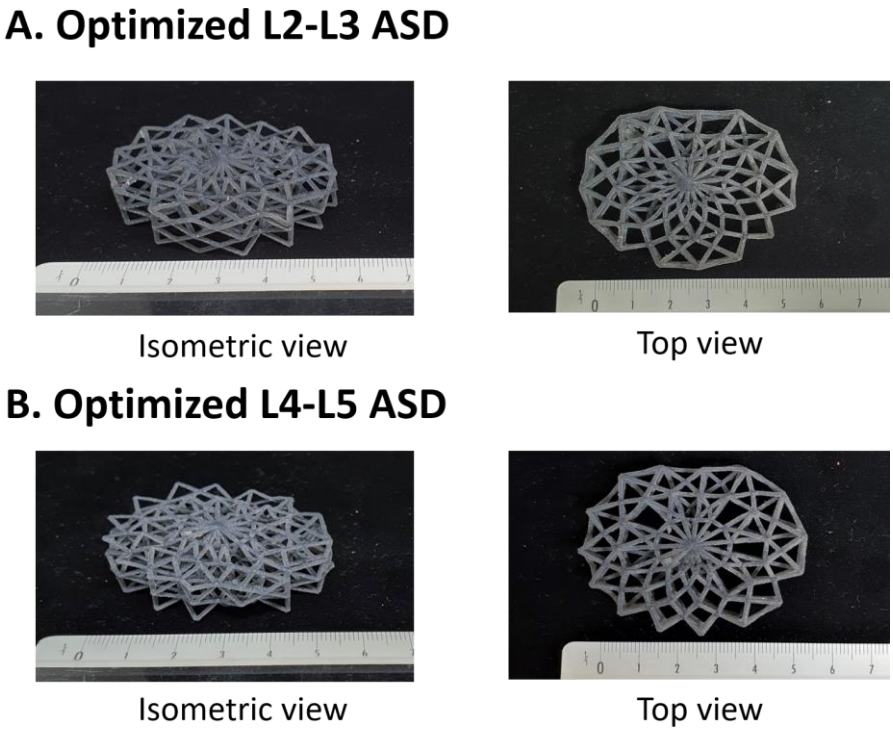

Fig. 5.15. 3D Printed prototypes of the optimized L2-L3 and L4-L5 ASD (unit: mm). The material used for printing is FLX9895.

5.5 Discussion

This section first evaluates the methodology used in this chapter and interprets the results in Section 5.5.1. Next, the limitations of this chapter are discussed in Section 5.5.2, followed by a Section 5.5.3 that presents the implications of this chapter for the thesis.

5.5.1 Methodology evaluation and results interpretation

The validity and generality of the proposed methodology for the design of a lattice-based ASD is verified by the good prediction accuracy of the ANN models and an excellent match of the normalized stiffness of the optimized ASDs with those of IVDs. The optimization process is finished within 10 minutes. Based on the optimized topology obtained in Step 1 and Step 2 in Fig. 5.1, Step 3 aims to reproduce the absolute stiffness values of an IVD. With the base material PEEK (Young's modulus ~= 3.6 GPa) that is a commonly biocompatible material for spinal implants and a corresponding 3D printing technique for fabricating PEEK-based parts [150], Step 3 is performed and results in a bar diameter of 0.1568 mm for the L2-L3 ASD and 0.1255 mm for the L4-L5 ASD. The stiffnesses of the two optimized lattice-based ASDs are presented in Fig. 5.16.

The proposed methodology is extendable in terms of the following aspects. First, the methodology is applicable to other ASD designs or patient-specific implants, such as a multi-material, monolithic ASD design where each voxel in the design can be assigned a different material. For the design of such ASD design, the methodology can be adjusted by replacing the unit-cell library that contains varying unit-cells with a material library that has multiple base materials with varying material properties. Second, the parameters used in this chapter, such as the cell size and unit-cells included in

the unit-cell library, can be adjusted to cover a wider range of anisotropic behaviors for other applications or to meet specific manufacturing constraints. Material and geometry nonlinearity can be further incorporated into the methodology, such as tension-only fibers that can potentially help reproduce an IVD's nonlinear load response [151].

The results interpretation will focus on the optimized results using two unit-cell libraries, the influence of cell size/grid division, and the ANN model performance. Fig. 5.10 and Fig. 5.13 show a fast convergence of the topology optimization using the GA algorithm. Given the unit-cell library with randomly selected unit-cells (Library A), the optimized ASDs fail to reproduce the relative amplitudes of IVD's stiffness with a lower torsional stiffness (Fig. 5.11). Nevertheless, the change of the unit-cell distribution over the optimization process (Fig. 5.10.C) implies that the proposed methodology is able to identify the critical region and the favorable unit-cell for improving the stiffness match with an IVD. This is reflected by the fact with the increase of generation number, more cells on the outer side in the radial direction of the grid that have a bigger lever arm are filled with unit-cell 3 that has a relatively high shear/compressive stiffness ratio. In comparison, the unit-cell library whose unit-cells are selected based on predefined heuristic (Library B) allows the optimized ASD to achieve an excellent stiffness match (Fig. 5.14). This shows the significant influence of the unit-cell library selection on the performance of the lattice-based ASD, whereas the heuristic that favors unit-cells with a higher shear/compressive stiffness ratio for determining the unit-cell library helps to increase the torsional stiffness of an IVD while balancing stiffness in other loading scenarios.

This chapter uses a grid division of 15×3×2 for the lattice-based ASD design. The influence of the grid division is explored by using a lattice with a grid division of 25×4×2 using Library A. The comparison of the optimized results shown in Fig. 5.11 and Fig. 5.17 implies that given Library A, a dense lattice (25×4×2) leads to an even lower normalized AR stiffness compared to a sparse lattice (15×3×2) and a worse stiffness match with an IVD. This can be explained by the dominant compressive stiffness and the relatively low shear/compressive stiffness ratio of the unit-cells included in Library A. Namely, the unit-cells in Library A provide a higher compressive/tensile stiffness compared to its shear stiffness. In flexion/extension and LB, the reaction moment is mainly contributed by the compressive reaction force from the compressed side of the lattice-based ASD and tensile reaction force from the stretched side of the lattice-based ASD, whereas in AR the reaction moment is mainly contributed by the shear reaction force of the lattice-based ASD. With an increase in the grid density, the dominant effect of the compressive/tensile stiffness relative to the shear stiffness of the cells is amplified, which explains the worse stiffness match with a denser grid. This again demonstrates the conflicting design criteria imposed on the ASD design, as the topology change of one single cell in the grid contributes to stiffness changes in multiple loading scenarios.

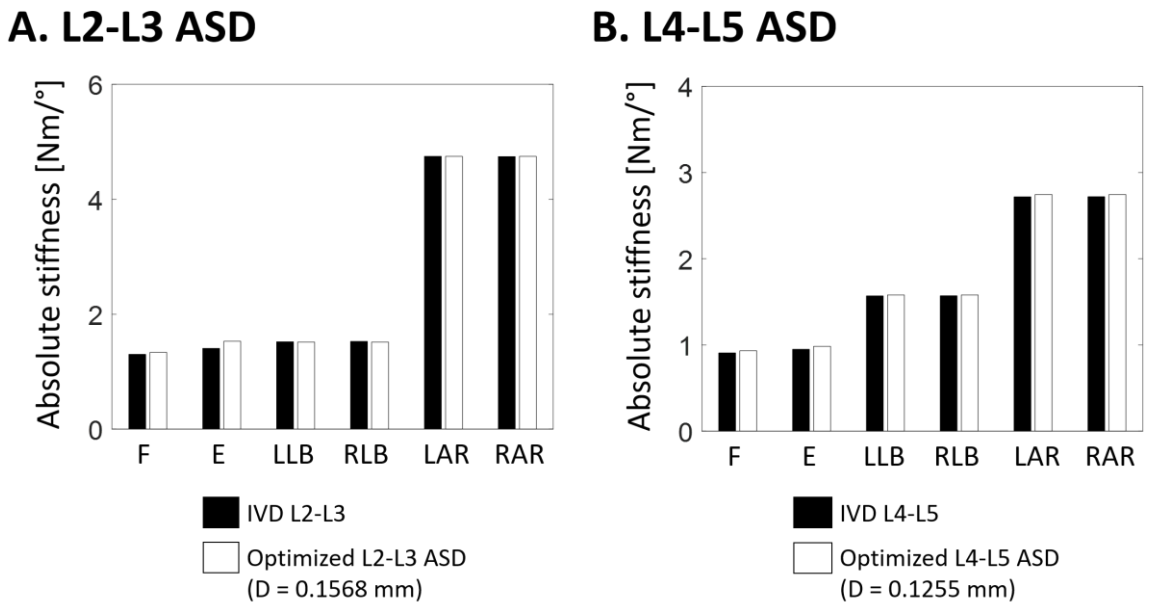

Fig. 5.16. The stiffnesses of the optimized human lumbar L2-L3 (A) and L4-L5 ASD (B) in six loading scenarios. The results are based on the biocompatible material PEEK that is commonly used for fabricating spinal implants. The L2-L3 ASD and the L4-L5 ASD have a bar diameter of 0.1568 mm and 0.1255 mm, respectively. In the bar plot, "optimized true" represents the stiffness calculated based on FE analysis, while the "IVD L2-L3" and "IVD L4-L5" are the stiffness of an IVD.

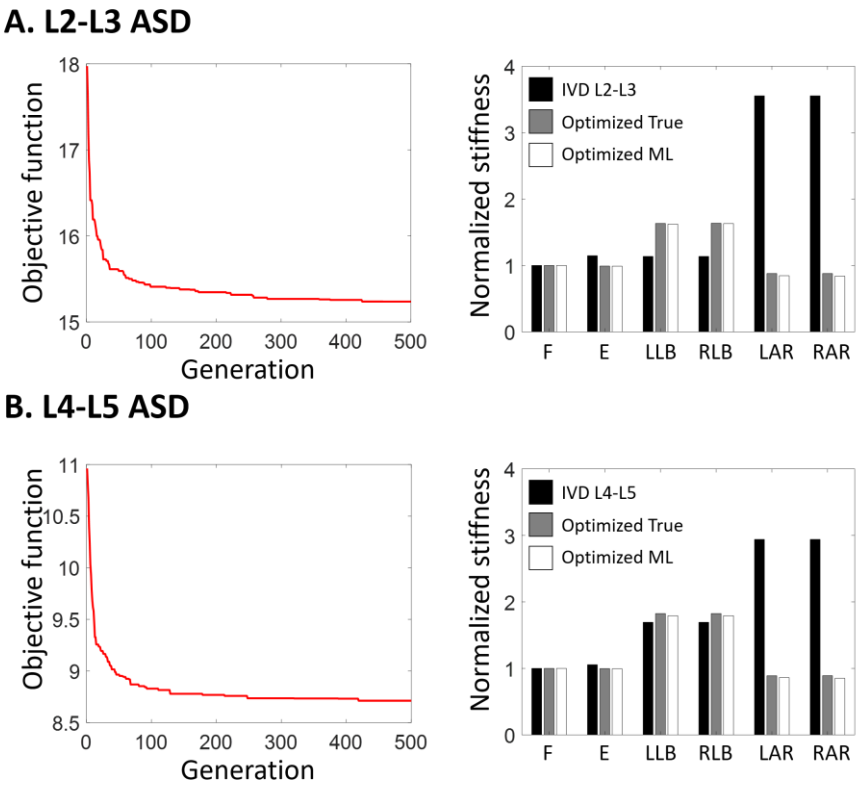

Fig. 5.17. The optimization process with a grid division of 25×4×2 given Library A for (A) a lumbar L2-L3 ASD and (B) a lumbar L4-L5 ASD. (left) The objective function values versus generation in the GA optimization process. (right) The optimized normalized stiffness in six loading scenarios: "optimized true" and "optimized ML" are the stiffness calculated based on FE analysis and the trained ML model, respectively, while "IVD L2-L3" and "IVD L4-L5" are the stiffness of an IVD.

Although both ANN models show a good prediction accuracy (> 0.97) with the given dataset (Fig. 5.9 and Fig. 5.12), CNN outperforms MLP in terms of prediction accuracy and training efficiency. The difference in prediction accuracy becomes more significant with the increase of grid density. Fig.

5.17 shows that with a grid division of 25×4×2, MLP and CNN achieve an average prediction accuracy in six loading scenarios of 0.968 and 0.996, respectively. Such difference be explained by the different neural network architectures. MLP takes flattened input where each neuron represents one cell in the grid. With the increase of the grid density, the amount of weights increases rapidly, which leads to weight redundancy and possible overfitting with a lower prediction accuracy. In comparison, the weights are shared in CNN and the layers are sparsely connected, which helps to mitigate weight redundancy and makes the neural network easier to go deeper to describe more complex relationships between the input and the output. The results presented in this chapter match the finding that shows CNN is more efficient in learning and more suitable for high-dimensional data [152].

5.5.2 Limitations

First limitation is the exclusion of the compressive loading scenario in the optimization. This can be solved by embedding the optimized lattice as a reinforcing structure into an elastic deformable matrix such as hydrogel. Our previous study shows that the matrix has a dominant effect on the compressive stiffness of an ASD, while the contribution of the reinforced structure is the most significant in rotational loading cases [82]. Therefore, the decoupled design of the matrix and the reinforcing lattice is a reasonable simplification for the complex, multi-objective ASD design problem. Second, this chapter only considers small deformations of the lattice-based ASD, therefore the member buckling and the responses of the lattice-based ASD at larger displacements are neglected.

5.5.3 Implications for the thesis

The good prediction accuracy of the ML models as well as the fast convergence of the optimization process show the effectivity of the ML-supported ASD design method for realizing an efficient ASD design process, which partially answers RQ3. One essential aspect that differentiates a ML-based methodology from a traditionally optimization-based methodology is how the model makes use of data [152]. For the ML-based method, the data generation is a one-time cost, as opposed to the ongoing cost for an optimization-based method. Besides, ML is able to extract hidden relationship in a problem to guide the design, whereas in traditional optimization-based design the data is only a by-product for evaluating the current optimization strategy. The way ML deals with data is especially valuable in patient-specific implant design, since it is time-consuming to restart the optimization each time given a new patient. Besides, the mechanical properties of human tissue or organ are supposed to lie within a certain predictable range, with a data-driven design the range of implant's mechanical properties and the corresponding optimized designs can be pre-stored to speed up the design process.

The biggest computational cost for the ML-supported computational design is the training data generation. In order to reach an acceptable prediction accuracy, a reasonably big amount of training dataset is needed, which takes a large amount of computational resources and time. To tackle this challenge, this chapter provides a good example of incorporating problem-specific heuristics into the design to avoid redundant data collection. Another possible strategy is to add symmetry into the design

to reduce the problem dimension, or use techniques such as VAE to cluster similar data together to guide future data collection.

This chapter proposes a lattice-based ASD design for natural mechanics restoration, which partially provides answer to RQ2. The adaptability of the lattice-based ASD to patient-specific mechanics is realized through adjusting the unit-cell distribution in the lattice. Considering the big variance of the unit-cells that can be included in a unit-cell library, this design differs from the ASD designs proposed in the previous chapters by providing structural adaptability. Such property allows the lattice-based ASD design to have more design freedom compared to the other ASD designs explored in this thesis. This again demonstrates the design opportunities provided by the multi-material 3D printing technique for ASD design, as the 3D printing technique allows for local variation both in structure and material. Additionally, this chapter shows that through varying a lattice's structure, the relative amplitudes of the ASD's stiffness in various loading scenarios can be adjusted, which again demonstrates the critical role of an ASD's structure for natural mechanical restoration. This finding coincides with that in Chapter 4 where a structure optimization for the fiber-like structure is first performed before material optimization. However, the lattice-based ASD suffers from proneness to material failure due to the high amount of small features. This ASD design also exhibits a strain-softening behavior at large deformations due to member buckling, which contradicts with the desired nature-mimicking strain-stiffening behavior of an IVD.

5.6 Conclusion

Inspired by the great potential of lattice structures to achieve a controlled anisotropy, this chapter proposes an innovative lattice-based ASD for restoring patient-specific anisotropic stiffnesses. To achieve an efficient design process, a systematic ML-supported methodology is proposed for the design of such lattice-based ASD. The whole optimization process finishes within minutes and the resultant optimized lattice-based ASD shows good stiffness match with an IVD. The results demonstrate the potential of a lattice-based ASD for restoring patient-specific anisotropy thanks to its structure-based adaptability, which partially answers RQ2. Besides, the effectivity of the proposed ML-supported design methodology is verified, which partially answers RQ3. This chapter also shows the superior performance of incorporating problem-specific heuristic in determining the unit-cells in a unit-cell library to balance the computational cost for generating training dataset and enough design freedom. The lattice-based ASD design is limited in terms of its proneness to material failure and its strain-softening load response.

Chapter 6. Design of a chainmail-based, multi-material ASD

This chapter has been adapted from a manuscript submitted to *Journal of the Mechanical Behavior of Biomedical Materials*:

Yu, Z., Shea, K., and Stanković, T. (2021). "The Application of an Additively Manufactured Flexible Chainmail in the Design of an Artificial Spinal Disc for Natural Mechanics Restoration."

6.1 Summary

One joint limitation of the four ASD design concepts proposed in the previous chapters is their lack of nature-mimicking strain-stiffening load response. Thus, to improve the previously proposed ASD designs, this chapter proposes a novel chainmail-based ASD and explores its feasibility of reproducing the IVD's nonlinear, anisotropic rotational responses in six rotational loading scenarios with the given manufacturing constraints. Besides, a methodology is proposed for the design of such chainmail-based ASD to realize a computationally efficient design process with the given manufacturing constraints. The overall workflow comprises an initial modelling of the chainmail unit cell based on a connector model, load response calculation of the chainmail sheet, and material optimization of the individual chainmail unit cells in the chainmail sheet. Results show that the proposed design not only shows a natural strain-stiffening load response, but also exhibits natural relative amplitudes of EZ stiffnesses in six rotational DOFs for different TDR surgical procedures. The design process is proven to be computationally efficient and finishes within several minutes. This chapter demonstrates the potential of incorporating structures inspired by flexible metamaterials into ASD design for natural mechanics restoration.

6.2 Background

This section first introduces the definition of mechanical metamaterials and the applications of chainmail-based metamaterial in Section 6.2.1. Next, the implications of the chainmail-based metamaterials for the ASD design are discussed in Section 6.2.2.

6.2.1 Mechanical metamaterials and chainmail-based metamaterials

With the recent advances in AM and digital fabrication, the concept of mechanical metamaterial gains lots of attention as a viable solution for complex design problems. Mechanical metamaterial are materials featured by purposefully designed micro-architectures that give rise to unique mechanical properties [153], such as extremal materials [154][155], negative compressibility materials [156][157], or materials that are ultra-light and ultra-stiff at the same time [158]. An emerging direction in the metamaterial research is the extension of the material property space with soft, flexible metamaterials whose response is highly nonlinear predominantly due to the flexible base material [153]. Their application would allow for the generation of designs whose response adheres continuously and accurately to large portions of the desired load-deflection response curve involving both small and large deformations. This is difficult to achieve using conventional metamaterials that are often designed for a certain fixed property such as ultra-high yield strength or materials with a negative Poisson's ratio [159].

Chainmail-based metamaterial is defined as metamaterials composed of interlinked rings. Research performed on such metamaterial mainly focuses on its application in changing the direction and the sign of the Hall electric field [160], whereas its unique mechanical behavior has not been studied extensively. One unique mechanical property of the chainmail-based metamaterial is its structure-based flexibility resulting from its movable joints [161]. When manufactured with rigid materials such as metal, the chainmail-like structure is used for making garments and fabrics for protection or for shielding objects [162–164], thanks to its rigidity to avoid stabbing and its flexibility to adapt to the freeform shapes of the object surfaces. The rigidity of the chainmail-like structure depends on the relative distance between the rings, thus decoupling its flexibility from the material properties of its constituent materials [165]. A micro-fabricated metallic chainmail is developed as a smart wearable electronic fabric that shows different electrical resistance under compression and stretching depending on the distance between the rings [166]. Chainmail-based metamaterial inspires the development of a surgical simulator that uses a fictitious chainmail-based structure to model the soft tissue deformations [167].

6.2.2 Implications for ASD design

The advancements of AM and mechanical metamaterials provide new design opportunities to tackle the challenge of ASD design. Inspired by the critical role of the collagen fiber network in AF [168], one solution is to incorporate a metamaterial that mimics the behavior of a collagen fiber network in the ASD design to restore the IVD's unique mechanics. There are two behavior similarities between a chainmail-based structure manufactured with flexible materials and the collagen fiber network in AF. First, when subjected to tensile load, the chainmail-based structure is able to go through gradual shape change to align in the loading direction and exhibit a strain-stiffening tensile response, which is similar to the un-crimping process of the collagen fibers upon loading. Second, a chainmail-based structure has separable joints that allow the structure to exhibit a negligible axial compressive and bending stiffness similar as the fiber's behavior. Such property differentiates the chainmail-based structure from other structures that likewise have a J-shaped, strain-stiffening tensile response but have relatively big compressive and bending stiffnesses, such as the helically coiled design [169]. Furthermore, a variation of the geometry, shape, and constituent material of individual ring together with ring interconnectivity provide new design opportunities to mimic the heterogeneous material/structure distribution in an IVD, which can potentially help to reproduce the IVD's anisotropic behavior.

6.3 Materials and methods

This section first presents the proposed ASD design involving a chainmail-based structure. Next, the approach used for the design of the flexible, multi-material chainmail-based structure for reproducing the nature-mimicking nonlinear and anisotropic rotational response is introduced.

6.3.1 Proposed ASD design

As shown in Fig. 6.1. A, the proposed ASD design mimics the composition of an IVD and consists of the top and bottom endplates, an artificial NP in the middle, and an artificial AF made from

a single- or multi-layer chainmail-based structure. The two rigid endplates have a patient-specific geometry to interface with adjacent vertebrae, while the artificial NP and the artificial AF are deformable to provide elasticity. The monolithic artificial NP approximates the shape of a cylinder. The chainmail-based structure is designed as a chainmail sheet that surrounds the artificial NP circumferentially. The chainmail sheet is composed of multiple chainmail unit cells, while each chainmail unit cell comprises one complete middle ring that is connected to two half rings on its top and bottom with movable joints (Fig. 6.1.A). The rational for the unit cell design is to allow for a large shape change due to the middle ring that is not rigidly connected to any other parts in the ASD and is therefore free to reorient and elongate along the direction of the applied force. The circumferentially neighboring chainmail unit cells are detached to decouple their behavior dependency. Therefore, the behavior of each chainmail unit cell is primarily determined by the relative movements of its attaching points on the top and bottom endplates. The amount of chainmail unit cells in the chainmail sheet is determined by assuring a big design space for achieving the desired kinematics while at the same time satisfying the manufacturing constraints imposed by the given 3D printing technique. The ASD design has a sagittal-plane symmetry to mimic the morphology of an IVD [94,170]. Such a symmetry helps to reproduce a nature-mimicking symmetric load response in left/right LB and left/right AR [8].

Inspired by [67], a functional decoupling strategy is used, so that the artificial NP and the artificial AF (i.e., the chainmail sheet) are responsible for the load bearing in compressive and rotational loading scenarios, respectively. To realize this, the artificial NP is detached from the top and bottom endplates to freely rotate and translate relative to the endplates in rotational loading scenarios, as illustrated in Fig. 6.1. B, which helps minimize the artificial NP's effect on the ASD's rotational response. In contrast, the chainmail sheet is rigidly connected to the top and bottom endplates. Since the focus of this study is to reproduce the natural rotational load response, the model only includes the chainmail sheet while excluding the artificial NP and the two endplates.

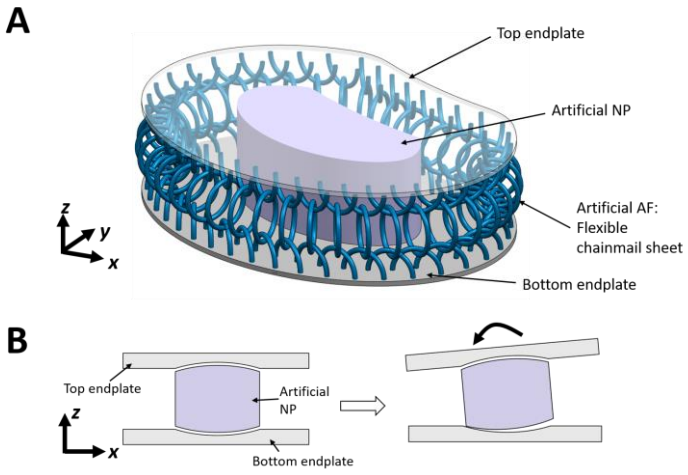

Fig. 6.1. Proposed ASD design involving a chainmail sheet. (A) The ASD consists of the top (shown transparent) and the bottom endplate, the middle artificial NP, and the flexible chainmail sheet that surrounds the artificial NP circumferentially (for simplicity only one layer of chainmail sheet is shown in the figure) as the artificial AF. (B) Illustration of the functional decoupling strategy for the ASD design where the artificial NP is detached from the top and bottom endplates to freely rotate

and translate relative to the endplates in rotational loading scenarios, which helps minimize the artificial NP's effect on the ASD's rotational response.

6.3.2 Methodology for the chainmail sheet design

This section first gives an overview of the methodology for the chainmail sheet design and then explains each step of the methodology in detail. The overall design process for the chainmail sheet design is shown in Fig. 6.2. In Step 1, the material properties of the base materials provided by the multi-material 3D printer are characterized, followed by the determination of the chainmail unit cell base geometry and the geometric scaling factor λ_g based on the dimensions of the ASD and the minimum allowable feature size of the 3D printing technique. Step 2 fabricates and characterizes the uniaxial tensile responses of the 3D printed chainmail unit cells made from different base materials, and determines the stiffness scaling factor λ_s based on the achievable stiffness range with the given base materials. Step 3 models the chainmail sheet using a connector that is a simplified model to describe the tensile and compressive behavior of a chainmail unit cell, followed by Step 4 that calculates the chainmail sheet's load response and a curve fitting of the load response using a bilinear constitutive model to obtain the chainmail sheet's EZ stiffnesses. Lastly, Step 5 optimizes the material distribution in the chainmail sheet to reproduce the relative amplitudes of EZ stiffnesses in six DOFs of a human lumbar L4-L5 spinal segment for different surgical scenarios. The human L4-L5 spinal segment is selected as the optimization target as it is one of the regions with the most frequent occurrence of IVD degeneration [171]. The computational modeling and optimization (Steps 3-5) are performed using Matlab.

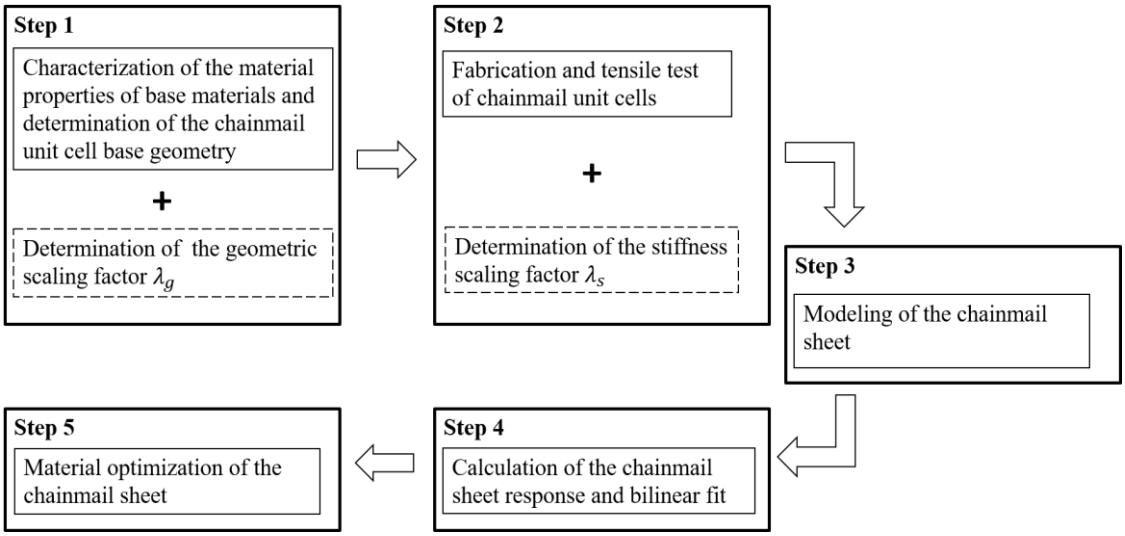

Fig. 6.2. Design process for the chainmail sheet. The solid-line rectangle represents the necessary steps independent of the 3D printing technique used, while the dashed-line rectangle represents optional steps dependent on the minimum allowable feature size and the available base materials of the given 3D printing technique.

Base material characterization and unit cell geometry determination

This section characterizes the base materials provided by the given 3D printing technique to give an overview of the achievable stiffness range of the base materials and determines the geometry of the chainmail unit cell based on the dimensions of an IVD and the minimum allowable feature size of the given 3D printing technique. Fig. 6.3 shows the technical drawing of the base geometry of the chainmail

unit cell. The dimensions of the rings in a unit cell are controlled by parameters D1 and D2 that refer to the filament diameter and the ring dimeter, respectively. The gripping plate is a rectangular prism whose dimensions are controlled by parameters P1, P2, and P3 that refer to the width, length, and height of the rectangular prism, respectively. The ratio D2/D1 should be set large enough to avoid ring collision when the chainmail unit cell is under compression for achieving a negligible compressive stiffness. Besides, the value of the filament diameter (D1) needs to comply with the minimum allowable feature size of the given 3D printing technique for achieving reliable mechanical properties and to ensure the strength of the interface between the rings and the gripping plates [172]. The constraint in D1 also restricts the value of D2. In this study, the ratio D2/D1 is set to 10 and the ring diameter D1 is set to 2 mm as an example. In the unloaded state of the ASD, the rings in the chainmail unit cells are designed as being just in contact without any shape change (Fig. 6.1.A). Considering the size of a human lumbar L4-L5 IVD with a height of 9 mm [94] and the minimum allowable feature size of the given 3D printing technique [173], the dimensions of the chainmail unit cell are uniformly scaled up by a geometric scaling factor λ_g of 4. Table 6.1 summarizes the unscaled and scaled geometric parameters of the chainmail unit cell.

Table 6.1. Geometric parameters of the chainmail unit cell.

	Gripping plate parameters			**Chainmail ring diameters**	
	P1 (Width)	P2 (Length)	P3 (Height)	D1 (Filament)	D2 (Ring)
Unscaled [mm]	6.5	4.5	0.75	0.5	5.0
Scaled [mm]	26.0	18.0	3.0	2.0	20.0

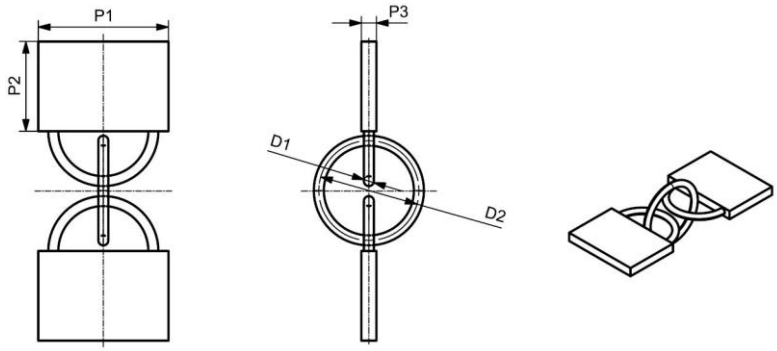

Fig. 6.3. Technical drawing of the chainmail unit cell with gripping plates for tensile tests. The dimensions of the rings are controlled by the filament diameter D1 and the ring diameter D2, while the dimensions of the gripping plates are controlled by the parameters P1, P2, and P3 that refer to the width, length, and the height of the rectangular prism, respectively.

Tensile tests of chainmail unit cells and stiffness scaling factor determination

This section introduces the test procedure to measure the uniaxial tensile response of the chainmail unit cells and determines the stiffness scaling factor to scale down the target values for optimization based on the achievable stiffnesses with the given base materials. Each type of chainmail unit cell is fabricated using one of the base materials for the rings and a stiff material for the gripping plates to secure the positioning during tensile tests. Given fourteen base materials, a total of fourteen types of chainmail unit cells are fabricated and their uniaxial tensile responses are measured. When manufacturing the chainmail unit cells, the whole unit cell except the middle ring lies on the plane of

the printing bed, while the middle ring is oriented at an angle of 30° relative to the printing bed to avoid overlap. The uniaxial tensile test is performed using an Instron ElectroPuls E3000 testing machine with a Dynacell load cell of 5 kN capacity. The starting position of the test is such that the rings are about to be in contact and the middle ring is perpendicular to the top/bottom half rings. A strain rate of 5 mm/min is used for the test to minimize the influence of the material's viscoelasticity on the chainmail unit cell's tensile response. For each chainmail unit cell type, its tensile response is obtained by the average tensile response of five specimens. The stiffness of the chainmail sheet is constrained by the achievable tensile stiffness range of the chainmail unit cells, which is further limited by the available stiffness range of the base materials. Therefore, a stiffness scaling factor λ_s of 1/50 is used as an example to scale down the target EZ stiffnesses to ensure that the target EZ stiffnesses lie within the EZ stiffness range of the chainmail sheet with the given base materials. Table 6.2 summarizes the parameters used for the chainmail sheet design.

Table 6.2. Summary of the parameters used in this study.

Parameter	Definition	Values
λ_g	Geometric scaling factor	4
D2	Ring diameter	20 mm
D1	Filament diameter	2 mm
λ_s	Stiffness scaling factor	1/50

Chainmail sheet modeling

This section presents the model of a chainmail sheet, the rational to use such model, and the limitations of the model. Since the reaction force of a chainmail unit cell is primarily determined by the relative movement of its corresponding attaching points at the top and bottom endplates, a connector is used as a simplified model of the tensile and compressive behavior of a chainmail unit cell (Fig. 6.4. A). The motivation to use the connector model is to improve the computational efficiency through avoiding the time-consuming contact modeling between the rings. The top and bottom nodes of the connector (the blue and the green point) are defined as midpoints of the two attaching points of the chainmail unit cell on the top and the bottom endplates, respectively. Like the chainmail unit cell, the connector can be in a shortened or elongated state under compressive or tensile forces. The tensile and compressive responses of the chainmail unit cell is assigned to the connector. Specifically, the tensile response of the chainmail unit cell or the connector in an elongated state is measured through the uniaxial tensile tests described in the previous section, and the compressive response of the chainmail unit cell or the connector in a shortened state has a zero reaction force due to joint separation. The direction of the tensile reaction force of the chainmail unit cell or the connector is approximated by a 3D vector between the connector's top node and bottom node, based on the assumption that the tensile reaction force is primarily due to the elongation of the middle ring that is able to reorient towards the loading direction. In summary, the amplitude of the reaction force F of the chainmail unit cell or the connector is considered as a function of its length change Δl and expressed as $F = f(\Delta l)$. When the length change Δl is greater than zero (i.e., in an elongated state), the amplitude of the reaction force follows the uniaxial tensile response of the chainmail unit cell; when the length change is smaller than zero (i.e., in a

compressed state), the reaction force is zero. The chainmail sheet is modelled using a series of connectors (Fig. 6.4. B) and its load response is calculated by adding up the responses of individual connectors.

Since the connector is a simplified model whose tensile response is based on the uniaxial tensile tests of the chainmail unit cell that is in a predetermined state, it does not fully describe the behavior of a chainmail unit cell. In real loading scenarios of an ASD, the relative orientation of the rings in the unloaded state can vary due to the movable joints. Additionally, the chainmail unit cell is subject to complex loads such as shear force that leads to misalignment of its top/bottom half rings in the unloaded state. Those two factors can potentially cause the deviation of the tensile response of the chainmail unit cell from the measured uniaxial tensile response that is assigned to the connector.

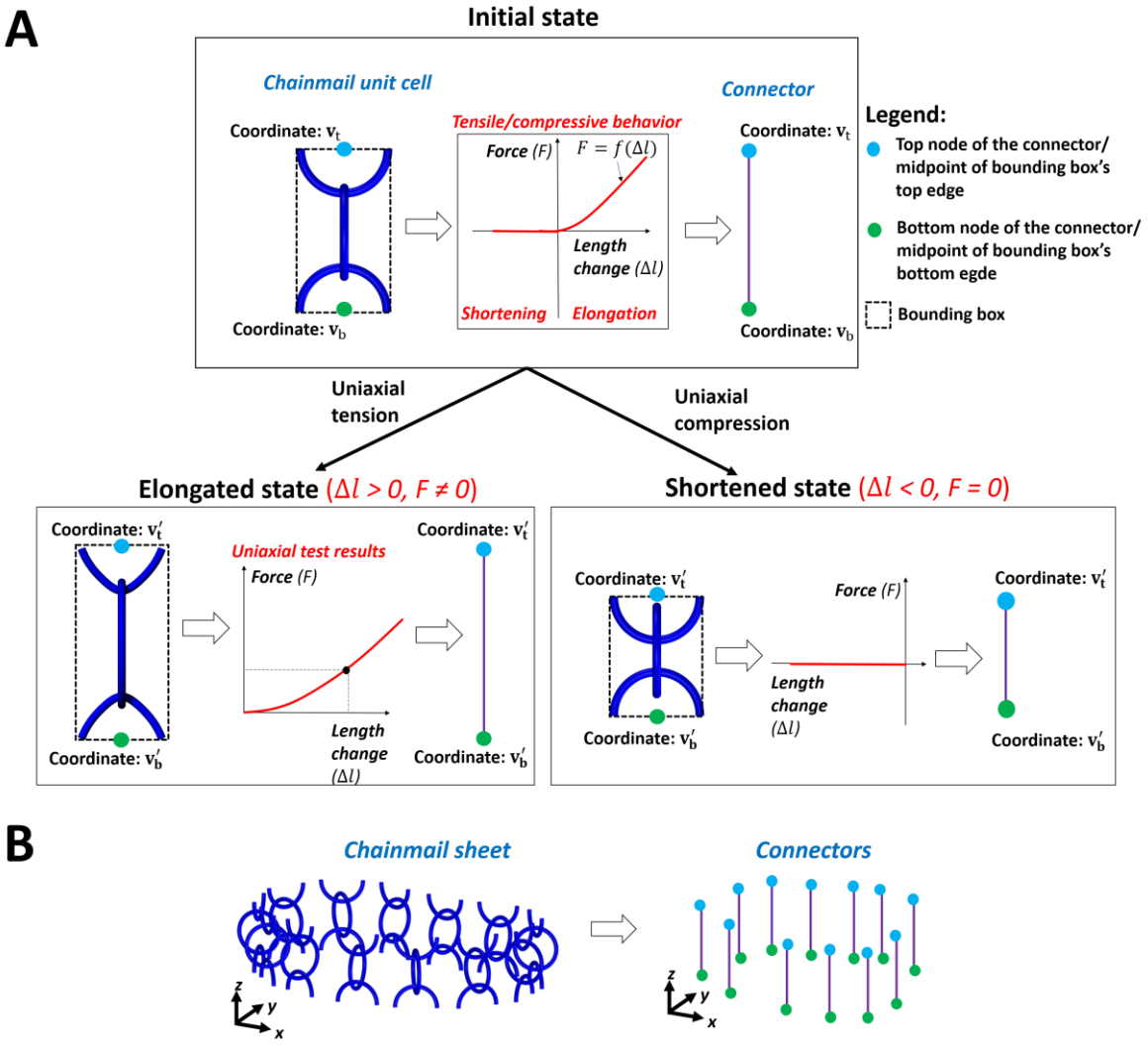

Fig. 6.4. Model of the chainmail unit cell and the chainmail sheet. (A) 2D projected view of the initial, elongated, and compressed states (loaded axially without shear force) of the chainmail unit cell and the connector model. The uniaxial compressive/tensile behavior of the chainmail unit cell is assigned to the connector, where the tensile response of the chainmail unit cell is obtained through uniaxial tensile tests and the unit cell's compressive response has a zero reaction force due to joint separation. The connector's reaction force amplitude F is formulated as a function of the connector's length change Δl: $F = f(\Delta l)$. When the connector is in an elongated state, its length change Δl is greater than zero and the corresponding amplitude of the reaction force follows the tensile response of the unit cell obtained through uniaxial tensile tests. In contrast, when the connector is in a compressed state, the connector's length change Δl is smaller than zero and a zero reaction force is resulted. (B) A series of connectors to model the behavior of a chainmail sheet.

Chainmail sheet response calculation and bilinear fitting

This section explains the method to calculate the chainmail sheet response and the bilinear fitting process to obtain the EZ stiffness of the chainmail sheet's response. Boundary conditions are added to the chainmail sheet to simulate the in-vitro mechanical test of an ASD under six most frequent rotational scenarios of a spine in everyday life [174]: flexion, extension, left/right LB, and left/right AR. The boundary conditions added are the same as used in Chapter 3. The algorithm for calculating the reaction moment of the chainmail sheet at a given rotation angle θ in a certain rotational DOF, which is referred to as M_R, is given in Table 6.3. As shown in Fig. 6.5, the calculation of M_R for multiple rotation angles that range from zero to the ROM in a certain DOF gives a set of discrete data points (shown as circles) that describe the moment-angle response of the chainmail sheet. The moment-angle response is then fitted into a curve $M_R(\theta)$ based on a bilinear constitutive model [9]:

$$\begin{aligned} M_R(\theta) &= E_1 \cdot \theta && \text{for } \theta \le \theta^* \\ M_R(\theta) &= E_2 \cdot (\theta - \theta^*) + E_1 \cdot \theta^* && \text{for} > \theta^* . \end{aligned} \tag{6.1}$$

In Eq. (6.1), the angle θ^* is defined as the transition angle at which the load response of the chainmail sheet switches from a small stiffness to a bigger stiffness. E_1, which is defined as the NZ stiffness, is the slope of the bilinear curve when θ is smaller than the transition angle θ^*. E_2, which is defined as the EZ stiffness, is the slope of the bilinear curve when θ is bigger than the transition angle θ^*. The bilinear fitting is modeled as an optimization problem in the scope of this work and is solved using a Matlab implementation of the bounded version of the original Nelder-Mead simplex method [103] in terms of E_1, E_2, θ^*.

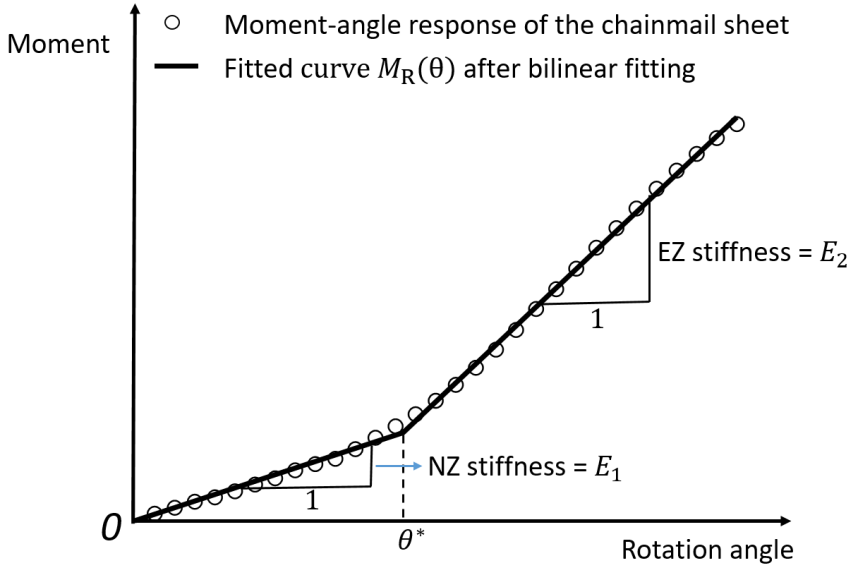

Fig. 6.5. Bilinear fitting of the moment-angle response of the chainmail sheet. The moment-angle response of the chainmail sheet is represented using a set of discrete data points shown as circles. The fitted curve $M_R(\theta)$ based on a bilinear constitutive model is characterized by three parameters: θ^*, E_1, and E_2. $\theta^*$is defined as the transition angle where the load response of the chainmail sheet switches from a small stiffness to a bigger stiffness; E_1 is the slope of the bilinear curve when θ is smaller than the transition angle θ^* and is considered as the NZ stiffness, and E_2 is the slope of the bilinear curve when θ is bigger than the transition angle $\theta^*$and is considered as the EZ stiffness.

Table 6.3. Pseudo-code of the algorithm used to calculate the reaction moment M_R of the chainmail sheet at a specific rotation angle θ in a certain rotational DOF.

Input: the rotation matrix $\mathbf{R}_\theta = \mathbf{R}(\theta)$ calculated at a specific angle θ in a certain rotational DOF, the initial coordinates of all the nodes lying on the top endplate $\mathbf{V}_\mathrm{t}$ and the nodes on the bottom endplate $\mathbf{V}_\mathrm{b}$, rotation center $\mathbf{c}$, the material set $\mathcal{M}$ with the available base materials

Output: the reaction moment $\mathbf{M}_\mathrm{R}$ at a specific angle θ in a certain rotational DOF

Set $\mathbf{M}_\mathrm{R} = 0$ % Zero the initial reaction moment of the chainmail sheet
For each *spring* **do**
    Find the initial coordinates of the bottom node $\mathbf{v}_\mathrm{t}$ and top node $\mathbf{v}_\mathrm{b}$ of the *spring*, in $\mathbf{V}_\mathrm{b}$ and $\mathbf{V}_\mathrm{t}$
    Calculate the initial length of the *spring* l_0 and the new coordinates of the top node $\mathbf{v}_\mathrm{t}' = \mathbf{R}_\theta\, \mathbf{v}_\mathrm{t}$
    Calculate the new length $l'$of *spring* and the spring axial length change $\Delta l = l' - l_0$
    If $\Delta l \leq 0$, **then** $\Delta f = 0$ % The length change is non-positive, the spring is in a compressed state
    Else % The length change is positive, the spring is in an elongated state
        Get the base material $x \in \mathcal{M}$ assigned to the *spring*
        Find the corresponding force-displacement curve of the chainmail unit cell given x
        Calculate the force amplitude Δf by interpolating over the force-displacement curve
        Calculate the force vector $\mathbf{f}_\theta = \Delta f \cdot \frac{\mathbf{v}_\mathrm{t}' - \mathbf{v}_\mathrm{b}}{\|\mathbf{v}_\mathrm{t}' - \mathbf{v}_\mathrm{b}\|}$ and the level arm $\mathbf{r} = \mathbf{c} - \mathbf{v}_\mathrm{t}'$
        Calculate the reaction moment of the *spring* $\mathbf{M}_\theta = \mathbf{r} \times \mathbf{f}_\theta$
        $\mathbf{M}_\mathrm{R} = \mathbf{M}_\mathrm{R} + \mathbf{M}_\theta$ % Add up the reaction moment of individual springs
End

Material optimization

This section states the problem formulation and the target values for the material optimization to allow the chainmail sheet to exhibit nature-mimicking relative amplitudes of EZ stiffnesses. The material optimization of the chainmail sheet is formulated as a discrete optimization problem for matching the chainmail sheet's EZ stiffness E_2^i, where the index i represents one of the six rotational loading scenarios, to the corresponding scaled-down target EZ stiffness denoted as $\bar{E}_2^i$ obtained using the stiffness scaling factor λ_s. The objective function of the optimization problem is:

$$\min_{\mathbf{x}} \Delta E_2 = \sum_{i=1}^{6} (E_2^i(\mathbf{x}) - \bar{E}_2^i)^2 \tag{6.2}$$

, where each item x_j ($j \in [1, N]$, and N is the amount of chainmail unit cells in the chainmail sheet) in design variable $\mathbf{x}$ represents the j th unit cell in the chainmail sheet to which one of the materials in the base material set $\mathcal{M}$ is assigned. Two chainmail sheets, i.e., a one-layer chainmail sheet with 40 unit cells and a two-layer chainmail sheet with 70 unit cells (40 unit cells in the outer layer and 30 unit cells in the inner layer) are optimized for restoring the relative amplitudes of rotational EZ stiffnesses of a human lumbar L4-L5 spinal segment for two surgical scenarios: TDR that includes a resection of the degenerated IVD together with the crucial ligaments (Scenario 1), and TDR that only includes a resection of the degenerated IVD (Scenario 2). Specifically, Scenario 1 requires a restoration of the mechanics of both the IVD and the crucial ligaments, while Scenario 2 only requires restoring VD's mechanics. Table 3 shows the target EZ stiffnesses that are calculated when the reaction moment lies between 7.5 and 10 Nm [125]. The derivative-free optimization algorithm GPS [175] implemented within the NOMAD software [176] is used for solving the optimization problem.

Table 6.4.The target EZ stiffnesses under two TDR surgical scenarios [125]**.**

		Flexion	Extension	Left LB	Right LB	Left AR	Right AR
Scenario 1 [Nm/◦]	**Unscaled EZ stiffnesses of an IVD plus crucial ligaments**	2.6316	3.0488	2.5773	2.5773	3.3333	3.3333
	Scaled EZ stiffnesses of an IVD plus crucial ligaments	0.0526	0.0610	0.0515	0.0515	0.0667	0.0667
Scenario 2 [Nm/◦]	**Unscaled EZ stiffnesses of an IVD alone**	0.7716	0.9690	1.4620	1.4620	1.4205	1.4205
	Scaled EZ stiffnesses of an IVD alone	0.0154	0.0194	0.0292	0.0292	0.0284	0.0284

6.4 Results

Section 6.4.1 presents the tensile responses of fourteen types of chainmail unit cells made from fourteen base materials. Section 6.4.2 then shows the validation results of using a connector whose tensile response is based on the uniaxial tensile test results to model the chainmail unit cell's tensile behavior. Lastly, Section 6.4.3 first presents the deformation modes and the representative moment-angle responses of the chainmail sheet in six rotational DOFs, then shows the EZ stiffnesses and the material distribution of the optimized one-layer and two-layer chainmail sheet for two TDR surgical scenarios. Section 6.4.3 ends with an illustration of a 3D printed prototype of the ASD design involving an optimized one-layer chainmail sheet for Scenario 1.

6.4.1 Tensile responses of the chainmail unit cells

This section presents the uniaxial tensile responses and the shape change process of the chainmail unit cell made from flexible base materials. The uniaxial tensile responses of the chainmail unit cells made from seven flexible base materials and seven rigid base materials are shown in Fig. 6.6. A and Fig. 6.6. B, respectively. Since the chainmail unit cells made from rigid base materials break before the filaments are fully aligned in the loading direction, therefore the seven flexible base materials are selected as material candidates that form the base material set $\mathcal{M}$ for the material optimization.

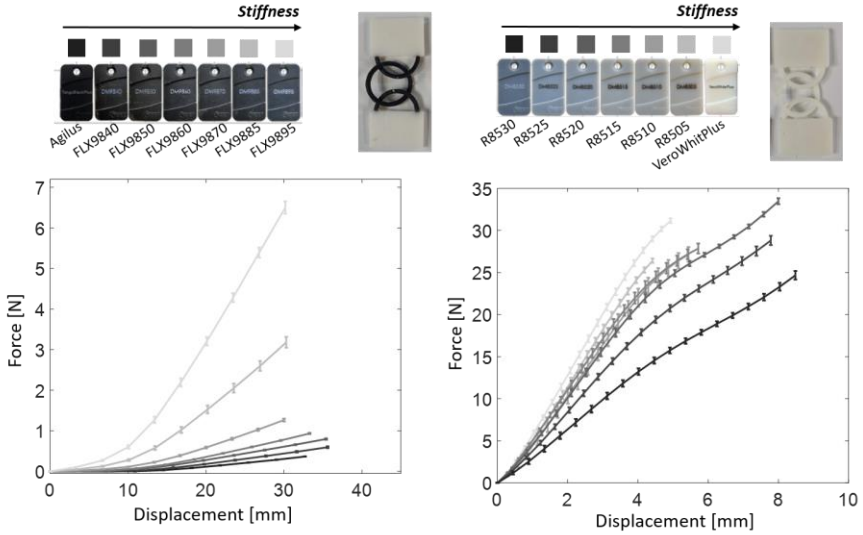

Fig. 6.6. The tensile force-displacement responses of fourteen types of chainmail unit cells. Each type of chainmail unit cell is fabricated with one of the fourteen base materials. Each curve is the average curve of five specimens that belong to the same chainmail unit cell type, with the error bars indicating the standard deviation of the responses of the five specimens. (A) Tensile responses of the seven types of chainmail unit cells made from flexible base materials, and (B) tensile responses of the seven types of chainmail unit cells made from rigid base materials.

6.4.2 Model validation

This section presents the model validation results to examine the influence of the two factors, i.e., relative orientation of the rings and alignment of the top/bottom rings in the unloaded state, on the accuracy of the connector model. Namely, Fig. 6.7 shows the influence of relative orientation of the rings in the unloaded state and Fig. 6.8 shows the influence of the alignment of the top/bottom rings in the unloaded state on the chainmail unit cell's tensile response. The linear stiffnesses shown in Fig. 6.7 and Fig. 6.8 are the slope of the linear region of the chainmail unit cell's tensile response using a bilinear fitting similar to the process illustrated in Fig. 6.5.

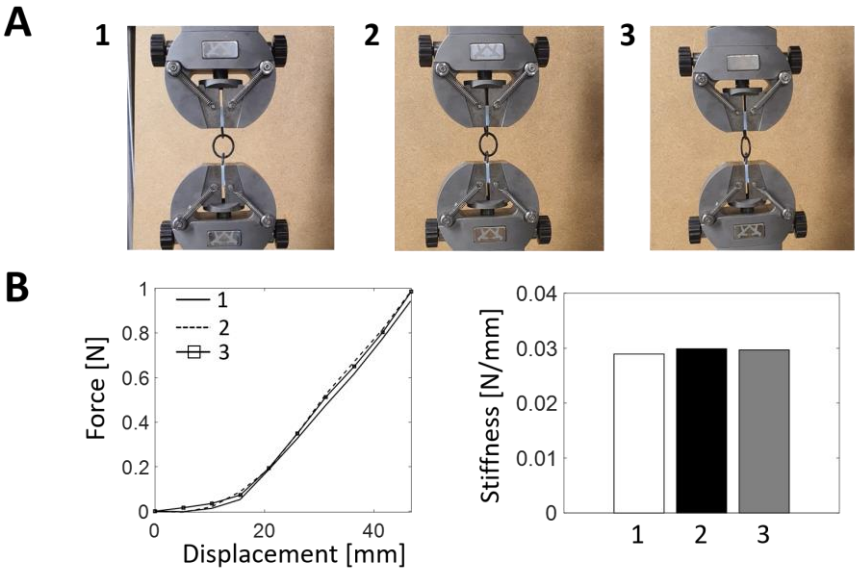

Fig. 6.7. The influence of relative orientation of the rings in a chainmail unit cell in the unloaded state on its tensile response. (A) Three variations of the relative orientations of the middle ring relative to the top/bottom half rings in a chainmail unit cell in the unloaded state: 1 = perpendicular, 2 = at an angle of ~45 degrees, 3 = at an angle of ~10 degrees. (B) The corresponding tensile responses and the corresponding linear stiffnesses using a bilinear fitting.

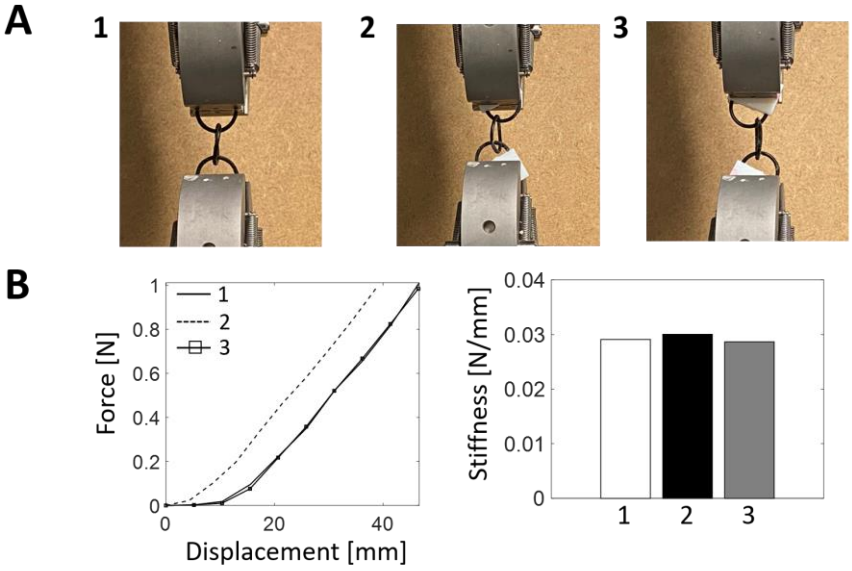

Fig. 6.8. The influence of alignment of the top/bottom rings in a chainmail unit cell in the unloaded state on its tensile response. (A) Three variations of the top/bottom rings alignment in a chainmail unit cell: 1 = aligned in the uniaxial direction, 2 = with a right shift, 3 = with a left shift. (B) The corresponding tensile responses and the corresponding linear stiffnesses using a bilinear fitting.

6.4.3 Response of the chainmail sheet and optimized results

This section presents the deformation modes and exemplary rotational responses of the chainmail sheet in six rotational DOFs, the EZ stiffnesses and rotational responses of the optimized chainmail sheets compared to target values, and a 3D printed prototype of the proposed ASD design. Fig. 6.9 shows the deformation modes and the representative moment-angle responses of the chainmail sheet in six rotational DOFs. The convergence plot of the material optimization process is given in Fig. 6.10, while each objective function evaluation takes ~0.9 seconds and a total of ~10 minutes is needed for the material optimization. The EZ stiffnesses and the material distribution of the optimized one- and two-layer chainmail sheet for restoring the relative amplitudes of EZ stiffnesses in six DOFs for Scenario 1 and Scenario 2 are shown in Fig. 6.11. Additionally, Fig. 6.12 shows the comparison of the moment-angle responses of the optimized chainmail sheet with those of IVD plus crucial ligaments (Scenario 1) and IVD alone (Scenario 2). A prototype of the 3D printed ASD with an optimized one-layer chainmail for Scenario 1 is illustrated in Fig. 6.13.

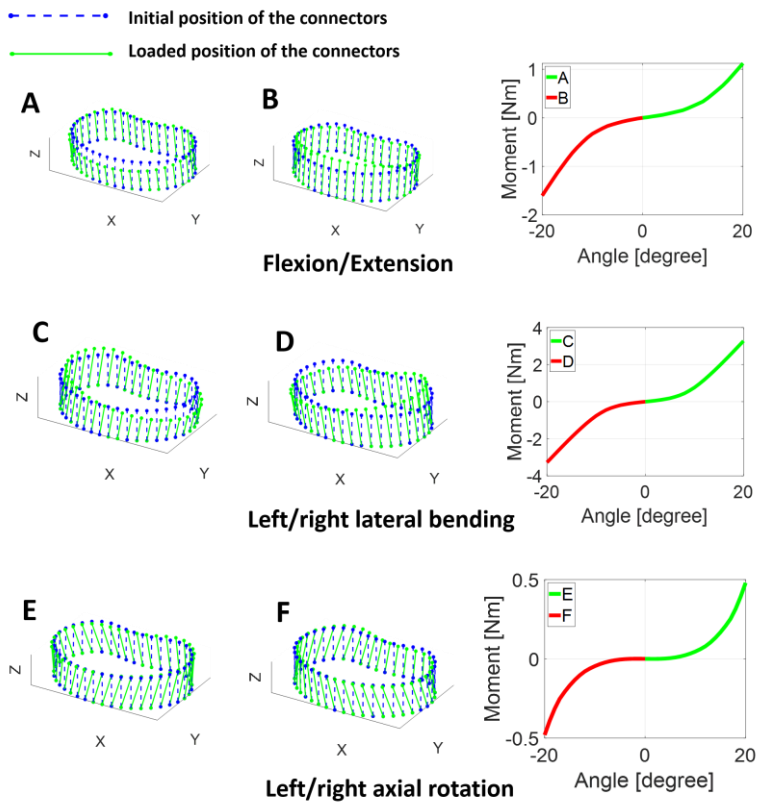

Fig. 6.9. Deformation modes of chainmail sheet in six rotational DOFs and the corresponding moment-angle responses using the connector model. As an example, the one-layer chainmail sheet has 40 chainmail unit cells with the base material FLX9895, and the maximum rotational angle in each DOF is set as 20 degrees.

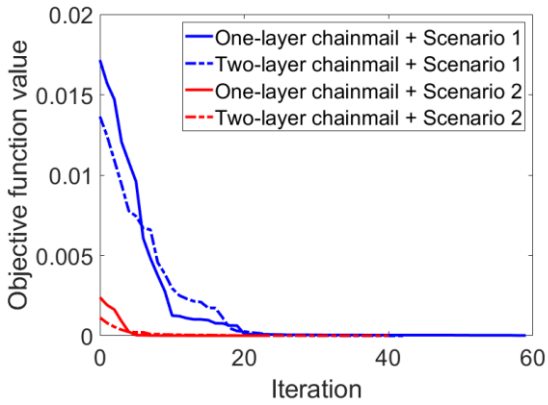

Fig. 6.10. The convergence plot of the optimization process: the starting point of the optimization is set as when all the chainmail unit cells are made from Agilus, and the stopping criteria is set as when the absolute objective function change is smaller than 1e-7 between two subsequent iterations or a maximal function evaluation of 5000 times is reached.

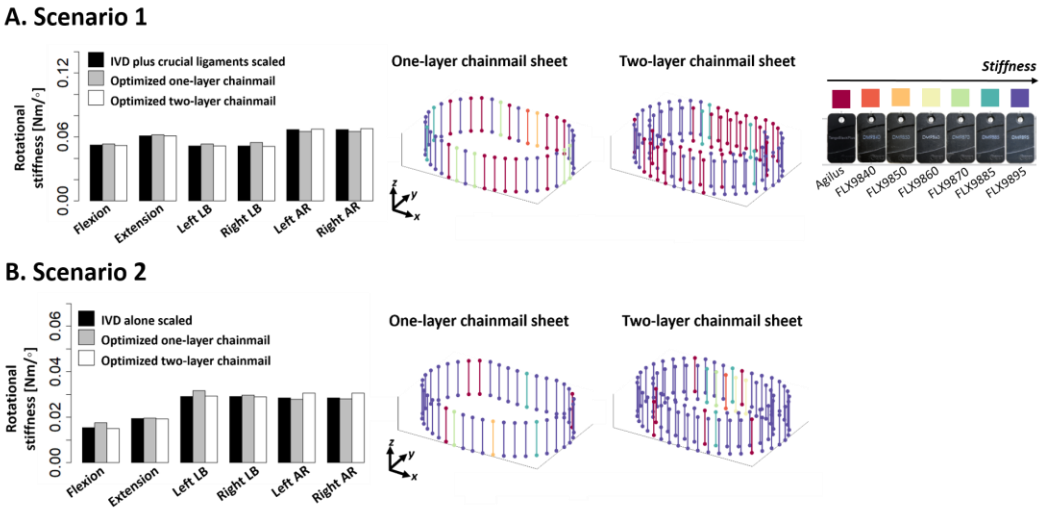

Fig. 6.11. The EZ stiffnesses and the material distribution of the optimized one- and two-layer chainmail sheet for Scenario 1 (A) and Scenario 2 (B). The first column shows the comparison of the EZ stiffnesses of the optimized chainmail sheet with the target values, while the second and third columns present the material distribution in the optimized chainmail sheet, respectively.

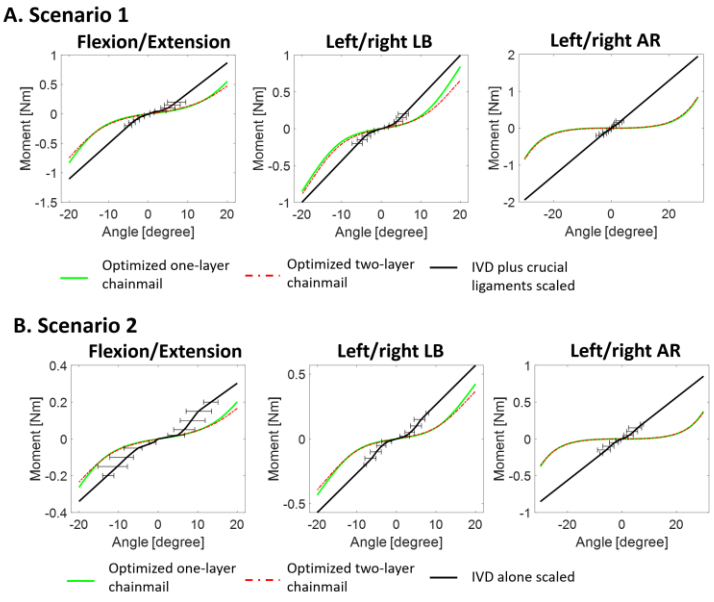

Fig. 6.12. Comparison of the moment-angle responses of the optimized one- and two-layer chainmail sheet with the responses of the IVD plus crucial ligaments (A) and an IVD alone (B). The data of the natural spinal segment including the error bars that show the minimum and the maximum ROM with the given moment is obtained from [125].

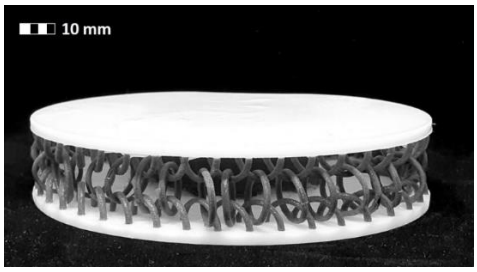

Fig. 6.13. 3D printed prototype of the proposed ASD design involving an optimized one-layer chainmail sheet for Scenario 1. The endplates are made from VW and the artificial NP is made from Agilus, and the one-layer chainmail sheet has the optimized material distribution for Scenario 1.

6.5 Discussion

The discussion section first interprets and assesses the results in Section 4.1. Next, Section 4.2 discusses the limitations of the proposed chainmail-based ASD design and possible future work to improve its performance.

6.5.1 Results interpretation and assessment

Fig. 6.9 shows that the chainmail sheet exhibits a nature-mimicking nonlinear rotational load response. Such nonlinear trend is attributed to the nonlinear tensile behavior of the chainmail unit cell, since the response of the chainmail sheet is the sum of the responses of individual chainmail unit cells. Fig. 6.6 shows that chainmail unit cells made from flexible base materials (referred to as "flexible" chainmail unit cells) exhibit a desired J-shaped tensile response similar to that of natural AF [9]. In contrast, the force-displacement responses of the chainmail unit cells made from rigid materials (referred to as "rigid" chainmail unit cells) exhibit a softening trend. The difference in the trend of the tensile responses of the "flexible" and "rigid" chainmail unit cells is due to the different base material behaviors. The seven flexible materials have a much larger breaking strain (~100%) compared to the seven rigid materials whose yield strains are around 4.5%. Therefore, the shape change is more significant among "flexible" chainmail unit cells, which explains the predominantly strain-stiffening tensile responses of the "flexible" chainmail unit cells and the strain-softening tensile responses of the "rigid" unit cells due to material yield. It can be concluded that the tensile response of the chainmail unit cell is determined by both its base material and its shape change.

The J-shaped responses of the "flexible" chainmail unit cells can be fitted using a bilinear model with an initial low stiffness at smaller displacements and a *linear stiffness* at bigger displacements, while the displacement that separates those two regions is referred to as the *transition displacement*. The comparable trend of the linear stiffnesses of the seven "flexible" chainmail unit cells and the base material stiffnesses shows that the linear stiffness of the chainmail unit cell is primarily determined by the base material stiffness. The transition displacements of the seven types of "flexible" chainmail unit cells are all at ~10 mm, implying that the seven "flexible" chainmail unit cells go through a comparable shape changing process. This also implies that the initial shape of the chainmail unit cell is critical in determining the transition displacement. Since the EZ stiffness and the transition angle in rotational scenarios of the chainmail-based ASD are determined by the transition displacements and the linear

stiffness of the chainmail unit cells, such mechanism of the “flexible” chainmail unit cell shows additional benefits of using a flexible chainmail sheet for ASD design, as the transition angle and EZ stiffness in rotational loading scenarios of the ASD can be independently adapted by adjusting the shape and the base material of the chainmail unit cell, respectively.

Fig. 6.7 shows that relative orientation of the rings in the unloaded state has little influence on the chainmail unit cell’s tensile response. Besides, Fig. 6.8 shows that alignment of the top/bottom rings influences the transition displacement of the chainmail unit cell’s tensile response due to different starting points of shape change, while having little influence on the linear stiffness of the unit cell’s tensile response. Considering that the optimization goal of this study is to reproduce the natural relative amplitudes of EZ stiffness that is determined by the linear stiffness of the chainmail unit cell, both of these factors have negligible effect on the optimization results, which verifies the application of a connector model. The good agreement of the linear stiffnesses presented in Fig. 6.7 and Fig. 6.8 also verifies the assumption that the tensile reaction force of a chainmail unit cell is mostly attributed to the reorientation and elongation of the middle ring.

Fig. 6.11 and Fig. 6.12 show that the EZ stiffnesses of the optimized chainmail sheet match well with the target values for different surgical scenarios. Generally, the EZ stiffnesses of the optimized two-layer chainmail match better to the target values compared to those of the one-layer chainmail, as more design variables and a bigger design space are available for the two-layer chainmail. The good match with the target values also verifies the adaptability of the multi-material chainmail sheet to meet personalized stiffness needs. Such adaptability is partially due to the negligible compressive stiffness of the chainmail unit cells, which causes that different subsets of the chainmail unit cells contribute to the reaction moment of the chainmail sheet in different rotational DOFs. For example, under flexion the chainmail unit cells that lie at the posterior side of the chainmail sheet are elongated and strained, while the unit cells that lie at the anterior side are shortened and relaxed. In comparison, under extension the chainmail unit cells that lie at the anterior position are elongated and strained, while the unit cells at the posterior side are shortened and relaxed. Such unique mechanism of the chainmail sheet contributes to a partial decoupling of the multi-objective optimization problem, as chainmail unit cells at different positions contribute to the ASD’s response in different loading scenarios at different degrees. The optimized material distribution in the chainmail sheet has an asymmetrical distribution about the sagittal plane, which can be attributed to the similar material properties of some base materials, such as Agilus and FLX9840. Nevertheless, the optimized EZ stiffnesses show a natural-mimicking symmetric EZ stiffness in left/right LB and in left/right AR. The optimization process of the chainmail sheet shows a fast convergence, which proves the efficiency of the GPS algorithm in handling nonlinear discrete optimization problems [177].

6.5.2 Limitations

First, the connector is a simplified model and does not take into account the sliding between rings resulting from shear force, as illustrated in Fig. 6.14. A. Such ring sliding before shape change

leads to a close-to-zero reaction force, as no shape change is initiated. However, since the length change Δl of the corresponding connector is greater than zero, the connector model produces a non-zero reaction force. That is to say, in real loading scenarios when shear forces are present, the transition displacement of chainmail unit cell's tensile response is larger than that of its uniaxial tensile response, which leads to a larger transition angle of the chainmail sheet than that calculated in this study. As demonstrated in Fig. 6.9, shear force is most significant in left/right AR while being minor in other rotational loading scenarios (i.e., flexion, extension, left/right LB). Second, this study only focuses on restoring the nonlinear trend and the nature-mimicking relative amplitudes of EZ stiffnesses in six rotational DOFs, while neglecting other metrics of an IVD's rotational response such as transition angle and NZ stiffness. Fig. 6.12 shows that the rotational responses of the optimized chainmail sheets exhibit a larger NZ range, i.e., an increased laxity, in each rotational DOF compared to the target values. Since the transition angle of the chainmail sheet is controlled by the chainmail unit cell's transition displacement that is further influenced by the initial shape of the chainmail unit cell, one possible solution to restore the natural NZ range is through adjusting the chainmail unit cell's shape. As illustrated in Fig. 6.14. B, various shapes of the chainmail unit cell can lead to different transition displacements, while having little influence on the linear stiffnesses of their tensile responses. Furthermore, a higher degree of initial filament alignment in the axial loading direction is related to a smaller transition displacement, which help lower the NZ range of the chainmail sheet.

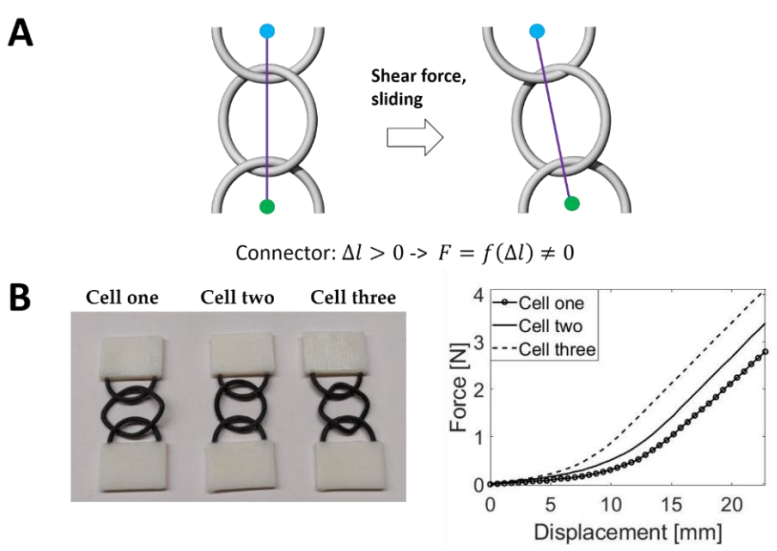

Fig. 6.14. (A) Illustration of the sliding between the rings that leads to a larger transition displacement of the connector's elongation response. Due to ring sliding, the reaction force of the chainmail unit cell remains close to zero, while an non-zero elongation length and non-zero reaction force are produced with the given connector model. **(B) The influence of the chainmail unit cell initial shape on its uniaxial tensile response.** All the chainmail unit cells are fabricated with the base material FLX9895. The uniaxial tensile test follows the same procedure stated in Section 2.2.2.

6.5.3 Implication for the thesis

This chapter incorporates a chainmail-like structure inspired by the flexible mechanical metamaterials into the ASD design for restoring the IVD's nonlinear, anisotropic load response, which is otherwise difficult to realize with the given materials and 3D printing technique. The chainmail-like structure shares some similar behaviors with collagen fiber network in an IVD: a negligible compressive

stiffness and the shape-changing ability. The good performance of the resultant ASD in realizing a nonlinear behavior demonstrates the great potential of incorporating mechanical metamaterials or metamaterials-inspired structures into the ASD design to achieve a natural-mimicking behavior. This chapter provides answer to RQ2 by proposing a promising ASD design concept. To realize an efficient design process, this chapter introduces a connector model to describe the behavior of a chainmail unit cell. Although the validity of the model is limited by the sliding between the rings in a chainmail unit cell, this model is a valid model for this chapter that optimizes the ASD to reproduce relative amplitudes of rotational EZ stiffnesses while contributing to a computationally efficient design process. The effectivity of using a simplified model provides answers to RQ3. Furthermore, this chapter discusses two major manufacturing constraints with the given 3D printer: the minimum allowable feature size, and the limited options of materials. Thus, this chapter introduces a geometric and a material scaling factor, which provides partial answer to RQ4 of realizing a patient-specific ASD design given the manufacturing constraints.

6.6 Conclusion

This chapter proposes a novel ASD design based on a flexible multi-material chainmail sheet to improve the ASD designs proposed in previous chapters while considering the manufacturing constrains of the given 3D printing technique. The design is inspired by the behavior similarities between the collagen fiber network and the chainmail-based structure, which provides answer to RQ2. To realize a patient-specific design, a computationally efficient methodology is proposed based on a connector model to describe the load response of the chainmail unit cell, which provides answer to RQ3. Results show that similar as the collagen fibers, the chainmail sheet is able to exhibit a nature-mimicking, nonlinear load response thanks to its shape-changing ability. Furthermore, through material optimization the chainmail sheet is able to reproduce the IVD's relative amplitudes of EZ stiffness in six loading scenarios under different TDR surgical scenarios. This design also takes into account the minimum allowable printing size and the material anisotropy of the given 3D printing technique, which provides answer to RQ4.

Chapter 7. Design comparison and testing of various ASD designs

This chapter has been adapted from a manuscript published in the journal *Materials & Design*: Yu, Z., Voumard, B., Shea, K., Stanković, T., 2021. Exploration of the influence of different biomimetic designs of 3D printed multi-material artificial spinal disc on the natural mechanics restoration. Mater. Des. 110046. https://doi.org/https://doi.org/10.1016/j.matdes.2021.110046

7.1 Summary

To give an overview of the ASD design concepts proposed in the previous chapters, Table 7.1 summarizes the ASD design concepts and lists the strengths and weaknesses of each ASD design. Chapters 3-6 focus on proposing conceptual designs of ASDs and investigating their performances through computational methods, while the performances of the ASD designs through mechanical tests are not explored yet. Besides, the influence of different biomimetic design concepts on the ASD's kinematics in conjunction with AM is still unclear. Therefore, this chapter fabricates four biomimetic, multi-material ASD designs (Discs 1-4) proposed in the previous chapters and measures their responses through *in vitro* mechanical tests.

Table 7.1. Overview of the multi-material ASD designs proposed in the previous chapters. The designs are listed in a chronological order in this thesis.

ASD design	Strengths	Weaknesses
Monolithic, biomimetic fiber-reinforced composite design (Chapter 3)	• Has the potential to reproduce the IVD's anisotropic stiffness in various loading scenarios thanks to the fiber layer with negligible bending resistance • Lowers the risk of material failure due to a monolithic design	• Lack of manufacturability due to the fiber layer that is vertical to the print bed and the small feature down to 0.1 mm • Exhibits a linear load response
Monolithic, solid design (Chapter 4)	• Easy to fabricate, no complex structures or small features involved • Lowers the risk of material failure due to a monolithic design	• Low torsional stiffness compared to stiffnesses in other rotational DOFs, unable to reproduce IVD's anisotropic stiffnesses due to conflicting objectives imposed • Exhibits a linear load response
Biomimetic design with a separate fiber-like layer (Chapter 4)	• Has the potential to reproduce the IVD's anisotropic stiffness in various loading scenarios thanks to the crisscross fiber-like layer that exhibits a larger torsional stiffness than a compressive stiffness	• Prone to material failure and interface delamination due to small feature • An initial structure optimization of the fiber-like layer is required to restore the natural anisotropy • Exhibits a linear load response
Lattice-based design (Chapter 5)	• Has the potential to restore the IVD's anisotropic stiffness in various loading scenarios through varying the topology • Big design freedom due to structural adaptability	• Prone to material failure and interface delamination due to small features • Exhibits a strain-softening response due to member buckling in the lattice • Constrained by the modeling complexity resulting from material anisotropy that is dependent on build orientation
Chainmail-based design (Chapter 6)	• Has the potential to restore the IVD's anisotropic stiffness in various loading scenarios due to the negligible compressive resistance of the chainmail-like structure • Shows a nature-mimicking nonlinear load response • Spares the effort of modeling the complex anisotropic material behavior dependent on factors such as build orientation and feature size	• Constrained by modeling complexity due to factors such as sliding between the rings and different load bearing mechanisms of chainmail unit cells fabricated with rigid and flexible base materials

Results show that all the four ASD designs exhibit a desired viscoelastic behavior and a chainmail-based ASD (Disc 4) is able to exhibit a nonlinear rotational load response as expected. This

shows the great potential of incorporating mechanical metamaterials inspired structures into the ASD design. In terms of restoring the IVD's anisotropy, the ASD designs that mimic the structure found in an IVD (Discs 2-4) outperform the design that solely mimics the IVD's material stiffness gradient (Disc 1). Additionally, all the designs show more comparable instant helical axis (IHA) and instant center of rotation (ICOR) to an IVD than a Charité ASD regarding location and moving direction. This chapter helps to determine the most favorable ASD design concept for developing a patient-specific ASD in the next chapter.

7.2 Methods

The methodology section starts with an explanation of the design and fabrication process of the four biomimetic ASD designs in Section 7.2.1. Next, Section 7.2.2 explains the *in vitro* mechanical testing setup and the test procedure to measure the rotational and compression load responses of the ASD designs. The data analysis approach to obtain the metrics that measure the *quantity* and *quality* of the motion of the ASD designs is clarified in Section 7.2.3.

7.2.1 Design and fabrication of biomimetic ASD designs

The designs of the four biomimetic ASD designs together with a fifth control design are illustrated in Fig. 7.1. All the ASD designs investigated equate in size to a human lumbar L4-L5 IVD as shown Fig. 7.2 [178] and share the same sandwiched structure that is composed of a compliant core and two rigid endplates. The rigid endplates are designed to replace the cartilage endplates to interface with adjacent vertebrae, while the compliant core is designed to provide elasticity in various loading scenarios. All the designs have a sagittal plane symmetry to achieve a symmetric load response in left and right loading scenarios. The explored ASDs have a total height of 14 mm: each endplate has a thickness of 2 mm, and the height of the core equals to 10 mm. The detailed component dimensions of each ASD design are provided in Table 7.2. The size of the smallest features in the ASD design is restricted by the minimum allowable printable size of the 3D printer to obtain reliable mechanical properties [28].

The core of Disc 1 that consists of a stiffer outer layer and a soft central cylinder resembles the solid ASD design proposed in Chapter 4. The core of Disc 2 is a composite design with an embedded crisscross fiber-like structure, which resembles the fiber-reinforced composite ASD design proposed in Chapter 3. With a core made from a separated crisscross fiber-like structure and a central cylinder, Disc 3 resembles the biomimetic ASD design proposed in Chapter 4. Disc 4 is based on the chainmail-based ASD design proposed in Chapter 6, except that the central cylinder is attached to the two endplates and each chainmail unit cell is made from two half elliptical rings as illustrated in Fig. 7.3. The chainmail unit cells in Disc 4 are positioned at the periphery of the endplates to amplify the unit cells' contribution to the ASD's rotational response by maximizing their level arms. Disc 1 mimics the material gradient at a macro level in an IVD where the AF is shown to be stiffer than NP, whereas Discs 2-4 mimic the collagen fiber network in an IVD. In addition, a control design with a homogenous core, i.e., Disc 5, is

also considered to explore the effect of different concepts of biomimicry on ASD's anisotropic performance.

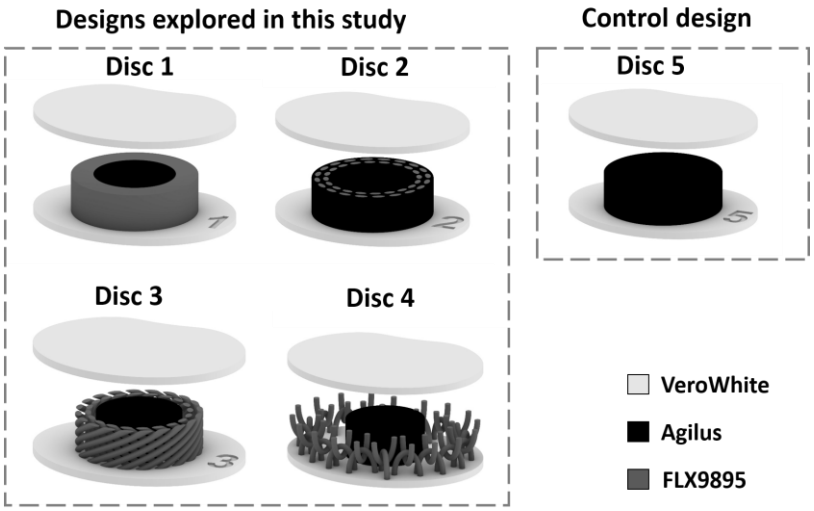

Fig. 7.1. The four biomimetic, multi-material ASD designs explored in this chapter together with a control design. The ASD designs share the same overall design concept that consists of two stiff endplates and a compliant core. The endplates are kept unchanged among the designs, while the soft core is varied. The core in Disc 1 consists of a softer central cylinder and a stiffer outer ring to mimic the functional stiffness gradient in an IVD at a macro level. The core of Disc 2 is a fiber-reinforced matrix composite, while the core of Disc 3 consists of a soft central cylinder and a surrounding stiffer crisscross fiber-like structure. Both Disc 2 and Disc 3 include a crisscross fiber-like structure to mimic the structure of IVD's crisscross collagen fiber network. The core of Disc 4 features a soft central cylinder and a surrounding chainmail-like structure. Disc 5 is the control design whose core is made from a single material to explore the effect of different concepts of biomimicry on ASD's anisotropic performance. The stiffest material referred to as VW ($E \approx 2$ GPa) is used to fabricate rigid endplates, while the two flexible, rubber-like materials referred to as Agilus ($E \approx 0.5$ MPa) and FLX9895 ($E \approx 5$ MPa) are used for the fabrication of the compliant core.

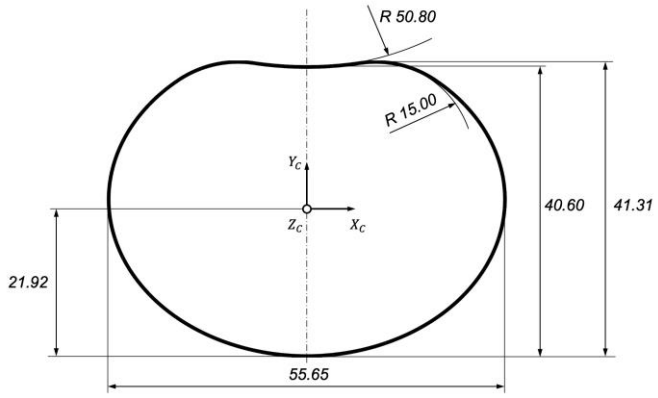

Fig. 7.2. The top-view of the proposed ASD design that equals to the size of a human L4-L5 disc (unit: mm). The height is 10 mm measured in the z-direction.

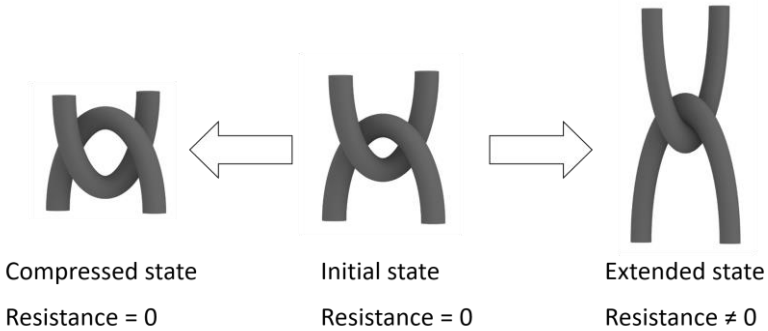

Fig. 7.3. Three states of the chainmail unit cell in Disc 4. The unit cell only provides a load resistance when being in an extended state.

Table 7.2. List of the detailed design parameters of the components in the cores of Discs 1-4.

<table>
<tr><th colspan="2">Disc 1</th><th colspan="6">Disc 2</th></tr>
<tr><td>NP</td><td>AF</td><td>Matrix</td><td colspan="5">Fiber-like structure</td></tr>
<tr><td>Diameter</td><td>Outer diameter</td><td>Diameter</td><td>Filament diameter</td><td>Inner layer diameter (Center line)</td><td>Outer layer diameter (Center line)</td><td>Filament orientation</td><td>Amount of filaments</td></tr>
<tr><td>22 mm</td><td>34 mm</td><td>34 mm</td><td>1.6 mm</td><td>26 mm</td><td>31 mm</td><td>=~60° to vertical axis</td><td>40 (20/layer)</td></tr>
<tr><th colspan="2">Disc 3</th><th colspan="6">Disc 4</th></tr>
<tr><td>NP</td><td>AF as a stand-alone fiber-like structure</td><td>NP</td><td colspan="5">Chainmail-like structure</td></tr>
<tr><td rowspan="3">22 mm</td><td rowspan="3">The design parameters are the same as for the fiber-like structure in Disc 2</td><td rowspan="3">22 mm</td><td>Filament diameter</td><td colspan="2">Diameter of the elliptical ring</td><td colspan="2">Amount of chainmail unit cells</td></tr>
<tr><td rowspan="2">1.6 mm</td><td>Major axis</td><td>Minor axis</td><td rowspan="2" colspan="2">19</td></tr>
<tr><td>13 mm</td><td>7.2 mm</td></tr>
</table>

7.2.2 Mechanical testing

Each specimen is tested in six DOFs to simulate the rotational loading scenarios and its angular bending responses are recorded. In addition, the specimen's compression response is measured through a compression test. The performances of the four ASD designs are evaluated based on metrics concerning the restoration of IVD's *quantity* and *quality* of motion, which involve the analyses of the specimen's rotational response with respect to the initial NZ and the subsequent EZ [37], as well as the hysteresis area and the compressive stiffness. The analysis of restoring the *quality* of motion also includes IHA and ICOR that provide temporal three-dimensional and two-dimensional information for describing ASD's motion pathway and more precisely evaluate an ASD's performance [179][180]. This is based on the finding that ICOR pattern is closely related to the spinal segment stability, while physiological IHAs and ICORs reduce the risk of facet and ligament overloading [181][182]. Thus, ICOR has been used in many studies to identify abnormal motion patterns [183][184].

Angular test*:* The specimens are secured to a customized six DOF, computer-controlled spine testing system [185] as shown in Fig. 7.4.A. The test facility is similar as the one used for testing IVDs [186]. The specimens are fixed to the test facility using two aluminum plates (one at the top and one at the bottom) that are connected to the endplates of the specimen using a superglue (cyanoacrylate adhesive, UHU, Germany) to avoid the relative movement between the aluminum plates and the specimens. The plates are manufactured with aluminum to minimize the effect of the stiffness of the plates on test results, and are designed to have a matching geometry with the specimens' endplates to increase the fixation stability. The testing system is able to apply pure moments that are recorded by a six DOF load cell (MC3A, AMTI, U.S.A.), while the resultant motion of the specimens is calculated based on the markers that are attached to the top and bottom rigid test facilities, which are then rigidly connected to the top and bottom endplates. The absolute positions of the markers in the 3D space are recorded by an optoelectronic motion analysis system (Optotrak Certus, NorthernDigital, Canada).

The specimens are loaded at a displacement control mode with a loading rate of 1°/s (ramp-loading). Each specimen is loaded sequentially in six DOFs: extension (negative rotation angle the x-axis), flexion (positive rotation angle along the *x*-axis), left and right LB (positive and negative rotation angle along the y-axis respectively), right and left AR (negative and positive rotation angle along the z-axis respectively). In each loading scenario, a pure moment is added at a certain DOF and repeated three times, while the specimen is allowed to move freely in the remaining five unloaded DOFs, thus allowing for a coupled motion. The stopping criteria of all the specimens are a maximal loading angle of 14° in flexion/extension, 12° in left/right LB, and 24° in left/right AR, or when the maximal allowable moment of the testing system 5 Nm is reached. The loading process is paused for two seconds when the maximal rotation angle is reached.

Compression test*:* An Instron ElectroPuls E3000 testing machine with a Dynacell loadcell of 3 kN capacity is used for obtaining the axial load responses of the specimens, as shown in Fig. 7.4.B. The specimens are loaded until a 10% strain with a strain rate of 0.001, 0.01, 0.02 s^{-1} sequentially to examine the effect of strain rate on the compressive response of the specimens. A ten-minute relaxing time is set for all the specimens in between subsequent tests to allow for stress relaxation.

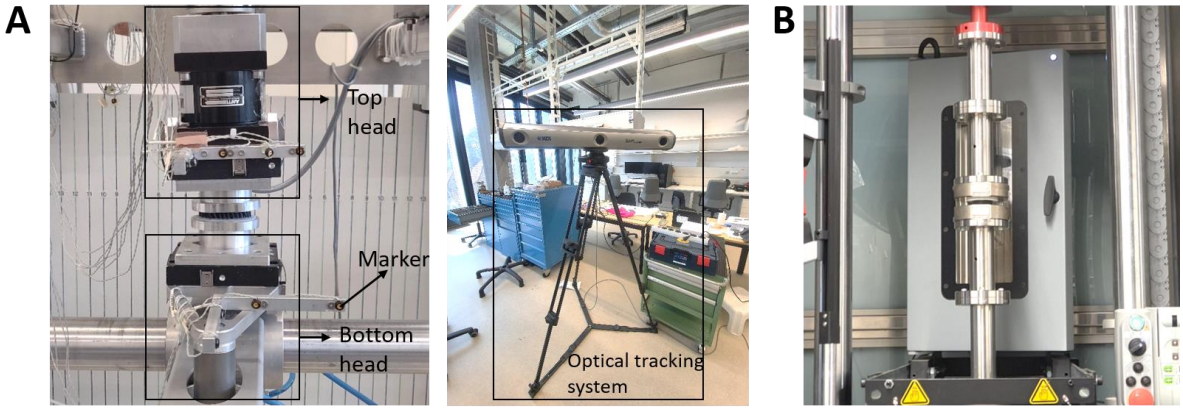

Fig. 7.4. Test facilities for the angular and compression test of the ASD specimens. (A) The angular test facility [187] includes a six-axis load cell (left) with a top and bottom head where the markers are attached, and an optical tracking system (right) that records the markers' locations in the 3D space. (B) The compressive test facility: the Instron ElectroPuls E3000 testing machine with a Dynacell loadcell of 3 kN capacity.

7.2.3 Testing data analysis

The load responses of the specimens in the angular and compression tests are then analyzed to derive the values of the metrics to measure the *quantity* and the *quality* of motion of the ASDs. The values of the metrics are then compared to a human L4-L5 lumbar IVD as well as a Charité ASD. The metrics used to measure the *quantity* of motion of the specimens are NZ range, hysteresis area, the NZ and the EZ stiffness. In addition, the compressive stiffness of the specimens under different strain rates are calculated. The sigmoidity is only shown for the ASD design with a significant nonlinear trend. In the end, the paths of the IHA and ICOR during the loading process are calculated based on the marker position of the top and bottom endplates recorded by the Optotrak system. The detailed data analysis procedure is given as follows.

Rotational and compressive test results analysis: For each rotational loading scenario, three cycles of the moment-angle load response of each specimen are recorded during the angular test, while the first 1.5 cycles are used as pre-conditioning to minimize the effect of the viscoelasticity and the specimen's response in the following cycle (1.5-2.5 cycle) is used for data evaluation [125]. For the load responses that show a significant nonlinear trend, five parameters are derived to describe the specimen's response: the NZ range, hysteresis area, the NZ and the EZ stiffness, and sigmoidity. While for load responses with a mostly linear trend, the NZ stiffness and sigmoidity are left out. The NZ and EZ stiffness are obtained through a bilinear regression for the rotational load response with a significant nonlinear trend, while the EZ stiffness is obtained through a linear regression for the load response with a mostly linear trend. To facilitate the anisotropy comparison of different ASD designs without the influence of base materials used for fabrication, normalized EZ stiffness is calculated through dividing the EZ stiffness of each specimen to its corresponding EZ stiffness in flexion. For each ASD design, the metrics derived from its five specimens are averaged and the standard deviations are calculated. For compression responses, the compression stiffness of each specimen at 4% and 8% strain with each strain rate (0.001, 0.01, 0.02 s^{-1}) is calculated using linear regression. To show that there exists a statistically significant difference among different ASDs, a one-way ANOVA test is performed on all the metrics, and a *p*-value less than 0.001 is considered to be statistically significant.

IHA and ICOR analysis: The local coordinate system whose origin is located in the geometric center of the ASD is denoted by $O_cX_cY_cZ_c$ according to ASTM norm [52], as shown in Fig. 7.5.A. Furthermore, Fig. 7.5.B illustrates the movement of the top and end bottom endplates of the ASD from time $t = t_1$ to $t = t_2$ with the fixed global coordinate system denoted by $O_1X_1Y_1Z_1$, the local coordinate system of the bottom endplate ($O_2X_2Y_2Z_2$), and the local coordinate system of the top endplate ($O_3X_3Y_3Z_3$).

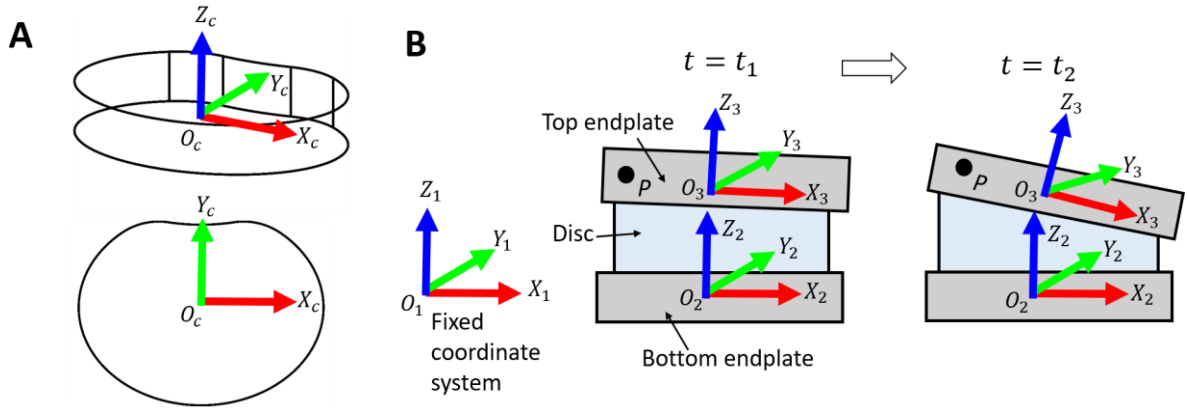

Fig. 7.5. The definition of the coordinate systems and the illustration of the top endplate's movement over time. (A) The disc coordinate system whose origin lies in the geometric center of the ASD. (B) The global coordinate system and the two local coordinate systems defined on the top and bottom endplate from time $t = t_1$ to $t = t_2$.

To describe the angular motion of the specimen, the motion of the top rigid endplate relative to the bottom rigid endplate needs to be calculated. Based on homogeneous coordinates, $\mathbf{p}_i = (x_i, y_i, z_i, 1)^{\mathrm{T}}$ denotes a certain point *P* lying on the top endplate in the coordinate system $O_iX_iY_iZ_i$, and

$\mathbf{T}_{ij}$ represents the transformation matrix from coordinate system $O_jX_jY_jZ_j$ to $O_iX_iY_iZ_i$. Thus, the coordinates of the point *P* at time $t = t_1$ and $t = t_2$ can be represented by:

$$\mathbf{p}_3^{(t_1)} = (\mathbf{T}_{23}^{(t_1)})^{-1}\,\mathbf{p}_2^{(t_1)} \tag{7.1}$$

$$\mathbf{p}_3^{(t_2)} = (\mathbf{T}_{23}^{(t_2)})^{-1}\mathbf{p}_2^{(t_2)} \tag{7.2}$$

Considering that the coordinates of the point *P* in the coordinate system of the top endplate ($O_3X_3Y_3Z_3$) stay the same from time $t = t_1$ to $t = t_2$, which means $\mathbf{p}_3^{(t_1)} = \mathbf{p}_3^{(t_2)}$. After substituting Eq. (7.1) and Eq. (7.2), it follows:

$$(\mathbf{T}_{23}^{(t_1)})^{-1}\mathbf{p}_2^{(t_1)} = (\mathbf{T}_{23}^{(t_2)})^{-1}\mathbf{p}_2^{(t_2)}, \text{ and } \mathbf{p}_2^{(t_2)} = \mathbf{T}_{23}^{(t_2)}(\mathbf{T}_{23}^{(t_1)})^{-1}\mathbf{p}_2^{(t_1)} \tag{7.3}$$

Therefore the transformation matrix $\overline{\mathbf{T}}$ from time $t = t_1$ to $t = t_2$ can be expressed as:

$$\overline{\mathbf{T}} = \mathbf{T}_{23}^{(t_2)}(\mathbf{T}_{23}^{(t_1)})^{-1} \tag{7.4}$$

Considering that

$$\mathbf{T}_{23} = (\mathbf{T}_{12})^{-1}\mathbf{T}_{13} \tag{7.5}$$

the transformation matrix $\overline{\mathbf{T}}$ from time $t = t_1$ to $t = t_2$ is finally expressed as:

$$\overline{\mathbf{T}} = (\mathbf{T}_{12}^{(t_2)})^{-1}\mathbf{T}_{13}^{(t_2)}\mathbf{T}_{12}^{(t_1)}(\mathbf{T}_{13}^{(t_1)})^{-1} \tag{7.6}$$

where $\mathbf{T}_{12}$ and $\mathbf{T}_{13}$ are recorded by the optical tracking system at discrete time points. Afterwards, the IHA is obtained based on the method proposed by C. Spoor [188] that calculates the helical axis direction based on $\overline{\mathbf{T}}$ at discrete time points. To facilitate the comparison of different ASD designs, in each DOF five discrete time points with equal time intervals that span from the neutral positon to the maximally loaded position are used for the IHA calculation. Next, the ICOR position is calculated by intersecting the IHA in flexion/extension, left/right LB, and left/right AR with the sagittal plane, the frontal plane, and the transverse plane, respectively.

7.3 Results

This section first shows the 3D printed ASD specimens based on the designs proposed in Fig. 7.1 (Section 7.3.1). Afterwards, the six-DOF angular and compressive responses of the specimens are shown and compared to an IVD and a Charité ASD in Section 7.3.2. In addition, the metrics that measure the *quantity* of motion and the nonlinearity of the load response of the five ASD designs are listed. In the end, Section 7.3.3 shows the IHA and ICOR path of the five ASD designs in six rotational loading cases and compares them to an IVD and a Charité ASD.

7.3.1 3D printed ASD specimens

Five specimens of each ASD design are fabricated and tested to minimize the effect of random errors. The amount of specimens required is determined according to ASTM norm (F2345-18). Examples of the 3D printed specimens of the five ASD designs are shown in Fig. 7.6. With the detailed composition of each ASD design based on three base materials illustrated in Fig. 7.1, the specimens are

manufactured using with the "matte" print option and are printed in a layer-by-layer manner along the Z_c axis of the disc coordinate system (Fig. 7.5.A), and the print head moves along the X_c axis while printing each layer. The support material of the specimens is then removed right after printing using a water jet and the specimens are stored in a dark place for about 24 hours before mechanical testing to minimize the influence of material aging on the specimens' mechanical properties [189].

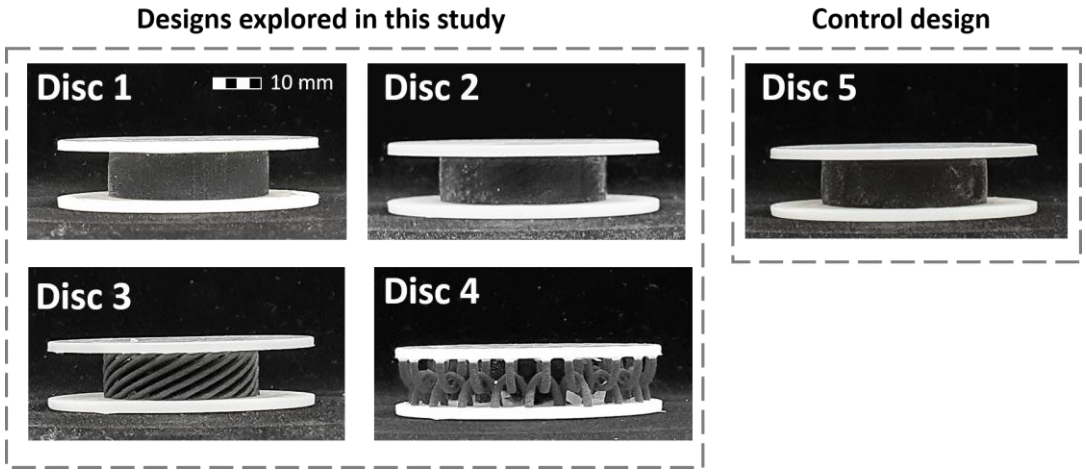

Fig. 7.6. Examples of 3D printed specimens of the five ASD designs. The specimens are manufactured with the "matte" print option. The support material of the specimens is removed right after printing using a water-jet and the specimens are stored in a dark place for about 24 hours before mechanical testing. Five specimens of each ASD design are fabricated for the subsequent mechanical testing.

7.3.2 Angular test and compressive test results

The data analysis procedure of the angular and compressive responses of the specimens is performed using an in-house developed script. Fig. 7.7 shows the angular responses of the five ASD designs and the comparison with an IVD's and a Charité ASD's, while the metrics derived from the angular responses for evaluating the ASD's performance are summarized and compared to an IVD in Fig. 7.8 [125][190]. The compressive stiffness of the five ASD designs at 4% and 8% strain are presented and compared to a human lumbar IVD [191] and a Charité ASD [192] in Fig. 7.9.

7.3.3 Instant helical axis (IHA) and instant center of rotation (ICOR) results

Based on the disc coordinate system shown in Fig. 7.5.A, five IHAs and ICORs are calculated in equally incremental time steps that span from the specimen's neutral position to the maximally loaded position in each rotational DOF. For illustration clarity, Fig. 7.10 and Fig. 7.11 show the 3D isometric views and the representative 2D projected views of one specimen's IHA of the five ASD designs. Besides, Fig. 7.10 provides a comparison of the IHAs of the ASD designs with a Charité ASD's and an IVD's [47][67]. Fig. 7.12 shows the corresponding ICORs of one specimen of each ASD design in six rotational DOFs. The comparison of the ICORs of the ASD designs with an IVD's and a Charité ASD's [193] is also presented in Fig. 7.12.

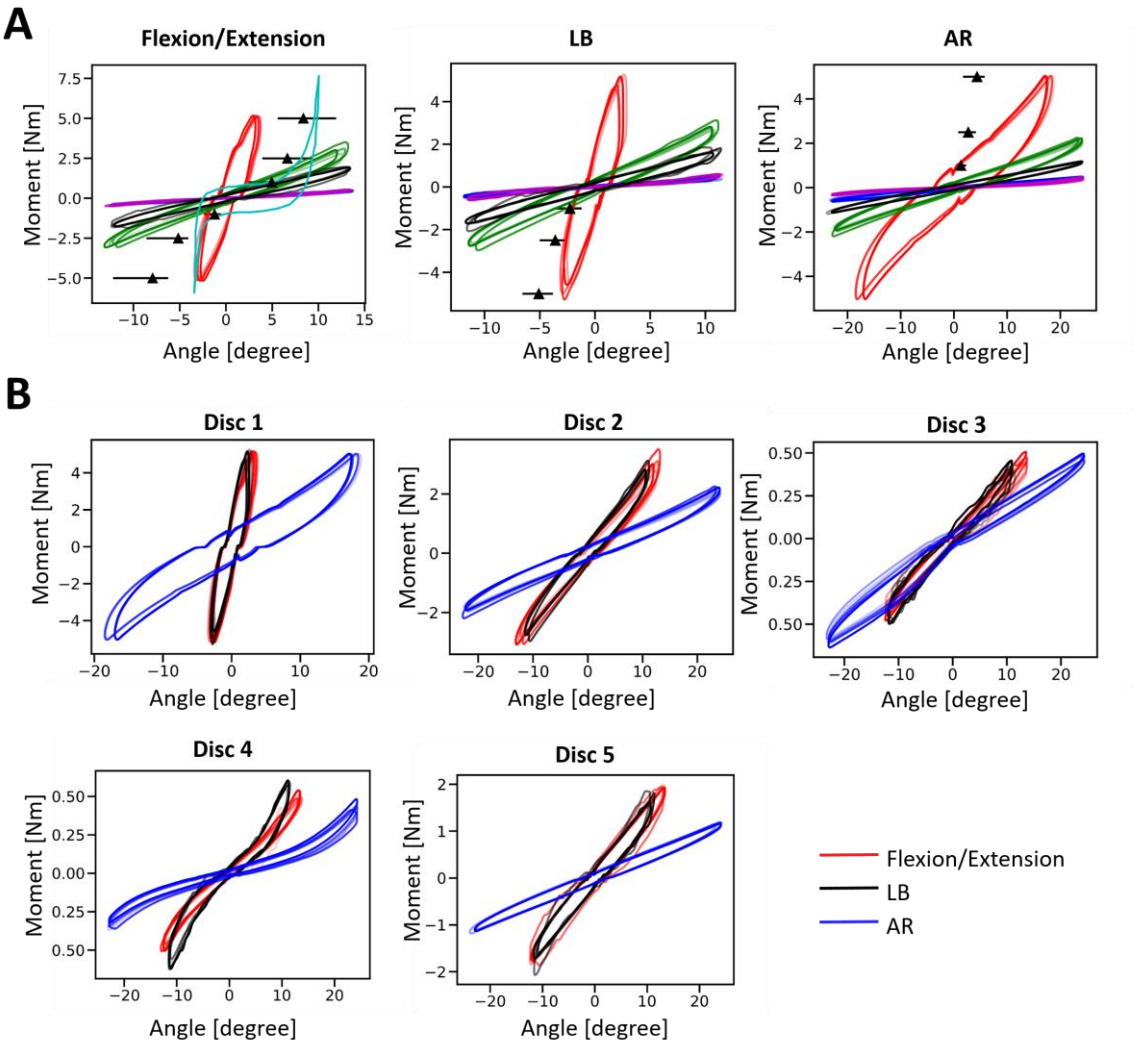

Fig. 7.7. The angular responses of all the specimens of the five ASD designs. The responses of different specimens that belong to the same ASD design are differentiated using different color transparencies. (A) Comparison of the angular responses of the five ASD designs with a human lumbar L4-L5 IVD [125] and a Charité ASD [12]. The IVD angular response is demonstrated using the median, minimum and maximum angle at a given moment. Due to data availability the comparison is not provided for all the loading scenarios. (B) The detailed angular responses of all the specimens of the five ASD designs.

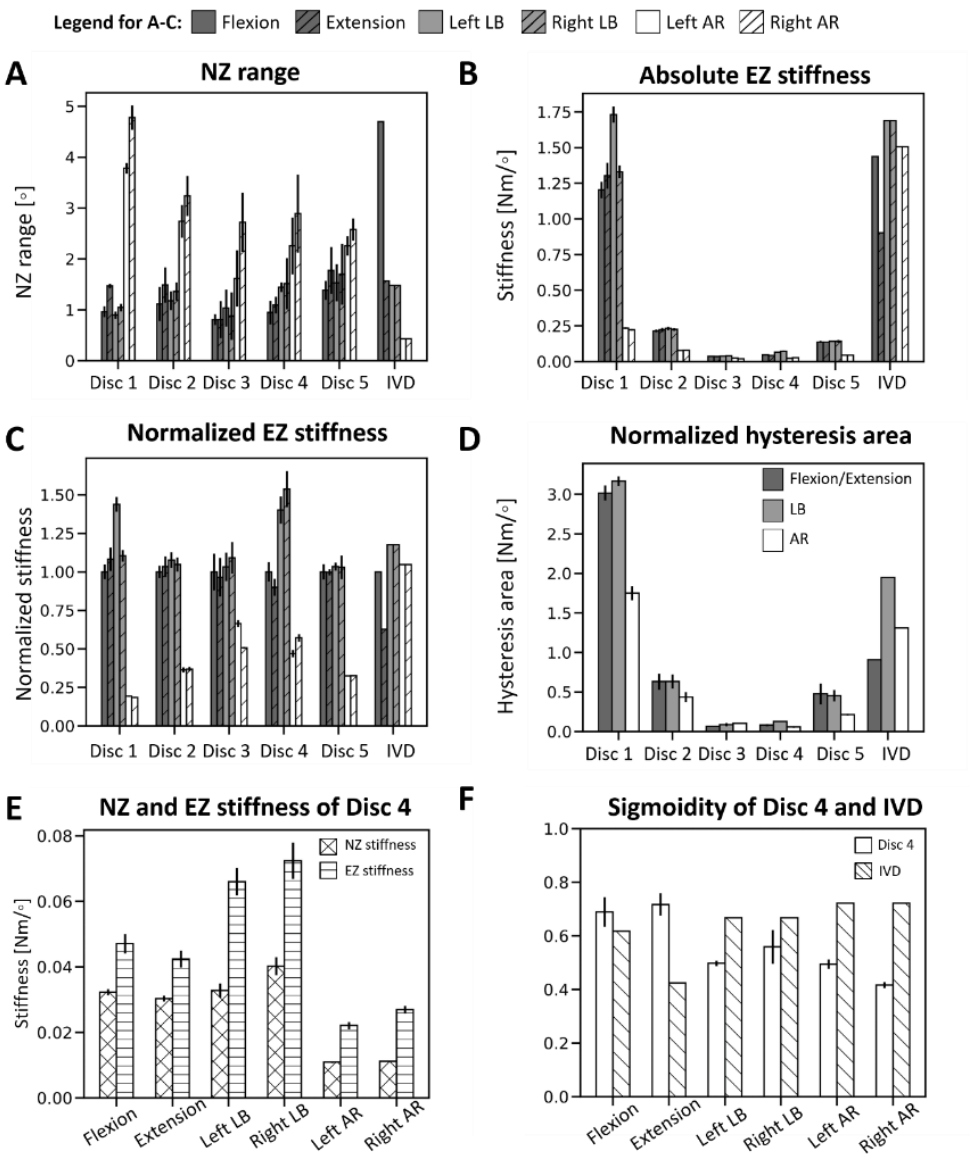

Fig. 7.8. Summary of the metrics for evaluating the performance of the five ASD designs in six rotational loading scenarios. The NZ range, EZ stiffness, and sigmoidity of the IVD are referenced from [125], while the normalized hysteresis area of IVD is referenced from [190].

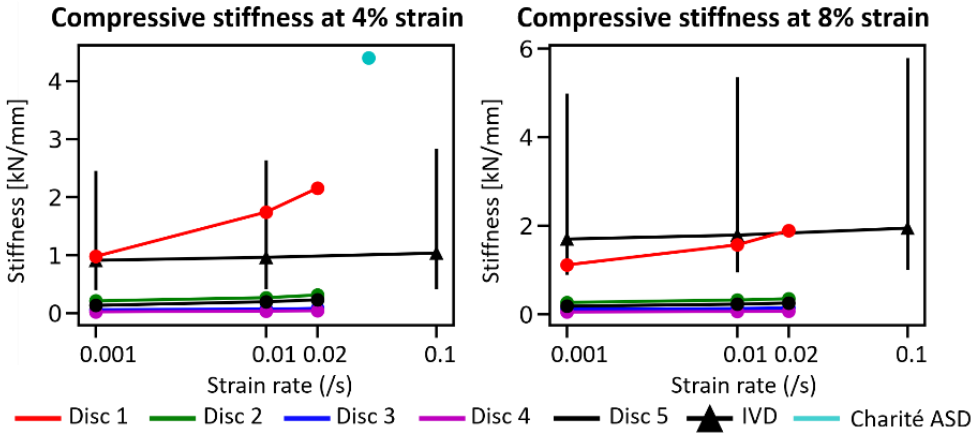

Fig. 7.9. The compressive stiffness of the five ASD designs at 4% and 8% strain. The compressive stiffness of the five ASD designs are compared to a human lumbar IVD [191] and a Charité ASD [192]. The vertical error bars of the IVD stiffness show the minimal and maximal stiffness of an IVD at a certain strain rate based on the findings from the literature [191], while the standard deviation of the compressive stiffness of the five ASD designs are all smaller than 0.05 kN/mm and are thus not shown in the figure.

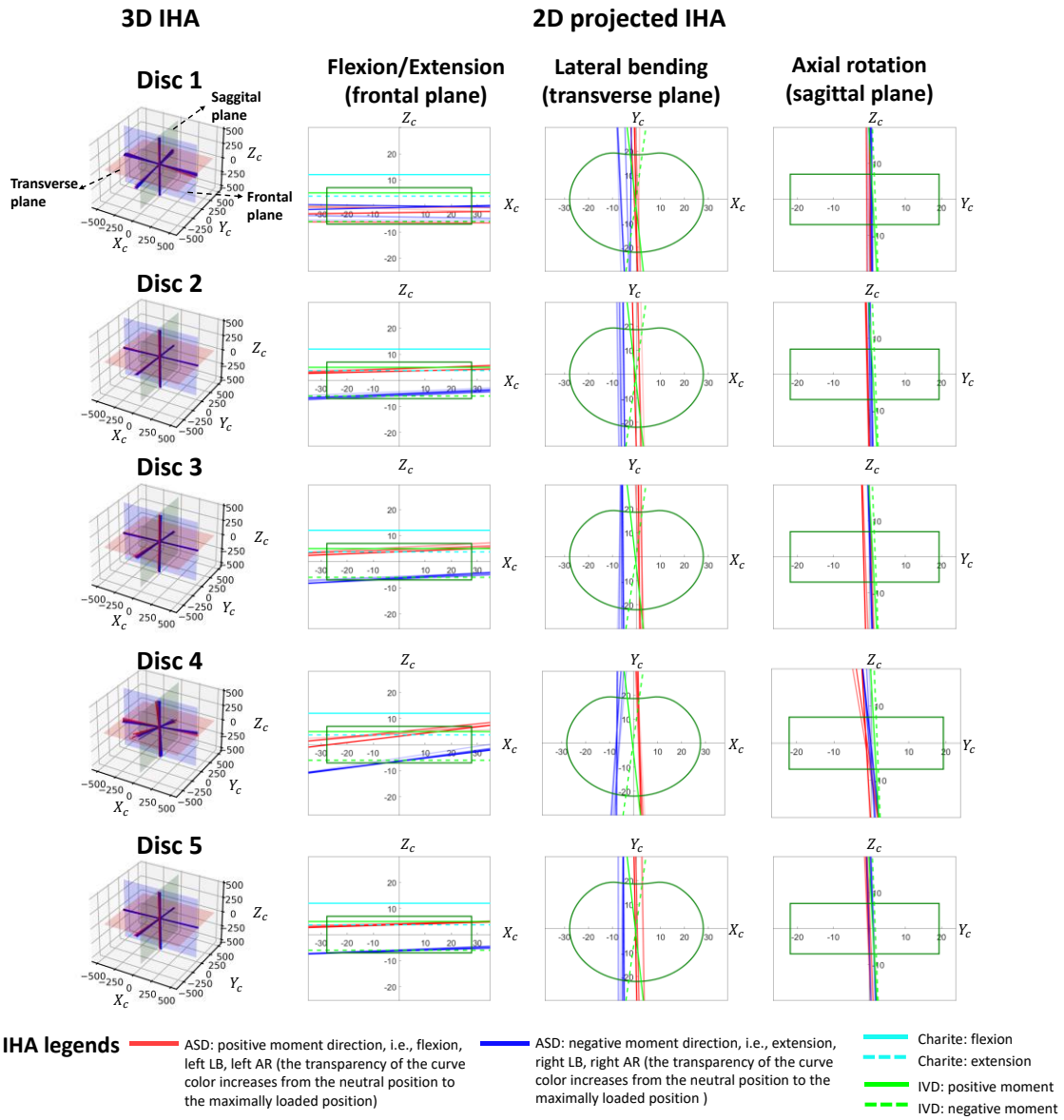

Fig. 7.10. 3D and 2D projected views of the IHAs of the five ASD designs in six rotational loading scenarios. The IHAs of the five specimens belonging to the same ASD design are similar in terms of location and moving direction, therefore for illustration clarity only IHAs of one specimen of each design are shown. In each loading scenario, five IHAs are calculated in equally incremental time steps that span from the neutral position to the maximally loaded position. The first column of the figure shows the 3D isometric views of the IHAs, while the other columns show the representative 2D projected views of the IHAs in flexion/extension, LB, and AR on 3 orthogonal 2D planes, i.e., $X_C Z_C, X_C Y_C, Y_C Z_C$, respectively. The contour of the ASD is illustrated using green solid line, while the IHAs of Charité ASD and IVD are referred from [47][67].

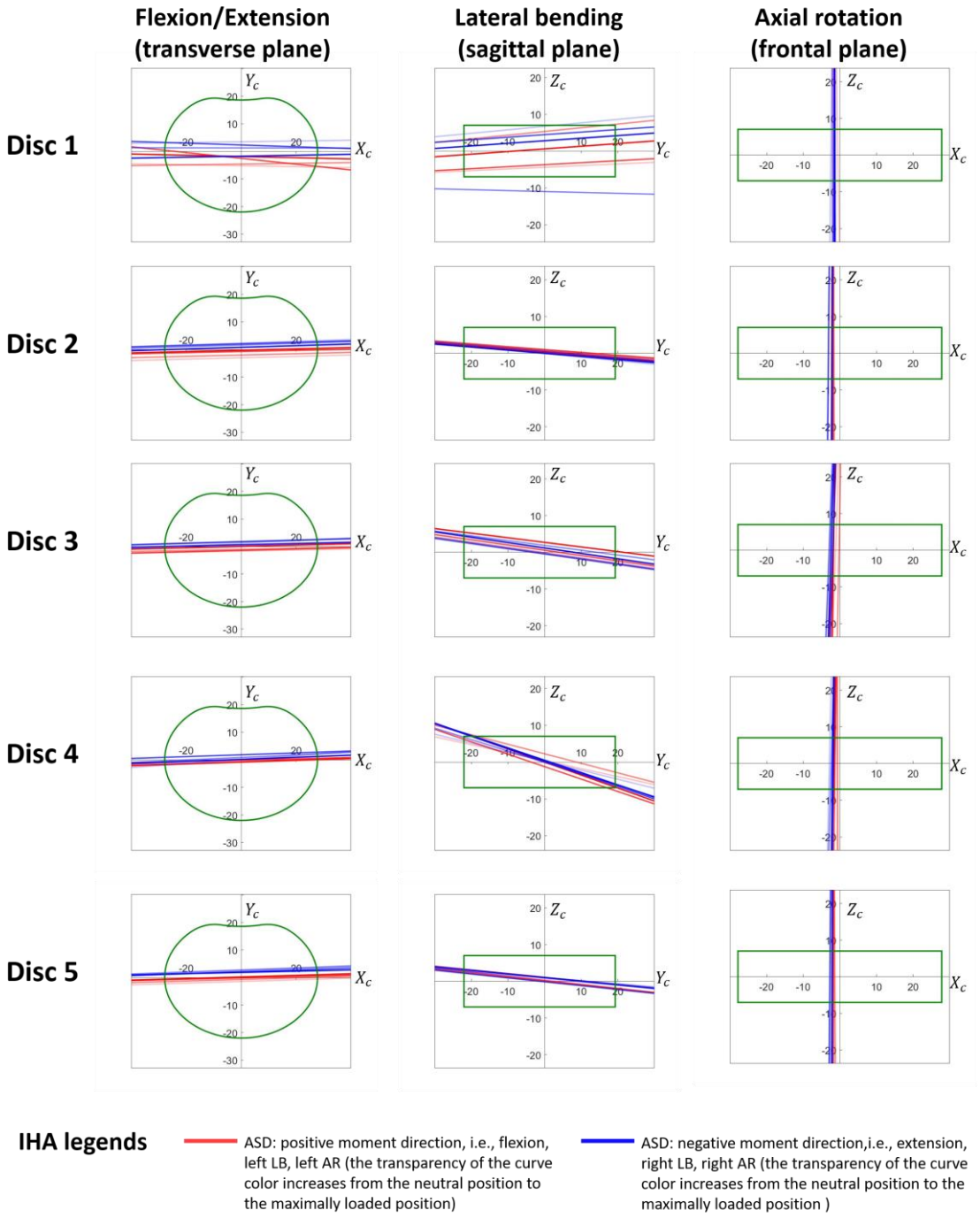

Fig. 7.11. Additional 2D projected views of the 3D IHAs of the five ASD designs in six rotational loading scenarios. Five IHAs are attained in each loading scenario. The contour of the ASD is illustrated in green. For illustration clarity only one IHAs of one specimen of each ASD design is shown.

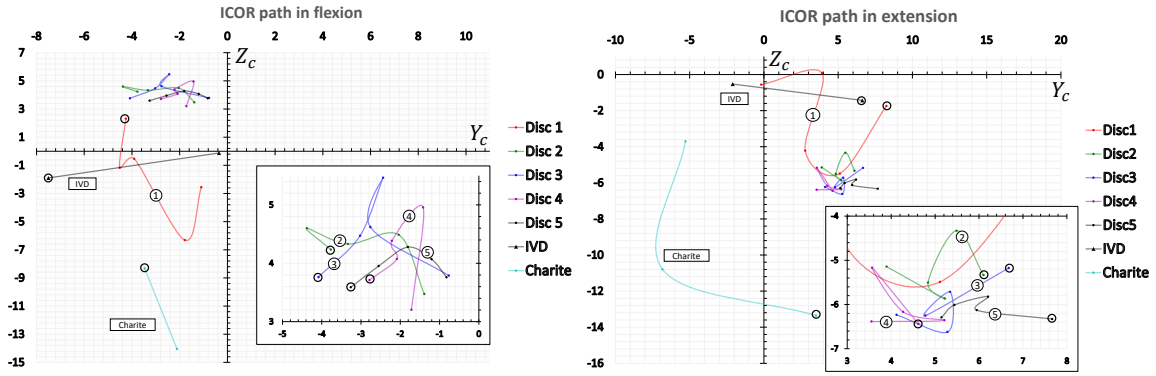

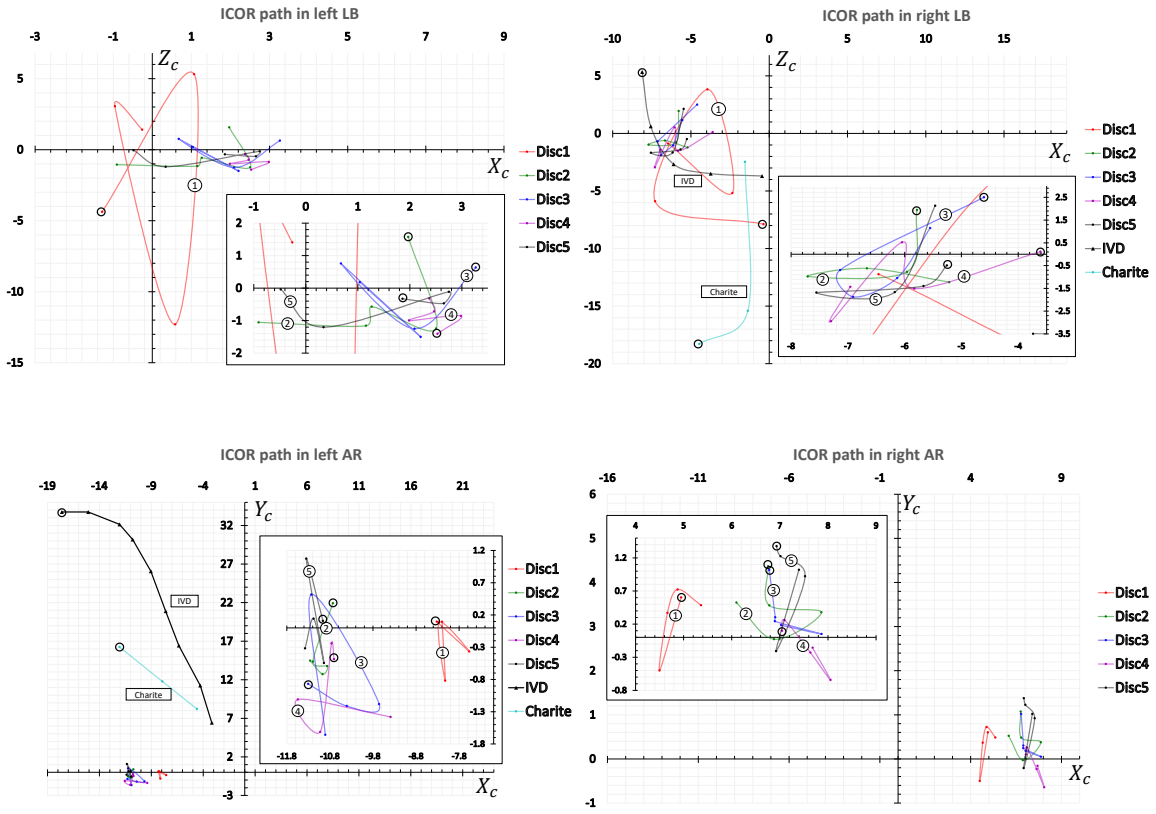

Fig. 7.12. ICOR and its moving path of the five ASD designs in six rotational loading scenarios (unit: mm). The ICOR is calculated by intersecting the IHAs in flexion/extension, LB, and AR with the sagittal plane, the frontal plane, and the transverse plane, respectively. In each loading scenario, five ICORs are calculated in equally incremental time steps that span from the neutral position to the maximally loaded position. For illustration clarity, only ICORs of one specimen of each design is shown. The black circle marks the end point of the ICOR's moving path that is illustrated with a smoothed line that interpolates the ICORs in the time sequence. To increase readability, the insets showing details of the ICOR paths are added to each chart. Due to lack of data from the literature the ICOR paths of the five ASD designs are not compared to an IVD's and a Charité ASD's in all the loading scenarios. The ICORs of the IVD and the Charité ASD are referred from [193].

7.4 Discussion

This section first interprets the results in Section 7.4.1. Next, Section 7.4.2 discusses the limitations of this section. Last, Section 7.4.3 presents the implications of this chapter for the thesis.

7.4.1 Results interpretation

Generally the dimensional standard deviation increases with the decrease of the feature size for the PolyJet 3D printing technique [194]. Based on the disc coordinate system, the relative dimensional standard deviations of the smallest feature of the proposed ASDs fabricated with support materials (i.e., 1.6 mm as shown in

Table ***7.2***) are ~2.29%, ~0.96%, and 1.83% in the X_c, Y_c, and Z_c direction, respectively [194]. The negligible effect of the dimensional deviation on the mechanical responses of the fabricated ASDs is verified by the good agreement of the load responses of the five specimens that belong to the same ASD design shown in Fig. 7.7. The good response agreement also proves the performance repeatability of the 3D fabricated specimens with the given 3D printer. Besides, it is to be noted that layer deposition direction, i.e., the object printing orientation, can influence the mechanical properties of the 3D

fabricated parts [189]. It is shown that the parts fabricated using VW with a longitudinal alignment along the direction vertical to the printing bed have a ~8% lower Young's modulus, a ~40% lower ultimate strength, and a 72% lower total strain at break compared to the parts with a longitudinal alignment along the direction parallel to the printing bed [189]. The variance in mechanical properties among parts fabricated with different orientations is mostly attributed to the layer-by-layer printing process. Additional factors that can contribute to the variance are differences in UV exposure and the number of active nozzles [189]. However, there lacks extensive data from the literature to characterize and model the influence of build orientation on the mechanical properties of parts with respect to all possible build directions and all the materials provided by the printer. Therefore, future studies should follow the same printing orientation used in this chapter for results reproducibility.

The angular responses of all the ASD designs are featured by a hysteresis loop with energy dissipation typical for viscoelastic materials. All the ASD designs except Disc 4 show a mostly linear angular response, which is similar to the behavior of the state-of-the-art viscoelastic ASDs [195]. The nature-mimicking nonlinear angular response of Disc 4 results from the unique shape-changing ability of its chainmail-like structure, which exhibits a lower resistance under small loads when the filaments are loose and a higher resistance under bigger loads when the filaments are strained. All the ASD designs show smooth angular responses and a lower AR stiffness compared to their corresponding stiffness in flexion/extension and LB (Fig. 7.7). In contrast, the Charité ASD is characterized by a negligible load resistance at small rotational angles and a sudden increase in its load resistance when the rotation angle reaches at a certain value. The two motion patterns typical for an IVD and a ball-and-socket ASD are defined as soft and hard load constraints, respectively (Fig. 7.13). All the five ASD designs explored in this chapter differ from Charité ASD by showing a natural, soft constraint. Regarding the compressive response, all the ASD designs are compressible and show a compressive stiffness closer to an IVD compared to the Charité ASD that is incompressible with an unnaturally high compressive stiffness, as shown in Fig. 7.9. Among all the ASD designs, Disc 1 most closely mimics the angular and compressive responses of an IVD in terms of the absolute values.

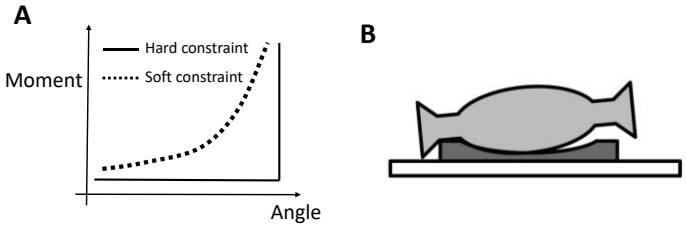

Fig. 7.13. Illustration of the soft and hard load constraint. (A) The soft load constraint (highlighted with a dotted line), which is featured by a gradual or smooth change in load resistance, is a typical motion pattern of an IVD. In contrast, the hard constraint (highlighted with a solid line) that is featured by a sudden load resistance change is a typical motion pattern of ball-and-socket ASD designs such as the Charité ASD. (B) Cause of the hard load constraint exhibited by the ball-and-socket ASD designs. The ASD's core moves freely relatively to the endplates at smaller angles and impinges on the endplate when reaching a certain rotation angle, which results in a motion pattern with a hard constraint.

The NZ ranges of the five ASD designs (Fig. 7.8.A) show a statistically significant difference in left/right AR ($p < .001$). Generally, the NZ ranges of the five ASD designs are close to IVD's in extension and LB, while being higher than IVD's in AR and lower than IVD's in flexion [196].

Nevertheless, the five ASD designs show more similar NZ ranges to an IVD compared to spinal fusion with much lower NZ ranges [197] and TDR using a Charité ASD with much higher NZ ranges [12]. An abnormal laxity/flexibility around the neutral position can lead to an unnatural load distribution within the other spinal components and may lead to pain [19]. EZ stiffness comparison shown in Fig. 7.8.B and Fig. 7.8.C provides insights into the effect of biomimetic design strategy on the ASD's anisotropic performance, while the normalized EZ stiffness (Fig. 7.8.C) facilitates the comparison by allowing the EZ stiffness of different designs to be at the same scale. The design concept of Disc 1 allows to realize bending and compressive stiffness comparable to those of an IVD, while lacking the ability to restore the natural torsional stiffness. According to Fig. 7.8.C, Disc 1 exhibits a ~42% reduction in its relative AR stiffness compared to Disc 5, implying that the stiffer outer layer disproportionally contributes to improving the bending and torsional stiffness. Compared to Disc 5, the introduction of a fiber-like structure (Disc 2 and Disc 3) and a chainmail-like structure (Disc 4) improves the ASD's relative AR stiffness by ~13%, ~80 %, and ~60 %, respectively. This shows that mimicking the IVD's material stiffness gradient is insufficient to restore the natural anisotropic behavior, while mimicking the IVD's structure (Discs 2-4) has greater potential for natural mechanics restoration. The normalized hysteresis areas of the five ASD designs (Fig. 7.8.D) show statistically significant differences ($p < .001$) in all the rotational loading scenarios and are correlated with the EZ stiffness, which matches the findings from the literature [198]. Disc 4 shows a pronounced nonlinear trend in its angular load response with distinct NZ and EZ (Fig. 7.8.E). Besides, the sigmoidity of Disc 4 in six loading scenarios is comparable to that of IVD (Fig. 7.8.F). The superior performance of Disc 4 again demonstrates the great potential of incorporating mechanical metamaterial inspired structures into the ASD design.

Fig. 7.10 and Fig. 7.11 show that the IHAs of the five ASD designs are mostly located near the origin of the disc coordinate system in all the loading scenarios and are mainly parallel to the X_c, Y_c, and Z_c axis in flexion/extension, LB, and AR, respectively. In addition, the IHAs of the five ASD designs are more similar to an IVD's compared to Charité ASD's regarding their location and orientation (Fig. 7.10). Furthermore, the five ASD designs (Fig. 7.12) show more comparable ICORs to an IVD compared to the Charité ASD regarding the ICOR's location and moving direction in flexion/extension and left/right LB. Particularly, the ICOR moves more anteriorly in flexion, more posteriorly in extension, and more cranially in LB. The ICORs of the Charité ASD generally show a bigger location variance [63]. The location deviation of the torsional ICORs of the five ASDs from IVD's is mostly due to the lack of facet joint that has been shown to have a significant role in torsion [193][199]. The ICOR paths of the IVD and Charité ASD are interpolated based on three discrete ICORs with discrete load magnitudes and an interval of ~3 Nm [193], which explains the path's smoothness compared to the ICOR path of the five ASD designs.

7.4.2 Limitations

First, the methodology is based on the assumption of a perfect fixation at the interface between the vertebrae and the ASD, while in practice the fixation strength at the implant-vertebrae interface is dependent on the bone-ingrowth level [200]. The difference in fixation strength can significantly influence the kinematics of the implanted spinal segment. Second, this chapter does not consider the effect of other spinal components, such as the facet joint that is shown to have a significant influence on the spinal segment's torsional behavior [201]. Third, considering the high individual-level variation of IVD's mechanics, such as the EZ stiffness [76] and the IHA [47], the metrics of the IVD only provide a relative comparison. Last, this chapter only focuses on the static load responses of the ASD, while the dynamic responses are not considered in this chapter.

7.4.3. Implications for the thesis

Through *in vitro* mechanical testing of the biomimetic ASD designs proposed in the previous chapters and performance comparison, this chapter provides answer to RQ2 and decides on the favorable ASD design concept for developing patient-specific ASD solutions. Results show that all the four biomimetic ASD designs show a lower torsional stiffness compared to its stiffness in other loadings scenarios, which implies the importance of incorporating a torsional reinforcement structure. Discs 1-4 employ different strategies to compensate for the low torsional resistance: Disc 1 employs a solid stiff outer layer, while Disc 2 and Disc 3 use a criss-cross fiber-like structure and Disc 4 uses a separated chainmail-like structure. Although the solid stiff outer layer in Disc 1 increases the absolute value of torsional stiffness, it lowers the normalized torsional stiffness compared to the stiffness in other loading scenarios, which implies conflicting objectives in multi-objective optimization as the stiff outer layer is involved in multiple loading scenarios. This again shows the importance of introducing a decoupling strategy in the ASD design. In comparison, Discs 2-4 involve structures that disproportionally contribute to the ASD's response in different loading scenarios, which helps to tackle the challenge of the conflicting multi-objective optimization.

7.5 Conclusion

This chapter systematically investigates and compares the performance of four biomimetic, multi-material ASD designs proposed in the previous chapters through mechanical testing to explore the influence of using multi-material AM and biomimicry on the performance of ASD design. The ASD's performance is evaluated in terms of restoring the unique viscoelastic, nonlinear, and anisotropic behavior of an IVD. All of the four ASD designs show a viscoelastic behavior with nature-mimicking mobile IHA and ICOR, while Disc 4 with a chainmail-like structure exhibits a distinct nature-mimicking nonlinear angular response. Besides, results show that biomimicry based on mimicking the IVD's structure has greater potential compared to mimicking the IVD's stiffness gradient alone to restore the natural anisotropic behavior, as the incorporation of a structure that mimics the IVD's structure helps partially decouple the multi-objective optimization problem formulated in ASD design. The

abovementioned results provide answer to RQ2 regarding the favorable ASD design concept for developing patient-specific ASD solutions in the next chapter. In addition, this chapter proves that multi-material AM is a good candidate technology for the design and fabrication of multi-material ASD.

Chapter 8. Design of a patient-specific, chainmail-based, multi-material ASD

8.1 Summary

The mechanical test results shown in Chapter 7 experimentally verify the potential of a chainmail-based ASD to reproduce nonlinear rotational load response of an IVD. Furthermore, Chapter 6 computationally verifies that through a material optimization, the chainmail-based ASD is able to reproduce the rotational stiffness of an IVD. The good stiffness match with an IVD is mostly attributed to the negligible compressive stiffness of the chainmail-like structure that partially decouples the formulated multi-objective optimization problem. Additionally, performance comparison of the chainmail-based ASD with other ASD designs (Table 7.1) shows that the chainmail-based ASD has additional benefit of saving the efforts of modeling the complex anisotropic material behavior [173]. This is realized by using a connector whose tensile behavior is measured through uniaxial tensile tests of the chainmail unit cell, which helps to improve the modeling accuracy. The application of a connector model also helps to realize an efficient computational design process by avoiding the time-consuming contact modeling between the rings in individual chainmail unit cells.

Inspired by the benefits of a chainmail-based ASD, this chapter develops a patient-specific ASD solution based on the chainmail-based ASD design concept to reproduce the IVD's nonlinear, anisotropic behavior in seven loading scenarios: compression, flexion/extension, left/right LB, and left/right AR. To design a feasible ASD for fabrication, the overall design process takes into account the manufacturing constraints imposed by the given 3D printer, i.e., the minimum allowable feature size for reliable mechanical properties and the limited options of base materials. Results show that the computational model exhibits a higher prediction accuracy for chainmail-based ASD designs with chainmail-like structures made from flexible materials. In addition, the chainmail-based ASD has great potential to restore patient-specific anisotropy despite limited base materials. This chapter has two main contributions:

- A systematic analysis is performed to explore how different design parameters in a chainmail-based ASD design concept influence the ASD's load response that is evaluated using different metrics.
- The model of the chainmail-based ASD is validated by comparing the load responses of the chainmail-based ASD measured through *in vitro* mechanical tests and those calculated by computational models.

8.2 Methods

This section first introduces the design concept of the chainmail-based ASD in Section 8.2.1. The mechanism of how different components and the corresponding design parameters control the load responses of the chainmail-based ASD is also introduced in this section. Next, the computational modeling procedure of the chainmail-based ASD is explained in Section 8.2.2. The procedure for

validating the proposed computational model is stated in Section 8.2.3. The detailed approach of using material optimization to restore patient-specific anisotropy is explained in Section 8.2.4.

8.2.1. Design concept

As illustrated in Fig. 8.1, the chainmail-based ASD explored in this chapter is comparable to that proposed in Chapter 6 but differs in two aspects: 1) the chainmail unit cell is composed of two half-elliptical rings, and 2) both the central cylinder and the chainmail-like structure are fixed to the two rigid endplates. The functions of different functional components in the ASD are summarized in Table 8.1. Four metrics are introduced to quantify the ASD's load response: compressive stiffness in compression together with NZ stiffness, EZ stiffness, and NZ range in rotational loading scenarios.

Due to the negligible compressive stiffness of the chainmail-like structure, the central cylinder is the only contributor to the ASD's compressive load response, while both the central cylinder and the chainmail-like structure contribute to ASD's rotational response. Therefore, as illustrated in Fig. 8.2, the rotational response of the ASD is a superposition of the responses of the central cylinder, i.e., the artificial NP, and the chainmail-like structure, i.e., the artificial AF. Whereas the response of the artificial NP is mostly linear due to its monolithic solid design, the response of the artificial AF is featured by a nonlinear trend. The angle at which the filaments in the chainmail-like structure start to bear load is defined as the *activation point* of the artificial AF. Such unique mechanism of the chainmail-like structure contributes to the ASD's nature-mimicking nonlinear rotational load response. During the whole ROM in rotation, the artificial NP contributes to the ASD's response in both NZ and EZ, while the artificial AF only contributes to the ASD's response in EZ beyond the activation point, i.e., after the filaments are strained and start to bear load.

Table 8.2 summarizes how different components in the chainmail-based ASD affect the metrics that quantify the ASD's load responses, together with possible strategies to adjust the ASD's load responses to meet patient-specific mechanics requirements. Specifically, the compressive stiffness and NZ stiffness are only influenced by the artificial NP and can be adjusted by varying its material composition. The EZ stiffness in rotation is influenced by both the artificial NP and the artificial AF and can be adjusted by varying the material composition of either the artificial NP or the artificial AF. The NZ range is controlled by the angle at the *activation point* of the artificial AF and can be adjusted by either changing the initial distance or the shape of the rings in the artificial AF. It is to be noted that the control of the metrics is not totally decoupled with the given ASD design concept, as varying the material composition of the artificial NP simultaneously changes ASD's NZ stiffness and compressive stiffness. An alternative design would be to detach the artificial NP from the two endplates as proposed in Chapter 6. However, the tight fixation between the artificial NP and the endplates provides more stability, while the artificial NP will contribute to the NZ stiffness. Therefore, the ASD design explored in this chapter employs a design concept of attaching the artificial NP to the two endplates.

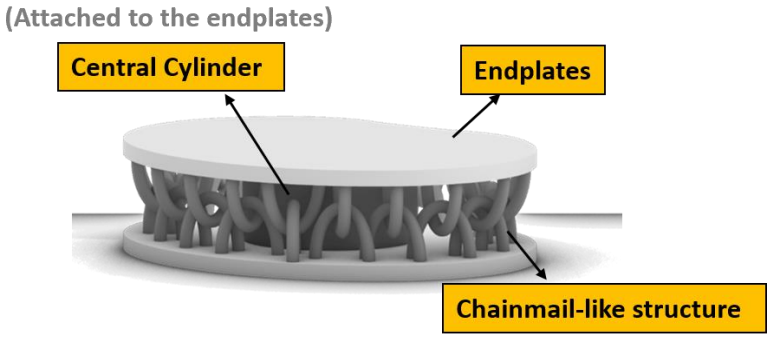

Fig. 8.1. The conceptual design of the chainmail-based ASD. The ASD is composed of two rigid endplates with a matching size and shape to the adjacent vertebrae, a central cylinder that works as an artificial NP to mainly provide support for compressive load, and a chainmail-like structure that works as an artificial AF to mainly provide support for rotational loads.

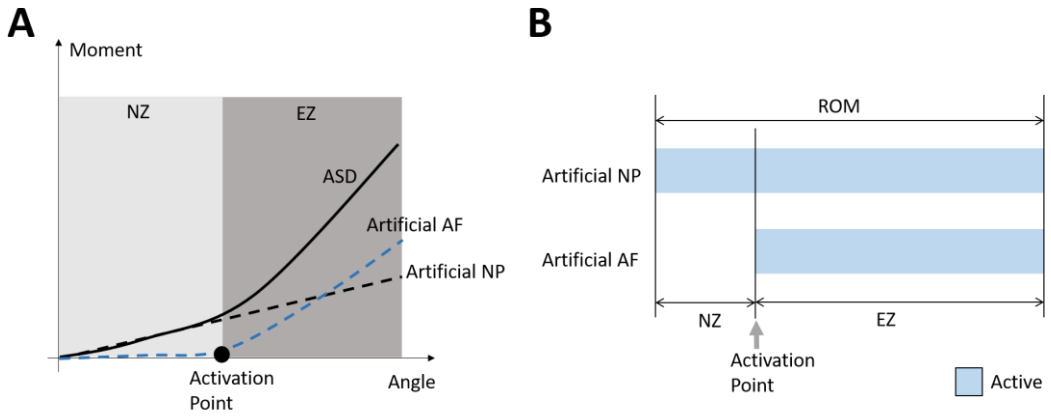

Fig. 8.2. Illustration of the mechanism of the chainmail-based ASD's rotational load response. (A) The rotational load response is featured by an initial NZ and a subsequent EZ. The response of the ASD is a superposition of the load responses of the artificial NP and the artificial AF. Whereas the response of the artificial NP is mostly linear due to its monolithic solid design, the response of the artificial AF is featured by a nonlinear trend. The critical angle where the filaments start to resist load in the artificial AF is defined as the *activation point*. (B) In the whole ROM, the artificial NP contributes to the ASD's response in NZ and EZ, while the artificial AF only contributes to ASD's response in EZ after reaching the activation point, i.e., after the filaments are strained and start to bear load. The active state of the components are represented using blue bars.

Table 8.1. The components in the chainmail-based ASD and their functions.

Components	Function
Endplates	Interface with adjacent vertebrae to homogenize the stress distribution at bone-implant interfaces
Central cylinder: artificial NP	Mainly provide support for compressive loads
Chainmail-like structure: artificial AF	Mainly provide support for rotational loads

Table 8.2. The metrics and the corresponding responsible components in the ASD design.

Metrics	Responsible components	Possible strategy for personalization
Compressive stiffness	Central cylinder	Adjusting the material of the central cylinder
NZ stiffness (rotation)	Central cylinder	Adjusting the material of the central cylinder
EZ stiffness (rotation)	Central cylinder + Chainmail-like structure	Adjusting the material of either the central cylinder or the chainmail-like structure
NZ range (rotation)	Chainmail-like structure	Either adjusting the distance or the shape of the rings in the chainmail-like structure

8.2.2 Computational model build

This section explains the detailed procedure for modeling the chainmail-based ASD to calculate its responses in seven loadings scenarios. As illustrated in Fig. 8.3, three components of the chainmail-based ASD are modeled separately using two models. One model referred to as the solid model involving the endplates and the central cylinder is built in ABAQUS, while the other model referred to

as the connector model involving the chainmail-like structure is built in Matlab following the procedure in Chapter 6. The rational to build two separate models is the independent contributions of the artificial NP and the artificial AF to the ASD's response. Besides, the MATLAB-implemented algorithm reduces the computational time significantly compared to that implemented in ABAQUS. The compressive response of the solid model is considered as that of the ASD, while the joint rotational responses of the solid model and the connector model are considered as that of the ASD.

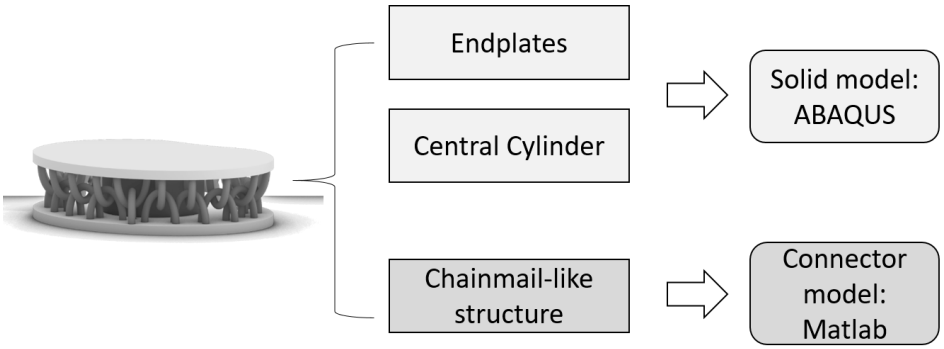

Fig. 8.3. Computational model of the chainmail-based ASD. The chainmail-based ASD is modeled separately using two models. One model referred to as the solid model involving the endplates and the central cylinder is built in ABAQUS, while the other model referred to as the connector model involving the chainmail-like structure is built in MATLAB.

8.2.3 Computational model validation

To validate the computational model, this section fabricates and tests the chainmail-based ASD in seven loading scenarios through in-vitro mechanical tests. The responses of the ASD measured through mechanical tests are then compared with those calculated by the computational model. Two representative chainmail-based ASD designs are fabricated: a flexible-chain ASD whose chainmail-like structure is made from flexible base material, and a rigid-chain ASD whose chainmail-like structure is made from rigid base material. The materials used for fabricating the two ASD designs are summarized in Table 8.3. The specimens are tested following the same test setup and test data analysis procedure described in Chapter 7. It is to be noted that for the mechanical test of the rigid-chain ASD, the test range in each loading scenario is limited to a relatively small angle to avoid material failure.

Table 8.3. Materials composition of the two ASD designs for model validation.

ASD type	Endplate	Central cylinder	Chainmail-like structure
Flexible-chain ASD	VW	Agilus	FLX9895
Rigid-chain ASD	VW	FLX9895	VW

8.2.4 Material optimization

Given the validated computational model, this section optimizes the material distribution in the ASD to restore the IVD's anisotropic stiffnesses, namely the compressive stiffness and the six rotational stiffnesses. The rotational stiffness of the ASD is calculated by dividing the maximum reaction moment by the maximum rotational angle, i.e., ROM. The design variable is defined as the constituent materials of the central cylinder and the individual chainmail unit cells in the chainmail-like structure. Given N chainmail unit cells in the chainmail-like structure, the optimization problem is formulated as:

$$\min f(\mathbf{x}) = \sum_{i=1}^{7} (S_i(\mathbf{x}) - S_i'(\mathbf{x}))^2$$
$$i = \text{loading case } \{1, \dots, 7\} \text{ denoting compression, flexion/extension, left/right LB, and left/right AR, respectively,} \tag{8.1}$$

where $\mathbf{x}$ with a dimension of $N + 1$ represents the material constituents of each unit cell in the chainmail-like structure and the central cylinder, S_i and S_i' represent the stiffness of the chainmail-based ASD and the IVD, respectively. Given m base materials, each element in design variable $\mathbf{x}$ can be assigned an integer whose value lies in between one and m. The optimization setup is same as in Chapter 6.

8.3 Results

This section first shows the tensile test results of chainmail unit cells made from fourteen base materials in Section 8.3.1. Next, Section 8.3.2 shows the solid model and the connector model to calculate the responses of the chainmail-based ASD. Section 8.3.3 then presents the mechanical test results of two representative ASD designs, as well as the comparison of the two ASDs' responses calculated using the computational model with those measured through mechanical tests. Finally, Section 8.3.4 shows the optimized stiffnesses and the corresponding optimized material distribution of the ASD for restoring the anisotropic stiffnesses of two IVDs: a human lumbar L2-L3 IVD, and a human L4-L5 IVD.

8.3.1 Tensile test results of the chainmail unit cells

This section shows the technical drawing of the chainmail unit cell, the tensile test setup, and the tensile responses of fourteen chainmail unit cells. As shown in Fig. 8.4, the major and minor axis of the diameter of the rings in a chainmail unit cell are set as 12 mm and 7 mm, respectively. The diameter of the rings is determined to allow the chainmail unit cell to fit into the height of the ASD design space while allowing for a gap between the two rings to facilitate support material removal. The filament diameter of the rings is set as 1.6 mm to meet the minimum allowable feature size with reliable mechanical properties of the given 3D printing technique. To avoid overlap during the printing, the two rings are oriented at an angle of 45° relative to each other. The printing bed overlaps with the x-y plane in Fig. 8.4, and the printing head moves along x-axis when printing each layer. Based on the fourteen base material provided by the given 3D printing technique, a total of fourteen types of chainmail unit cells are fabricated and tested. The average tensile force-displacement response of three specimens is considered as the tensile load response of the corresponding chainmail unit cell type. Fig. 8.5 shows the tensile test setup for the chainmail unit cells. The two rings of the chainmail unit cells made from flexible materials are parallel to each other, whereas the two rings of the chainmail unit cell made from the rigid materials are perpendicular to each other. The test rate is set as 10 mm/min to measure the static responses of the unit cells. Fig. 8.6 shows the final average force-displacement response of the fourteen types of chainmail unit cells. For the chainmail unit cells made from rigid materials, an experience-

based force threshold of 8 N is used for defining the test starting point during the data analysis, i.e., when the rings start to come into contact.

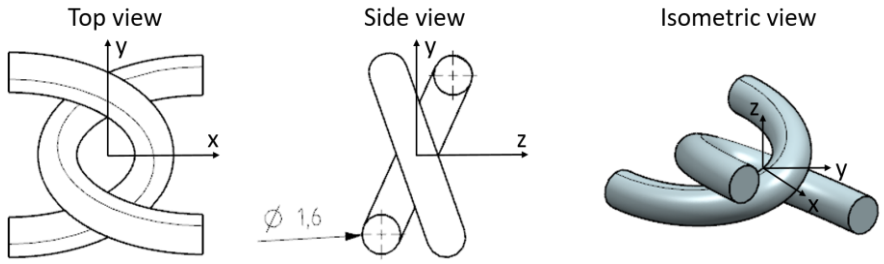

Fig. 8.4. Technical drawing of a chainmail unit cell. The major and minor axis of the rings diameter are 12 mm and 7 mm, respectively, while the filament diameter of the rings is 1.6 mm. To avoid overlap during the printing, the two rings are oriented at an angle of 45° relative to each other. The printing bed overlaps with the x-y plane, while the printing head moves along x-axis when printing each layer.

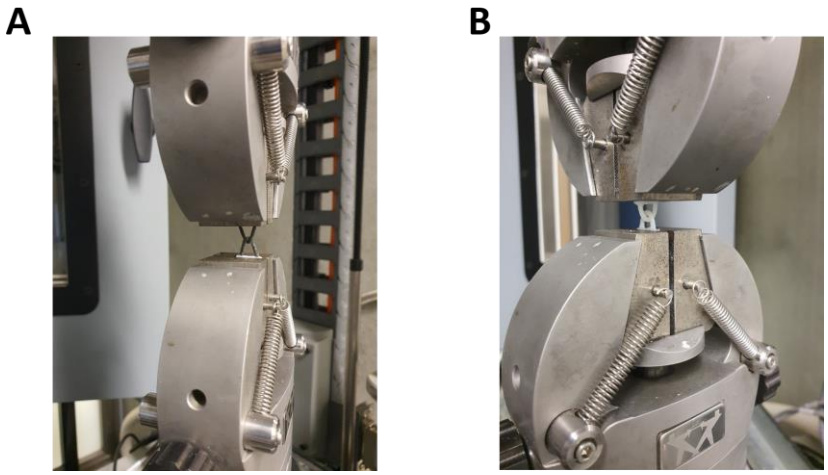

Fig. 8.5. Tensile test setup for the flexible (A) and rigid (B) chainmail unit cells. The two rings of the chainmail unit cell made from flexible materials are initially parallel to each other, whereas the two rings of the chainmail unit cell made from rigid materials are initially perpendicular to each other .

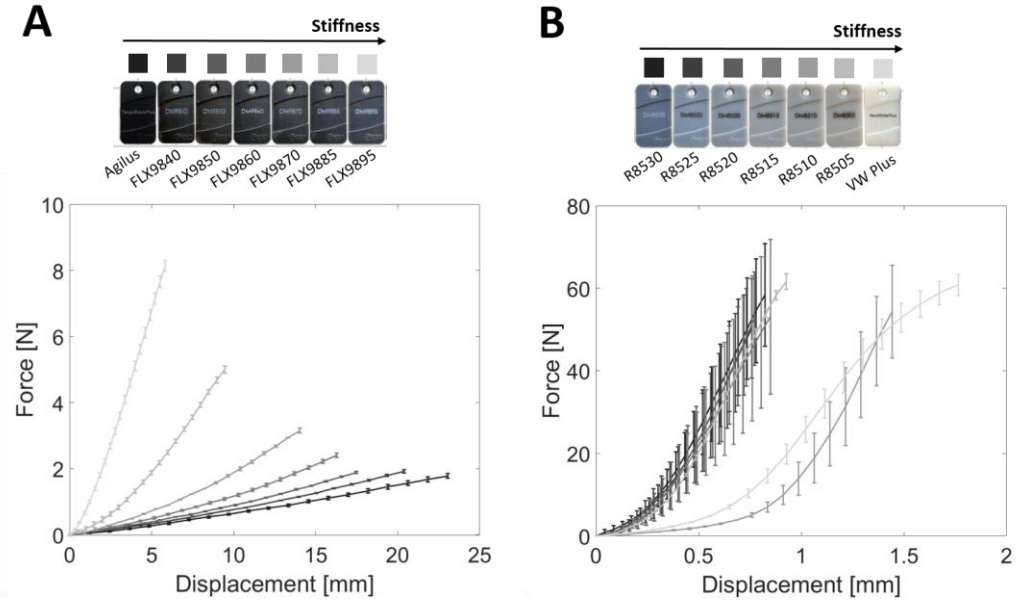

Fig. 8.6. The average tensile force-displacement responses of the fourteen types of chainmail unit cells. The figure shows the average response of the three specimens that belong to the same chainmail unit cell type, with the error bars indicating the standard deviation of the reaction force at a certain displacement of the three specimens. For the chainmail unit cells made from rigid materials, an experience-based force threshold of 8 N is used for defining the test starting point, i.e., when the rings start to come into contact.

8.3.2 Computational model

The computational model is build based on the procedure stated in Section 8.2.2. The solid model of the endplates and the central cylinder meshed using solid elements is shown in Fig. 8.7.A. The mesh density is determined using a mesh convergence analysis to ensure that the model's response only has minor improvement with a further mesh refinement. A conformal mesh is generated at the interfaces between the endplates and the artificial NP where their meshes share the same nodes to model a rigid connection between those two parts without relative movements. Besides, the chainmail-like structure is modeled using a series of connectors, as illustrated in Fig. 8.7.B. Each chainmail unit cell in the chainmail-like structure can be assigned a certain base material among the fourteen materials provided by the given 3D printing technique. The response calculation of the chainmail-like structure follows the same procedure as in Chapter 6. Both models have the same boundary condition as stated in Chapter 3.

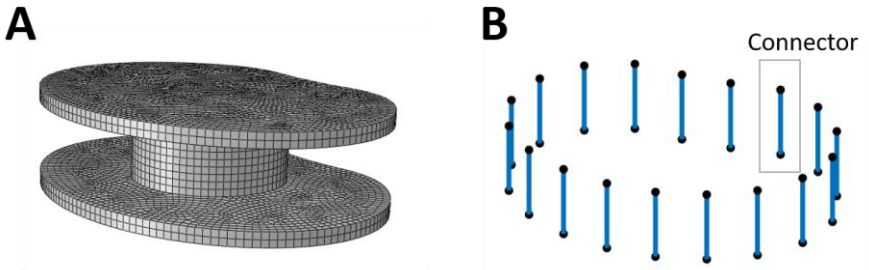

Fig. 8.7. Models of the chainmail-based ASD. (A) The solid model involves the top/bottom endplates and the artificial NP. The mesh density is determined using a mesh convergence analysis to ensure that the model's response only has minor improvement with a further refinement of the mesh. A conformal mesh is generated at the interfaces between the endplates and the artificial NP where their meshes share the same nodes to model a rigid connection between those two parts without relative movements. (B) The chainmail-like structure is modeled as a series of connector. Each connector can be assigned a certain base material among the fourteen materials provided by the given 3D printing technique. Therefore, each connector is assigned the uniaxial tensile response of the corresponding chainmail unit cell with the same base material.

8.3.3 Computational model validation

The following sections first show the responses of the two representative ASD designs measured through mechanical tests. Next, the responses of the two ASD designs calculated using the computational model are presented. Lastly, the responses measured through mechanical tests and calculated using the computational model are compared for model validation.

Mechanical test results

For each chainmail-based ASD design, three specimens are fabricated and tested. The dimensions of the ASD that equal to the average size of a human lumbar IVD are given in Chapter 7. For the data analysis of the compressive responses, the starting point is set as when the force-displacement curve starts to exhibit a mostly linear trend to avoid the influence of uneven endplates due to manufacturing imperfection. The data analysis of the rotational results follows the same procedure as presented in Chapter 7. Fig. 8.8 shows examples of the 3D printed ASD specimens and their representative responses measured from mechanical tests.

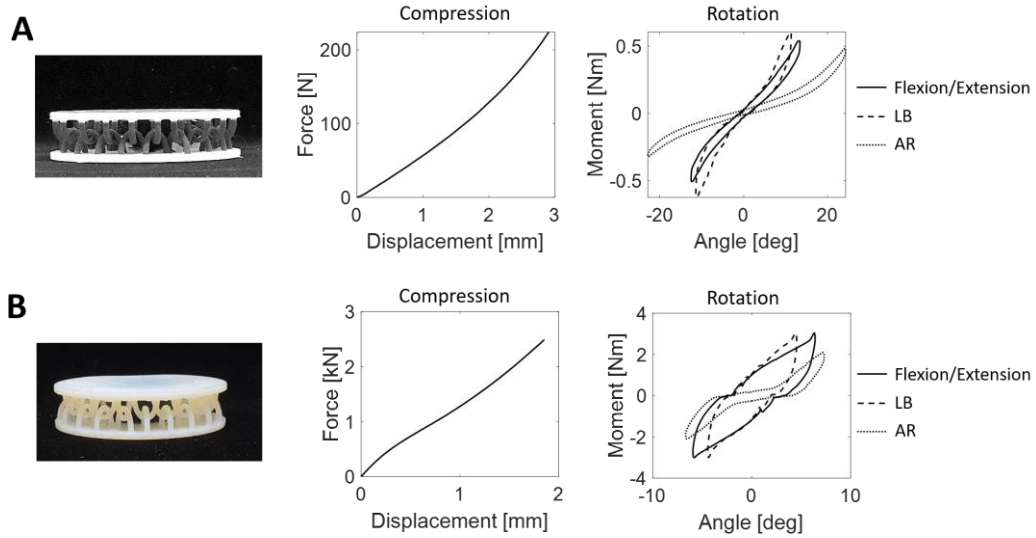

Fig. 8.8. Representative load responses of the flexible-chain ASD (A) and rigid-chain ASD (B) in seven loading scenarios. The first column shows the specimen of the ASD design, while the 2nd and 3rd column shows the compressive responses that only include load test and rotational responses that include load-unload tests of the corresponding ASD design.

Computational model results

To explore the influence of the material model, the compressive responses of the solid model using different material models are compared in Fig. 8.9. For the linear elastic material model, the Young's moduli of the base material Agilus, FLX9895, and VW are set as 0.638 MPa, 14 MPa, and 2618 MPa, respectively. For the hyperelastic material model, a Yeoh model [202] is used for modeling the behavior of Agilus, while a Marlow model [203] and an Arruda-Boyce model [204] are used for modeling the behavior of FLX9895 and VW, respectively.

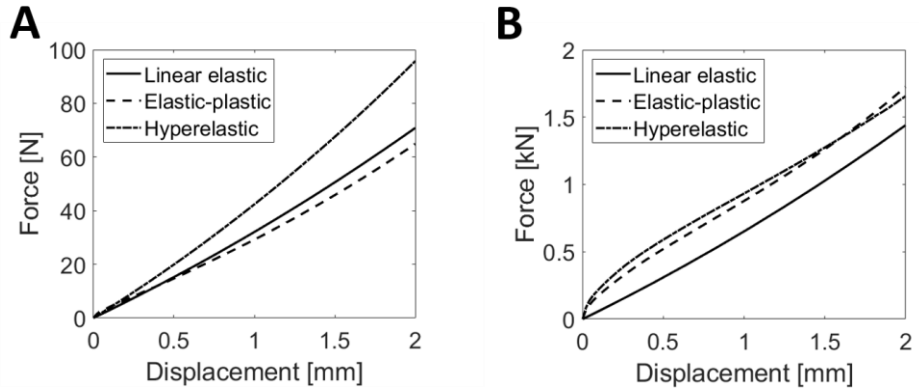

Fig. 8.9. Compressive responses of the flexible-chain ASD (A) and the rigid-chain ASD (B) based on different material models. For the linear elastic material model, the Young's moduli of the base material Agilus, FLX9895, and VW are set as 0.638 MPa, 14 MPa, and 2618 MPa, respectively. For the hyperelastic material model, a Yeoh model is used for modeling the behavior of Agilus, while a Marlow model and an Arruda-Boyce model are used for modeling the behavior of FLX9895 and VW, respectively.

To validate the Matlab-implemented algorithm for calculating the response of the chainmail-like structure, the responses of the connector model calculated by the Matlab-implemented algorithm is compared with those calculated using an ABAQUS model in Fig. 8.10. In the ABAQUS model, each connector is modeled as a wire whose behavior is defined using a nonlinear connector element. The CORs of the chainmail-like structure are based on the mechanical test results from Chapter 7 (Table 8.4). It is to be noted that for one single evaluation of the chainmail-like structure's response in six

loading scenarios takes ~0.5 s for the Matlab-implemented algorithm versus ~15s for the ABAQUS model. Using the validated Matlab-implemented algorithm, the rotational responses of the chainmail-based ASD is then obtained by adding up the responses of the artificial NP and the artificial AF, the procedure of which is illustrated in Fig. 8.11.

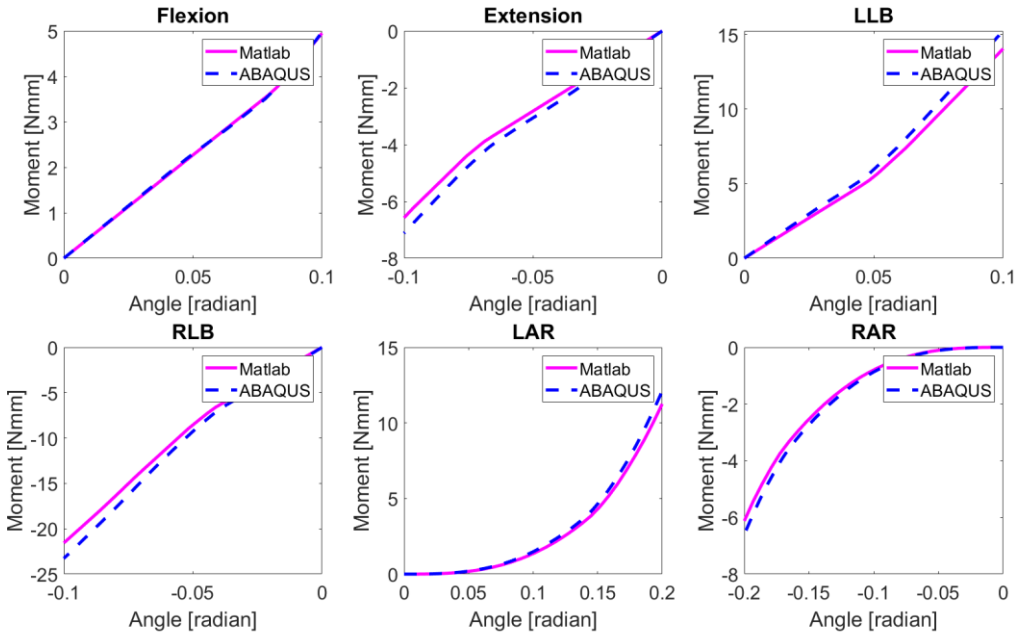

Fig. 8.10. Comparison of the moment-angle responses of the connector model calculated using the Matlab-implemented algorithm and an ABAQUS model. In the ABAQUS model, each connector is modeled as a wire whose behavior is defined by a nonlinear connector element.

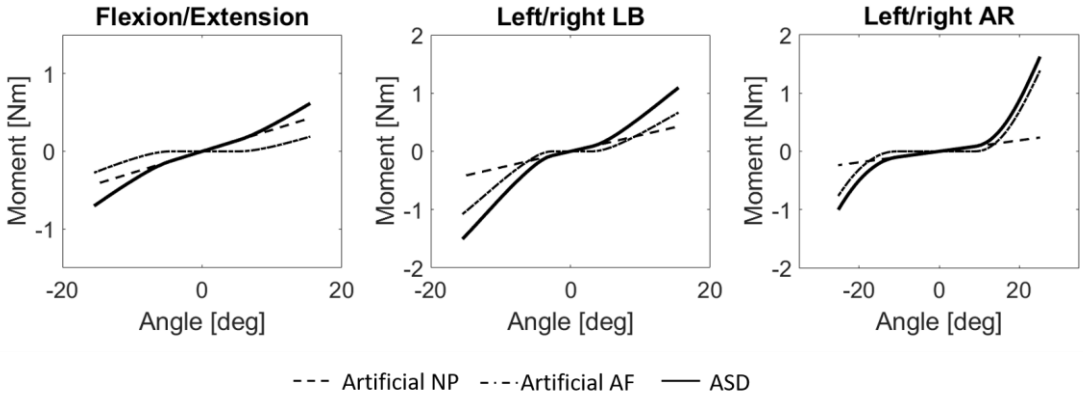

Fig. 8.11. Illustration of curve superposition to obtain the response of the chainmail-based ASD. The dashed line shows the response of the artificial NP, while the dash dotted line shows the response of the artificial AF. The superposition of the artificial NP and artificial AF gives the response of the ASD shown in solid line.

Table 8.4. The COR for the response calculation of the chainmail-like structure.

Loading scenario	COR	Loading scenario	COR
Flexion	[0,0,5]	Right LB	[-6,0,0]
Extension	[0,0,-6]	Left AR	[-11.5,0,0]
Left LB	[2,0,0]	Right AR	[6.5,0,0]

Results comparison

Fig. 8.12 shows the comparison of the ASD's compressive response and the compressive stiffness of the two ASD designs using the computational model and measured through mechanical tests.

The compressive stiffness of the two ASD designs is calculated using a linear regression of the ASD's force-displacement curve when its response reaches a mostly linear region: at a displacement between 0 and 0.3 mm for the flexible-chain ASD and between 0.5 and 0.8 mm for the rigid-chain ASD. Fig. 8.13 shows the comparison of the rotational responses of the chainmail-based ASD calculated by the computational model and measured through mechanical tests. Fig. 8.14 then shows the comparison of the derived metrics through fitting the rotational responses shown in Fig. 8.13 with a bilinear regression model as stated in Chapter 6.

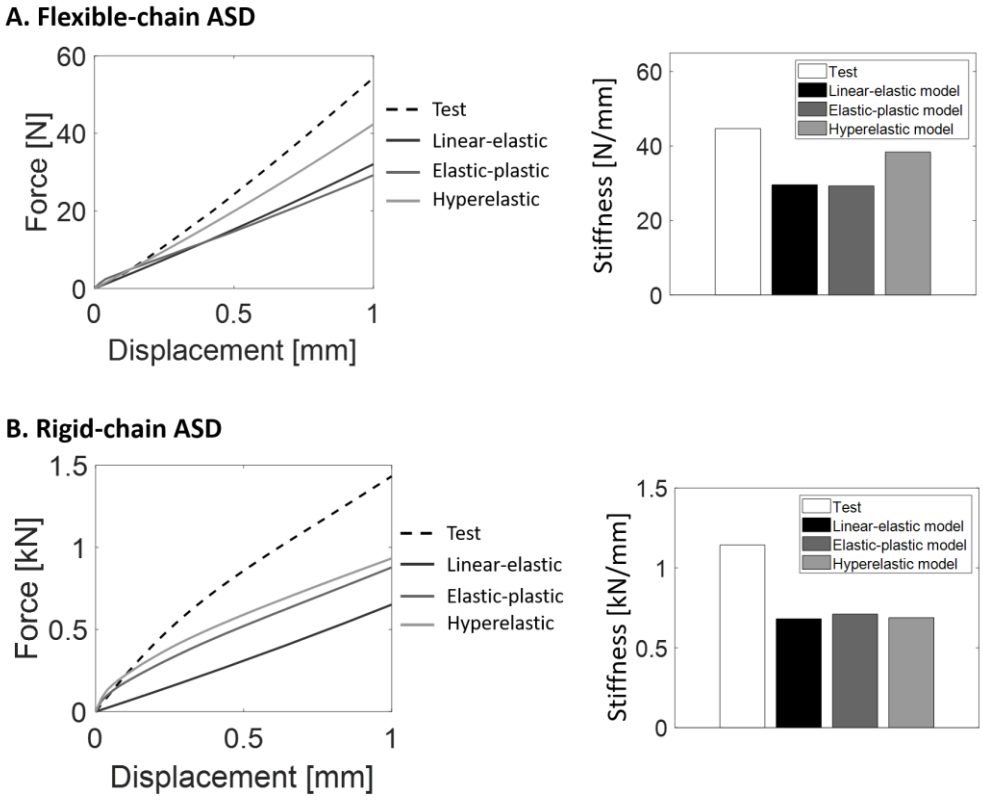

Fig. 8.12. The comparison of the ASD's compressive response and compressive stiffness based on FE model and mechanical test. The compressive stiffness of the two ASD designs is calculated based on a linear regression of the force-displacement curve when the displacement is between 0 and 0.3 mm for the flexible-chain ASD and between 0.5 and 0.8 mm for the rigid-chain ASD when the response reaches a mostly linear region. "Test" is the average force-displacement curve of the three specimens measured through mechanical tests. "Linear-elastic" represents the responses based on the solid model with a linear elastic material model, while "Elastic-plastic" and "Hyperelastic" represent responses based on the solid model with a elastic-plastic material model and a hyperelastic material model, respectively.

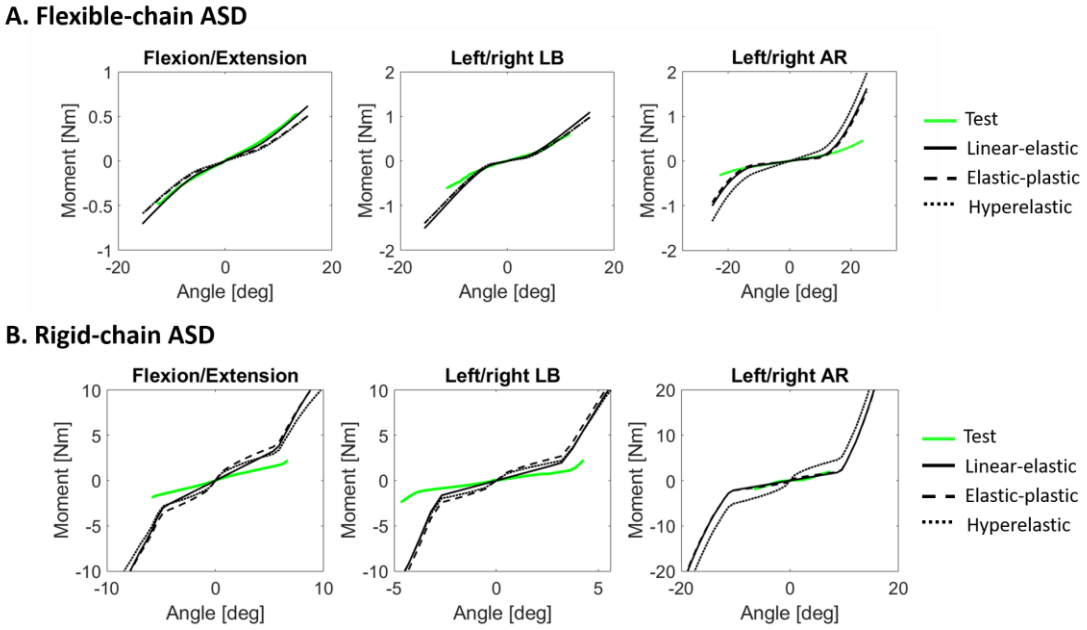

Fig. 8.13. The comparison of the ASD's rotational responses calculated with the computational model and measured from mechanical tests. "Test" represents the average force-displacement curve of the three specimens measured through mechanical tests. "Linear-elastic" represents the responses based on the solid model with a linear elastic material model, while "Elastic-plastic" and "Hyperelastic" represent responses based on the solid model with an elastic-plastic material model and a hyperelastic material model, respectively.

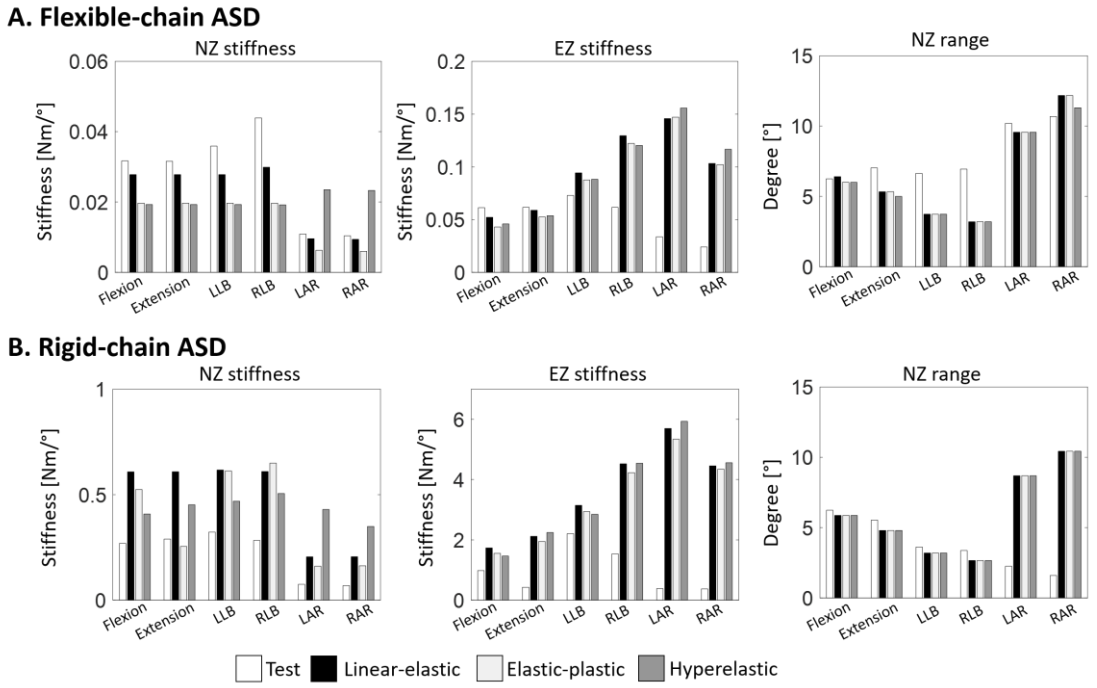

Fig. 8.14. The comparison of metrics derived from the ASD's rotational load responses. The metrics are derived through performing the data analysis procedure in Chapter 6 based on the rotational responses shown in Fig. 8.13.

8.3.4 Material optimization for patient-specific ASD design

The constituent materials of the artificial NP and the individual chainmail unit cells in the artificial AF are optimized in this section for restoring the anisotropic stiffnesses in seven loading scenarios of two IVDs: a human L2-L3 IVD, and a human L4-L5 IVD. The stiffness of the two IVDs are presented in Table 8.5. The stiffnesses in LLB and RLB as well as in LAR and RAR are averaged to allow for a symmetric load response in left and right loading scenarios. An initial material

optimization of the artificial NP shows that FLX9895 allows the ASD to exhibit a compressive stiffness in the physiological range, i.e., between 580 N/mm and 1326 N/mm. Next, the material distribution in the chainmail-like structure is optimized to reproduce IVD's six rotational stiffnesses. Each objective function evaluation takes ~0.9 seconds and a total of ~10 minutes is needed for the material optimization. After curve superposition to obtain the rotational response of the chainmail-based ASD, the optimized stiffnesses of the chainmail-based ASD and the corresponding optimized material distribution in the chainmail-like structure are shown in Fig. 8.15.

Table 8.5. The stiffness of two human lumbar IVDs in seven loading scenarios [125] [126]. The unit of the compressive stiffness is N/mm, while the unit of the rotational stiffness is Nm/°.

Disc type	Compressive stiffness	Stiffness in flexion	Stiffness in extension	Stiffness in LLB/RLB	Stiffness in LAR/RAR
L2-L3 lumbar IVD [126]	580-1326	1.14	0.76	1.06	1.49
L4-L5 lumbar IVD (specimen 1) [126]	580-1326	0.93	0.98	1.58	2.75
L4-L5 lumbar IVD (specimen 2) [125]	-	0.60	0.53	0.98	1.15

***:** "-" represents lack of data from the literature with the given IVD specimen.

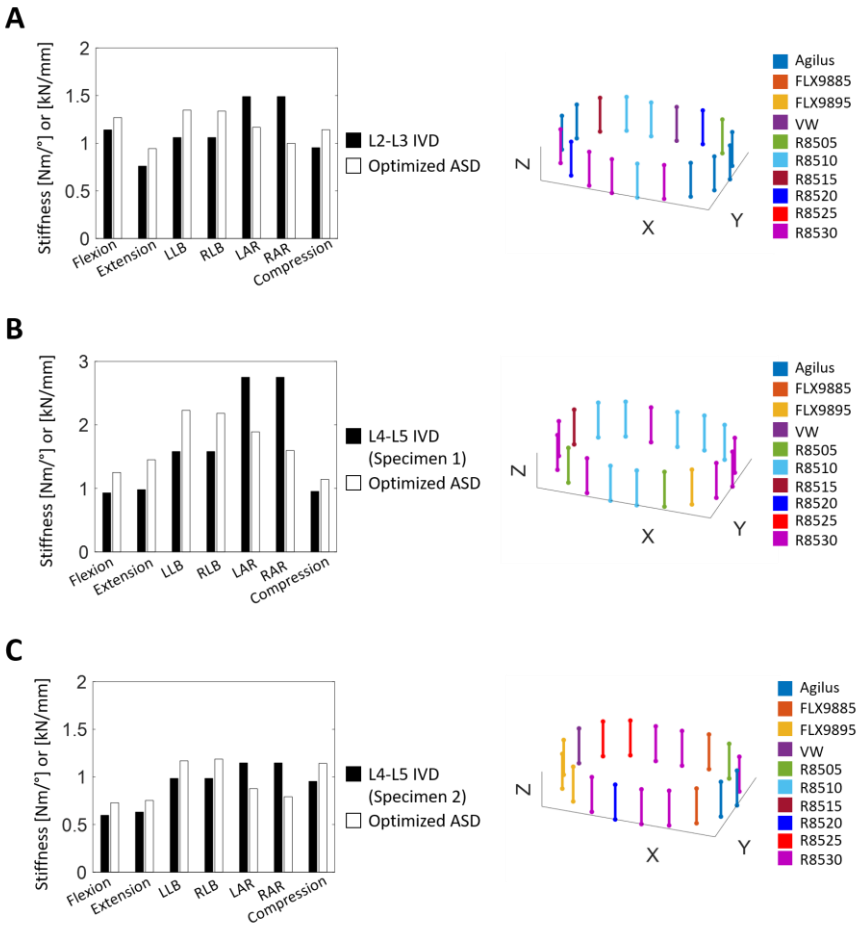

Fig. 8.15. The stiffnesses of the optimized chainmail-based ASD and the material distribution in the chainmail-like structure. This includes L2-L3 ASD (A), L4-L5 ASD for specimen 1 (B), and L4-L5 ASD for specimen 2 (C).

8.4 Discussion

This section sequentially discusses the load bearing mechanism of chainmail unit cells fabricated with rigid and flexible materials, mechanical test results of the two ASD designs, the

validation results of the computational model, and the material optimization results. This section ends with a discussion of the implications of this chapter for the thesis.

8.4.1 Load bearing mechanism of chainmail unit cells

Fig. 8.6 shows that the chainmail unit cells fabricated with flexible materials, which are referred to as flexible unit cells in the following text, show a nonlinear trend in their tensile responses with a small variance among different specimens. In contrast, the tensile responses of the unit cells made from rigid materials, which are referred to as rigid unit cells in the following text, mostly show a linear trend with a bigger variance among different specimens. Such behavior difference is attributed to the different load bearing mechanisms of the two types of unit cells. For the flexible unit cell, the main mechanisms that determine its tensile load response are shape change and filament alignment in the loading direction. At small displacements, the gradual shape changing of the flexible unit cell leads to a nonlinear tensile load response. At bigger displacements when the filaments are maximally aligned in the loading direction, the flexible unit cell maximally bears the load while exhibiting a linear load response. Therefore, the position variance of the initial contact point of the rings has a negligible influence on its tensile response, which also contributes to the small variance among the tensile responses of different specimens. In contrast, the shape change of the rigid unit cell is not significant due to the rigidity of its base material. The load bearing mechanism of the rigid unit cell is mostly due to the blocking of two rings at the contact point upon tensile loading, i.e., from non-contact to contact. Such mechanism makes the unit cell's response more sensitive to position variance of the initial contact point of the rings, which also explains the bigger variance among the load responses of different specimens that belong to the same unit cell type. The loading bearing mechanism of the rigid unit cell also complicates the determination of the starting point in tensile tests, as the reaction force is already non-negligible when the rings in a unit cell slide relative to each other.

In addition, it is to be noted that the nonlinearity of the tensile responses of the flexible unit cells is less pronounced compared to the responses of the flexible unit cells in Chapter 6. This is because the unit cell design in Chapter 6 allows for a larger degree of shape change due to the freely movable middle ring, whereas the unit cell design in this chapter only has two half elliptical rings that are rigidly connected to the endplates. The advantage of using a unit cell as shown in this chapter compared to the design in Chapter 6 is the unnecessity of geometric scaling, as the dimension of the unit cell in this chapter matches the minimum allowable feature size of the given 3D printing technique as well as the dimension of the ASD design space. Besides, the unit cell design in this chapter allows less sliding compared to the unit cell design in Chapter 6, as only one movable joint is available with the given unit cell design in this chapter compared to the two movable joints in Chapter 6.

8.4.2 Mechanical test results

The mechanical test results of the two ASD designs (Fig. 8.8) show that both ASD designs show a nonlinear rotational load response with distinct NZ and EZ. Due to the different load bearing

mechanisms of the flexible and rigid unit cells, the flexible-chain ASD exhibits a smooth transition between the NZ and EZ, whereas the rigid-chain ASD shows a hard transition. In terms of the compressive response of the two ASDs, the response of the flexible-chain ASD exhibits a mostly linear trend, while the response of the rigid-chain ASD exhibits a nonlinear trend, which is due to the different behavior of the base material. As shown in Fig. 8.16, the material behavior of Agilus that makes up the artificial NP in the flexible-chain ASD is featured by a mostly linear trend at small strains, whereas the material behavior of FLX9895 exhibits a nonlinear trend already at small strains.

Fig. 8.17 illustrates the performance repeatability of different specimens of the two ASD designs. It can be concluded that in all the loading scenarios, different specimens of flexible-chain ASD show a good agreement in their responses, while a bigger variation is present among the responses of differ specimens of rigid-chain ASD. The repeatability difference can be explained by two major factors: the difference in base material behavior, and the difference in loading bearing mechanisms of the rigid and soft unit cells. In view of the fact that in the data analysis of the compressive responses, the starting point is determined based on when the force-displacement response starts to exhibit a mostly linear trend to avoid the effect of uneven endplates, the artificial NP is already preloaded at the starting point of the force-displacement curve for data analysis with a certain strain distribution profile. Given the significantly nonlinear material behavior of FLX9895, different strain distribution profiles at the starting point of data analysis will lead to different load responses. In contrast, the mostly linear material behavior of Agilus minimizes the influence of different strain distribution profiles at the starting point of data analysis. Additionally, since the response of the rigid unit cell is significantly affected by the initial contact point of the rings, the rotational responses of rigid-chain ASD also show a big variance. Further, it is observed during the mechanical test that the chainmail-like structure in the rigid-chain ASD is prone to break, therefore only a small rotation angle is used for testing the rigid-chain ASD. This hinders the accurate comparison of the rigid-chain ASD's responses measured through mechanical tests with those calculated using a computational model, as the test data that describes the rigid-chain ASD's load responses at higher angles is missing. Nevertheless, the mechanical test results provide a good benchmark for qualitatively validating the computational model.

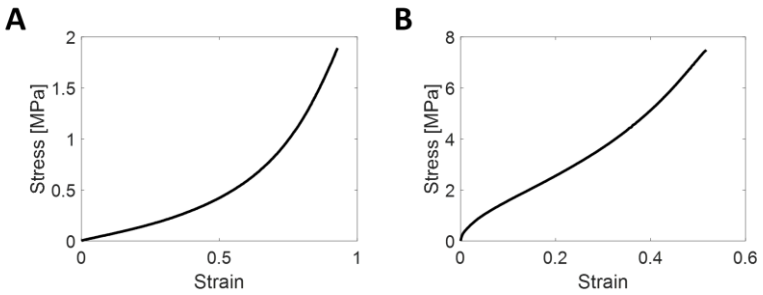

Fig. 8.16. The stress-strain response of the Agilus (A) and FLX9895 (B) for fabricating the artificial NP in two chainmail-based ASD designs. At small strains, Agilus is mostly featured by a linear stress-strain behavior, whereas FLX9895 is featured by an overall nonlinear stress-strain behavior.

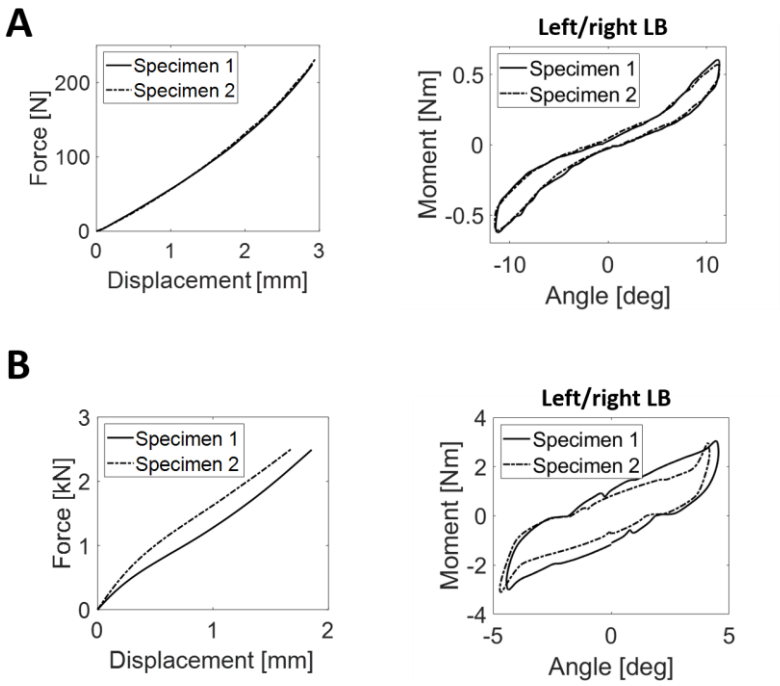

Fig. 8.17. Illustration of the performance repeatability of the flexible-chain ASD (A) and rigid-chain ASD (B). The compressive responses of different specimens that belong to the same ASD design are shown on the left, while the rotational responses of different specimens in LB are shown on the right.

8.4.3 Computational model validation

Fig. 8.9 shows that the material model used has an influence on the compressive response of the ASD: the elastic-plastic or the hyperelastic model is able to capture the nonlinear compressive response of the ASD, whereas linear elastic model is unable to capture such nonlinear response. The good agreement of the rotational response calculated using the Matlab-implemented algorithm and that using the ABAQUS model in Fig. 8.10 validates the Matlab-implemented algorithm. The comparison of the compressive response in Fig. 8.12 shows that the computational model generally predicts well the reaction force at small displacements, while the model tends to underpredict the reaction force at bigger displacements, which can be attributed to the inaccuracy of the material models at bigger strains.

The comparisons of the rotational response in Fig. 8.13 and the derived metrics in Fig. 8.14 show that the model of the flexible-chain ASD is generally more accurate in matching mechanical test results compared to the model of the rigid-chain ASD. For both the flexible-chain ASD and the rigid-chain ASD, the computational model shows a relatively low prediction accuracy in left/right AR. The deviation in flexible-chain ASD is mostly due to the sliding between rings in the chainmail unit cells resulting from shear force. The chainmail unit cell first goes through an initial sliding phase where there is no reaction force before bearing load, whereas in the connector model a nonzero length change and a consequent nonzero reaction force are generated due to relative movement of the connector's nodes. This phenomenon is most significant in left/right AR, which explains the deviation of the computational model and the mechanical test. After this initial sliding phase in left/right AR, the flexible unit cells will go through shape change and start to bear load in left/right AR, whereas the rigid unit cells will block each other and start to bear load. Since the connector model depends on length change to calculate

reaction force, such blocking-induced load bearing mechanism of the rigid unit cell is not taken into consideration. The sliding explains the advanced *activation point* (i.e., a lower NZ range) predicted by the model for the flexible-chain ASD in all the loading scenarios. The sliding together with the blocking-induced load bearing mechanism of rigid unit cells explain the delayed *activation point* (i.e., a higher NZ range) predicted by the computational model for the rigid-chain ASD in left/right AR, and the advanced *activation point* (i.e., a lower NZ range) in flexion, extension, and left/right LB.

The base material behavior of the artificial NP is shown to have a determinant effect on the NZ stiffness, which is reflected in the different prediction accuracies using different material models. It can be concluded that the hyperplastic material model tends to overestimate the torsional stiffness as shown in both ASD designs. Overall, the linear elastic model shows good accuracy for modeling the ASD's response. Due to the significant nonlinear material behavior of FLX9895, the model of the rigid-chain ASD has a lower prediction accuracy in terms of NZ stiffness compared to the flexible-chain ASD. Regarding the EZ stiffness, the model of the flexible-chain ASD predicts the EZ stiffness well except in right LB and left/right AR due to sliding. Due to the lack of test data to describe the response of the rigid-chain ASD at bigger angles, the EZ stiffnesses of the rigid-chain ASD from tests are generally lower than those predicted by the model.

In addition to sliding, alternative material models, and different loading mechanisms of rigid and flexible chainmail unit cells, additional factors that can potentially influence the prediction accuracy of the computational model are the initial relative orientations of the rings in a chainmail unit cell, the initial distance between the rings in a chainmail unit cell, and the COR position. The discrepancy in the initial relative orientation and distance between the rings among different chainmail unit cells is resulted from the movable joint. The influences of those additional factors are explored using a parametric study. To explore the influence of relative orientations between the rings, three specimens of the chainmail unit cell made from Agilus and VW are fabricated and tensile tests are performed with different initial relative orientations of the rings. Results in Fig. 8.18 show that the tensile responses of both the flexible and rigid unit cells are not significantly influenced by the initial relative orientations of the rings. The third specimen of the rigid unit cell with an initial relative orientation of 60° shows an early material failure already at small strains, which explains the deviation of its response from the other two specimens. The influence of the initial distance between the rings and COR on the rotational load response of the chainmail-like structure are shown in Fig. 8.19 and Fig. 8.20, respectively. It can be concluded that both the initial distance between the rings and COR have a significant influence on the chainmail-like structure's rotational response by impacting the NZ range and the EZ stiffness.

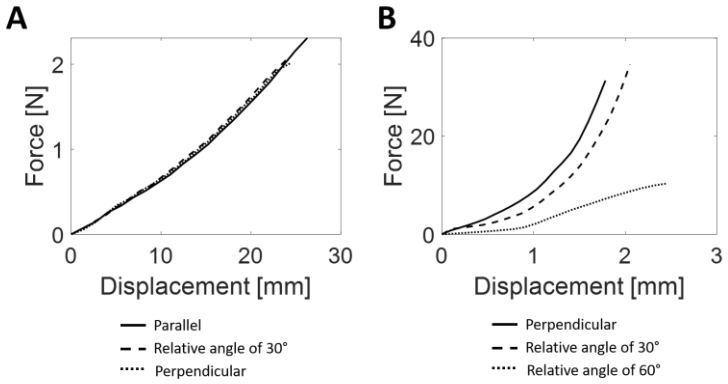

Fig. 8.18. The influence of the initial relative orientations of the rings on the tensile response of the chainmail unit cell fabricated with Agilus (A) and VW (B). The third specimen of the rigid unit cell with a relative angle of 60° between its rings goes through an early material failure before being strained.

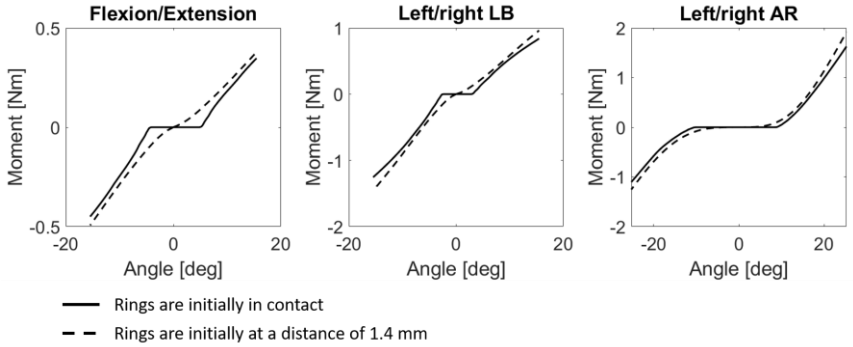

Fig. 8.19. The influence of initial distance between rings in a chainmail unit cell on the rotational response of the chainmail-like structure. With the same constituent material and the same COR, the solid line represents the response of the chainmail-like structure when the rings are initially in contact, while the dashed line represents the response of the chainmail-like structure when the rings have an initial distance of 1.4 mm.

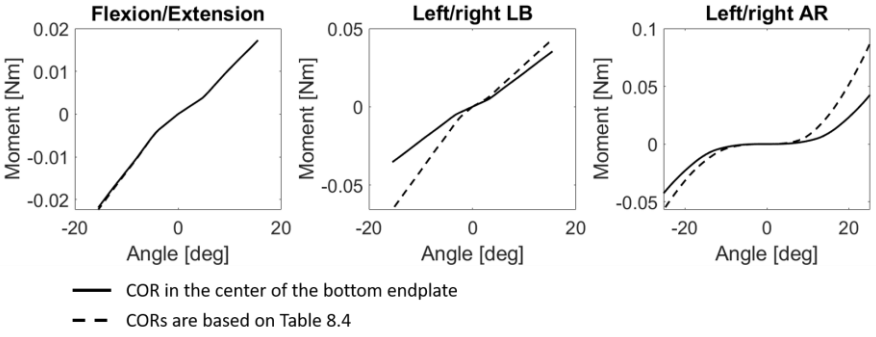

Fig. 8.20. The influence of COR position on the rotational response of the chainmail-like structure. The responses are calculated based on the same constituent material and the same initial distance of chainmail unit cells. The solid line represents the response of the chainmail-like structure when the CORs are in the geometric center of the bottom endplate, while the dashed line shows the response of the chainmail-like structure based on the positions of the CORs given in Table 8.4.

8.4.4 Material optimization

As shown in Table 8.5, the IVD's anisotropic stiffness varies with factors such positions in the spine and patients, which verifies the necessity of having a personalized ASD design that can meet patient-specific mechanism requirements. Especially, the compressive stiffness of an IVD measured in the literature shows a high individual-level variance resulted from its dependency on factors such as water content [205] and amplitude of preload during the test [206], therefore a range of physiological compressive stiffness is used as the optimization goal in this chapter. The optimization results shown in

Fig. 8.15 show a relatively good match between the stiffness of the optimized ASD and the IVD. The worse fitness of L4-L5 (Specimen 1) can be explained by the limited material options. Fig. 8.15 also implies that the optimization process is able to recognize critical chainmail unit cells to restore natural anisotropy. This can be seen in the optimized material distribution in Fig. 8.15.A and Fig. 8.15.C where flexible materials are assigned to the chainmail unit cells on the lateral side with bigger level arms to reduce the amplitude of LB stiffness relative to stiffnesses in other loading scenarios. The stiffness match is expected to be further improved with the incorporation of more base materials that cover a wider range of stiffness. Despite the fact that the validation of the optimized ASD is hindered by the vulnerability of the rigid material that is prone to failure, the optimization results show the potential of the chainmail-based ASD design to restore patient-specific anisotropy in seven loading scenarios.

8.4.5 Implications for the thesis

In order to answer RQ4, this chapter performs the complete workflow for the design of a patient-specific ASD design based on the favorable chainmail-based ASD design concept determined in Chapter 7 through the computational design method for the realization of such ASD design concept developed in Chapter 6. This chapter explores the ability of the chainmail-based ASD design in meeting patient-specific mechanical requirements given the manufacturing constraints of the 3D printer. The overall workflow starts with a systematic analysis of the ASD design concept to clarify how different design parameters control the load responses, followed by computational model build and validation, and the final material optimization. The implications derived from each step of the workflow for this thesis will be discussed sequentially in the following paragraphs.

First, to achieve a controlled response in each loading scenario, an ASD design needs to have a set of design parameters. Ideally, the response of the ASD design quantified using different metrics can be controlled independently by different design parameters to avoid coupling effect. For example, if we want to adapt the NZ stiffness in flexion through adjusting one design parameter, we want the other metrics in flexion (e.g., NZ range, EZ stiffness, etc) as well as the metrics in other loading scenarios (e.g., NZ stiffness and range, EZ stiffness, compressive stiffness, etc) to be unaffected. Such independent control will facilitate the design of a patient-specific ASD to meet personalized mechanics requirements. However, considering the complex loading scenarios of an IVD, such independent control is difficult to realize. For example, in this chapter the material composition of the central cylinder affects both the compressive stiffness and the rotational NZ stiffness of the chainmail-based ASD.

Second, the computational model needs to balance the computational cost and the prediction accuracy. In this chapter, a simplified connector is used to model the behavior of a chainmail unit cell. Despite its computational efficiency, this model neglects mechanisms such as sliding and different load bearing mechanisms of the flexible and rigid chainmail unit cells, which weakens its prediction accuracy. Whether certain details should be included in the computational model depends on factors such as optimization goal and the additional computational cost required. The complexity in developing a

realistic model to fully describe the chainmail unit cell's behavior under different loads is one limitation of the chainmail-based ASD design. One possible solution to tackle this challenge is to use a mechanism-based mechanical metamaterial such as rotating squares [207] in the future ASD design to achieve a more controlled motion.

Lastly, the material optimization should favor material candidates with high breaking strain as well as high extendibility. Such materials allow for large shape changes in the chainmail unit cells while helping to avoid material failure. The seven rigid materials provided by the given 3D printer are not ideal candidates since they have low breaking strains that limit the maximum rotation angle of the ASD. Furthermore, extensive studies for characterizing the material properties are required to develop a more realistic material model, which helps improve the prediction accuracy of the computational model.

8.5 Conclusion

This chapter designs a patient-specific ASD based on a chainmail-based ASD design concept to explore its performance in restoring patient-specific anisotropy in seven loading scenarios given the manufacturing constrains. A complete workflow is presented that includes design concept analysis, building the FE model and validating it through comparing to experimental tests, and a material optimization. Results show that both rigid-chain and flexible-chain ASD designs exhibit a nonlinear rotational load response, while the flexible-chain ASD has higher performance repeatability among different specimens and better accuracy with the given computational model. To further improve the accuracy of the computational model, rings sliding and a blocking-induced load bearing mechanism of rigid unit cells need to be incorporated into the model. Furthermore, the material optimization results show great potential of the chainmail-based ASD to restore patient-specific anisotropy despite limited materials.

Chapter 9. General design guidelines for multi-material ASD fabricated with multi-material AM

9.1 Summary

Through the exploration of different multi-material ASD designs concepts and different strategies for realizing a computationally efficient design process, this section summarizes the challenges in ASD design and presents some general guidelines on how to devise alternative ASD design concepts and how to automatically design a patient-specific ASD.

9.2 Guidelines for developing multi-material ASD design concepts

This section first gives an overview of the key principles for developing multi-material ASD design concepts in Section 9.2.1. Next, the challenges faced by multi-material ASD design are listed in Section 9.2.2. Lastly, Section 9.2.3 discusses potential strategies to tackle the challenges.

9.2.1 Overview

As shown in Fig. 9.1.A, an elastomeric ASD is composed of two parts: the rigid endplates for interfacing with adjacent vertebrae and a flexible elastomeric core for providing flexibility. The design process is primarily focused on the elastomeric core whose deformation mechanism and load response can be considered as a result of the motion of individual springs and their interactions in a node-spring network, as illustrated in Fig. 9.1.B. Such abstraction is comparable to the connector model proposed in Chapter 6 and coincides with the mass spring model commonly used for modeling soft tissue deformation [208]. Considering the complex loadings scenarios of the spine and the ASD in everyday life, the springs are subject to complex loads such as tension, compression, shear, or a combination of the abovementioned loads.

Given the node-spring network, the problem formulation of designing an elastomeric ASD to reproduce the nonlinear, viscoelastic behavior properties of an IVD can be viewed as designing individual spring behaviors, the spring interactions, as well as the node topology in a node-spring network, as illustrated in Fig. 9.2. For the design of individual spring behavior (Fig. 9.2.A), examples are using a fiber with a linear axial force-displacement response (Chapter 3) or a chainmail unit-cell with a nonlinear axial force-displacement response (Chapter 6). For designing spring interactions (Fig. 9.2.B), possible options are with and without interaction between springs. Examples are with spring interactions between the artificial NP and AF given the fiber-reinforced composite disc (Chapter 3) and without interactions given the biomimetic design (Chapter 4). The design of the node topology (Fig. 9.2.C) concerns the nodes' spatial relations. For example, the tuning of the orientation of the members in a fiber-like structure of the biomimetic disc (Chapter 4) is comparable to adjusting the node topologies.

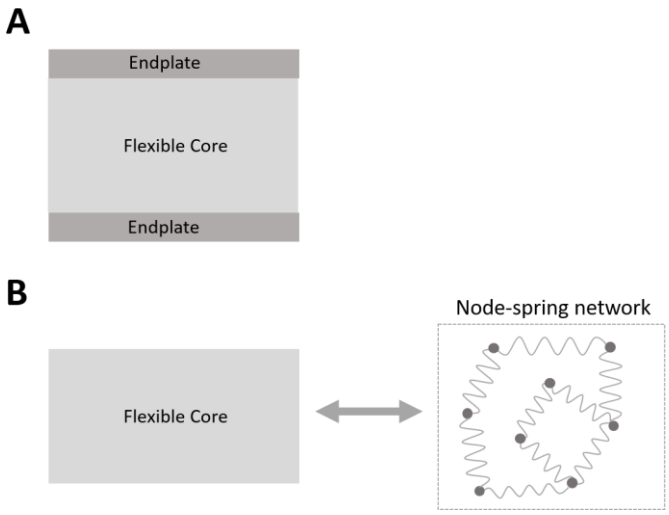

Fig. 9.1. Illustration of the composition of an elastomeric ASD (A) and the abstraction of the flexible core for ASD design formulation (B). An elastomeric ASD is composed of two parts: the rigid plates and the flexible elastomeric core (A). The elastomeric core is the domain for multi-material ASD design. The deformation mechanism and response of the elastomeric core can be considered as a result of individual motions and interactions of a series of springs in a node-spring network (B). This concept is comparable to the connector model proposed in Chapter 6 and coincides with the mass spring system used for modeling the behavior of soft tissues [208].

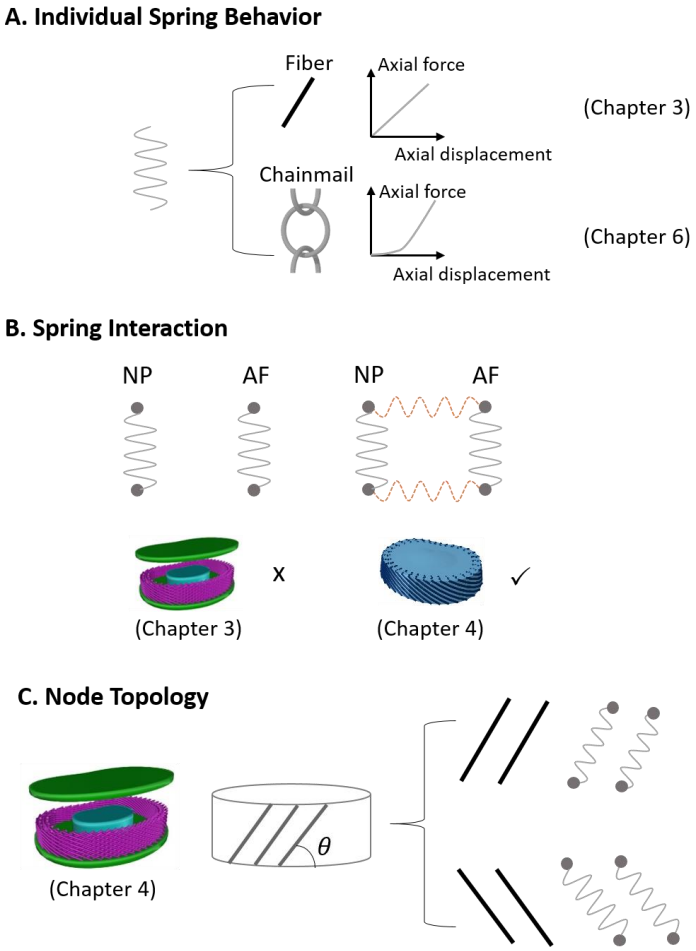

Fig. 9.2. Three aspects to consider for designing the node-spring network to reproduce an IVD's mechanics. (A) Individual spring behavior. For example, in Chapter 3 a fiber with a linear axial force-displacement response is used for designing individual spring behavior. In Chapter 6, a chainmail unit-cell with a nonlinear axial force-displacement response is used. (B) Spring interaction. Examples are with spring interactions between the artificial NP and AF with the fiber-reinforced composite disc in Chapter 3 and without interactions with the biomimetic design in Chapter 4. (C) Node topology. For example, the tuning of the orientation of the members in a fiber-like structure of the biomimetic disc in Chapter 4 is comparable to adjusting the node topologies.

9.2.2 Challenges

The challenges for the multi-material ASD design mainly originate from three aspects: the complex behavior of a natural IVD, the extensive design space, and the manufacturing constraints imposed by the given 3D printing technique. The complex motion of the IVD imposes multiple conflicting criteria for ASD design, and the design problem is further complicated by the extensive design space resulting from the innumerable combinations of individual spring behaviors, spring interactions, and spring network organization.

The manufacturing constraints mainly concern the manufacturability of the proposed ASD design and can be divided into two categories: constraints from the materials and constraints from the minimum allowable feature size for reliable mechanical properties. Constraints from materials can be divided into three aspects. First, only limited options of base materials are available, such as the given 3D printer in this thesis only provides fourteen base materials. Second, the materials used for ASD fabrication need to meet certain criteria such as biocompatibility, high strength, and high breaking strain. Third, due to fabrication limits, the 3D printed parts have an anisotropic material property dependent on feature size and build orientation [173], which adds complexity to the computational modeling. Constraints on the minimum allowable feature size is due to the printing resolution of the given 3D printing technique. Furthermore, the maximum allowable feature size is constrained by the dimensions of the IVD. For example, the height of a human lumbar IVD is in between 7 mm to 10 mm.

9.2.3 Strategies

This section will introduce possible strategies to tackle the challenges in the ASD design given in Section 9.2.2. First, considering multiple conflicting design criteria, the design of individual spring behavior and the spring interactions can be decoupled, which allows different springs to contribute to the ASD's load response in different loading scenarios at different degrees. The tuning of the ASD's behavior in a certain loading scenario can therefore be accomplished by only adjusting the corresponding responsible springs. If we define the springs that contribute to the ASD's load response significantly as "active" and the springs that have negligible contributions as "inactive", a decoupling strategy sets different subsets of springs as "active" in different loading scenarios, which helps decouple the multi-objective optimization problem.

Second, to tackle the challenge of the extensive design space resulting from the innumerable combinations of individual spring behaviors, spring interactions, and spring network organization, one possible solution is to fix most of the design variables while only optimizing a small subset of the design variables. This strategy helps to reduce the dimension of the design space, which facilitates the design process. For example, biomimetic structures found in an IVD and fiber-like behaviors can be used to design the spring network organization and the spring behavior, respectively. Additional methods include the application of topology optimization and mechanical metamaterials to design the individual

spring behavior, the spring interactions, or the spring network organization. Another possible strategy is to use design variable linking to reduce the problem dimension.

Third, in view of the manufacturing constraints, an appropriate 3D printing technique needs to be selected for the fabrication of a multi-material ASD. An ideal 3D printing technique should meet the following criteria:

1) provides a broad range of base materials with varying Young's moduli. For the chainmail-based ASD proposed in Chapter 6, material with a Young's modulus at the range of several hundred MPa is required for natural rotational stiffness. Besides, the base material is required to be biocompatible for fabricating implantable medical devices [209] and have high strength and breaking strain to allow for big shape changes.
2) has a good printing resolution to allow for the fabrication of small features with reliable mechanical properties. For the biomimetic fiber-reinforced composite design proposed in Chapter 3, a minimum feature size of 0.1 mm is needed.

9.3 Guidelines for computational methods for patient-specific ASD design

This section first gives an overview of the computational method for designing a patient-specific, multi-material ASD in Section 9.3.1. Next, the challenges for designing a patient-specific, multi-material ASD are discussed in Section 9.3.2. Lastly, the possible strategies to tackle the challenges are listed in Section 9.3.3.

9.3.1 Overview

The computational design method starts with computational modeling of a certain multi-material ASD, validating the model, and optimization of the multi-material ASD such as material distribution. For the computational modeling, commonly used tool is FE analysis. The optimization algorithm needs to comply with the properties of the optimization problem. An ideal computational method needs to involve a digitalized workflow to design a patient-specific ASD with reasonable time and resources. Additionally, the computational method is expected to be automated without requirements for engineering expertise to allow the surgeons to independently design a patient-specific ASD, which helps to improve the current time-consuming iterative design process between surgeons and engineers [210].

9.3.2 Challenges

First, the FE analysis usually requires a long computation time while possibly suffering from convergence issues. The computational time and cost are further increased significantly and the convergence is further complicated when involving more complex behaviors such as contact, large deformations, and nonlinear material behaviors. Second, the implant design requires expertise in CAD software, FE modeling, and engineering optimization [210], which hinders the realization of a computational method that allows for an automatic generation of patient-specific ASD for surgeons

without the need of engineers. Third, only mechanics within a certain range can be achieved given one ASD design concept together with a specific 3D printing technique. Therefore, the required patient-specific stiffness may lie outside the realizable range.

9.3.3 Strategies

This section introduces possible solutions to tackle the challenges listed in Section 9.3.2. In view of the high computational cost of FE analysis, there are two possible strategies. The first strategy is to simplify the FE model by avoiding details such as contact and large deformations, etc. However, model simplification is often accompanied with reducing modeling accuracy, which needs to be balanced in the modeling. The second strategy is to use ML techniques either as regression model to replace time-consuming FE analysis or as a tool to reduce the high-dimensional search space for implant design [211]. The application of ML techniques for automating engineering tasks for patient-specific implant design, such as automatic tuning of an ASD's material composition, can potentially allow the surgeons to design and fabricate patient-specific ASD independently at the point of care [212]. This will also potentially help realize a wider application of patient-specific implants in the clinics, as the current development process of patient-specific implants can take around several months due to the iterative collaboration between engineers and surgeons [26]. Additionally, to make sure that the ASD design meets patient-specific stiffness requirements, the design method can pre-store multiple ASD design concepts with their corresponding achievable mechanics as an inventory. With a given patient, the system can efficiently match a suitable ASD design for patient-specific implant design and fabrication.

9.4 General guidelines of ASD design

This section summarizes the strategies to address the challenges in the ASD design discussed in this chapter as general guidelines for the further development of a multi-material ASD fabricated with multi-material AM. Among seven guidelines proposed, Guidelines 1-4 focus on multi-material ASD design concept development, while Guidelines 5-7 focus on the computational design methods. Fig. 9.3 summarizes the guidelines for the multi-material ASD design by presenting the workflow for developing patient-specific ASDs including challenges and possible mitigations strategies.

- *Guideline 1*: The deformation mechanism of the elastomeric core of a multi-material ASD can be considered as a result of individual motions of springs in a note-spring network and their interactions. Therefore, in order to reproduce the complex nonlinear, anisotropic, and viscoelastic behavior of an IVD, the design of individual spring behavior, the spring interactions, and the node topology need to be considered to achieve a controlled nature-mimicking motion in each loading scenario.
- *Guideline 2*: To address the multiple conflicting design criteria imposed on the ASD design, a decoupling strategy that enables different springs to contribute to ASD's load response in different loading scenarios at different degrees is proven to be effective. With such decoupling strategy, the tuning of the ASD's response in a certain loading scenario can be accomplished by

only adjusting the corresponding responsible springs, which minimizes the effect on the ASD's responses in other loading scenarios.

- *Guideline 3*: To reduce the dimension of the extensive design space resulting from the innumerable combinations of individual spring behavior, spring interactions, and spring network organization, one possible solution is to fix most of the design variables while only optimizing a small subset of the design variables. Examples of such strategies is the incorporation of biomimetic structures for designing the spring network and springs with fiber-like behaviors for designing the spring behavior. Additional methods include the application of topology optimization and mechanical metamaterials to determine individual spring behavior, spring interactions, or spring network organization. Another possible strategy is to use design variable linking to reduce the problem dimension.
- *Guideline 4*: An appropriate 3D printing technique needs to be selected for the fabrication of a multi-material ASD. Ideally, the given 3D printing technique provides a wide range of implantable biomaterials with high breaking strain and strength to allow for large deformations of the ASD. Besides, the material behaviors need to be characterized with extensive studies to improve the accuracy of the computational model. The 3D printing technique ideally has a good printing resolution to allow for the fabrication of small features with reliable mechanical properties.
- *Guideline 5*: The high computational cost of FE analysis can be mitigated by using a simplified FE model to avoid time-consuming details such as contact modeling or by using ML techniques to build a regression model to replace FE analysis.
- *Guideline 6*: To realize an automated design method for surgeons to independently design patient-specific ASDs at the point of care, the overall workflow should ideally automate engineering tasks such as CAD modeling and FE analysis to improve the current time-consuming development process that requires a collaboration between the surgeons and the engineers. ML is a promising technique for automating certain engineering tasks such as FE analysis.
- *Guideline 7*: To make sure that the ASD design is able to meet a wide range of patient-specific mechanics requirements, the design method can pre-store multiple ASD design concepts with corresponding achievable mechanics as an inventory. With a given patient, the system can efficiently match a suitable ASD design concept for implant design and fabrication.

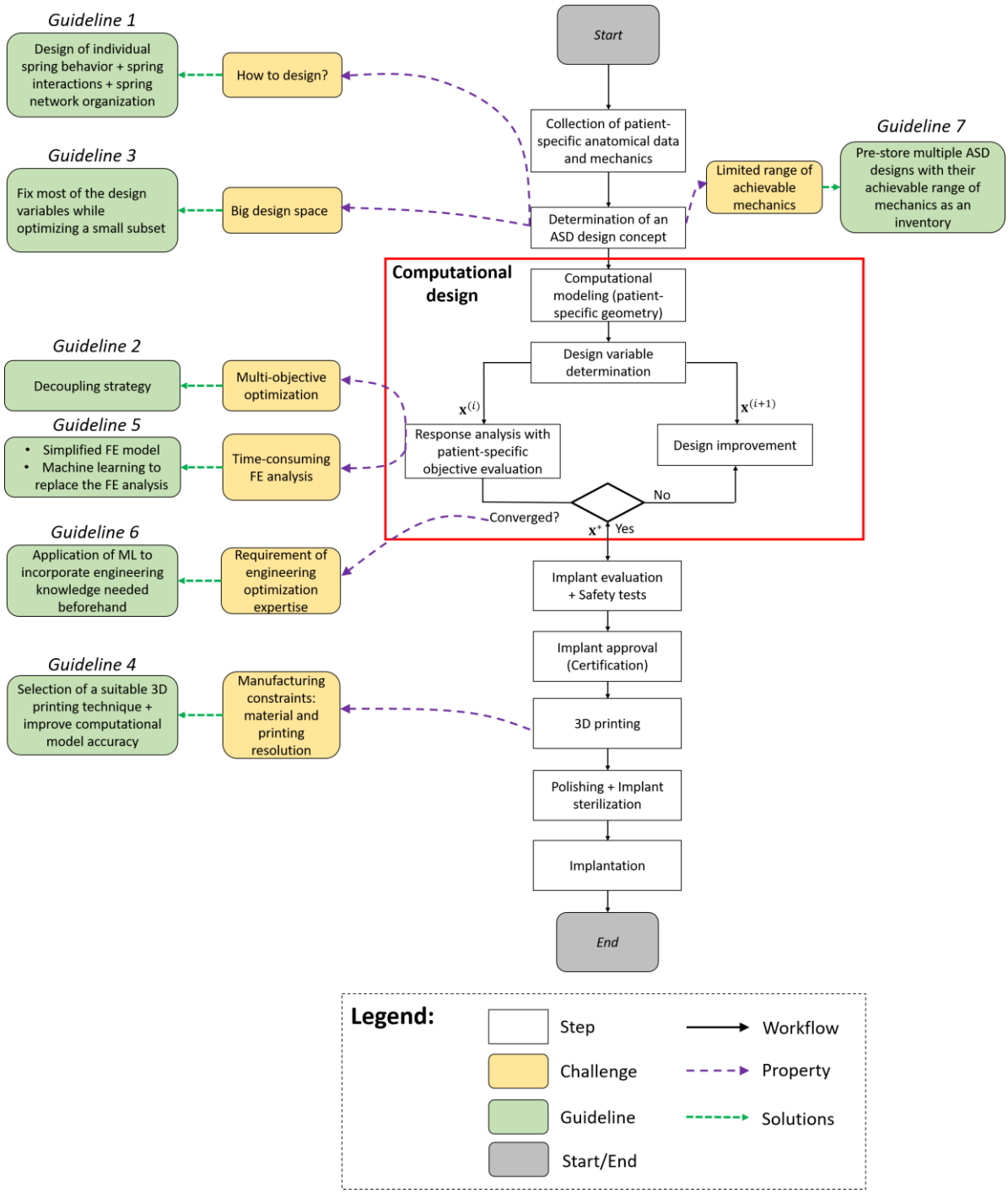

Fig. 9.3. Workflow for developing patient-specific ASDs including challenges and possible mitigations strategies. The steps after computational design of patient-specific ASDs are referenced from [26].

Chapter 10. Discussion and outlook

This chapter first reviews the RQs proposed in Chapter 1 and discusses the resulting knowledge obtained throughout the research performed in this thesis. Next, the limitations of this work and how it could be improved in the future are discussed.

10.1 Principle findings and contributions

Main RQs: Which multi-material ASD design concept has the potential to reproduce the patient-specific mechanics of an IVD while meeting the manufacturing constraints of a given multi-material AM technique? How can a design concept be automatically tuned to produce a patient-specific ASD that meets customized design requirements?

The main RQs are motivated by the lack of a multi-material ASD design concept that can be fabricated with multi-material AM while taking into account the manufacturing constraints, as well as the lack of a design method that is able to produce a patient-specific ASD design with reasonable computational time and resources. This shows the two focuses of this thesis: 1) the exploration of a favorable multi-material ASD design concept for meeting ASD design criteria, and 2) the development of a computationally-efficient design method to automatically design a patient-specific ASD for restoring customized mechanics. The main RQs are addressed by investigating the following four RQs.

RQ1: What are the design criteria for a patient-specific ASD that can be fabricated with multi-material AM?

This RQ aims to clarify the criteria for the design of a multi-material ASD to determine the design goal and the scope of this thesis. Based on literature review, Chapter 2 first provides a systematic overview of the mechanical properties of an IVD and the state-of-the-art ASD designs. The limitations of the state-of-the-art ASD designs demonstrate that an oversimplified ASD design is insufficient for natural mechanics restoration, and that an elastomeric ASD design has great potential to achieve satisfactory clinical outcomes of TDR. The design criteria of an ASD can be divided into two categories: 1) clinical design criteria that concern the clinical outcomes of TDR, and 2) biomechanical design criteria that concern the perseveration of the biomechanical functions of the implanted spinal segment. Considering the complex loading scenarios of the spine, the key of ASD design is identified as to restore a controlled, nature-mimicking motion in each loading scenario.

Contributions:

- Clarification of the IVD's mechanics and the mechanism that leads to its unique behavior, which serves as an inspiration for ASD design. *(Chapter 2)*
- Literature review of the strengths and weaknesses of the state-of-the-art ASDs, which demonstrates the insufficiency of the oversimplified first-generation ASD design and the great potential of a monolithic, viscoelastic, second-generation ASD design. *(Chapter 2)*

- Clarification of the ASD design criteria that can be divided into clinical and biomechanical design criteria and determination of the scope of this thesis. *(Chapter 2)*
- Clarification of the metrics used for quantifying the mechanics of an ASD that includes the restoration of the IVD's *quantity* and *quality* of motion. *(Chapter 2)*

RQ2: With the design criteria clarified in RQ1, what are the potential alternative design concepts?

This RQ explores different multi-material ASD design concepts to determine the most favorable ASD design for developing patient-specific ASDs. To achieve that, Chapters 3-6 sequentially propose and explore the performance of five ASD design concepts based on biomimicry and structures inspired by mechanical metamaterials. The strengths and weaknesses of the five ASD designs explored throughout the thesis are summarized in Table 7.1.

The monolithic, biomimetic, fiber-reinforced composite design proposed in Chapter 3 has the potential to reproduce IVD's anisotropic stiffness in various loading scenarios due to its fiber layer with a negligible bending resistance. In addition, this design lowers the risk of material failure due to its monolithic design. However, this design is limited in its manufacturability due to the vertically oriented fiber layer that is difficult to fabricate with the given 3D printer. Besides, this design exhibits a mostly linear rotational response, which deviates from the nonlinear rotational response of an IVD.

The monolithic, solid design proposed in Chapter 4 is easy to fabricate, as no complex structures or small features are included in the design, which also lowers the risk of material failure. However, this design is unable to reproduce the IVD's anisotropic stiffness due to conflicting objectives. Namely, the torsional stiffness of this design is always lower than its stiffnesses in other load scenarios. Lastly, this design also shows a load response with a mostly linear trend. In comparison, the biomimetic design with a separate fiber layer proposed in Chapter 4 can potentially reproduce the IVD's natural anisotropic stiffness thanks to its crisscross fiber-like layer that provides a higher torsional stiffness than a compressive stiffness, although an initial structural optimization of the fiber-like layer is required before the material optimization. In contrast to the abovementioned two monolithic designs, this design is more prone to material failure and interface delamination between the crisscross fiber-like layer and the two endplates due to small features. The proneness to delamination is most significant in AR where a large shear force is present at the interface. In addition, this design likewise shows a mostly linear load response, which is attributed to the insignificant shape change of the fiber-like layer upon loading.

The lattice-based design proposed in Chapter 5 also has the potential to reproduce the IVD's anisotropic stiffness through varying the lattice's topology. This design also provides the largest design freedom among all the ASD design concepts explored due to its structural adaptability. However, this design has the highest proneness to material failure among all the designs due to the large amount of small features, i.e., members in a lattice. The interface between the lattice and the endplates is also prone

to delamination. Besides, this design exhibits a strain-softening load response due to member buckling, which likewise deviates from the desired strain-stiffening load response.

In comparison to the abovementioned four designs, the chainmail-based design proposed in Chapter 6 is able to show a nonlinear rotational load response due to its large shape change ability upon loading. In addition, this design has the potential to restore the IVD's anisotropic stiffnesses due to the negligible compressive resistance of the chainmail-like structure that partially decouples the multi-objective optimization problem. However, this design suffers from modeling complexity due to factors such as siding between the rings in individual chainmail unit cells and different load bearing mechanisms of chainmail unit cells made from rigid and flexible materials.

Based on the conceptual designs proposed in the previous chapters, Chapter 7 fabricates and performs mechanical tests on four out of the five ASD designs to evaluate their performance in meeting the design criteria clarified in RQ1. The lattice-based design proposed in Chapter 5 is excluded from the mechanical tests due to its proneness to material failure and delamination. Results show that all the four ASD designs exhibit a viscoelastic behavior. In addition, the chainmail-based ASD design exhibits a nonlinear rotational load response as expected and has the potential to restore the natural motion in terms of *quantity* and *quality* of motion. Additional design criteria in RQ1, i.e., the implantation stability as well as the restoration of IVD height and sagittal alignment, can be fulfilled by 1) a proper design of the endplates' shape to achieve an anatomical match with the adjacent vertebrae, and 2) a proper design of the ASD's wedge angle and height to meet patient-specific geometric requirements.

Contributions:

- Proposal of five innovative ASD design concepts based on biomimicry and structures inspired by mechanical metamaterials, which serves as inspiration for the design of next-generation viscoelastic ASDs. *(Chapter 3-6)*
- Evaluation of the performance of the five ASD design concepts in restoring natural mechanics using computational design methods. *(Chapter 3-6)*
- Fabrication and mechanical testing of the ASD designs to evaluate and compare their strengths and weaknesses to determine the favorable ASD design concept. *(Chapter 7)*
- Demonstration of the potential of incorporating structures inspired by mechanical metamaterials into the ASD design for natural mechanics restoration. *(Chapter 5-7)*

RQ3: With the design criteria clarified in RQ1 and the ASD design concepts proposed in RQ2, how can a patient-specific ASD be automatically designed to restore customized mechanics?

The general workflow for the computational design of a patient-specific ASD includes an initial modeling of one ASD design concept, model validation, and a final material or structure optimization. A computationally-efficient method that allows for the automatic design of a patient-specific ASD helps reduce the development time and cost, while ensuring the satisfactory performance of the patient-

specific ASD. Such automated design method can potentially allow surgeons to independently design patient-specific ASDs.

To develop an effective computational method that provides patient-specific ASDs for reproducing customized mechanics, three requirements need to be met: 1) a realistic computational model to predict the ASD's response, 2) a proper selection of design variables for optimization, and 3) a powerful optimization algorithm to solve the formulated optimization problem. A realistic computational model provides accurate simulation results to describe real-world objects and is a critical step in the overall computational design workflow. To realize a patient-specific ASD design, the modeling also needs to take into account patient-specific geometric information. In this thesis the geometric information is based on the dimensions of a human IVD from literature, while in real clinical scenarios the geometric information can be obtained through segmentation of the region of interest from Computed Tomography (CT) Scan. An example of using a commonly used CT segmentation tool 3D-Slicer [213] for extracting the patient-specific geometry is illustrated in Fig. 10.1. A proper selection of the design variables for optimization determines the manufacturability of the ASD as well as the convergence of the optimization process. The application of a powerful optimization algorithm for solving the formulated optimization problem helps improve the performance of the optimized ASD by avoiding that the optimization process gets stuck in a local optimum and helping to reach convergence. As shown in Fig. 4.1, the formulated optimization problem for patient-specific ASD design is featured by 1) being multi-objective, 2) having costly and noisy objective function evaluation with implicit models due to the dependence on commercial FE software, and 3) having no directly available derivatives that are also difficult to calculate. Therefore, this thesis uses derivative-free optimization algorithms, such as the direct search algorithm Nelder-Mead used in Chapter 3 and the GPS algorithm used in Chapter 4, 6, and 8, and the evolutionary algorithm GA used in Chapter 5.

Additionally, to realize a computationally-efficient design process, the computational method needs to find reasonably good solutions within reasonable computational time and cost. To achieve this, efforts can be made to improve the computational efficiency in modeling or optimization. Several strategies used in this thesis to improve the efficiency of the modeling are listed as follows:

1) The boundary conditions added to the ASD are simplified as pure angles and displacements, which spares the modeling of adjacent spinal components such as vertebrae and ligaments and thus avoids the time-consuming contact in the FE model.
2) In Chapter 3 and 4, the crisscross fiber layer is modeled using two-node beam elements instead of solid elements to improve computational efficiency.
3) In Chapter 5, CNN is used as a regression model to replace the time-consuming FE analysis.
4) In Chapter 6, the modeling of the chainmail unit cell in a chainmail-like structure is simplified as a connector to avoid solid and contact modeling.

For improving the efficiency of optimization, several strategies used in this thesis are:

1) In Chapter 3, a bio-inspired design variable linking is used to reduce the problem dimension.
2) In Chapter 4, a general-purpose k-means based clustering method is used to cluster similar design variables together to reduce the problem dimension.

Contributions:

- Proposal of a general workflow that includes an initial computational modeling, model validation, followed by optimization for the design of a patient-specific ASD. *(Chapter 3 and Chapter 8)*
- Identification of the characteristics of the formulated patient-specific ASD design problem and key aspects for realizing a computationally-efficient design process. *(Chapter 4)*
- Demonstration of possible strategies to improve the efficiency of the computational design process such as model simplification, problem dimension reduction through design variable linking, and the application of a regression model to replace the time-consuming FE analysis. *(Chapter 3-5)*
- Demonstration of the potential of using ML to realize an efficient, automated patient-specific ASD design process, which inspires future applications of ML in patient-specific implant design. *(Chapter 4 and 5)*

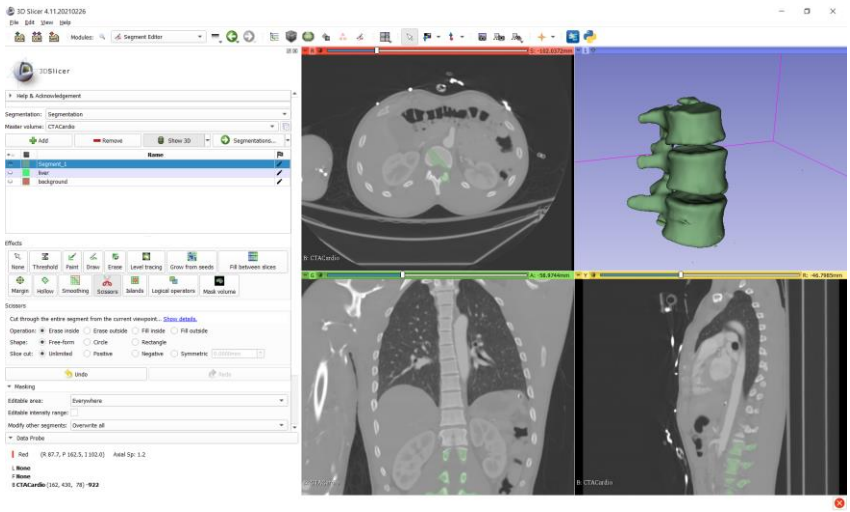

Fig. 10.1. Illustration of the CT scan segmentation using 3D-Slicer software platform to extract the patient-specific geometry for patient-specific ASD modeling.

RQ4: Given the ASD design concept proposed in RQ2 and the computational design method developed in RQ3, how can a patient-specific ASD be designed and fabricated given the manufacturing constraints of a multi-material AM technique?

With the given 3D printer as a proof-of-concept, the manufacturing constraints mainly originate from two aspects: the materials and the feature size. In view of the materials, the stiffnesses of the fourteen base materials lie at two extremities: the seven flexible materials have Young's moduli in between ~0.4-5.5 MPa, while the seven rigid materials have Young's moduli in between ~1.17-2 GPa. Therefore, there lacks available materials with a Young's modulus in between 5.5 MPa and 1.17 GPa,

which limits the achievable stiffness range of the fabricated ASD. In addition, the seven rigid materials have a yield strain of ~0.05, which limits the maximum allowable rotational angle of the ASD when fabricated with rigid materials. Lastly, the fabricated parts with the given 3D printer have an anisotropic material behavior dependent on factors such as build orientation, feature size, and raw material expiry date [214][173][189]. Therefore, the validation of the computational model is critical to quantify the influence of those factors and their interactions on the mechanical response of the fabricated ASD. For example, Fig. 10.2 shows that the model accuracy of Disc 5 in Chapter 7 whose compliant core is made from Agilus is not significantly influenced by those factors and their interactions. However, the influence is design-specific and needs to be re-evaluated given a new design concept with its specific parameters such as feature size and feature orientation. To systematically quantify and understand the influence of different factors and their interactions on the load response of the fabricated parts, an extensive study is required. In view of feature size, the maximum and minimum allowable feature size of one ASD design concept is limited by the intervertebral space and the printing resolution of the given 3D printing technique, respectively.

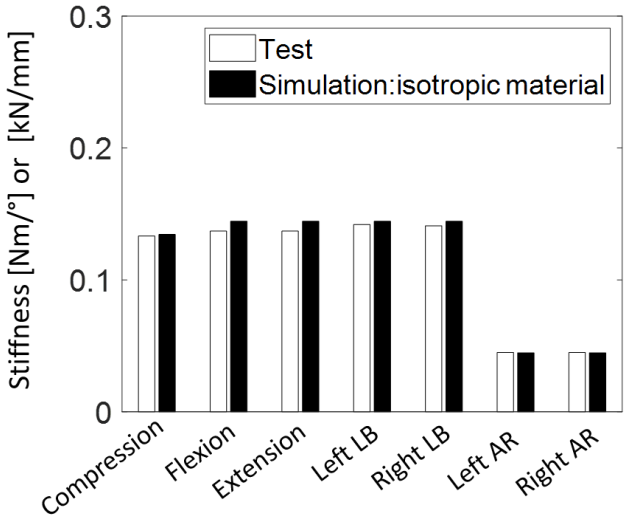

Fig. 10.2. The load response comparison of Disc 5 in Chapter 7 whose compliant core is made from Agilius based on computational model and mechanical test.

Based on the comparison of the strengths and weaknesses of different ASD design concepts in RQ2, Chapter 8 designs a patient-specific ASD solution based on the chainmail-based ASD for reproducing the mechanics of two IVDs: a human lumbar L2-L3 and a L4-L5 IVD. The feature dimension is determined based on the minimum allowable feature size with reliable mechanical properties of the given 3D printer. The computational model of the chainmail-based ASD is based on the connector model in Chapter 6, which is a simplified model to describe the behavior of the chainmail unit cell. Despite its contribution to achieving computationally efficient optimization, this simplified model neglects the sliding between the rings in a chainmail unit cell as well as the different loading bearing mechanisms of chainmail unit cells made from rigid and flexible materials. Validation results show that the computational model shows a lower prediction accuracy in left/right AR due to sliding and for designs whose chainmail-like structure is made from rigid materials. The computational model

shows a satisfactory prediction accuracy for load responses of the chainmail-based ASD with a chainmail-like structure made from flexible materials in flexion/extension and LB where less sliding between the rings is present. The good anisotropic stiffness match of the optimized ASD to two IVDs demonstrates the great potential of the multi-material chainmail-based ASD design to reproduce patient-specific mechanics. Based on the knowledge obtained throughout this thesis, Chapter 9 summarizes the challenges of the multi-material ASD design together with some general guidelines for the future development of multi-material ASD fabricated with multi-material AM.

Contributions:

- Identification of manufacturing constraints for the development of a patient-specific ASD with the given Stratasys Objet500 Connex3 inkjet-based, multi-material 3D printer. *(Chapter 6 and Chapter 8)*
- Identification of major challenges for the multi-material ASD design fabricated with multi-material AM and proposal of general guidelines to tackle such design challenges. *(Chapter 9)*
- Development of a patient-specific ASD based on the most favorable chainmail-based ASD design to demonstrate its potential in reproducing patient-specific mechanics. *(Chapter 8)*
- Validation of the computational model of the chainmail-based ASD and a systematic analysis of key factors that can potentially influence the model's accuracy. *(Chapter 8)*

10.2 Limitations and future work

The section presents the main limitations of this thesis and possible future work for improving this thesis. First, the ASD design throughout this thesis is based on the assumption of a perfect fixation between the ASD and the adjacent vertebrae. In real clinical scenarios, the ASD stability is described by a short-term stability that is dependent on the initial constraining mechanism and a long-term stability that typically relies on osteointegration of the ASD into surrounding bone [215]. Future studies should include more realistic boundary conditions into the computational model to more closely simulate the clinical settings, such as adaptable boundary conditions based on the osteointegration level. In the future, the *in vitro* mechanical test should also involve an insertion of the ASD into a cadaver spinal segment to provide a more realistic clinical test setup.

Second, the IVD goes through more complex loading conditions other than the seven loading scenarios considered in this work. As shown in Fig. 2.1, the IVD also goes through shear and tensile loads [45], together with complex loading scenarios such as simultaneous flexion plus LB [216]. Future studies should include a full set of loading scenarios in the optimization problem formulation to allow the ASD to fully restore natural mechanics. The incorporation of more loading scenarios will further complicate the optimization problem, which requires novel decoupling strategies to facilitate the efficient problem solving.

Third, the optimization performed in this work focuses on restoring the anisotropic stiffnesses, while other metrics such as NZ range and NZ stiffness are not extensively considered in this work. Chapter 6 and Chapter 8 provide possible strategies of through varying the shape and initial distance of the rings in the chainmail unit cells to adjust the NZ range. Future studies can include the exploration of innovative design concepts to restore the metrics that are unexplored in this thesis.

Lastly, this work does not consider the biocompatibility of the materials and further certification of the proposed ASD design for translating into clinical use. The qualified biomaterials for implants are expected to meet requirements concerning durability, biocompatibility, and corrosion resistance [217]. Future studies should search for a more suitable multi-material 3D printing technique that provides implant biomaterials for ASD fabrication. To ensure the accuracy of the computational model, additional mechanical properties of the base materials, such as viscosity, shear modulus, and fatigue limit, also need to be characterized. In addition to requirements for materials, the ASD fabrication needs to comply with a set of rules and regulations for 3D printed medical devices to ensure the safety, quality, and efficacy before entering into market [218]. Although there is no 3D printing-targeted regulatory framework available, the existing regulations for medical devices are comprehensive and also applicable to 3D printed implants. Factors that determine the regulatory framework for 3D printed medical devices involve the location of the market where the product is targeted for (i.e., Europe, United States, Australia, etc), the product's risk category, and whether certain exemptions may apply, etc. In particular, 3D printed, personalized medical devices that are manufactured specifically for one particular patient can be exempted from most, if not all, regulatory requirements [219]. The definition of customized medical device is limited to being not generally available (i.e., not for commercial distribution) and no more than five devices per device type per year for one manufacturer [220]. Such rules aim to provide an efficient mechanism for providing patient care by putting the responsibility for ensuring compliance to regulations such as materials safety on the manufacturers [220]. An exemption for customized devices will only be issued when a series of conditions are met, such as that the manufacture and use of the device occur under appropriate quality management systems and that a documentation is provided by the health institution(s) to justify that the target patient's specific needs cannot be met by an equivalent device available on the market. Additional product regulations such as product liability and criminal law should also be considered for the 3D printing technique [221]. It is to be noted that the regulations for 3D printed, customized medical devices are still controversial, as some stakeholders think that the regulations are simply unworkable and lead to excessive costs [222]. Future studies should involve an extensive study to define the relative regulation framework for certifying the patient-specific ASD and develop a comprehensive certification plan.

Chapter 11. Summary and conclusion

This thesis performs a pioneering work in exploring the feasibility of using multi-material AM for the design and fabrication of patient-specific, multi-material ASDs that improve the state-of-the-art. Different conceptual designs of ASD are proposed in this thesis and their performances are evaluated using computational design methods and mechanical tests. This works shows the great potential of incorporating biomimetic structures into the ASD design for natural mechanics restoration, as demonstrated by the good performances of the ASD designs proposed in Chapters 3-6. Especially, the strategy of incorporating a chainmail-like structure into the ASD design (Chapter 6) helps restore the nonlinear rotational load response of an IVD. The mechanical test of the 3D printed ASD designs performed in Chapter 7 validates the design concepts by showing that the incorporation of a biomimetic crisscross fiber-like structure does help to improve the ASD's torsional stiffness and that the chainmail-based ASD does show a strain-stiffening response. Considering the great potential of the chainmail-based ASD, this design concept is used in Chapter 8 for realizing a patient-specific ASD with a validated computational model. Despite the limited options of base materials, the optimized ASD is able to show a viscoelastic, nonlinear, anisotropic behavior with reasonably good stiffness match to an IVD.

The computational design process to develop a patient-specific ASD proposed in this thesis involves an initial modeling of one ASD design concept and subsequent material optimization. To improve the efficiency of the computational design, Chapter 3 employs a bio-inspired design variable linking to reduce the problem dimension, while Chapter 4 proposes a more general-purpose design variable linking method through clustering. Chapter 5 further provides a strategy of using ANN to replace the time-consuming FE analysis. The proposed computational method is proven to be effective to develop patient-specific ASDs with customized mechanics. Besides, with strategies of problem dimension reduction and using regression model, the efficiency of the computational design process can be significantly improved. Chapter 9 summarizes the challenges in the multi-material ASD design fabricated with multi-material AM and provides some general guidelines based on the knowledge obtained throughout this work. Although constrained by a simplified FE model and limited loading scenarios considered, this thesis successfully provides alternative, verified multi-material ASD design concepts fabricated with multi-material AM, as well as an effective and efficient computational method to design them. The designs proposed serve as inspiration for future ASD design and general guidelines are given for their future development.

References

[1] G.B.J. Andersson, Epidemiology of low back pain Epidemiology of low back pain, 6470 (2017). https://doi.org/10.1080/17453674.1998.11744790.

[2] I.A. Steenstra, J.H. Verbeek, M.W. Heymans, P.M. Bongers, Prognostic factors for duration of sick leave in patients sick listed with acute low back pain: A systematic review of the literature, Occup. Environ. Med. 62 (2005) 851–860. https://doi.org/10.1136/oem.2004.015842.

[3] M.L. Skovron, Epidemiology of low back pain, Baillieres. Clin. Rheumatol. 6 (1992) 559–573. https://doi.org/10.1016/S0950-3579(05)80127-X.

[4] M. Szpalski, R. Gunzburg, M. Mayer, Spine arthroplasty: A historical review, Eur. Spine J. 11 (2002) 65–84. https://doi.org/10.1007/s00586-002-0474-y.

[5] T. Oichi, Y. Taniguchi, Y. Oshima, S. Tanaka, T. Saito, Pathomechanism of intervertebral disc degeneration, Jor Spine. 3 (2020) 1–9. https://doi.org/10.1002/jsp2.1076.

[6] M.D. Humzah, R.W. Soames, Human intervertebral disc: Structure and function, in: Anat. Rec., 1988: pp. 337–356. https://doi.org/10.1002/ar.1092200402.

[7] M.D. Humzah, R.W. Soames, Human lntervertebral Disc: Structure and Function, 356 (1988) 337–356.

[8] M.G. Gardner-Morse, I.A.F. Stokes, Structural behavior of human lumbar spinal motion segments, J. Biomech. 37 (2004) 205–212. https://doi.org/10.1016/j.jbiomech.2003.10.003.

[9] D.M. Elliott, L.A. Setton, Anisotropic and Inhomogeneous Tensile Behavior of the Human Anulus Fibrosus: Experimental Measurement and Material Model Predictions, J. Biomech. Eng. 123 (2001) 256. https://doi.org/10.1115/1.1374202.

[10] X.D. Cui, H.T. Li, W. Zhang, L.L. Zhang, Z.P. Luo, H.L. Yang, Mid- to long-term results of total disc replacement for lumbar degenerative disc disease: A systematic review, J. Orthop. Surg. Res. 13 (2018) 1–12. https://doi.org/10.1186/s13018-018-1032-6.

[11] J.J. Yue, R. Bertagnoli, P.C. McAFEE, H.S. An, Motion preservation surgery of the spine: advanced techniques and controversies, Elsevier Health Sciences, 2008.

[12] P. O'Leary, M. Nicolakis, M.A. Lorenz, L.I. Voronov, M.R. Zindrick, A. Ghanayem, R.M. Havey, G. Carandang, M. Sartori, I.N. Gaitanis, Response of Charite total disc replacement under physiologic loads: prosthesis component motion patterns, Spine J. 5 (2005) 590–599.

[13] Jp. Lemaire, W. Skalli, F. Lavaste, A. Templier, F. Mendes, A. Diop, V. Sauty, E. Laloux, Intervertebral disc prosthesis: results and prospects for the year 2000, Clin. Orthop. Relat. Res.

337 (1997) 64–76.

[14] K.R. Chin, J.R. Lubinski, K.B. Zimmers, B.E. Sands, F. Pencle, Clinical experience and two-year follow-up with a one-piece viscoelastic cervical total disc replacement, J. Spine Surg. 3 (2017) 630–640. https://doi.org/10.21037/jss.2017.12.03.

[15] J. yves Lazennec, A. Aaron, O. Ricart, J.P. Rakover, The innovative viscoelastic CP ESP cervical disk prosthesis with six degrees of freedom: biomechanical concepts, development program and preliminary clinical experience, Eur. J. Orthop. Surg. Traumatol. 26 (2016) 9–19. https://doi.org/10.1007/s00590-015-1695-1.

[16] E.C. Benzel, I.H. Lieberman, E.R. Ross, R.J. Linovitz, J. Kuras, K. Zimmers, Mechanical characterization of a viscoelastic disc for lumbar total disc replacement, J. Med. Devices, Trans. ASME. 5 (2011) 1–7. https://doi.org/10.1115/1.4003536.

[17] A.G. Patwardhan, M.N. Tzermiadianos, P.P. Tsitsopoulos, L.I. Voronov, S.M. Renner, M.L. Reo, G. Carandang, K. Ritter-Lang, R.M. Havey, Primary and coupled motions after cervical total disc replacement using a compressible six-degree-of-freedom prosthesis, Eur. Spine J. 21 (2012) 618–629. https://doi.org/10.1007/s00586-010-1575-7.

[18] S. Blumenthal, P.C. McAfee, R.D. Guyer, S.H. Hochschuler, F.H. Geisler, R.T. Holt, R.J. Garcia, J.J. Regan, D.D. Ohnmeiss, A Prospective, Randomized, Multicenter Food and Drug Administration Investigational Device Exemptions Study of Lumbar Total Disc Replacement With the CHARITÉ™ Artificial Disc Versus Lumbar Fusion: Part I: Evaluation of Clinical Outcomes, Spine (Phila. Pa. 1976). 30 (2005). http://journals.lww.com/spinejournal/Fulltext/2005/07150/A_Prospective,_Randomized,_Multicenter_Food_and.3.aspx.

[19] A.G. Patwardhan, R.M. Havey, Prosthesis design influences segmental contribution to total cervical motion after cervical disc arthroplasty, Eur. Spine J. (2019) 1–9. https://doi.org/10.1007/s00586-019-06064-4.

[20] W.J. Choy, R.J. Mobbs, Comment Current state of 3D-printed custom-made spinal implants, Lancet Digit. Heal. 1 (2019) e149–e150. https://doi.org/10.1016/S2589-7500(19)30081-0.

[21] M.J. Mirzaali, A. Herranz de la Nava, D. Gunashekar, M. Nouri-Goushki, R.P.E. Veeger, Q. Grossman, L. Angeloni, M.K. Ghatkesar, L.E. Fratila-Apachitei, D. Ruffoni, E.L. Doubrovski, A.A. Zadpoor, Mechanics of bioinspired functionally graded soft-hard composites made by multi-material 3D printing, Compos. Struct. 237 (2020). https://doi.org/10.1016/j.compstruct.2020.111867.

[22] T. Chen, J. Mueller, K. Shea, Integrated Design and Simulation of Tunable, Multi-State

Structures Fabricated Monolithically with Multi-Material 3D Printing, Sci. Rep. 7 (2017) 1–8. https://doi.org/10.1038/srep45671.

[23] J.L. Burnard, W.C.H. Parr, W.J. Choy, W.R. Walsh, R.J. Mobbs, 3D-printed spine surgery implants: a systematic review of the efficacy and clinical safety profile of patient-specific and off-the-shelf devices, Eur. Spine J. 29 (2020) 1248–1260. https://doi.org/10.1007/s00586-019-06236-2.

[24] A.Q.A. TEO, D.Q.K. NG, P. LEE, G.K. O'NEILL, Point-of-Care 3D Printing: A Feasibility Study of Using 3D Printing for Orthopaedic Trauma, Injury. (2021). https://doi.org/10.1016/j.injury.2021.02.041.

[25] A. Gonzalez Alvarez, P.L. Evans, L. Dovgalski, I. Goldsmith, Design, additive manufacture and clinical application of a patient-specific titanium implant to anatomically reconstruct a large chest wall defect, Rapid Prototyp. J. 27 (2021) 304–310. https://doi.org/10.1108/RPJ-08-2019-0208.

[26] K. Willemsen, R. Nizak, H.J. Noordmans, R.M. Castelein, H. Weinans, M.C. Kruyt, Challenges in the design and regulatory approval of 3D-printed surgical implants: a two-case series, Lancet Digit. Heal. 1 (2019) e163–e171. https://doi.org/10.1016/S2589-7500(19)30067-6.

[27] R.J. Mobbs, M. Coughlan, R. Thompson, C.E. Sutterlin, K. Phan, The utility of 3D printing for surgical planning and patient-specific implant design for complex spinal pathologies: Case report, J. Neurosurg. Spine. 26 (2017) 513–518. https://doi.org/10.3171/2016.9.SPINE16371.

[28] P. Honigmann, N. Sharma, B. Okolo, U. Popp, B. Msallem, F.M. Thieringer, Patient-specific surgical implants made of 3D printed PEEK: Material, technology, and scope of surgical application, Biomed Res. Int. 2018 (2018). https://doi.org/10.1155/2018/4520636.

[29] T. Amin, W.C.H. Parr, R.J. Mobbs, Opinion piece: patient-specific implants may be the next big thing in spinal surgery, J. Pers. Med. 11 (2021). https://doi.org/10.3390/jpm11060498.

[30] J. Noailly, J.A. Planell, D. Lacroix, On the collagen criss-cross angles in the annuli fibrosi of lumbar spine finite element models, Biomech. Model. Mechanobiol. 10 (2011) 203–219.

[31] J.H. Yoder, Intervertebral disc structure and mechanical function under physiological loading quantified non-invasively utilizing MRI and image registration, (2014).

[32] J.J. Cassidy, A. Hiltner, E. Baer, Hierarchical structure of the intervertebral disc, Connect. Tissue Res. 23 (1989) 75–88. https://doi.org/10.3109/03008208909103905.

[33] X. Gao, Q. Zhu, W. Gu, An Anisotropic Multiphysics Model for Intervertebral Disk, 83 (2016) 1–8. https://doi.org/10.1115/1.4031793.

[34] D.M. Elliott, L.A. Setton, Anisotropic and Inhomogeneous Tensile Behavior of the Human Anulus Fibrosus: Experimental Measurement and Material Model Predictions, J. Biomech. Eng. 123 (2001) 256. https://doi.org/10.1115/1.1374202.

[35] Y. Fujita, D.R. Wagner, A.A. Biviji, N.A. Duncan, J.C. Lotz, Anisotropic shear behavior of the annulus fibrosus : effect of harvest site and tissue prestrain, 22 (2000) 349–357.

[36] H.L. Guerin, D.M. Elliott, Quantifying the contributions of structure to annulus fibrosus mechanical function using a nonlinear, anisotropic, hyperelastic model, J. Orthop. Res. 25 (2007) 508–516.

[37] M.M. Panjabi, The stabilizing system of the spine. Part II. neutral zone and instability hypothesis, J. Spinal Disord. 5 (1992) 390–397. https://doi.org/10.1097/00002517-199212000-00002.

[38] K. Gelse, E. Pöschl, T. Aigner, Collagens - Structure, function, and biosynthesis, Adv. Drug Deliv. Rev. 55 (2003) 1531–1546. https://doi.org/10.1016/j.addr.2003.08.002.

[39] K. Luoma, H. Riihimäki, R. Luukkonen, R. Raininko, E. Viikari-Juntura, A. Lamminen, Low back pain in relation to lumbar disc degeneration, Spine (Phila. Pa. 1976). 25 (2000) 487–492.

[40] K.D. Van Den Eerenbeemt, R.W. Ostelo, B.J. Van Royen, W.C. Peul, M.W. Van Tulder, Total disc replacement surgery for symptomatic degenerative lumbar disc disease: A systematic review of the literature, Eur. Spine J. 19 (2010) 1262–1280. https://doi.org/10.1007/s00586-010-1445-3.

[41] E. Dawson, J. Bernbeck, The surgical treatment of low back pain, Phys. Med. Rehabil. Clin. 9 (1998) 489–495.

[42] P. Frelinghuysen, R.C. Huang, F.P. Girardi, F.P. Cammisa, Lumbar total disc replacement part I: Rationale, biomechanics, and implant types, Orthop. Clin. North Am. 36 (2005) 293–299. https://doi.org/10.1016/j.ocl.2005.02.014.

[43] R. Bertagnoli, J.J. Yue, R. V. Shah, R. Nanieva, F. Pfeiffer, A. Fenk-Mayer, T. Kershaw, D.S. Husted, The treatment of disabling single-level lumbar discogenic low back pain with total disc arthroplasty utilizing the prodisc prosthesis: A prospective study with 2-year minimum follow-up, Spine (Phila. Pa. 1976). 30 (2005) 2230–2236. https://doi.org/10.1097/01.brs.0000182217.87660.40.

[44] R.D. Guyer, P.C. McAfee, R.J. Banco, F.D. Bitan, A. Cappuccino, F.H. Geisler, S.H. Hochschuler, R.T. Holt, L.G. Jenis, M.E. Majd, J.J. Regan, S.G. Tromanhauser, D.C. Wong, S.L. Blumenthal, Prospective, randomized, multicenter Food and Drug Administration investigational device exemption study of lumbar total disc replacement with the CHARITÉ artificial disc versus lumbar fusion: Five-year follow-up, Spine J. 9 (2009) 374–386.

https://doi.org/10.1016/j.spinee.2008.08.007.

[45] H.J. Wilke, K. Wenger, L. Claes, Testing criteria for spinal implants: Recommendations for the standardization of in vitro stability testing of spinal implants, Eur. Spine J. 7 (1998) 148–154. https://doi.org/10.1007/s005860050045.

[46] U.L.F. Fernstrom, Arthroplasty with intercorporal endoprothesis in herniated disc and in painful disc, Acta Chir Scand Suppl. 357 (1966) 154–159.

[47] M.A. Rousseau, D.S. Bradford, R. Bertagnoli, S.S. Hu, J.C. Lotz, Disc arthroplasty design influences intervertebral kinematics and facet forces, Spine J. 6 (2006) 258–266. https://doi.org/10.1016/j.spinee.2005.07.004.

[48] C.A.M. Jacobs, C.J. Siepe, K. Ito, Viscoelastic cervical total disc replacement devices: Design concepts, Spine J. 000 (2020). https://doi.org/10.1016/j.spinee.2020.08.007.

[49] S. Botolin, C. Puttlitz, T. Baldini, A. Petrella, E. Burger, C. Abjornson, V. Patel, Facet joint biomechanics at the treated and adjacent levels after total disc replacement, Spine (Phila. Pa. 1976). 36 (2011) 27–32. https://doi.org/10.1097/BRS.0b013e3181d2d071.

[50] C.K. Park, K.S. Ryu, W.H. Jee, Degenerative changes of discs and facet joints in lumbar total disc replacement using ProDisc II: Minimum two-year follow-up, Spine (Phila. Pa. 1976). 33 (2008) 1755–1761. https://doi.org/10.1097/BRS.0b013e31817b8fed.

[51] R. Lehman, A. Bevevino, D. Brewer, A. Skelly, P. Anderson, A systematic review of cervical artificial disc replacement wear characteristics and durability, Evid. Based. Spine. Care. J. 3 (2012) 31–38. https://doi.org/10.1055/s-0031-1298606.

[52] C.K. Lee, V.K. Goel, Artificial disc prosthesis: Design concepts and criteria, Spine J. 4 (2004). https://doi.org/10.1016/j.spinee.2004.07.011.

[53] P. O'Leary, M. Nicolakis, M.A. Lorenz, L.I. Voronov, M.R. Zindrick, A. Ghanayem, R.M. Havey, G. Carandang, M. Sartori, I.N. Gaitanis, S. Fronczak, A.G. Patwardhan, Response of Charité total disc replacement under physiologic loads: Prosthesis component motion patterns, Spine J. 5 (2005) 590–599. https://doi.org/10.1016/j.spinee.2005.06.015.

[54] A.E. Bowden, H.L. Guerin, M.L. Villarraga, A.G. Patwardhan, J.A. Ochoa, Quality of motion considerations in numerical analysis of motion restoring implants of the spine, Clin. Biomech. 23 (2008) 536–544. https://doi.org/10.1016/j.clinbiomech.2007.12.010.

[55] W. Anderst, E. Baillargeon, W. Donaldson, J. Lee, J. Kang, Motion Path of the Instant Center of Rotation in the Cervical Spine, Spine (Phila Pa 1976). 38 (2013) E594–E601. https://doi.org/10.1097/BRS.0b013e31828ca5c7.Motion.

[56] Y. Kotani, B.W. Cunningham, K. Abumi, A.E. Dmitriev, N. Hu, M. Ito, Y. Shikinami, P.C. McAfee, A. Minami, Multidirectional flexibility analysis of anterior and posterior lumbar artificial disc reconstruction: In vitro human cadaveric spine model, Eur. Spine J. 15 (2006) 1511–1520. https://doi.org/10.1007/s00586-006-0086-z.

[57] C. Barrey, A. Darnis, Current strategies for the restoration of adequate lordosis during lumbar fusion, World J. Orthop. 6 (2015) 117–126. https://doi.org/10.5312/wjo.v6.i1.117.

[58] M.F. Eijkelkamp, C.C. Van Donkelaar, A.G. Veldhuizen, J.R. Van Horn, J.M. Huyghe, G.J. Verkerke, Chapter 2 Requirements for an artificial intervertebral disc, Int J Artif Organs Int. J. Artif. Organs. 24 (2001) 311–21.

[59] K. Büttner-Janz, R.D. Guyer, D.D. Ohnmeiss, Indications for lumbar total disc replacement: Selecting the right patient with the right indication for the right total disc, Int. J. Spine Surg. 8 (2014). https://doi.org/10.14444/1012.

[60] J.P. Kostuik, Alternatives to spinal fusion, Orthop. Clin. North Am. 29 (1998) 701–715. https://doi.org/10.1016/S0030-5898(05)70042-0.

[61] R.J. Mobbs, J.X. Julian Li, K. Phan, Anterior longitudinal ligament reconstruction to reduce hypermobility of cervical and lumbar disc arthroplasty, Asian Spine J. 11 (2017) 943–950. https://doi.org/10.4184/asj.2017.11.6.943.

[62] M.M. Panjabi, The Stabilizing System of the Spine . Part II . Neutral Zone and Instability Hypothesis, 5 (1992) 390–397.

[63] T. Zander, A. Rohlmann, G. Bergmann, Influence of different artificial disc kinematics on spine biomechanics, Clin. Biomech. 24 (2009) 135–142. https://doi.org/10.1016/j.clinbiomech.2008.11.008.

[64] P.C. McAfee, B.W. Cunningham, V. Hayes, F. Sidiqi, M. Dabbah, J.C. Sefter, N. Hu, H. Beatson, Biomechanical analysis of rotational motions after disc arthroplasty: Implications for patients with adult deformities, Spine (Phila. Pa. 1976). 31 (2006) 152–160. https://doi.org/10.1097/01.brs.0000234782.89031.03.

[65] A. Faizan, V.K. Goel, S.R. Garfin, C.M. Bono, H. Serhan, A. Biyani, H. Elgafy, M. Krishna, T. Friesem, Do design variations in the artificial disc influence cervical spine biomechanics? A finite element investigation, Eur. Spine J. 21 (2012) 653–662. https://doi.org/10.1007/s00586-009-1211-6.

[66] G. Denozière, D.N. Ku, Biomechanical comparison between fusion of two vertebrae and implantation of an artificial intervertebral disc, J. Biomech. 39 (2006) 766–775. https://doi.org/10.1016/j.jbiomech.2004.07.039.

[67] O. David, M. Shoham, Compliant Mechanism as a Motion-Preserving Artificial Spinal Disc: A Novel Concept, J. Eng. Sci. Med. Diagnostics Ther. 3 (2020) 1–10. https://doi.org/10.1115/1.4045609.

[68] Y. Shikinami, Y. Kawabe, K. Yasukawa, K. Tsuta, Y. Kotani, K. Abumi, A biomimetic artificial intervertebral disc system composed of a cubic three-dimensional fabric, Spine J. 10 (2010) 141–152. https://doi.org/10.1016/j.spinee.2009.10.008.

[69] M. Javaid, A. Haleem, Additive manufacturing applications in medical cases: A literature based review, Alexandria J. Med. 54 (2018) 411–422. https://doi.org/10.1016/j.ajme.2017.09.003.

[70] P. Tack, J. Victor, P. Gemmel, L. Annemans, 3D-printing techniques in a medical setting: A systematic literature review, Biomed. Eng. Online. 15 (2016) 1–21. https://doi.org/10.1186/s12938-016-0236-4.

[71] J. Haq, N. Patel, K. Weimer, N.S. Matthews, Single stage treatment of ankylosis of the temporomandibular joint using patient-specific total joint replacement and virtual surgical planning, Br. J. Oral Maxillofac. Surg. 52 (2014) 350–355. https://doi.org/10.1016/j.bjoms.2014.01.004.

[72] K. Phan, A. Sgro, M.M. Maharaj, P. D'Urso, R.J. Mobbs, Application of a 3D custom printed patient specific spinal implant for C1/2 arthrodesis, J. Spine Surg. 2 (2016) 314–318. https://doi.org/10.21037/jss.2016.12.06.

[73] N. De Beer, C. Scheffer, Reducing subsidence risk by using rapid manufactured patient-specific intervertebral disc implants, Spine J. 12 (2012) 1060–1066. https://doi.org/10.1016/j.spinee.2012.10.003.

[74] A. Katsuura, S. Hukuda, Y. Saruhashi, K. Mori, Kyphotic malalignment after anterior cervical fusion is one of the factors promoting the degenerative process in adjacent intervertebral levels, Eur. Spine J. 10 (2001) 320–324. https://doi.org/10.1007/s005860000243.

[75] N. Meisel, C. Williams, An Investigation of Key Design for Additive Manufacturing Constraints in Multimaterial Three-Dimensional Printing, J. Mech. Des. Trans. ASME. 137 (2015) 1–9. https://doi.org/10.1115/1.4030991.

[76] I.A.F. Stokes, M. Gardner-Morse, A database of lumbar spinal mechanical behavior for validation of spinal analytical models, J. Biomech. 49 (2016) 780–785. https://doi.org/10.1016/j.jbiomech.2016.01.035.

[77] T. Chen, J. Mueller, K. Shea, Design and fabrication of a bistable unit actuator with multi-material additive manufacturing, Annu. Int. Solid Free. Fabr. Symp. . (2016) 2060–2076.

[78] W. Anderst, E. Baillargeon, W. Donaldson, J. Lee, J. Kang, Motion path of the instant center of

rotation in the cervical spine during in vivo dynamic flexion-extension: implications for artificial disc design and evaluation of motion quality following arthrodesis, Spine (Phila. Pa. 1976). 38 (2013) E594.

[79] H. Schmidt, F. Heuer, U. Simon, A. Kettler, A. Rohlmann, L. Claes, H. Wilke, Application of a new calibration method for a three-dimensional finite element model of a human lumbar annulus fibrosus, 21 (2006) 337–344. https://doi.org/10.1016/j.clinbiomech.2005.12.001.

[80] G. Marini, S.J. Ferguson, Modelling the influence of heterogeneous annulus material property distribution on intervertebral disk mechanics, Ann. Biomed. Eng. 42 (2014) 1760–1772. https://doi.org/10.1007/s10439-014-1025-5.

[81] A. Malandrino, J. Noailly, D. Lacroix, Regional annulus fibre orientations used as a tool for the calibration of lumbar intervertebral disc finite element models, Comput. Methods Biomech. Biomed. Engin. 16 (2013) 923–928. https://doi.org/10.1080/10255842.2011.644539.

[82] Z. Yu, K. Shea, T. Stankovic, A Computational Method for the Design of an Additively Manufactured Personalized Artificial Spinal Disc With Physiological Stiffness Under Multiple Loading Conditions, J. Mech. Des. 141 (2019) 101406. https://doi.org/10.1115/1.4043931.

[83] T.J.R. Hughes, The finite element method: linear static and dynamic finite element analysis, Courier Corporation, 2012.

[84] T.E. Bruns, D.A. Tortorelli, Topology optimization of non-linear elastic structures and compliant mechanisms, 190 (2001).

[85] M.S. Shephard, M.W. Beall, R.M. O'bara, B.E. Webster, Toward simulation-based design, Finite Elem. Anal. Des. 40 (2004) 1575–1598.

[86] T.G. Kolda, R.M. Lewis, V. Torczon, Optimization by Direct Search: New Perspectives on Some Classical and Modern Methods, SIAM Rev. 45 (2005) 385–482. https://doi.org/10.1137/s003614450242889.

[87] M. Costas, J. Díaz, L. Romera, S. Hernández, A multi-objective surrogate-based optimization of the crashworthiness of a hybrid impact absorber, Int. J. Mech. Sci. 88 (2014) 46–54. https://doi.org/10.1016/j.ijmecsci.2014.07.002.

[88] A.-T. Nguyen, S. Reiter, P. Rigo, A review on simulation-based optimization methods applied to building performance analysis, Appl. Energy. 113 (2014) 1043–1058.

[89] W. Spendley, G.R. Hext, F.R. Himsworth, Sequential Application of Simplex Designs in Optimisation and Evolutionary Operation of Simplex Designs in Optimisation and Evolutionary, 1706 (2012).

[90] R. Fletcher, Practical methods of optimization, John Wiley & Sons, 2013.

[91] J.A. Nelder, R. Mead, A Simplex Method for Function Minimization, Comput. J. 7 (1965) 308–313. https://doi.org/10.1093/comjnl/7.4.308.

[92] M.A. Luersen, R. Le Riche, F. Guyon, A constrained , globalized , and bounded Nelder – Mead method for engineering optimization, 54 (2004) 43–54. https://doi.org/10.1007/s00158-003-0320-9.

[93] A. Cozad, N. V. Sahinidis, D.C. Miller, Learning surrogate models for simulation-based optimization, AIChE J. 60 (2014) 2211–2227. https://doi.org/10.1002/aic.14418.

[94] R. Korez, B. Likar, F. Pernuš, T. Vrtovec, Parametric modeling of the intervertebral disc space in 3D: Application to CT images of the lumbar spine, Comput. Med. Imaging Graph. 38 (2014) 596–605. https://doi.org/10.1016/j.compmedimag.2014.04.008.

[95] R. Eberlein, G.A. Holzapfel, C.A.J. Schulze-, An Anisotropic Model for Annulus Tissue and Enhanced Finite Element Analyses of Intact Lumbar Disc Bodies, 5842 (2007). https://doi.org/10.1080/10255840108908005.

[96] T. Belytschko, R.F. Kulak, A.B. Schultz, J.O. Galante, Finite element stress analysis of an intervertebral disc, J. Biomech. 7 (1974) 277–285. https://doi.org/10.1016/0021-9290(74)90019-0.

[97] M.H. Wright, Nelder, Mead, and the Other Simplex Method, Doc. Math. I (2012) 271–276. http://math.uiuc.edu/documenta/vol-ismp/42_wright-margaret.pdf.

[98] S.H. Tan, E.C. Teo, H.C. Chua, Quantitative three-dimensional anatomy of cervical, thoracic and lumbar vertebrae of Chinese Singaporeans, Eur. Spine J. 13 (2004) 137–146. https://doi.org/10.1007/s00586-003-0586-z.

[99] H.P. Mehta, E.R. Santos, D. Sembrano, J N; Hunt, MA; Parr, A; Polly Jr., DW; Nuckley, Radiographic Measurement of Cervical Disc Height and the Inter-Surgeon Variability in its Application, (2012) 2192.

[100] H.S. Kim, J.S. Song, W. Heo, J.H. Cha, D.Y. Rhee, Comparative Study between a Curved and a Wedge PEEK Cage for Single-level Anterior Cervical Discectomy and Interbody Fusion, 9 (2012) 181–186.

[101] A.A. White, M.M. Panjabi, Clinical biomechanics of the spine, Lippincott, 1978.

[102] S.P. Moroney, A.B. Schultz, J.A.A. Miller, G.B.J. Andersson, Load-displacement properties of lower cervical spine motion segments, J. Biomech. 21 (1988) 769–779. https://doi.org/10.1016/0021-9290(88)90285-0.

[103] J. D'Errico, fminsearchbnd,fminsearchcon, (2012).

[104] E. Eltes, Automated detection , 3D segmentation and analysis of high resolution spine MR images using statistical shape models Automated detection , 3D segmentation and analysis of high resolution spine MR images using statistical, (n.d.). https://doi.org/10.1088/0031-9155/57/24/8357.

[105] S. Razavi, B.A. Tolson, D.H. Burn, Numerical assessment of metamodelling strategies in computationally intensive optimization, Environ. Model. Softw. 34 (2012) 67–86. https://doi.org/10.1016/j.envsoft.2011.09.010.

[106] A.J. Michalek, M.R. Buckley, L.J. Bonassar, I. Cohen, J.C. Iatridis, Measurement of local strains in intervertebral disc anulus fibrosus tissue under dynamic shear: Contributions of matrix fiber orientation and elastin content, J. Biomech. 42 (2009) 2279–2285. https://doi.org/10.1016/j.jbiomech.2009.06.047.

[107] S. Shan, G.G. Wang, Survey of modeling and optimization strategies to solve high-dimensional design problems with computationally-expensive black-box functions, (2010) 219–241. https://doi.org/10.1007/s00158-009-0420-2.

[108] L.M. Hvattum, F. Glover, Finding local optima of high-dimensional functions using direct search methods, Eur. J. Oper. Res. 195 (2009) 31–45. https://doi.org/10.1016/j.ejor.2008.01.039.

[109] H. Sun, H. V. Burton, H. Huang, Machine learning applications for building structural design and performance assessment: State-of-the-art review, J. Build. Eng. 33 (2021) 101816. https://doi.org/10.1016/j.jobe.2020.101816.

[110] K. Deb, K. Saxena, D., Searching for Pareto-optimal solutions through dimensionality reduction for certain large-dimensional multi-objective optimization problems, 2006 IEEE Congr. Evol. Comput. (2006) 3353--3360. http://www.rkursem.com/bbase/bibitem-30165.html.

[111] A. Brand, M. Stanford, C. Swan, How do tissues respond and adapt to stresses around a prosthesis? A primer on finite element stress analysis for orthopaedic surgeons., Iowa Orthop. J. 23 (2003) 13.

[112] L. Angeles, Some Approximation Concepts for Structural Synthesis, 12 (n.d.). https://doi.org/10.2514/3.49321.

[113] U. Kirsch, Approximate Models for Structural Optimization, 1 (n.d.) 289–325.

[114] R.M. Plckettjr, Automated Structural Synthesis Using a Reduced Number of Design Coordinates, (1973). https://doi.org/10.2514/3.50489.

[115] P. Hajela, The Controlled Growth Method — A Tool for Structural Optimization, 20 (n.d.) 1440–

1441. https://doi.org/10.2514/3.51204.

[116] H.J.C. Barbosa, A.C.C. Lemonge, C.C.H. Borges, A genetic algorithm encoding for cardinality constraints and automatic variable linking in structural optimization, Eng. Struct. 30 (2008) 3708–3723. https://doi.org/10.1016/j.engstruct.2008.06.014.

[117] F. Camastra, A. Vinciarelli, Clustering methods, Adv. Inf. Knowl. Process. (2015) 131–167. https://doi.org/10.1007/978-1-4471-6735-8_6.

[118] N. Aulig, M. Olhofer, State-based representation for structural topology optimization and application to crashworthiness, 2016 IEEE Congr. Evol. Comput. CEC 2016. (2016) 1642–1649. https://doi.org/10.1109/CEC.2016.7743985.

[119] K. Liu, D. Detwiler, A. Tovar, Optimal design of nonlinear multimaterial structures for crashworthiness using cluster analysis, J. Mech. Des. Trans. ASME. 139 (2017) 1–11. https://doi.org/10.1115/1.4037620.

[120] H. Dong, B. Song, P. Wang, Z. Dong, Surrogate-based optimization with clustering-based space exploration for expensive multimodal problems, Struct. Multidiscip. Optim. 57 (2018) 1553–1577. https://doi.org/10.1007/s00158-017-1826-x.

[121] E. Holmberg, B. Torstenfelt, A. Klarbring, Stress constrained topology optimization, Struct. Multidiscip. Optim. 48 (2013) 33–47. https://doi.org/10.1007/s00158-012-0880-7.

[122] P. Berkhin, A survey of clustering data mining techniques, in: Group. Multidimens. Data, Springer, 2006: pp. 25–71.

[123] D. Arthur, S. Vassilvitskii, k-means++: The advantages of careful seeding, Society for Industrial and Applied Mathematics, 2007.

[124] R.L. Thorndike, Who belongs in the family?, Psychometrika. 18 (1953) 267–276. https://doi.org/10.1007/BF02289263.

[125] F. Heuer, H. Schmidt, Z. Klezl, L. Claes, H.-J. Wilke, Stepwise reduction of functional spinal structures increase range of motion and change lordosis angle, J. Biomech. 40 (2014) 271–280. https://doi.org/10.1016/j.jbiomech.2006.01.007.

[126] S. Wang, W.M. Park, H.R. Gadikota, J. Miao, Y.H. Kim, K.B. Wood, G. Li, A combined numerical and experimental technique for estimation of the forces and moments in the lumbar intervertebral disc, Comput. Methods Biomech. Biomed. Engin. 16 (2013) 1278–1286. https://doi.org/10.1080/10255842.2012.668537.

[127] L.J. Gibson, Cellular solids, Mrs Bull. 28 (2003) 270–274.

[128] O. Weeger, N. Boddeti, S.K. Yeung, S. Kaijima, M.L. Dunn, Digital design and nonlinear

simulation for additive manufacturing of soft lattice structures, Addit. Manuf. 25 (2019) 39–49. https://doi.org/10.1016/j.addma.2018.11.003.

[129] S. Xu, J. Shen, S. Zhou, X. Huang, Y.M. Xie, Design of lattice structures with controlled anisotropy, Mater. Des. 93 (2016) 443–447. https://doi.org/10.1016/j.matdes.2016.01.007.

[130] A.A. Zadpoor, Meta-biomaterials, Biomater. Sci. 8 (2020) 18–38. https://doi.org/10.1039/c9bm01247h.

[131] D. Chen, M. Skouras, B. Zhu, W. Matusik, Computational discovery of extremal microstructure families, Sci. Adv. 4 (2018) 1–8. https://doi.org/10.1126/sciadv.aao7005.

[132] J. Nguyen, S. in Park, D. Rosen, Heuristic optimization method for cellular structure design of light weight components, Int. J. Precis. Eng. Manuf. 14 (2013) 1071–1078. https://doi.org/10.1007/s12541-013-0144-5.

[133] K. Willemsen, R. Nizak, H.J. Noordmans, R.M. Castelein, H. Weinans, M.C. Kruyt, Challenges in the design and regulatory approval of 3D-printed surgical implants: a two-case series, Lancet Digit. Heal. 1 (2019) e163–e171. https://doi.org/10.1016/S2589-7500(19)30067-6.

[134] J. Kang, E. Dong, D. Li, S. Dong, C. Zhang, L. Wang, Anisotropy characteristics of microstructures for bone substitutes and porous implants with application of additive manufacturing in orthopaedic, Mater. Des. 191 (2020) 108608. https://doi.org/10.1016/j.matdes.2020.108608.

[135] S. Kumar, S. Tan, L. Zheng, D.M. Kochmann, Inverse-designed spinodoid metamaterials, Springer US, 2020. https://doi.org/10.1038/s41524-020-0341-6.

[136] A. Andrade, M. Costa, L. Paolucci, A. Braga, F. Pires, H. Ugrinowitsch, H.J. Menzel, A new training algorithm using artificial neural networks to classify gender-specific dynamic gait patterns, Comput. Methods Biomech. Biomed. Engin. 18 (2015) 382–390. https://doi.org/10.1080/10255842.2013.803081.

[137] V. Hernandez, N. Rezzoug, P. Gorce, G. Venture, Force feasible set prediction with artificial neural network and musculoskeletal model, Comput. Methods Biomech. Biomed. Engin. 21 (2018) 740–749. https://doi.org/10.1080/10255842.2018.1516763.

[138] M.C. Messner, Convolutional Neural Network Surrogate Models for the Mechanical Properties of Periodic Structures, J. Mech. Des. 142 (2020) 1–6. https://doi.org/10.1115/1.4045040.

[139] L. Wu, L. Liu, Y. Wang, Z. Zhai, H. Zhuang, D. Krishnaraju, Q. Wang, H. Jiang, A machine learning-based method to design modular metamaterials, Extrem. Mech. Lett. 36 (2020) 100657. https://doi.org/10.1016/j.eml.2020.100657.

[140] F. Liu, X. Jiang, X. Wang, L. Wang, Machine learning-based design and optimization of curved beams for multistable structures and metamaterials, Extrem. Mech. Lett. 41 (2020) 101002. https://doi.org/10.1016/j.eml.2020.101002.

[141] G.X. Gu, C.T. Chen, M.J. Buehler, De novo composite design based on machine learning algorithm, Extrem. Mech. Lett. 18 (2018) 19–28. https://doi.org/10.1016/j.eml.2017.10.001.

[142] S. Bonfanti, R. Guerra, F. Font-Clos, D. Rayneau-Kirkhope, S. Zapperi, Automatic design of mechanical metamaterial actuators, Nat. Commun. 11 (2020) 1–10. https://doi.org/10.1038/s41467-020-17947-2.

[143] P.Z. Hanakata, E.D. Cubuk, D.K. Campbell, H.S. Park, Accelerated Search and Design of Stretchable Graphene Kirigami Using Machine Learning, Phys. Rev. Lett. 121 (2018) 255304. https://doi.org/10.1103/PhysRevLett.121.255304.

[144] L. Wang, Y.C. Chan, F. Ahmed, Z. Liu, P. Zhu, W. Chen, Deep generative modeling for mechanistic-based learning and design of metamaterial systems, Comput. Methods Appl. Mech. Eng. 372 (2020) 113377. https://doi.org/10.1016/j.cma.2020.113377.

[145] T. Xue, T.J. Wallin, Y. Menguc, S. Adriaenssens, M. Chiaramonte, Machine learning generative models for automatic design of multi-material 3D printed composite solids, Extrem. Mech. Lett. 41 (2020) 100992. https://doi.org/10.1016/j.eml.2020.100992.

[146] Y. Kiarashinejad, S. Abdollahramezani, A. Adibi, Deep learning approach based on dimensionality reduction for designing electromagnetic nanostructures, Npj Comput. Mater. 6 (2020) 1–12. https://doi.org/10.1038/s41524-020-0276-y.

[147] A. Kurtz, intralattice, Github. (2015). https://github.com/dnkrtz/intralattice.

[148] G.D. Cheng, Y.W. Cai, L. Xu, Novel implementation of homogenization method to predict effective properties of periodic materials, Acta Mech. Sin. Xuebao. 29 (2013) 550–556. https://doi.org/10.1007/s10409-013-0043-0.

[149] A. Panesar, M. Abdi, D. Hickman, I. Ashcroft, Strategies for functionally graded lattice structures derived using topology optimisation for Additive Manufacturing, Addit. Manuf. 19 (2018) 81–94. https://doi.org/10.1016/j.addma.2017.11.008.

[150] M.J. Harding, S. Brady, H. O'Connor, R. Lopez-Rodriguez, M.D. Edwards, S. Tracy, D. Dowling, G. Gibson, K.P. Girard, S. Ferguson, 3D printing of PEEK reactors for flow chemistry and continuous chemical processing, React. Chem. Eng. 5 (2020) 728–735. https://doi.org/10.1039/c9re00408d.

[151] D.A. Dupré, D.J. Cook, J.B. Bellotte, M.Y. Oh, D. Whiting, B.C. Cheng, Disc nucleus fortification for lumbar degenerative disc disease: A biomechanical study, J. Neurosurg. Spine.

24 (2016) 708–714. https://doi.org/10.3171/2015.8.SPINE141043.

[152] W. Ma, Z. Liu, Z.A. Kudyshev, A. Boltasseva, W. Cai, Y. Liu, Deep learning for the design of photonic structures, Nat. Photonics. 15 (2021) 77–90. https://doi.org/10.1038/s41566-020-0685-y.

[153] A.A. Zadpoor, Mechanical meta-materials, Mater. Horizons. 3 (2016) 371–381. https://doi.org/10.1039/c6mh00065g.

[154] G.W. Milton, A. V. Cherkaev, Which elasticity tensors are realizable?, J. Eng. Mater. Technol. Trans. ASME. 117 (1995) 483–493. https://doi.org/10.1115/1.2804743.

[155] M. Kadic, T. Bückmann, R. Schittny, M. Wegener, On anisotropic versions of three-dimensional pentamode metamaterials, New J. Phys. 15 (2013). https://doi.org/10.1088/1367-2630/15/2/023029.

[156] J.N. Grima, R. Caruana-Gauci, Mechanical metamaterials: Materials that push back, Nat. Mater. 11 (2012) 565–566. https://doi.org/10.1038/nmat3364.

[157] R. Gatt, J.N. Grima, Negative compressibility, Phys. Status Solidi - Rapid Res. Lett. 2 (2008) 236–238. https://doi.org/10.1002/pssr.200802101.

[158] L.R. Meza, S. Das, J.R. Greer, Strong, lightweight, and recoverable three-dimensional ceramic nanolattices, Science (80-.). 345 (2014) 1322–1326. https://doi.org/10.1126/science.1255908.

[159] R. Lakes, K.W. Wojciechowski, Negative compressibility, negative Poisson's ratio, and stability, Phys. Status Solidi Basic Res. 245 (2008) 545–551. https://doi.org/10.1002/pssb.200777708.

[160] C. Kern, V. Schuster, M. Kadic, M. Wegener, Experiments on the Parallel Hall Effect in Three-Dimensional Metamaterials, Phys. Rev. Appl. 7 (2017) 1–6. https://doi.org/10.1103/PhysRevApplied.7.044001.

[161] M. Beecroft, Digital interlooping: 3D printing of weft-knitted textile-based tubular structures using selective laser sintering of nylon powder, Int. J. Fash. Des. Technol. Educ. 12 (2019) 218–224. https://doi.org/10.1080/17543266.2019.1573269.

[162] D. Sim, Roman Chain-Mail: Experiments to Reproduce the Techniques of Manufacture, Britannia. 28 (1997) 359. https://doi.org/10.2307/526776.

[163] G. Torrens, I. Campbell, W. Tutton, Design issues in military footwear and handwear, Woodhead Publishing Limited, 2012. https://doi.org/10.1016/B978-1-84569-699-3.50007-4.

[164] J.M. Chua, NASA Eyeing "Chain Mail" Fabric for Use in Space, (2017). https://www.space.com/36719-nasa-chain-mail-space-fabric.html (accessed November 3, 2019).

[165] M. Ransley, P. Smitham, M. Miodownik, Active chainmail fabrics for soft robotic applications, (2017).

[166] J. Engel, C. Liu, Creation of a metallic micromachined chain mail fabric, J. Micromechanics Microengineering. 17 (2007) 551–556. https://doi.org/10.1088/0960-1317/17/3/018.

[167] S. Misra, K.T. Ramesh, A.M. Okamura, Modeling of tool-tissue interactions for computer-based surgical simulation: A literature review, Presence Teleoperators Virtual Environ. 17 (2008) 463–491. https://doi.org/10.1162/pres.17.5.463.

[168] U.M. Ayturk, J.J. Garcia, C.M. Puttlitz, The micromechanical role of the annulus fibrosus components under physiological loading of the lumbar spine, J. Biomech. Eng. 132 (2010) 2–9. https://doi.org/10.1115/1.4001032.

[169] Y. Ma, X. Feng, J.A. Rogers, Y. Huang, Y. Zhang, Design and application of "J-shaped" stress-strain behavior in stretchable electronics: A review, Lab Chip. 17 (2017) 1689–1704. https://doi.org/10.1039/c7lc00289k.

[170] E.B. Van Der Houwen, P. Baron, A.G. Veldhuizen, J.G.M. Burgerhof, P.M.A. Van Ooijen, G.J. Verkerke, Geometry of the intervertebral volume and vertebral endplates of the human spine, Ann. Biomed. Eng. 38 (2010) 33–40. https://doi.org/10.1007/s10439-009-9827-6.

[171] S. Saleem, H.M. Aslam, M.A.K. Rehmani, A. Raees, A.A. Alvi, J. Ashraf, Lumbar disc degenerative disease: Disc degeneration symptoms and magnetic resonance image findings, Asian Spine J. 7 (2013) 322–334. https://doi.org/10.4184/asj.2013.7.4.322.

[172] T.S. Lumpe, J. Mueller, K. Shea, Tensile properties of multi-material interfaces in 3D printed parts, Mater. Des. 162 (2019) 1–9. https://doi.org/10.1016/j.matdes.2018.11.024.

[173] J. Mueller, K. Shea, Buckling, build orientation, and scaling effects in 3D printed lattices, Mater. Today Commun. 17 (2018) 69–75. https://doi.org/10.1016/j.mtcomm.2018.08.013.

[174] B.W. Cunningham, J.D. Gordon, A.E. Dmitriev, N. Hu, P.C. Mcafee, Biomechanical Evaluation of Total Disc Replacement Arthroplasty : An In Vitro Human Cadaveric Model, 28 (2003) 110–117.

[175] C. Bogani, M.G. Gasparo, A. Papini, Generalized Pattern Search methods for a class of nonsmooth optimization problems with structure, J. Comput. Appl. Math. 229 (2009) 283–293. https://doi.org/10.1016/j.cam.2008.10.047.

[176] S. Le Digabel, Algorithm 909:NOMAD: Nonlinear Optimization with the MADS Algorithm, ACM Trans. Math. Softw. 37 (2011) 1–15. https://doi.org/10.1145/1916461.1916468.

[177] V. Gardeux, M.G. Mahamed, R. Chelouah, P. Siarry, F. Glover, Adaptive pattern search for

large-scale optimization, Appl. Intell. 47 (2017) 319–330. https://doi.org/10.1007/s10489-017-0901-8.

[178] G. Michaela, H. Denise, M. Liebensteiner, B.C. Michael, Footprint mismatch in lumbar total disc arthroplasty, Eur. Spine J. 17 (2008) 1470–1475. https://doi.org/10.1007/s00586-008-0780-0.

[179] A.M. Ellingson, D.J. Nuckley, Altered helical axis patterns of the lumbar spine indicate increased instability with disc degeneration, J. Biomech. 48 (2015) 361–369. https://doi.org/10.1016/j.jbiomech.2014.11.010.

[180] W. Anderst, E. Baillargeon, W. Donaldson, J. Lee, J. Kang, Motion path of the instant center of rotation in the cervical spine during in vivo dynamic flexion-extension: Implications for artificial disc design and evaluation of motion quality after arthrodesis, Spine (Phila. Pa. 1976). 38 (2013). https://doi.org/10.1097/BRS.0b013e31828ca5c7.

[181] S.D. Gertzbein, J. Seligman, R. Holtby, K.W. Chan, N. Ogston, A. Kapasouri, M. Tile, Centrode characteristics of the lumbar spine as a function of segmental instability, Clin. Orthop. Relat. Res. 208 (1986) 48–51.

[182] M.A. Rousseau, D.S. Bradford, T.M. Hadi, K.L. Pedersen, J.C. Lotz, The instant axis of rotation influences facet forces at L5/S1 during flexion/extension and lateral bending, Eur. Spine J. 15 (2006) 299–307. https://doi.org/10.1007/s00586-005-0935-1.

[183] H. Hwang, J.A. Hipp, P. Ben-Galim, C.A. Reitman, Threshold cervical range-of-motion necessary to detect abnormal intervertebral motion in cervical spine radiographs, Spine (Phila. Pa. 1976). 33 (2008) 261–267. https://doi.org/10.1097/BRS.0b013e31816b88a4.

[184] N. Subramanian, C.A. Reitman, L. Nguyen, J.A. Hipp, Radiographic assessment and quantitative motion analysis of the cervical spine after serial sectioning of the anterior ligamentous structures, Spine (Phila. Pa. 1976). 32 (2007) 518–526. https://doi.org/10.1097/01.brs.0000256449.95667.13.

[185] P. Gédet, P.A. Thistlethwaite, S.J. Ferguson, Minimizing errors during in vitro testing of multisegmental spine specimens: Considerations for component selection and kinematic measurement, J. Biomech. 40 (2007) 1881–1885. https://doi.org/10.1016/j.jbiomech.2006.07.024.

[186] M.A. Stadelmann, G. Maquer, B. Voumard, A. Grant, D.B. Hackney, P. Vermathen, R.N. Alkalay, P.K. Zysset, Integrating MRI-based geometry, composition and fiber architecture in a finite element model of the human intervertebral disc, J. Mech. Behav. Biomed. Mater. 85 (2018) 37–42. https://doi.org/10.1016/j.jmbbm.2018.05.005.

[187] M.A. Stadelmann, G. Maquer, B. Voumard, A. Grant, D.B. Hackney, P. Vermathen, R.N. Alkalay, P.K. Zysset, Integrating MRI-based geometry, composition and fiber architecture in a finite element model of the human intervertebral disc, J. Mech. Behav. Biomed. Mater. 85 (2018) 37–42. https://doi.org/10.1016/j.jmbbm.2018.05.005.

[188] C.W. Spoor, F.E. Veldpaus, Rigid body motion calculated from spatial co-ordinates of markers, J. Biomech. 13 (1980) 391–393.

[189] J. Mueller, K. Shea, C. Daraio, Mechanical properties of parts fabricated with inkjet 3D printing through efficient experimental design, Mater. Des. 86 (2015) 902–912. https://doi.org/10.1016/j.matdes.2015.07.129.

[190] S.A. Zirbel, D.K. Stolworthy, L.L. Howell, A.E. Bowden, Intervertebral disc degeneration alters lumbar spine segmental stiffness in all modes of loading under a compressive follower load, Spine J. 13 (2013) 1134–1147. https://doi.org/10.1016/j.spinee.2013.02.010.

[191] N. Newell, D. Carpanen, G. Grigoriadis, J.P. Little, S.D. Masouros, Material properties of human lumbar intervertebral discs across strain rates, Spine J. 19 (2019) 2013–2024. https://doi.org/10.1016/j.spinee.2019.07.012.

[192] M.C. Dahl, S. Jacobsen, N. Metcalf Jr, R. Sasso, R.P. Ching, A comparison of the shock-absorbing properties of cervical disc prosthesis bearing materials, ESAS. 5 (2011) 48–54. https://doi.org/10.1016/j.esas.2011.01.002.

[193] H. Schmidt, S. Midderhoff, K. Adkins, H.J. Wilke, The effect of different design concepts in lumbar total disc arthroplasty on the range of motion, facet joint forces and instantaneous center of rotation of a L4-5 segment, Eur. Spine J. 18 (2009) 1695–1705. https://doi.org/10.1007/s00586-009-1146-y.

[194] M.R. Silva, A.M. Pereira, Á.M. Sampaio, A.J. Pontes, Assessment of the dimensional and geometric precision of micro-details produced by material jetting, Materials (Basel). 14 (2021) 1–18. https://doi.org/10.3390/ma14081989.

[195] R.D. Guyer, L.I. Voronov, R.M. Havey, S. Khayatzadeh, G. Carandang, K.R. Blank, S. Werner, J. Rubin, N. Padovani, A.G. Patwardhan, Kinematic assessment of an elastic-core cervical disc prosthesis in one and two-level constructs, JOR Spine. 1 (2018) e1040. https://doi.org/10.1002/jsp2.1040.

[196] G.R. Buttermann, B.P. Beaubien, Biomechanical characterization of an annulus-sparing spinal disc prosthesis, Spine J. 9 (2009) 744–753.

[197] B.P. Beaubien, A. Derincek, W.D. Lew, K.B. Wood, In vitro, biomechanical comparison of an anterior lumbar interbody fusion with an anteriorly placed, low-profile lumbar plate and

posteriorly placed pedicle screws or translaminar screws, Spine (Phila. Pa. 1976). 30 (2005) 1846–1851. https://doi.org/10.1097/01.brs.0000174275.95104.12.

[198] M.G. Gardner-Morse, I.A. Stokes, Physiological axial compressive preloads increase motion segment stiffness, linearity and hysteresis in all six degrees of freedom for small displacements about the neutral posture, J. Orthop. Res. 21 (2003) 547–552. https://doi.org/10.1016/S0736-0266(02)00199-7.

[199] H. Schmidt, F. Heuer, H.J. Wilke, Interaction between finite helical axes and facet joint forces under combined loading., Spine (Phila. Pa. 1976). 33 (2008) 2741–2748. https://doi.org/10.1097/brs.0b013e31817c4319.

[200] M. Takahata, Y. Kotani, K. Abumi, Y. Shikinami, T. Kadosawa, K. Kaneda, A. Minami, Bone ingrowth fixation of artificial intervertebral disc consisting of bioceramic-coated three-dimensional fabric, Spine (Phila. Pa. 1976). 28 (2003) 637–644. https://doi.org/10.1097/01.BRS.0000051918.47287.3E.

[201] S.E. Bezci, A. Eleswarapu, E.O. Klineberg, G.D. O'Connell, Contribution of facet joints, axial compression, and composition to human lumbar disc torsion mechanics, J. Orthop. Res. 36 (2018) 2266–2273. https://doi.org/10.1002/jor.23870.

[202] O.H. Yeoh, Some forms of the strain energy function for rubber, Rubber Chem. Technol. 66 (1993) 754–771.

[203] R.S. Marlow, A general first-invariant hyperelastic constitutive model, Const. Model. Rubber. (2003) 157–160.

[204] E.M. Arruda, M.C. Boyce, A three-dimensional constitutive model for the large stretch behavior of rubber elastic materials, J. Mech. Phys. Solids. 41 (1993) 389–412.

[205] S.E. Bezci, A. Nandy, G.D. O'Connell, Effect of hydration on healthy intervertebral disk mechanical stiffness, J. Biomech. Eng. 137 (2015) 1–8. https://doi.org/10.1115/1.4031416.

[206] H. Schmidt, A. Shirazi-Adl, C. Schilling, M. Dreischarf, Preload substantially influences the intervertebral disc stiffness in loading-unloading cycles of compression, J. Biomech. 49 (2016) 1926–1932. https://doi.org/10.1016/j.jbiomech.2016.05.006.

[207] J.N. Grima, K.E. Evans, Auxetic behavior from rotating triangles, J. Mater. Sci. 41 (2006) 3193–3196. https://doi.org/10.1007/s10853-006-6339-8.

[208] K. Golec, K. Golec, H. Mass, S. System, T. Simulation, C.L.B.E.L. Yon, Hybrid 3D Mass Spring System for Soft Tissue Simulation To cite this version : HAL Id : tel-01761851 Hybrid 3D Mass Spring System for Soft Tissue Simulation, (2018).

[209] D.F. Williams, On the mechanisms of biocompatibility, Biomaterials. 29 (2008) 2941–2953. https://doi.org/10.1016/j.biomaterials.2008.04.023.

[210] R. Du, Y.X. Su, Y. Yan, W.S. Choi, W.F. Yang, C. Zhang, X. Chen, J.P. Curtin, J. Ouyang, B. Zhang, A Systematic Approach for Making 3D-Printed Patient-Specific Implants for Craniomaxillofacial Reconstruction, Engineering. 6 (2020) 1291–1301. https://doi.org/10.1016/j.eng.2020.02.019.

[211] N. Kozic, S. Weber, P. Büchler, C. Lutz, N. Reimers, M.Á. González Ballester, M. Reyes, Optimisation of orthopaedic implant design using statistical shape space analysis based on level sets, Med. Image Anal. 14 (2010) 265–275. https://doi.org/10.1016/j.media.2010.02.008.

[212] J. Li, J. Egger, Towards the Automatization of Cranial Implant Design in Cranioplasty, Springer, 2020.

[213] A. Fedorov, R. Beichel, J. Kalpathy-Cramer, J. Finet, J.-C. Fillion-Robin, S. Pujol, C. Bauer, D. Jennings, F. Fennessy, M. Sonka, 3D Slicer as an image computing platform for the Quantitative Imaging Network, Magn. Reson. Imaging. 30 (2012) 1323–1341.

[214] T. Stanković, J. Mueller, K. Shea, The effect of anisotropy on the optimization of additively manufactured lattice structures, Addit. Manuf. 17 (2017) 67–76. https://doi.org/10.1016/j.addma.2017.07.004.

[215] L.H.S. Sekhon, J.R. Ball, Artificial cervical disc replacement: Principles, types and techniques, Neurol. India. 53 (2005) 445–450. https://doi.org/10.4103/0028-3886.22611.

[216] H. Schmidt, A. Kettler, A. Rohlmann, L. Claes, H.J. Wilke, The risk of disc prolapses with complex loading in different degrees of disc degeneration - A finite element analysis, Clin. Biomech. 22 (2007) 988–998. https://doi.org/10.1016/j.clinbiomech.2007.07.008.

[217] A.F. von Recum, Handbook of biomaterials evaluation: scientific, technical and clinical testing of implant materials, CRC Press, 1998.

[218] J.J. Tobin, G. Walsh, Medical product regulatory affairs: pharmaceuticals, diagnostics, medical devices, John Wiley & Sons, 2008.

[219] R.J. Klepinski, Old customs, ancient lore: the development of custom device law through neglect, Food Drug LJ. 61 (2006) 237.

[220] Center for Devices and Radiological Health, Custom Device Exemption: Guidance for Industry and Food and Drug Administration Staff Public Comment, (2014).

[221] L.B. Moses, Regulating in the face of sociotechnical change, in: Oxford Handb. Law, Regul. Technol., 2017.

[222] Therapeutic Goods Administration, Proposed regulatory changes related to personalised and 3D printed medical devices - Consultation paper, (2017).